

University of Eastern Piedmont “Amedeo Avogadro”

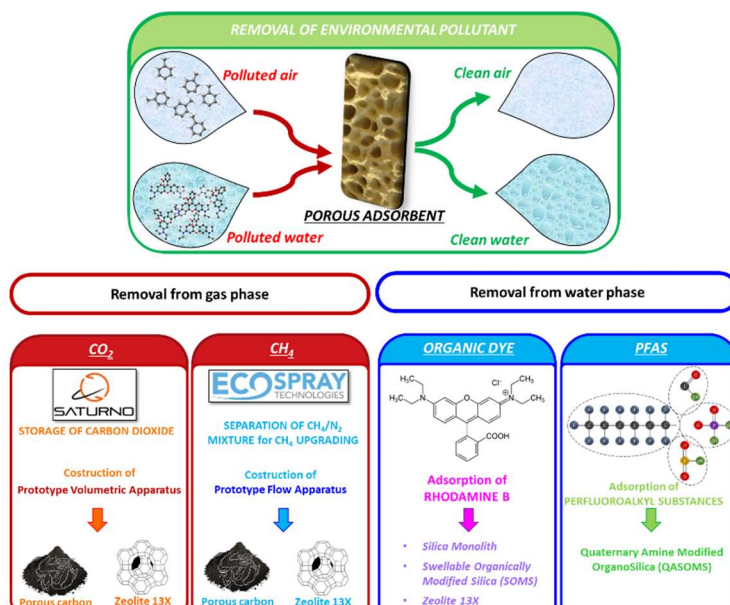
Department of Sciences and Technological Innovation

Ph.D. Program in “Chemistry & Biology”

Cycle XXXV, a.y. 2019-2022

SSD: CHIM02

Optimization of porous materials for environmental purposes



Vanessa Miglio

Supervisor: Prof.ssa Chiara Bisio

Ph.D. Program Co-Ordinator: Prof. Gian Cesare Tron

University of Eastern Piedmont “Amedeo Avogadro”

Department of Sciences and Technological Innovation

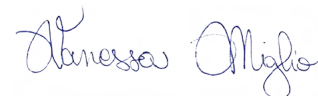
Ph.D. Program in “Chemistry & Biology”

Cycle XXXV, a.y. 2019-2022

SSD: CHIM02

***Optimization of porous materials for
environmental purposes***

Vanessa Miglio



Supervisor: Prof.ssa Chiara Bisio



Ph.D. Program Co-Ordinator: Prof. Gian Cesare Tron



UNIVERSITÀ DEL PIEMONTE ORIENTALE

DOTTORATO DI RICERCA
IN CHEMISTRY & BIOLOGY

Via Duomo, 6
13100 – Vercelli (ITALY)

DECLARATION AND AUTHORISATION TO ANTIPLAGIARISM DETECTION

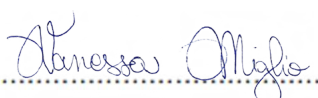
The undersigned **Vanessa Miglio** student of the Chemistry & Biology
Ph.D course (XXXV Cycle)

declares:

- to be aware that the University has adopted a web-based service to detect plagiarism through a software system called “Turnit.in”,
- his/her Ph.D. thesis was submitted to Turnit.in scan and reasonably it resulted an original document, which correctly cites the literature;

acknowledges:

- his/her Ph.D. thesis can be verified by his/her Ph.D. tutor and/or Ph.D Coordinator in order to confirm its originality.

Date: 10/11/2022 Signature: 

Contents

Chapter 1	1
<i>Methodologies for the removal of environmental pollutants</i>	
Introduction	2
1.1 Environmental pollution	3
1.1.1 Evidence of climate change	4
1.1.2 Environmental agreements for climate change remediation	6
1.2 Air Pollution	10
1.2.1 Greenhouse Effect	11
1.3 CO ₂ and CH ₄ greenhouses gases	16
1.3.1 CO ₂ storage	16
1.3.2 Adsorbent materials for the removal of CO ₂	21
1.3.3 Methane storage and biomethane production	25
1.4 Water pollution	33
1.5 Remediation of water pollutants	37
1.5.1 Organic Dye: Rhodamine B	37
1.5.2 Perfluoroalkyl substances (PFAS)	41
Conclusions	46
References	47
Chapter 2	69
<i>Outline</i>	
References	74
Chapter 3	75
<i>Synthesis and characterization of silica-based materials for environmental purposes</i>	
Introduction	76
3.1 Silica monoliths	77
3.1.1 Synthesis of Silica Monoliths	80
3.1.2 Characterization of Silica Monoliths	81
3.2 Swellable Organically Modified Silica (SOMS)	85
3.2.1 Quaternary Amine Modified Organosilica (QA-SOMS)	88
3.2.2 Synthesis of SOMS	90
3.2.3 Synthesis of QA-SOMS	94

3.2.4	Characterization of Silica-SOMS	94
3.2.5	Characterization of Silica-QA-SOMS	105
3.3	Commercial Zeolite	115
3.3.1	Characterization of Zeolite 13X	116
	Conclusions	122
	References	123
Chapter 4		129
	<i>Porous carbons for environmental purposes</i>	
	Introduction	130
4.1	Activated Porous Carbons	131
4.1.1	Methods for the preparation of activated carbons	133
4.1.2	Chemical activation with KOH	133
4.2	Physico-chemical properties of commercial porous carbons	135
4.3	Porous carbons derived from Hyper Cross-linked Polymers (HCPs)	143
4.3.1	Hyper Cross-linked Polymers (HCPs)	143
4.3.1.1	Preparation methodology of HCP from polystyrene waste (HCP-PS)	146
4.3.2	Synthesis of HCP-PS	148
4.3.3	Characterization of HCP-PS	148
4.3.4	Synthesis of porous carbon (C-PS) from HCP-PS	151
4.3.5	Characterization of C-PS	152
	Conclusions	153
	References	156
Chapter 5		161
	<i>Prototype for gas adsorption measurements</i>	
	Introduction	162
5.1	Volumetric apparatus for gas adsorption in static conditions	163
5.1.1	Calibration of the components of the system	164
5.1.2	Operating method for adsorption measurements	167
5.1.3	Validation of measurements	172
5.2	Volumetric apparatus for adsorption measurements in flow conditions	174

Conclusions	178
References	179
Chapter 6	181
<i>Study of carbon dioxide storage capacity by porous carbons and Valorisation of biomethane</i>	
Introduction	182
6.1 CO ₂ adsorption isotherms	184
6.2 CH ₄ adsorption isotherms	191
6.3 N ₂ adsorption isotherms	195
6.4 Adsorption measurements in flow conditions	198
6.4.1 Adsorption measurements of the 85% CH ₄ – 15% N ₂ gas mixture	198
6.4.2 Adsorption measurements of the 50% CH ₄ – 50% N ₂ gas mixture	201
Conclusions	203
References	205
Chapter 7	209
<i>Evaluation of the adsorption properties of inorganic and hybrid organic-inorganic materials from liquid phase</i>	
Introduction	210
7.1 Removal of Rhodamine B using inorganic and hybrid organic-inorganic materials	211
7.1.1 Experimental conditions	212
7.1.2 Study of the regeneration capacity of Silica-SOMS after Rhodamine B adsorption	218
7.2 Removal of Perfluorinated Alkyl Substances (PFAS)	221
7.2.1 Liquid phase NMR spectroscopy for the determination of PFAS concentration in solution	224
7.2.2 Silica-QA-SOMS for PFAS removal	229
7.2.3 Study of PFAS adsorption kinetic	234
7.2.4 Study of the interaction between the Silica-QA-SOMS and PFAS molecules by solid state NMR spectroscopy	236
Conclusions	245
References	247

Chapter 8	251
<i>General Conclusion</i>	
List of publications	259
Acknowledgement	261
Appendix	265
<i>Instrumental parameters</i>	

Chapter 1

Methodologies for the removal of environmental pollutants

Introduction

Environmental pollution is one of the most significant problems facing humanity and other living things on Earth today; it is defined as “the contamination of the physical and biological components of the Earth/atmosphere system to such an extent that normal environmental processes are impaired”^[1].

Pollution is a change in the environment that occurs when something is introduced into it that is harmful to ecosystems and the health of living things.

Pollutants may be substances that already exist in nature, but they become contaminants when they exceed natural levels. Any use of natural resources to an extent that exceeds nature's ability to regenerate itself can result in pollution of any environmental compartment.

In general, when the environment is unable to manage and neutralize harmful by-products of human activities without suffering structural or functional impairment to its system, pollution takes place.

Due to population growth, technological progress, and urbanization, the demand for natural resources on earth is great and constantly increasing.

There are three primary types of pollution: air, water, and soil.

In this introductory chapter, an overview of air and water pollution is given. Special attention is given to the main types of pollutants found in these environmental compartments and the consequences associated with them.

Since the focus of this thesis is on the use of porous materials for pollutant removal, the types of pollutants used in subsequent chapters are presented in more detail.

1.1 Environmental pollution

Pollution is one of the greatest global emergencies facing society today, and it must be addressed and eliminated for the sake of the health and preservation of the planet^[2]. Although it has always existed, it increased significantly at the turn of the 19th century with the onset of the Industrial Revolution^[3]. As the population grew, industry also developed rapidly, leading to an increase in anthropogenic activities. The constant increase in energy demand as a result of technological development has adversely affected the environment in the form of environmental degradation and pollution.

Pollutants may result from harmful by-products of human activities or they may be products of natural origin, and in this case they are considered as such only if they are present beyond normal levels. Man-made pollutants may be chemical, biological, or nuclear^[4]. Many industrial activities, such as manufacturing, agriculture, transportation, etc., have been releasing large amounts of pollutants in various forms into the air, water, and soil for decades. For example, the most common pollutants include greenhouse gases, nitrogen oxides (NO_x), sulphur oxides, suspended particulate matter, volatile organic compounds (VOCs), polycyclic aromatic hydrocarbons (PAHs), pesticides, herbicides, insecticides, narcotics, hydrocarbons, heavy metals, pathogens, mutagens, and teratogens^[5].

If these substances remain in the environment for a long period, they can bioaccumulate and affect the health of living beings. Therefore, it is very important to limit their emissions as much as possible, increasing eco-efficiency in various industries, and removing pollutants already present in various environmental compartments^[6].

1.1.1 Evidence of climate change

Climate is defined as “the complex of weather conditions that characterize a place or region in the course of a year, averaged over a long period of time”^[7], *i.e.*, it is a statistical description in terms of averages and variations of significant quantities over a period of months to millions of years. According to the definition of the World Meteorological Organization, the classical averaging period is 30 years.

Human-induced changes overlap with naturally occurring changes and generally extend over time periods much longer than the human lifetime. Climate change is a permanent change in weather conditions: it includes regular changes in temperature, precipitation, humidity, and wind intensity, as well as sea level rise and changes in the incidence of extreme events^[8]. Because of these changes, the integrity and survival of many species are at risk, accelerating biodiversity loss and increasingly altering ecosystem structures^[9].

Climate data such as the global temperature rise of the earth, the air and the oceans, the rise of the sea level, the loss of ice at the earth's poles and in mountain glaciers provide clear evidence that global warming of the planet is taking place^[10]. According to scientists at the National Oceanic and Atmospheric Administration (NOAA), the global surface temperature in 2021 was the sixth-highest since 1880^[11]. In an independent analysis of global temperature data, NASA found that 2021 was the sixth-warmest year on record. The average global surface temperature in December 2021, along with that of 2016, was the fifth highest in the 142 recorded, exceeding the 20th century average by 0.84°C^[11].

Figure 1.1 shows annual global temperatures from 1880 to 2021 compared with the 20th century average.

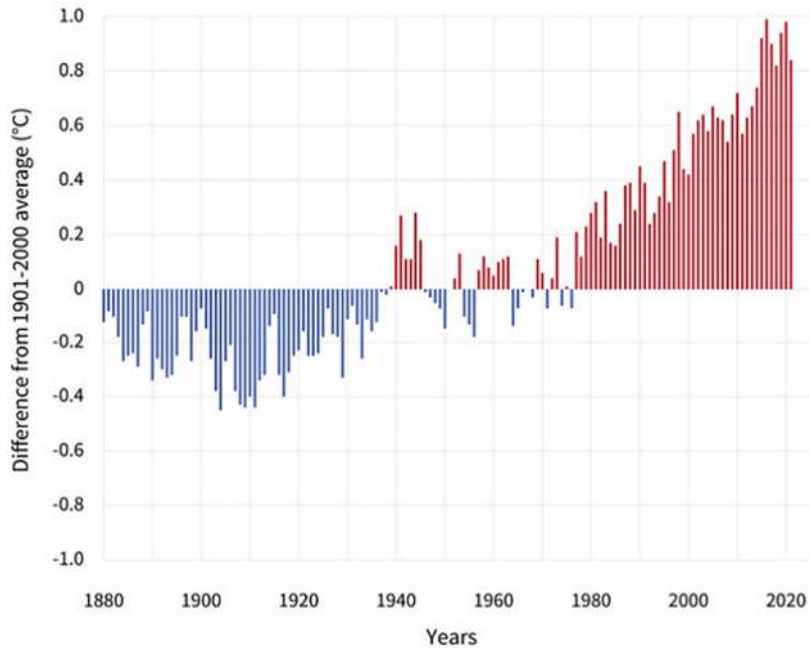


Figure 1.1 – Global average surface temperature from 1880 to 2021. Data from NOAA NCEI^[12].

The Northern hemisphere surface temperature in 2021 was 1.09°C higher than the 20th century average^[11]. Global land and ocean temperatures in 2021 were 1.04°C above average. From 1880 until 1981 the annual global surface temperature increased by an average of +0.08°C per decade; after that the average rate of increase has more than doubled (+0.18°C)^[11].

In addition to rising global land, air, and ocean temperatures, climate change has also led to loss of ice at the earth's poles and in mountain glaciers, rising sea levels, and an intensification in the frequency and severity of extreme weather phenomena such as heat waves, forest fires, hurricanes, floods, droughts, and precipitation, and changes in vegetation and cloud cover^[13,14].

The Global Heat Content stored in the Oceanic belts (OHC), has increased continuously since 2015, reaching an all-time high in 2021^[11]. Both Arctic and Antarctic sea ice extent also varied significantly^[11].

In recent decades, certain types of extreme weather events have changed around the world. For example, in addition to an increase in phenomena such as extreme

precipitation, droughts and wildfires, floods, hurricanes and tornadoes, there have been many more extreme heat waves and less frequent but more intense cold waves^[11,14,15].

Climate change also has a major impact on human health, accelerating resistance to antimicrobials and increasing the likelihood of contracting certain food-, water-, and vector-borne diseases; a recent example is the coronavirus pandemic^[16].

1.1.2 Environmental Agreements for climate change remediation

International Environmental Law (IEL) is a authority that involves the whole world population in the safeguard of the environment^[17]. This comprehensive discipline is based on a compendium of statements, treaties and rules that have developed simultaneously with scientific knowledge and consciousness of the recent state of the climate situation.

Prior to the 1960s, environmental awareness was low, and international initiatives to regulate the environment were few and isolated. Everything changed when the community, scientific and otherwise, became aware of the dangers threatening the Earth.

The first United Nations Conference on the Human Environment produced the *Stockholm Declaration* (1972), the first essay to recognize the right to a healthy environment through 26 principles, including the principle of cooperation among states and the obligation of states to guarantee that activities under their jurisdiction do not harm the environment of other states^[18].

In addition, the United Nations General Assembly designed the United Nations Environment Program (UNEP), which is now the main agency for environmental issues^[19]. After Stockholm, national governments also began drafting numerous local environmental laws.

In 1983, the United Nations established the World Commission on Environment and Development (Brundtland Commission), which in 1987 produced the report *Our*

Common Future: the first document to discuss sustainable development, to meet the needs of the present, but with an eye toward the needs of future generations as well^[20].

At that time, some of today's global environmental problems began to emerge, making the need for international cooperation, especially between more developed and poorer countries, even more apparent.

In 1987, the signing of the *Montreal Protocol* provided the first example of international cooperation to combat ozone depletion^[21].

In 1988, the Intergovernmental Panel on Climate Change (IPCC) was founded by the World Meteorological Organization (WMO) and by the United Nations Environment Program (UNEP). The IPCC is the principal international body responsible for reviewing and assessing the latest scientific, technical, and socioeconomic information on climate change, with the goal of providing the world with a clear and scientifically sound overview of the current state of knowledge on climate change and its potential ecological and socioeconomic impacts^[22].

In 1992, a conference was held in Rio De Janeiro where two conventions were presented for signature by national governments: the United Nations Framework Convention on Climate Change (UNFCCC) and the Convention on Biological Diversity^[23]. The *Rio Declaration* was also adopted, reaffirming the *Stockholm Declaration* and the *Agenda 21* action program, which continues to lead governments in their environmental protection activities^[24].

From that point on, all major economic treaties began to incorporate the goals of environmental protection and sustainable development.

In 1997, the Conference of the Parties (COP), composed of the signatories of the UNFCCC, presented the *Kyoto Protocol*, which provides for 38 developed countries and the European Union to reduce or limit greenhouse gas emissions^[25].

In 2000, in New York, 189 countries adopted the *Millennium Declaration*, recognizing the need for sustainable economic growth and development and being mindful of respect for human rights.^[26]

In 2002, in Johannesburg, 190 countries participated in the United Nations World Summit on Sustainable Development to fulfil the commitments made at the Rio Summit. There, they adopted the *Declaration on Sustainable Development*, which focuses on development and poverty reduction^[27].

Starting in 2008, the first commitment period of the Kyoto Protocol began: thirty-seven industrialized countries and the European Union pledged to reduce their emissions by an average of 5% below 1990 levels by 2012.

In 2009, at the Conference Of the Parties (COP15) in Copenhagen, developed countries signed the *Climate Finance Commitment*, pledging to mobilize \$100 billion in annual funding starting in 2020 to help developing countries implement mitigation and adaptation measures^[28].

In 2012, the United Nations hosted the *Third Conference on Sustainable Development*, which brought together 192 member states, private sector companies, nongovernmental and other organizations^[29]. The result was a non-binding document entitled “*The Future We Want*”; in this document, nations reaffirmed their commitment to ecological development and promoting a sustainable future.

That same year, the *Doha Amendment* was adopted, in which countries committed to reducing their emissions by at least 18 percent below 1990 levels by 2020^[30].

In 22 April 2016, the Earth’s Day, the *Paris Agreement* (2016) is signed, under which signatory countries commit to preventing the planet's average temperature from rising by 2°C, compared to pre-industrial levels, and to remain below a 1.5°C increase^[31]. In addition, the agreement aspires to strengthen the capacity of nations to address the effects of climate change by decreasing greenhouse gas emissions and increasing climate restoration pathways^[32,33]. The document requires all Parties to report regularly on their emissions and implementation activities. A comprehensive review will be conducted every five years to examine collective progress toward the goal of the agreement and inform future individual Party actions. The Agreement was initially ratified by 55 countries representing at least 55 percent of global emissions; by 2017, signatory countries had increased to 125.

Finally, in 2017 the Inter-American Court of Human Rights drafted *Advisory 23*, which affirmed that human rights depend on the existence of a healthy environment, and that climate change due to environmental degradation can undermine these rights^[34].

1.2 Air pollution

Air pollution is defined as “any change in the regular composition or physical state of air due to the presence in atmosphere of one or more substances in such quantity and with such characteristics as to: (I) alter the normal environmental and health conditions of the air; (II) constitute danger or direct or indirect harm to human health; (III) impair recreational activities and other legitimate uses of the environment; and (IV) alter biological resources and ecosystems and public and private material assets”^[35].

Air pollution occurs with the addition of harmful chemical, physical or biological substances to the earth's atmosphere^[36].

Air pollutants are generally classified into primary and secondary.

- *Primary pollutants* are released into the atmosphere directly as a result of the process that originated them, either due to human processes (e.g., combustion sources, industrial processes, vehicular activities, agriculture, mining, etc.) or natural processes (e.g., volcanic activities, dust storms, etc.)^[37].
- *Secondary pollutants*, on the other hand, are substances that are developed by chemical-physical reactions among the primary pollutants themselves or with substances in the atmosphere. They often involve atmospheric oxygen and can be activated by solar energy ^[38].

Each pollutant possesses a different residence time in the atmosphere, depending on its nature and stability; as long as it remains in the atmosphere it can contribute to pollution and to the eventual formation of secondary pollutants^[39]. In addition, pollutants are not only confined to a specific area, but can be transported over long distances; this can contribute to damage to different environmental areas.

Air pollution can cause serious health problems for both the ecosystem and living creatures. For example, it is associated with an increase in cardiovascular and

10

respiratory diseases (decreased lung function and increased respiratory symptoms such as shortness of breath, cough, and asthma), the occurrence of neurobehavioral disorders and damage to the central nervous system, disruption of the endocrine, reproductive, and immune systems, respiratory irritation, and the occurrence of cancers leading to premature death^[40,41].

Air pollutant can also cause damage to plants' health, altering their physiology, biochemistry and morphology^[42].

The main air pollutants that need to be monitored are carbon dioxide (CO₂), carbon monoxide (CO), chlorofluorocarbons (CFCs), sulphur dioxide (SO₂), volatile organic compounds (VOC_s), nitrogen oxides (NO_x), dioxins, polycyclic aromatic hydrocarbons (PAHs), particulate matter (PM), and suspended radioactive pollutants.

Among them, the so-called greenhouse gases produced by human activities deserve special mention, as they are responsible for amplifying the *Greenhouse Effect* associated with rising temperatures and, in particular, climate change.

1.2.1 Greenhouse Effect

Of all the energy emitted by the Sun, only a small portion (5.45×10^{24} J) is received by the Earth by radiative transmission^[43]. However, it is enough to create a climatic environment suitable for the life of living beings and has allowed their preservation over the past 3-4 billion years.

The climate change that afflicts our planet can be attributed mainly to anthropogenic activities due to the increasing urbanisation of population centres. This is due to the increased production of pollutants that are released into the atmosphere. This mainly involves the *Greenhouse Gases* (GHG), which are responsible for the progressive increase in average air temperature. Greenhouse gases produced and emitted on Earth (CO₂, CH₄, N₂, H₂O, O₃, NO_x, CFCs)^[44] remain trapped in the atmosphere, where they accumulate and interact with infrared radiation, limiting the propagation

of heat radiated by the Earth and causing an increase in global temperature (*Greenhouse Effect*)^[45]. The greenhouse effect (Figure 1.2) is in itself a natural phenomenon and is of fundamental importance as it enables the development of life on Earth: without it, the average temperature on Earth would be around -20 °C^[46]; whereas in reality it has been between 0 and 40 °C for the last billion years, with an average of 15 °C^[11].

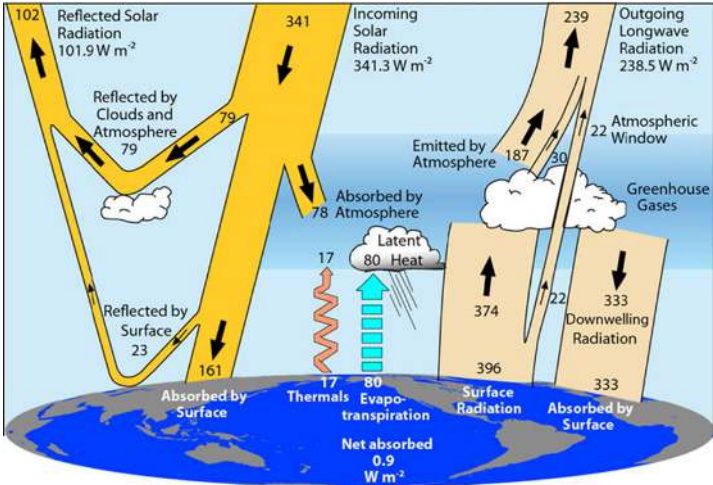


Figure 1.2 – Schematic representation of Global Sun-Earth Energy Flow (W/m²)^[47].

Most greenhouse gases, such as carbon dioxide (CO₂), methane (CH₄), nitrous oxide (N₂O), water vapour (H₂O), and ozone (O₃), occur naturally in the atmosphere as a result of geological activities and biological processes that have occurred during Earth's evolution. However, with population growth, anthropogenic activities such as fossil fuel burning, deforestation, agriculture, and industrial waste, etc., have also increased, so that the concentration of natural gases in the atmosphere has increased drastically^[8]. Due to the continuous increase in the development of industrial sectors and uncontrollable anthropogenic activities, the problem of emissions has become increasingly burdensome, negatively affecting human and ecosystem health^[48]. In addition, there is the concentration of synthetic greenhouse gases

(chlorofluorocarbons (CFCs), perfluorocarbons, hydrofluorocarbons, sulphur compounds, etc.).

The increase in greenhouse gas concentration in the atmosphere leads to an abnormal increase in temperature (*Enhanced Greenhouse Effect*) with associated climate complications such as altered precipitation patterns and severe weather events, melting of polar ice and extinction of species, rising sea levels, and receding snowpacks^[49]. In fact, even though the amount of solar energy Earth receives has followed the Sun's natural cycle, with no net increase since the 1950s, the Earth's global temperature has increased significantly (Figure 1.3).

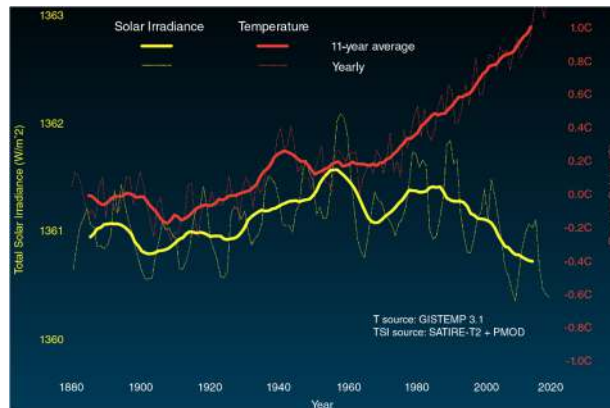


Figure 1.3 – Comparison of changes in global surface temperature (—) and the solar energy the Earth receives (—) in W/m^2 , since 1880^[10]. Credit: NASA/JPL-Caltech.

While the natural greenhouse effect has played an important role in keeping Earth's climate habitable, it is the intensification in this “*Enhanced Greenhouse Effect*”, resulting from the release of GHGs into the atmosphere due to increased human activity, that is causing the greatest global concern for our planet^[50]. The Intergovernmental Panel on Climate Change (IPCC) predicts a 3.7 °C increase in global average temperature by 2100^[51].

In developing a comprehensive strategy to reduce greenhouse gas emissions, it is important to quantitatively compare the contribution to the greenhouse effect of a given amount of each gas.

For this reason, a *Global Warming Potential* (GWP) index has been established, which is based on the ratio of the radiative forcing of an equal emission of two different gases^[52]; it expresses the contribution to the greenhouse effect of a GHGs relative to the effect of CO₂, whose reference potential is 1.

Each GWP value is calculated for a specific time interval (usually 20, 100, or 500 years).

Global warming potentials for various greenhouse gases are shown in Table 1.1.

Table 1.1 - Values of GWP of different gases, for 100-year time horizon^[53].

Gas	Lifetime (years)	Global Warming Potential
CO ₂	-	1
CH ₄	12	25
N ₂ O	114	298
CFC-11	45	4750
CFC-12	100	10900
SF ₆	3200	22800

Among the various GHGs, water vapor is the main culprit by absorbing the largest amount of infrared radiation; however, since its concentration in the atmosphere is definitely limited, it is neglected in the GWP calculation^[54].

The contribution of each gas to the greenhouse effect is mainly determined by its radiative effect, abundance, residence time in the atmosphere, and ability to promote the formation of other greenhouse gases^[55].

Climate Forcing measures the radiative forcing (or heating effect) caused by GHGs in atmosphere^[15]; both the radiative forcing (W/m²) and the annual Greenhouse Gas

Index, for the Long-Living Greenhouse Gases are reported in Figure 1.4; they are based on the change in the concentration of these gases in the Earth's atmosphere.

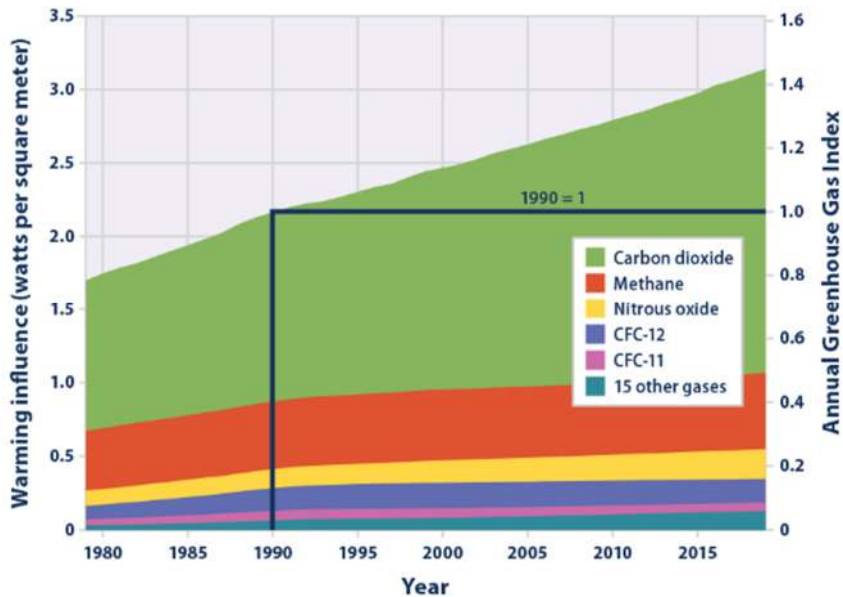


Figure 1.4 – Radiative Forcing Caused by different Greenhouse Gases, from 1979 to 2019^[56].

In 2019, the net influence of greenhouse gases on warming increased significantly compared to 1990. Among the greenhouse gases, the largest contribution to global warming was from carbon dioxide, followed by methane.

Nowadays, many governments have issued climate proclamations with the goal of reducing greenhouse gases emissions^[57].

For example, the European Union attaches specific importance to the strong increase of renewable energy since the early 2000s. Specifically, the European Union has set a 2030 target to reduce GHG emissions by 40% compared to 1990 and to increase the share of renewable energy in energy consumption to at least 27%^[58]. Currently, only about 20% of the energy consumed in the European Union comes from renewable energy sources^[59].

1.3 CO₂ and CH₄ greenhouse gases

The amount of methane and carbon dioxide in the atmosphere is expanding dramatically (Figure 1.5).

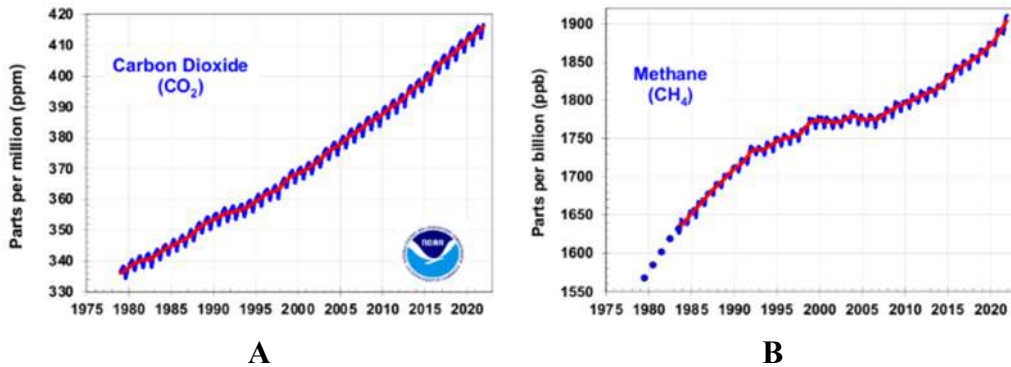


Figure 1.5 – Amount of Carbon Dioxide (A) and Methane (B) in atmosphere from 1980 to 2020. Data recorded by NOAA's Global Monitoring Laboratory^[56].

One of the objectives of this thesis is the use of different types of adsorbent materials to remove these two greenhouse gases from the atmosphere. In particular, the storage capacity of these two gases through different porous materials is investigated. Since methane is produced together with other gases as a waste product of the anaerobic digestion process in Municipal waste landfills, the ability of different materials to separate methane from binary mixtures will be also studied.

1.3.1 CO₂ storage

Although the natural carbon cycle controls CO₂ concentration in the Earth's atmosphere, atmospheric CO₂ emissions continue to increase each year, both from natural emissions and anthropogenic activities that have steadily increased due to rapid industrialization and urban development^[60,61]. Natural emission sources, which are partly responsible for carbon dioxide emissions, are mainly volcanic activities and soil degradation processes. Anthropogenic activities such as vehicular traffic,

industrial activities (chemical, food, electronic, cement, oil), deforestation, power plants, waste treatment, etc., are the main cause of the increase in atmospheric CO₂ concentration^[62,63]; in particular, carbon dioxide emissions are directly related to the combustion of fossil fuels, which are the main source of energy worldwide^[64].

Global CO₂ emissions from energy combustion and industrial processes increased in 2021, reaching the highest annual level ever: According to an analysis by the International Energy Agency, emissions increased by 6% from 2020 to 36.3 gigatons^[65]. In July 2022, the atmospheric CO₂ concentration was 418 ppm (the pre-industrial level in 1750 was 280 ppm)^[66], and it is projected to rise to a potentially dangerous level of 550 ppm by 2050 and 570 ppm by 2100^[49,64]. However, it is estimated that the ideal level of atmospheric CO₂ should not exceed 350 ppm^[67]. Given this worrisome scenario, it is of utmost importance to find strategies to decrease the amount of CO₂ released into the atmosphere, especially CO₂ capture technologies need to be introduced and improved^[68].

There are three main strategies to reduce CO₂ emissions^[69]:

- Improving the energy efficiency of carbon-fired power plants^[70,71];
- using renewable and non-carbon energy resources instead of fossil fuels^[72];
- introduction of carbon capture and storage (CCS) technologies^[73,74].

Carbon Capture and Storage (CCS) systems aim to capture CO₂ produced during combustion and in industrial streams so that it cannot be released into the atmosphere^[75]. This can significantly reduce CO₂ emissions (estimated to be 19% of global CO₂ emissions by 2050 if regularly applied^[71]) without affecting fossil fuel use until a renewable, clean energy source is found to replace it^[76,77].

As shown in Figure 1.6, CCS process involves four main steps^[78–80]:

- capture of carbon dioxide originating from power plants and industrial processes;

- compression of the gas;
- transport of the captured and compressed CO₂;
- underground storage of the captured CO₂.

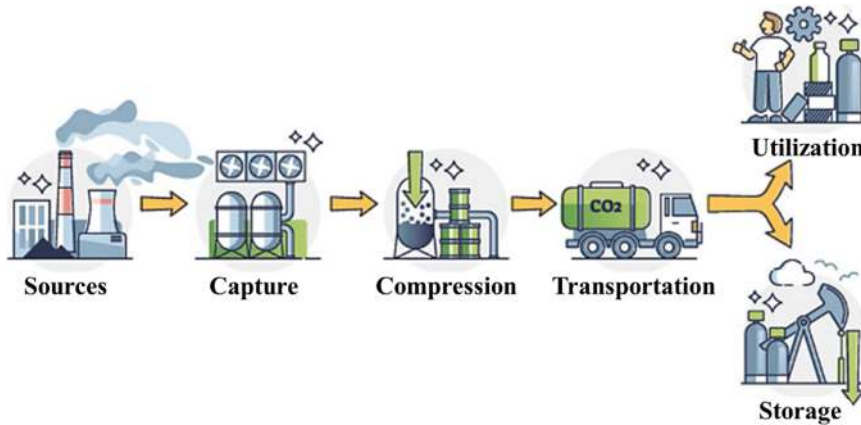


Figure 1.6 – Scheme of Carbon Capture and Storage (CCS) process. Adapted from^[81].

There are three main strategies for capturing CO₂ from large point emission sources, depending on the combustion method and the composition of the gas stream^[64,82]:

- *Pre-combustion capture.* Pre-combustion strategies consist of a series of treatments to the fuel to remove carbon dioxide before the combustion reaction occurs. Pre-combustion capture can also refer to the capture of CO₂ that is an unwanted by-product of a process reaction^[83,84]. With this method, it is possible to remove all of the carbon dioxide produced and separate a stream consisting only of hydrogen from a stream consisting only of carbon monoxide^[85]. However, since a significant amount of steam is required for high carbon monoxide conversion, this results in lower electricity generation, which is a drag on the overall efficiency balance of the implant^[83]. This strategy is used in integrated gasification combined cycle power plants, fertilizer production plants, and natural gas wells^[69,84].
- *Oxy-fuel combustion separation.* In this strategy, a fuel is burned in an environment with pure oxygen instead of air, producing a flue gas (off-gas)

with a high concentration of carbon dioxide, water vapor, and small amounts of other impurities, but free of nitrogen and its oxidic compounds^[49,68]. This method allows post-combustion streams with a CO₂ content of about 80%; however, the use of pure O₂ as an oxidant results in a high heat generation, which is too high to perform the separation, and in the need to subsequently recirculate the combustion gas to lower the temperature^[83]. Oxyfuel combustion is used only in fossil fuel power plants and in the cement, iron and steel industries^[86].

- *Post-combustion capture.* In this process, carbon dioxide is captured and removed from flue gas streams after the combustion reaction before the stream containing the by-products is released to the atmosphere^[77,87]. CO₂ is separated from flue gases using various methods such as cryogenic distillation, absorption, membrane technology, microalgae separation, etc.^[63,84,88]. This strategy is effectively used in existing plants, but it is difficult to obtain a CO₂ stream with a high degree of purity (> 95%) due to the low concentrations in the streams to be treated^[68,83].

Among the CCS technologies mentioned above, post-combustion capture, in conjunction with the adsorption method, is the most promising and cost-effective so far, as it can be used in both existing and newly designed power plants and in different types of industries and facilities^[64,89,90]. The success of CCS technologies depends on the efficiency of CO₂ adsorption, ease of operation, production costs, and the yield of adsorbents used in the process^[91].

Solid adsorbents are at the heart of this technology and therefore it is important to develop effective adsorbents for CO₂ capture^[92].

The most widely used adsorption strategies to remove CO₂ from a gas mixture are mainly based on two phenomena: absorption of the gas into a liquid solvent and adsorption onto a solid material^[68,83].

- *Absorption* is a process in which a component is removed from a gas stream by a liquid solution. This process can lead to the formation of new products when a chemical reaction occurs between the solvent and the gas^[93]. This separation method can be used to obtain gas streams with a purity of more than 98%, which is why it is widely used for CO₂ removal in industrial plants. This is achieved by using suitable adsorbent that have high selectivity towards the carbon dioxide molecule^[94]. The most common solvents used for adsorption are amine-based compounds, alkali metal carbonates and ionic liquids^[95]. Unfortunately, despite good results in carbon dioxide removal, this strategy has several drawbacks, including the high cost of the solvents, their volatility and easy degradation, corrosion problems in some parts of the system, and finally a high energy requirement for the regeneration of the absorption solution^[95].
- *Adsorption* by porous solids is a surface process that depends strongly on the properties and functionalities of the surface^[82]. Gas molecules interact with the surface of a porous solid and establish interactions: if the interactions are weak (i.e van der Waals, dipole-dipole interactions), the gas is retained by the material through steric and kinetic affinities, and the adsorption is called physical and is completely reversible^[96]; if, on the other hand, stronger interactions are established, true chemical bonds are formed between the gas molecules and the surface, and the adsorption is called chemical^[97]. Adsorption by solid porous adsorbents is considered a promising method for carbon capture because it is inexpensive, has a well-developed pore structure, requires little energy for regeneration, and has excellent cyclic stability^[98,99]. This process is carried out by pressure swing adsorption (PSA), which allows the adsorption of a gas at high pressure and consequently the regeneration of the adsorbent at low pressure. Therefore, it is possible to separate the gas and release it later by modulating the pressure of the process so that the adsorbent

is available again for a new separation cycle^[95]. An alternative is adsorption by vacuum swing adsorption (VSA), in which adsorption is performed on a porous solid when the pressure of the whole process is less than 1 atm, or by temperature swing adsorption (TSA), in which adsorption is performed at low temperatures while desorption and regeneration of the material is performed with increasing temperature^[95,100].

1.3.2 Adsorbent materials for the removal of CO₂

In the case of physisorption the interactions between CO₂ and the adsorbing surface is often dominated and limited by the value of the electric quadrupole moment (EQM)^[101]. Studies have shown that the EQM value of CO₂ is three times higher than the EQM value of N₂, resulting in a stronger distribution of CO₂ on the adsorbent surface than that of nitrogen^[102].

The carbon dioxide selection process is based on the van der Waals attraction between the gas molecules and the adsorbent surface, and on the pole/ion and pole/pole interactions between the CO₂ quadrupole and the ionic and polar sites on the surface of the solid adsorbent.

The adsorption of CO₂ at room temperature is mainly determined by physisorption, and the gas adsorption is directly related to the porous structure of the adsorbent surface^[103,104]. The number of gas molecules trapped in the porosity of the material increases with increasing operating pressure until the maximum capacity is reached. It has been reported that narrow micropores (0.33-1 nm) are mainly responsible for CO₂ adsorption performance; however, the suitable micropore size for CO₂ adsorption strongly depends on the adsorption temperature and pressure^[90].

An adsorbent material to be used efficiently in an industrial process must meet several criteria:

- it must be economical: the price must not exceed 10-20 euros/kg^[105];
- it must be completely regenerable^[106];

- it must have a high surface area with numerous active adsorption sites;
- it must have good performance in cyclic adsorption-desorption cycles (1000)^[49];
- it must be selective for CO₂ in co-presence with other species^[107];
- it must have a CO₂ adsorption capacity of at least 130-180 g/kg (3-4 mol/kg)^[108,109];
- it must have fast adsorption/desorption kinetics^[49];
- it must be thermally and chemically stable, i.e., it must withstand temperature and pressure variations without changing its microstructure and morphology^[49];
- if functionalized, the groups anchored on its surface must be resistant to oxidizing agents^[96].

In physisorption, textural properties (porosity size distribution, micropore fraction and size, total pore volume, surface area) play a crucial role in the interaction between CO₂ molecules and the adsorbent surface^[90,110].

In particular, studies have shown that the high carbon dioxide storage performance is due to the combined effect of these properties^[79,111,112]. Most studies have reported that microporosity is the main factor for effective CO₂ adsorption, as the narrow volume of micropores makes a greater contribution to the storage^[112]. In addition, the interconnected mesoporous and microporous structure is believed to promote the rapid diffusion of CO₂ molecules while improving the accessibility of the micropores in the adsorbent^[113,114].

The most commonly used materials for CO₂ physisorption are zeolites, clays, alumina, silica gels, metal-organic frameworks (MOFs), and porous carbons^[115,116]. Moreover, silica functionalized with amine groups, amino-functionalized activated carbon, metal-based sorbents (oxides), impregnated alumina supported,

hydrocalcite-like compounds and alkali carbonates are used for chemisorption processes^[115,116].

Zeolites have a well-defined crystal structure with microporous voids and are therefore capable of selectively adsorbing CO₂^[117]. In addition, the adsorption of CO₂ is promoted by the interaction between its high quadrupole moment (-14.3×10^{40} cm²) and the electric field generated by the structural cations in the zeolite^[118]. The highest CO₂ storage performance is obtained with sodium zeolites, which have a large surface area^[119].

For example, Cavenati et al. showed that the CO₂ adsorption capacity at 1 atm and 25°C for zeolite 13X was 205.1 g/kg^[120]. In contrast, Harlick and coworkers performed experiments at 22°C and 1 atm with zeolite NaY and found CO₂ adsorption of 179 g/kg^[121]. Hernández-Huesca and coworkers tested mordenite and clinoptilolite, at 17°C and 1 atm, and found a CO₂ adsorption of 79 and 75 g/kg, respectively^[122].

Metal–organic frameworks (MOF) are a class of porous coordination polymers constructed from a combination of metal ions or clusters and organic ligands^[123,124]. They possess a robust 3D structure, with a network of channels and uniform pores, a permanent porosity and modular nature, and they are also characterized by a large surface area and tunable pores^[125,126].

To improve CO₂ capture performance, MOFs are pre- or post-modified by functionalizing the ligands or metal center with amine groups; as the CO₂ diffuses into the pores, it interacts with the amine ends to form chemisorbed species^[127].

Several studies reported high CO₂ adsorption capacity, ranging from 35 to 400 g/kg at 25°C and 1 bar^[126,128–132]. The adsorption capacities of MOFs are related to their high surface areas and, in some cases, can increase at high pressures^[128,130,133]. The mechanism of selective adsorption in MOFs is due to the molecular sieving effect and adsorbate-surface and adsorbate-adsorbate interactions^[134,135]. However, MOFs

have disadvantages, such as low material stability, and high synthesis and recycling costs^[134,136].

Among the various adsorbents that can be used, porous carbon materials have increasingly attracted the attention of many researchers because of their advantageous properties, such as high porosity, low production cost, high efficiency, and excellent stability^[92].

The adsorption rate and adsorption capacity of porous carbons depend strongly on the pore structure, diffusion processes, and available surface area^[137].

Several studies have found that the presence of narrow micropores smaller than 1 nm is responsible for carbon dioxide adsorption, since pores with a size two to three times larger than the kinetic diameter of CO₂ (0.33 nm) are the most suitable candidates for adsorption of CO₂ molecules^[138,139]. Moreover, it has been demonstrated that the presence of a pore size distribution with narrow micropores leads to excellent performance in the storage of carbon dioxide at room temperature and pressure^[140,141]. At pressures below 1 bar, the ultramicropores (with a diameter of less than 0.7 nm) are responsible for adsorption, while at high pressures, the adsorption capacities are related to the specific surface area, the amount of mesopores and the total pore volume^[112,142].

Porous carbons exhibit moderate CO₂ adsorption capacity at low pressures (*ca.* 150 g/kg), similar to those of zeolites, which, as with all physicosorbent materials, decreases with increasing temperature^[116]. At high pressures, however, they exhibit a high CO₂ storage capacity^[143].

For example, in the work of Casco and coworkers^[144], several porous coals derived from petroleum pitch were tested at 25°C and pressures of 1 bar and 35 bar; they performed CO₂ adsorption of 100-160 g/kg at 1 bar pressure, while their adsorption capacity increased significantly at high pressure and they were able to store about 500-1500 g/kg of CO₂.

Tu *et al.*, prepared a porous carbon from bio-tar, with excellent textural properties, (a specific surface area of 2595 m²/g and a total porous volume of 1.3 cc/g); this carbon showed excellent CO₂ adsorption capabilities, sequestering, at a temperature of 25°C and a pressure of 1 bar, about 235 g/kg of CO₂^[110].

Among the most widely used materials for CO₂ chemisorption are amine-functionalized silicas. Mesoporous silicas are low-cost materials that possess good textural properties and excellent stability^[130,145–148]. They are usually functionalized with amines by wet impregnation or chemical grafting^[149]. The carbon dioxide that is adsorbed by the functionalized silicas reacts chemically with the amine group, thus forming carbamate, bicarbonate and zwitterionic products^[150].

For example, Vilarrasa-García and co-workers synthesized different mesoporous silicas and tested them for CO₂ adsorption up to a pressure of 1 bar, both before and after functionalization with different amine groups (APTES, PEI, TEPA)^[151].

The functionalized silicas showed higher CO₂ uptake at low pressure compared to the same non-functionalized silicas, due to the presence of chemical sites that adsorb CO₂ more strongly than the physical sites. The highest performance was obtained with a silica functionalized with APTES (aminopropyltriethoxysilane), which adsorbed 64 g/kg of CO₂ at a pressure of 1 bar.

1.3.3 Methane storage and biomethane production

To cope with the environmental problems, advanced technologies for organic waste management and simultaneous renewable energy generation are needed^[152]. Fossil fuels stand out as the primary source of energy for industrial activities and daily sustenance^[153]; their use and high carbon footprint pose a great threat to the environment as they have led to major challenges such as global warming due to high greenhouse gas emissions and climate change, which causes health and environmental problems^[57].

Among the available alternatives for energy production, biogas is an increasingly used solution to generate an alternative energy source, since it has a high methane content [58,154,155]; it is considered a renewable and clean energy source and is the most immediate solution to solve global energy problems^[156,157]: in fact, biomethane is a full substitute for fossil natural gas, since it has a CH₄ content greater than 97%_{vol}^[158].

Raw biogas is produced mainly by anaerobic digestion of a wide range of organic waste from biomass (urban, industrial and agricultural waste, manure, municipal waste, etc.), using microbes and enzymes at medium to high temperatures^[153,158–161]. Valorization of organic waste is a successful strategy for its sustainable management through methods that produce higher value-added bioproducts and reduce environmental health impacts^[162–164]. Biogas production is rapidly increasing as a means to reduce the environmental impact of organic biomass^[157], and prevent to contribute to greenhouse gas emissions and leachate to groundwater^[158,165–168]. Using environmental wastes for anaerobic digestion, instead of sending it to landfills, is helpful in combating climate change, as methane contributes to 90% of total greenhouse gases worldwide, which are mainly produced in landfills^[157,165]. For this reason, there is growing interest in the process of anaerobic digestion to produce biogas and convert it into biomethane, especially from negatively valued feedstocks such as organic waste^[158].

The composition of the raw biogas strongly depends on the nature of the initial biomasses, but in general the stream is mainly composed of methane (50-75%_{vol}) and carbon dioxide (24-50%_{vol})^[155,157,169–172]. The percentage of these two main fractions varies depending on the type of feedstock and the operating conditions of the bioreactor^[154]. In addition, depending on the source of the organic feedstock waste, the biogas stream may contain other compounds that are present in small amounts but may affect the properties of the biogas^[172]; typically hydrogen (1-5%_{vol}), nitrogen (0-3%_{vol}), water vapor (5-10%_{vol}), oxygen (0-1%_{vol}), carbon

monoxide, ammonia, hydrogen sulphide, aromatic and halogenated compounds, siloxanes, volatile organic compounds and hydrocarbons are present^[173–175].

Biomethane can be used for a variety of purposes: it can be used for heating and electricity generation, it can be used in the public and/or private transport sector, or it can be injected into the natural gas grid after removing impurities^[57,176,177].

Furthermore, all of the carbon dioxide produced from the combustion of biomethane is “biogenic” (carbon-neutral) because it comes from a biomass that absorbed a equivalent amount of CO₂ during its growth^[158]. Therefore, the role of biomethane in decarbonizing energy sources is of paramount importance.

The production of biomethane by upgrading biogas proves to be the most favourable in terms of technological reliability, economic feasibility, and environmental sustainability^[178].

In the context of reduced fossil fuel use and a circular economy, biogas production is increasing, but raw biogas requires purification steps before it can be used as biomethane. In order to use biogas as an alternative to natural gas, it must have a minimum methane content of 95%_{vol}^[179–181]; therefore, a separation between the methane, CO₂ and other non-combustible gaseous components must take place before it can be used, and in addition the remaining trace contaminants present must be removed^[182,183]. The process of removing all these impurities to obtain a high-purity gas in a high-quality stream is known as biogas upgrading^[184]. The ultimate goal is to regulate the biomethane concentration to an optimal level to maximize the high energy content of the mixture, usually around 95-99% methane^[58,181,185]. The adsorption/removal of impurities from the biogas stream will appreciably improve the efficiency of the biogas for further use as a renewable energy fuel^[157].

The biogas is treated mainly in two stages: first, the raw biogas is cleaned through the removal of toxic composites, then it is upgraded, that is, the CO₂ content is

adjusted to establish a sufficiently high calorific value of the biogas^[57,186], as higher CO₂ concentration reduces its calorific value^[187].

Then a further process of separation of the remaining gases present takes place.

Biogas Upgrading technologies are mainly derived from the gas refining manufacturing. These processes use different approaches to exploit the physical, chemical, and biological properties of the gas components^[188].

Upgrading systems consist of biogas pre-treatments, major CO₂ separation processes, processes for separation of the remaining components, and compression of biomethane; at the end of the process, the resulting biomethane will be injected into the national gas grid, and solid and liquid wastes generated during all processes will be disposed of^[58].

Thus, the overall biogas production and purification processes require many technical advances (use of environmental wastes as feedstock, pretreatment technologies, use of additives to enhance the performance of anaerobic digestion) in order to improve the quality, quantity, and long-term sustainability of biogas utilization^[171,189,190].

The environmental impact of upgrading techniques depends on the characteristics of the selected technologies, such as methane losses, electrical and thermal energy consumption, chemical and material inputs, waste and wastewater produced, and off-gas emissions^[191].

Currently, there is no predominant technology for upgrading raw biogas; all have advantages and disadvantages; the choice of the appropriate technology depends on the end use of the biogas, economic aspects, and the efficiency of the upgrading process^[192].

Among the different methods of biogas purification and upgrading, only four are well established in the industrial processes: membrane separation, water scrubbing, chemical adsorption and pressure adsorption; they are largely governed by three mechanisms: membrane separation, absorption and adsorption^[171].

Others are less widely used, such as physical organic scrubbing, cryogenic separation technologies and biological methods^[171].

The complications with these methods are high energy utilization, use of expensive chemicals and high operating costs.

Separation of gas mixture components is a process of selective adsorption-desorption of gaseous components on the surfaces of porous adsorbent materials, in which the selection of the adsorbent and the process are highly dependent on the type of feed and products; it is necessary to use an adsorbent that selectively adsorbs the desired component to effectively separate CH₄-N₂ mixtures^[193]; there are different categories of porous sorbents that can be used, such as zeolites, and porous carbon materials.

In general, adsorption is based on the van der Waals forces and the electrostatic attractive forces between the porous adsorbent and the gas molecules. The strength of the adsorption forces is therefore directly related to the size, polarizability, dipole and quadrupole moments of the adsorbate molecules and is determined by the surface chemistry and pore structure of the adsorbents.

Pressure Swing Adsorption (PSA) is a typical process for gas separation, based on adsorption, where regeneration of the adsorbent can be achieved due to the different adsorption capabilities at different pressures^[193]. PSA technology is based on the porous material being able to adsorb certain target molecules from a gas mixture selectively, which will then be released by going to apply different pressure values on the adsorbent^[185,194].

The separation process is based on the principles of selective adsorption affinity for different molecular dimensions of gas molecules, particularly CO₂ (0.33 nm) and CH₄ (0.38 nm)^[195,196].

By choosing the correct porous material, having a specific pore size, carbon dioxide can be preferentially sequestered, excluding methane molecules from retention within the porosity of the adsorbent^[197].

The adsorbent materials that are used must remain both mechanically and thermally stable during long-term use; the most commonly used are zeolites, activated carbon, polymer sorbents, and silica gel, as they have high adsorption efficiency^[119,195,198,199]. A schematic of the PSA process is shown in Figure 1.7.

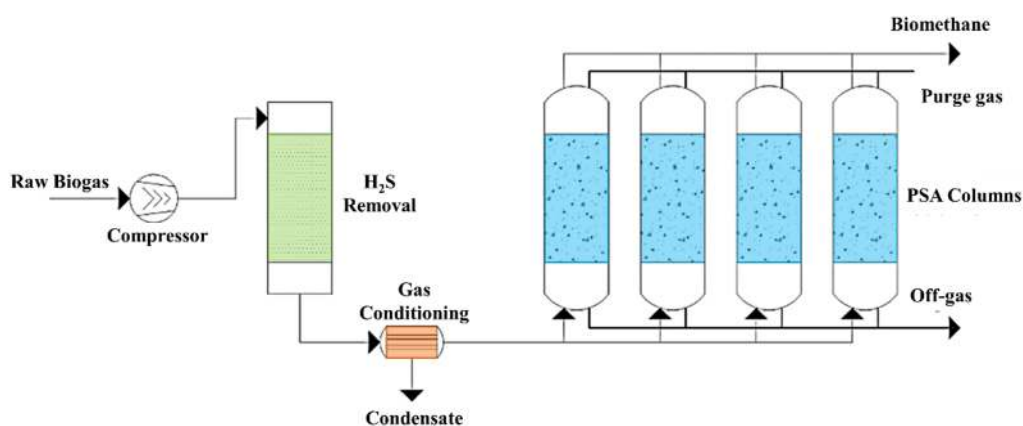


Figure 1.7 - Process flow diagram of Pressure Swing Adsorption system. Adapted from^[58].

The PSA process consists of an initial phase in which there is a pretreatment phase of raw biogas to remove H₂S, due to the irreversibility of its adsorption, and a drying phase to remove water^[158,172].

Then the remaining biogas is compressed to a variable pressure of 4-10 bar and introduced toward adsorption columns (usually 4 or 6 interconnected in series), which are filled with an adsorbent material^[58,192,200]. The process is continuous: initially, the adsorbent material contained in the columns adsorbs impurities in the gas stream (CO₂), passing methane that is collected at the top of the column^[58,158,172]; subsequently, after saturation of the material in the column, a pressure drop allows desorption of the adsorbed gas and regeneration of the adsorbent bed^[58,158,194,201]. The upgraded biogas leaves the saturated column and passes to another column that has already been regenerated to achieve continuous operation, and at the end of the

entire process, the biomethane leaves the adsorption system with a pressure between 3 and 6 bar^[58,172,202].

PSA technologies based on selective adsorption of CH₄ and selective adsorption of N₂ are commercially available for small and medium gas processing plants due to their advantages (compact module, simple and stable process, and low operating costs)^[203].

Methane adsorption can be performed using various microporous physisorbent materials with adjustable pore size^[101,204]. Indeed, since the kinetic diameter of methane is 0.38 nm, it must have pore sizes of less than 2 nm in order to have a good interaction with the adsorbent material^[205]. However, mesopores also play a relevant role in adsorption as they allow mass transfer of CH₄ inside and outside the micropores of the adsorbent^[195,196,206].

Activated carbons are the most commonly used materials, but zeolites, silicas, porous coordination polymers (PCPs), porous organic polymers (POPs), and metal-organic frameworks (MOFs) can also be used^[206].

In Byamba-Ochir's study, several porous carbons were made from anthracite and pelletized; PMAC1/2-C3-65 carbon with a surface area of 1460 m²/g showed the best performance in methane adsorption, storing about 30 g/kg methane at 1 bar pressure and 175 g/kg at 35 bar pressure^[207]. In fact, it is known that carbon has a higher adsorption capacity for methane at high pressures^[144].

However, the separation of methane from binary mixtures that also contain nitrogen is particularly difficult because the molecular sizes of these gases are similar, resulting in low selectivity^[208].

Selectivity for a target gas A (in this case methane) over an interfering gas B (in this case nitrogen) is defined as the ratio of the response of the adsorbent material to gas

A to the response to gas B^[209]. The selectivity of the material is defined as the ratio of its best adsorption to its second best adsorption^[210].

Porous carbons (with a selectivity of 1.9-4.0) or polymer rubbers (with a selectivity of less than 5)^[211-213] can be also used.

To increase the selectivity of porous carbons, they can, for example, be functionalized with organic reagents with by low-temperature plasma treatment, as reported in the work of Yang et al^[214].

Other materials have too low selectivity to be used industrially, such as silicalite pellets (selectivity of 3.4) or glassy polymers (selectivity of less than 3)^[213,215].

1.4 Water Pollution

Although 71% of the Earth's surface is covered by water, only a small fraction of it is available as fresh water. About 97% of the total water accessible on Earth is found in the oceans and is too salty to drink or be used to irrigate land; the remaining 3% is fresh water. Of the available fraction of fresh water, about 2% is locked in ice caps or glaciers; therefore, only a very small fraction of the total volume of water on Earth is readily available^[3]. This makes water an extremely valuable resource; therefore, on July 28, 2010, the United Nations recognized “the right to safe and clean water and sanitation as a human right essential to the full enjoyment of life and all human rights”^[216]. Safeguarding water resources is essential to preserving the quality of life and health of living beings^[146].

Pollution of natural waters, by both biological and chemical contaminants, is a universal problem. There are few populated areas in both developed and developing countries that do not suffer from at least one form of water contamination (nutrient pollution, oxygen depletion, microbiological pollution, groundwater pollution, etc.). Water pollution has been defined as “any direct or indirect alteration of the physical, thermal, chemical, biological, or radioactive properties of any part of the environment by the discharge, emission, or deposition of waste, so as to adversely affect any beneficial use or cause a condition that is hazardous or potentially hazardous to public health, safety, or welfare or to animals, birds, wildlife, aquatic life, or plants of any description”^[217].

A contaminant becomes a pollutant when it is present in higher concentrations than permissible limits and, therefore, may cause adverse biological effects^[218].

Increasing industrialization, agricultural activities, and population growth worldwide are causing environmental stress due to the release of polluted wastewater into the environment^[115,219].

Water pollution can be industrial, agricultural, or civil.

Pollution of agricultural origin results from the excessive and incorrect use of fertilizers and pesticides in land treatment; for example, the discharge of phosphate- and nitrate-containing fertilizers into rivers, lakes and seas produces eutrophication conditions, while the discharge of pesticides (insecticides and herbicides) into streams or soils results in the destruction of the life forms present^[220,221].

Pollution of industrial origin is related to processing residues, and occurs through the discharge of toxic and non-biodegradable substances from production processes into water bodies. In some cases, it also results from the discharge of cooling water from plants into water bodies: since they possess high temperatures, a temperature change is generated that causes the alteration of aquatic ecosystems and the variation of vital processes^[220,221].

Domestic water pollution is produced by household discharges, which contain organic substances and/or detergents; it results from reduced efficiency of sewage treatment plants, which are designed to treat and purify the pollutant load in sewers^[220,221].

Any kind of pollution can affect the health of the flora and fauna involved, harming both the ecosystem and human health by going to the water supply.

There are two main routes by which pollutants reach water: direct pollution occurs when pollutants are poured directly into waterways without any purification treatment; indirect pollution, on the other hand, occurs when pollutants reach waterways via air and soil^[222].

The problem of pollution is accompanied by an increasing need for water due to human activities and especially the growth of the world's population. So, the removal of pollutants from contaminated water is an urgent need^[223].

The most common water pollutants are:

- *Inorganic pollutants*. They are non-biodegradable toxic elements that, if present in trace amounts, can cause adverse health effects. Examples are ammonia and chlorides: these, when mixed with other pollutants, can produce additional toxic by-products in the form of gaseous compounds^[224].
- *Heavy metal ions*. Depending on their oxidation state, they can be extremely toxic or even, carcinogenic, teratogenic and mutagenic^[225]. For example, ions capable of forming lipophilic compounds, such as methylmercury, can bioaccumulate in tissues. Metals such as Arsenic, Barium, Cadmium, Chromium, Copper, Mercury, and Lead can be toxic when present in low concentrations in the ppb range^[226].
- *Persistent Organic Pollutants (POPs)*. POPs consist mainly of man-made chemicals and exhibit marked persistence against degradation processes^[227]. They include organochlorine compounds, dioxins, furans, pesticides, herbicides, etc. They have high residence times and high environmental mobility^[228]. In addition, being hydrophobic and lipophobic, they are bioaccumulative and extremely toxic.
- *Organic dyes*. The structure of dyes is complex and varied; there are more than 5,000 varieties of dyes with different chemical configurations^[229]. They are usually soluble molecules in polar solvents and possess a molecular structure consisting of condensed aromatic rings and conjugated π - π systems^[230]. Dyes are generally classified according to the two methods of application and chemical structure. Based on the chemical structure classification, dyes are mainly divided into eight categories: azo dyes, indigo dyes, nitro and nitroso dyes, triaryl methane dyes, phthalocyanine dyes, anthraquinone dyes, sulphur dyes and heterocyclic dyes^[231,232]. These molecules may be carcinogenic, teratogenic, or mutagenic to organisms.

- *Emerging Contaminants (ECs)*. They are synthetic or natural chemicals that are not usually monitored in the environment, but have the potential to enter the ecosystem and cause ecological and/or human health effects^[233]. These are pharmaceuticals, pesticides, industrial chemicals, surfactants, complexing agents, disinfection products, estrogens and personal care products^[219,234]. All of these compounds can be present in aquatic systems in concentrations ranging from 0.001 to 100 ppb.

1.5 Remediation of water pollutants

Since in this PhD thesis, adsorbent materials were synthesized for the purpose of testing their performance to remove two different types of pollutants from water (with particular emphasis on an organic dye, the Rhodamine B, and perfluoroalkyl compounds), notions about these molecules will be discussed in more detail below.

1.5.1 Organic Dye: Rhodamine B

Rhodamine B (*N*-[9-(*ortho*-carboxyphenyl)-6-(diethylamino)-3*H*-xanthen-3-ylidene] diethyl ammonium chloride) is a water-soluble triaryl methane dye of a xanthene class (Figure 1.8).

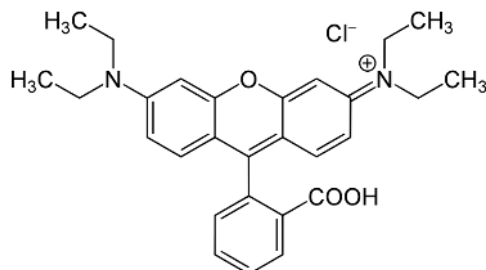


Figure 1.8 – Chemical structure of Rhodamine B.

Rhodamine B is a weak acid (pKa 4.2) with good solubility (34 g L⁻¹) in water. At low pH values the organic part is a cation in which the positive charge is shared by the two anilinic atoms. At pH values larger than 4.2, the carboxylic group is predominantly deprotonated and the prevalent form of Rhodamine B is a Zwitterion^[235]. RhB possess the follow molecular dimension: 1.44 nm x 1.09 nm x 0.64 nm.

Rhodamine B is widely used in the textile, cosmetic, photographic, leather, paper, and plastics industries as a dye, and also in the food industry as a food dye; in chemistry it is used as a fluorescent tracer, or as a metal chelating reagent^[236–239]. Although its use is widespread, this molecule is toxic to animals and humans, causing

irritation to the skin, eyes and respiratory system; some carcinogenicity, reproductive and developmental toxicity, mutagenicity and teratogenicity, as well as neurotoxicity and chronic toxicity have also been reported for Rhodamine B and its metabolites^[240,241].

Furthermore, being an organic pigment, it has a high capability to alter the environment due to its intense colour and optical emission, and can therefore significantly interfere with biological cycles related to photosynthetic processes^[242]. Over the years, various technologies have been employed to remove Rhodamine B and other organic dyes from wastewater^[235,243].

For example, P. Sarkar *et al.*, have used microorganism, such as bacteria, fungi and algae for a biodegradation, biosorption, and biocoagulation of dyes^[244]. G. Muthuraman et collaborators performed a solvent extraction to separate different dyes dissolved in immiscible solvents^[245]. R. Tripp and D. Clifford have used ion exchange resins^[246], while A. Leujo *et al.*, have removed organic pollutants using cyclodextrin nanosponge as adsorbent materials^[247]. Ramos and collaborators relied on the conversion of ozone to the reactive forms of oxygen to go and destroy the dye molecule^[248], while Bello *et al.*, instead, exploited the Fenton oxidation reaction, using the hydroxyl radicals generated by the reaction between hydrogen peroxide with divalent iron^[249]. Another removal methods is to use coagulants, in combination with an electric current, to promote heterocoagulation, flocculation and electroflocculation reactions^[250].

The limitations associated with these methodologies have led scientists to develop and study more promising and effective new technologies.

A widely used degradation method is photocatalysis; it is based on the fact that when a catalyst is exposed to UV light, electrons are promoted from the valence band to the conduction band and, as a result, an electron-lacuna pair is produced. Both the electron in the conduction band and the vacancy in the valence band, can migrate to the surface of the catalyst, where they can enter into a redox reaction with other

species on the surface^[251]. In most cases, the positive charge of the gap and the negative charge of the electron, reacting with water molecules, will generate hydroxyl radicals and superoxide anion radicals. The product radicals will then attack the organic dye and degrade it by oxidizing it^[252].

Since photocatalytic degradation is a process that takes place on the surface of the catalyst, this technique is often used in combination with the adsorption method, as it too turns out to be a surface phenomenon.

Adsorption is one of the most suitable methods for Rhodamine B dye removal from wastewater. Adsorption is a separation technique in which the components accumulate at the interfaces of two phases (solid-liquid); in this way adsorbent material segregates dye molecules from polluted water and accumulates it on its surface.

Adsorption is an exceptional method for dye removal because it does not involve specific removal conditions or wastewater pretreatment^[253].

The factors that most influence the adsorption process for removal of Rhodamine B are the follows:

- the concentration of the dye itself: high concentration of RhB leads to greater adsorption;
- the amount of material in contact with the RhB solutions, since the number of active sites for adsorption increases with increasing material amount;
- the contact time between the adsorbent material and the dye: in fact, as it increases, the quantity of removed dye increases;
- temperature: adsorption is an exothermic process, an increase in temperature leads to a decrease in the amount adsorbed;
- pH and surface charge of the adsorbent: above pH 4.2 values, the Rhodamine B will be deprotonated to form the Zwitterionic form^[254], while the surface of the adsorbent material will be negative at a pH value above its zero charge point (PZC). Since Rhodamine B is a cationic dye, it will be more absorbed

by a material having a very negative surface charge, as the interaction due to an electrostatic attraction between the surface of the material and the Rhodamine B will be larger^[255];

- particle pore size: the adsorption of Rhodamine B is improved using a material with larger pore diameter, since the access to the active sites by the dye is greater if the adsorbent material has large mesopores^[256,257];
- morphology and specific surface area: the microstructure and porous materials are able to adsorb a larger amount of Rhodamine B than bulk materials, as a large surface area of the microstructure allows access to a more active site^[258]. Furthermore, a high specific surface area leads to a better contact area with the Rhodamine B molecules^[259].

In the last decade, researchers have studied various types of adsorbents for the removal of dyes from water^[260]. Among organic materials, various biomass-based adsorbents have been used such as green banana peel powder^[261–263].

In addition, activated carbon has been widely used because it has a large surface area, high pore volume, and excellent chemical properties^[264–266].

For example, sugar activated carbon and a charcoal developed by agricultural wastes were used to remove Rhodamine B from an aqueous solution, and the results showed an adsorption efficiency of about 98.28% and 96%, respectively, with an adsorption capacity of 123.46 mg/g and 105.3 mg/g, respectively^[264,267].

Inorganic adsorbents are commonly used to remove rhodamine B from water because they are usually inexpensive, abundant, and sustainable materials^[268]

Among the various types of synthetic zeolites, beta zeolite is most commonly used for the adsorption of Rhodamine B because it has large pores interwoven in a three-dimensional network and a high Si/Al ratio^[269].

Clay minerals are also used as adsorbents for cationic pollutants because they have a large surface area and high cation exchange potential^[270]. Clay can remove up to 70% RhB from wastewater^[271].

In addition, silica and titania particles, nanocomposites (such as ZnFe_2O_4), and polymer resins (such as Dowex 5WX8) are also used^[146,260,272].

For example, in the study by Rasalingam S. *et al.* it was shown that two different types of mesoporous silica (i.e. MCM48 and MCM41) are able to remove Rhodamine B from a solution with high dye concentration (10M), 87 % and 81 %, respectively^[235]; in detail, they showed a maximum adsorption capacity of 0.4 g/kg and 0.39 g/kg, respectively.

1.5.2 Perfluoroalkyl substances (PFAS)

Perfluoroalkyl substances (PFAS) are a class of amphiphilic molecules composed of a hydrophobic alkyl chain of various lengths, linear or branched, totally fluorinated, and a hydrophilic functional group placed at the head of the chain.

The hydrophilic functional group can impart a neutral, positive or negative charge to the molecule, so these compounds can take the form of cationic, anionic or neutral surfactants depending on the type of hydrophilic group and the pH of the medium in which they are found. The most frequent anionic end groups are carboxylates ($-\text{COO}^-$), sulfonates ($-\text{SO}_3^-$) and phosphates ($-\text{OPO}_3^{3-}$)^[273].

PFAS owe their properties to the carbon-fluorine bond, which is one of the shortest and strongest chemical bond; for this reason, they are very stable and persistent substances^[274]. In addition, they exhibit hydrophobic and lipophobic properties, which are mainly attributed to the low polarizability of fluorine atoms. Some PFAS are found to be very stable even at high temperatures (above 150°C) and have very interesting properties from an industrial point of view: they are not flammable, are not degradable under strong acidic or basic conditions, resistant to oxidizing agents and to photolysis process, and not subject to conventional biodegradation processes^[275]. These characteristics allow their use under extreme pH and high

temperature conditions, but simultaneously make them extremely persistent and easily bioaccumulated^[276].

This property also makes these compounds highly resistant to breakdown in the environment, receiving them the nickname “*forever chemicals*.”

PFASs are a very large group of organic compounds (over 4700 organic chemicals^[277]) that differ in carbon chain length and polar functional group. The two largest groupings, within the PFAS category, are named PFCA (perfluoroalkyl acids), which possess a carboxylic acid as the hydrophilic group, and PFSA (sulfonated perfluoroalkanes) with a sulfonic group as the polar group^[278]. Within these two groups, two other subclasses can be distinguished based on the length of the fluorocarbon chain: long-chain PFAS (a PFCA with eight or more carbon atoms or a PFSA with six or more carbon atoms), or short-chain PFAS (a PFCA with seven or less carbon atoms or a PFSA with five or less carbon atoms)^[274].

The perfluorinated chain and the presence of a polar functional group impart surfactant and amphiphilic properties to these molecules. Because of these properties, perfluoroalkyl substances have been widely used since the 1950s in many industrial fields and for very diverse purposes^[279].

PFAS are used in the manufacturing process of great many everyday items: textiles, kitchen utensils, cleaning products, nonstick cookware, food packaging films, inks, fire-fighting foams, and are compounds used in the production processes of fluoropolymers such as polytetrafluoroethylene (PTFE) and polyvinylidene fluoride (PVDF)^[277]. Fluorosynthetic firefighting foams have been widely used since the 1970s for firefighting operations; as a result, large volumes of unflammable materials were stored and handled^[277].

Another important use of PFOA is in the production of Gore-Tex®, a durable, waterproof material characterized by high breathability and biocompatibility, used in the manufacture of sportswear and health care products such as vascular prostheses, heart valves, suture threads, and cosmetic surgery. Gore-Tex® is also

used in the aerospace industry (as a lining for astronaut suits and others) and as an insulation material in electronic components^[280].

As described by the Organization for Economic Co-operation and Development (OECD/UNEP, 2013), the most common PFAS use sectors are: aviation, aerospace and defence, automotive, biocides, construction products, cables and wiring, energy, household products, metal plating, papers and packaging, petroleum and mining production, semiconductors, carpets and upholstery and medical items.

PFASs are often simply added in the manufacturing process of a material and thus are not always chemically bound to it, resulting in easy release into the environment at every stage of a manufactured product's life cycle: from synthesis, to use, and finally to disposal^[281]. Interest in PFASs as emerging persistent contaminants arose when relevant levels were found in various environmental matrices located both in areas surrounding production and use facilities, but also in regions farther away^[277].

Concerns toward human and animal health arose when PFOA and PFOS have been detected in biological samples such as tissues of various kinds and biological fluids (milk, urine and blood). PFAS do not accumulate in fatty tissues, but they have a high affinity for proteins, with which they can bind very strongly, leading to their preferential accumulation in high-protein tissues such as kidney, liver, blood, and breast milk^[282]. Bioaccumulation and biomagnification of PFASs increase with increasing fluorocarbon chain length; sulfonated perfluoroalkyl acids are also more bioaccumulative than perfluoroalkyl carboxylic acids with the same chain length^[274]. High levels of PFASs have been found to be toxic, particularly Perfluorooctanesulfonic Acid (PFOS) and Perfluorooctanoic Acid (PFOA) are highly toxic and suspected carcinogens^[283,284].

The toxicity of PFASs results from the mechanisms of interaction they have, primarily, with receptors and cellular proteins and, consequently, affect the biotransformation of drugs, nutrients, and metabolites; thus, modifying numerous

enzymatic activities and the transport kinetics of many endogenous and exogenous molecules^[285].

Because of their high solubility in water, PFAS possess high mobility in the environment through water and soil, and can travel long distances from where they are spilled. As substances composed of anionic, cationic and zwitterionic species, it is difficult to remove them from the ecosystem and break them down into simpler elements^[277].

Various removal technologies are available for treating PFAS-contaminated water, and these consist of separation and decomposition techniques.

Removal methods include: standard techniques (such as flocculation, coagulation, sedimentation, and filtration), adsorption techniques (such as the use of activated carbon, minerals, biomaterials, resins, nanomaterials and ion exchange polymers), foam fractionation and ozofractionation^[286], membrane technologies including reverse osmosis and nanofiltration. Degradation methods, on the other hand, include oxidation (chemical, electrochemical, and photochemical)^[287], reduction, ultrasonic techniques, and biological remediation^[288].

Most available methods, especially conventional techniques, are not very effective in removing PFAS due to various aspects, including cost and unworkability^[289]. Technologies available to date show several limitations, including high energy demand, very low removal rates, very high costs, and the need to use destructive techniques to remove PFASs after separating them from water and accumulating them in another phase (solid or liquid)^[290].

Adsorption is an effective technique for PFASs removal and is considered the best and most studied technique for water treatment due to its environmental friendliness, availability of a wide range of adsorbents, high effectiveness, low cost, simplicity of design, and ease of use.

The adsorption mechanism of PFASs is governed by electrostatic interaction, hydrophobic effects, ion exchange, hydrogen bonding and van der Waals forces^[291]. With this technique, PFASs can be concentrated from the liquid to the solid phase; subsequently, the adsorbent material must be treated and regenerated so that adsorbed PFASs can be removed and destroyed. This aspect has the greatest impact on the operating costs of the adsorption technology because of the energy required to regenerate or replace the adsorbent and to handle and treat the waste^[292].

Activated carbons are widely used materials for adsorptive removal of PFASs^[293]; being generally nonpolar they adsorb PFASs mainly through physical and hydrophobic interactions^[294]. However, one of the disadvantages associated with them is their non-selectivity toward specific PFASs^[274].

Anion exchange resins are considered the most efficient adsorbents for PFAS removal in terms of removal capacity, cost, and regeneration^[294]. Due to anion exchange, they are able to bind short-chain PFASs, while the removal of long-chain PFASs occurs through the formation of micelles/emulcels and/or their agglomeration on the surface of the resins^[295–297].

Moreover, the adsorption rate and removal capacity of PFASs are strongly influenced by their hydrophobicity^[298].

Stebel and his collaborators have used novel organic-inorganic hybrid materials for PFAS adsorption that have the unique ability to swell in the presence of organic solvents; swelling significantly increases the pore volume of the material, allowing fluorinated molecules to be trapped within^[299].

Minerals such as nano-metal oxides, hydrotalcites, silica, clays, etc., have also been investigated for PFAS removal because their large surface area, porous structure, and functional groups enable fast kinetics, high adsorption capacity, and good reusability, as well as the ability to have specific functional groups on their surface^[300,301]. The adsorption mechanism is mainly based on electrostatic and hydrophobic interactions, hydrogen bonding, ion exchange, and surface complexation^[302].

Conclusions

Given the results of the literature study, it became clear that environmental pollution is a problem for both the ecosystem and all living things that inhabit the Earth.

Global climate change is directly linked with increased environmental pollution: it is considered a major threat to the planet and life on it.

Removal of pollutants from the gas and water phase by adsorption process has been shown to be one of the best strategies to deal with this problem.

Therefore, the objective of this PhD thesis is to apply several types of porous adsorbents, with different physico-chemical properties, for greenhouse gas capture and water remediation.

Further details are described in Chapter 2.

References

- [1] I. V. Muralikrishna, V. Manickam, *Environmental Management: Science and Engineering for Industry*, Butterworth-Heinemann, An Imprint Of Elsevier, Oxford, United Kingdom ; Cambridge, MA, **2017**.
- [2] D.-P. Häder, A. T. Banaszak, V. E. Villafaña, M. A. Narvarte, R. A. González, E. W. Helbling, *Science of The Total Environment* **2020**, 713, 136586.
- [3] Anji Reddy Mareddy, Anil Shah, Naresh Davergave, *Environmental Impact Assessment Theory and Practice*, Elsevier Science, **2017**.
- [4] M. Gawlik-Kobylińska, *Applied Sciences* **2022**, 12, 8315.
- [5] R. K. Ibrahim, M. Hayyan, M. A. AlSaadi, A. Hayyan, S. Ibrahim, *Environ Sci Pollut Res* **2016**, 23, 13754–13788.
- [6] P. Yadav, J. Singh, D. K. Srivastava, V. Mishra, in *Environmental Sustainability and Economy*, Elsevier, **2021**, pp. 111–120.
- [7] “Enciclopedia Treccani,” can be found under <https://www.treccani.it/enciclopedia/clima>, **n.d.**
- [8] K. Abbass, M. Z. Qasim, H. Song, M. Murshed, H. Mahmood, I. Younis, *Environ Sci Pollut Res* **2022**, 29, 42539–42559.
- [9] W. Leal Filho, U. M. Azeiteiro, A.-L. Balogun, A. F. F. Setti, S. A. R. Mucova, D. Ayal, E. Totin, A. M. Lydia, F. K. Kalaba, N. O. Oguge, *Science of The Total Environment* **2021**, 779, 146414.
- [10] “Global Climate Change - Vital Signs of the Planet,” can be found under <https://climate.nasa.gov/>, **n.d.**
- [11] “Climate Change: Global Temperature | NOAA Climate.gov,” can be found under <http://www.climate.gov/news-features/understanding-climate/climate-change-global-temperature>, **n.d.**
- [12] “National Centers for Environmental Information (NCEI),” can be found under <https://www.ncei.noaa.gov/>, **n.d.**

- [13] A. P. Cracknell, C. Varotsos, *Understanding Global Climate Change: Modelling the Climatic System and Human Impacts*, CRC Press, Boca Raton, **2021**.
- [14] J. M. Melillo, T. (T. C.) Richmond, G. W. Yohe, *Climate Change Impacts in the United States: The Third National Climate Assessment*, U.S. Global Change Research Program, **2014**.
- [15] “U.S. Environmental Protection Agency | US EPA,” can be found under <https://www.epa.gov/>, **n.d.**
- [16] D. Feliciano, J. Recha, G. Ambaw, K. MacSween, D. Solomon, E. Wollenberg, *Climate Policy* **2022**, 22, 427–444.
- [17] “International Environmental Law: History and milestones,” can be found under <https://aida-americas.org/en/blog/international-environmental-law-history-and-milestones>, **2020**.
- [18] L. B. Soiin, *The Stockholm Declaration on the Human Environment* **1972**, 94.
- [19] C. A. Petsonk, *Am. U. J. Int’l L. & Pol’y* **1989**, 5, 351–392.
- [20] G. H. Brundtland, **1987**.
- [21] UNEP, **2020**, 960.
- [22] “IPCC — Intergovernmental Panel on Climate Change,” can be found under <https://www.ipcc.ch/>, **n.d.**
- [23] *UNITED NATIONS FRAMEWORK CONVENTION ON CLIMATE CHANGE* **1992**, 33.
- [24] United Nations Conference on Environment & Development, **1992**.
- [25] S. Oberthür, H. Ott, *The Kyoto Protocol: International Climate Policy for the 21st Century*, Springer, New York, **1999**.
- [26] “United Nations Millennium Declaration,” can be found under <https://www.ohchr.org/en/instruments-mechanisms/instruments/united-nations-millennium-declaration>, **n.d.**

- [27] L. Hens, B. Nath, *Environment, Development and Sustainability* **2003**, 5, 7–39.
- [28] UNFCCC, “Climate Finance | UNFCCC,” can be found under https://unfccc.int/topics/climate-finance/the-big-picture/climate-finance-in-the-negotiations/climate-finance?gclid=CjwKCAjwkaSaBhA4EiwALBgQaANSsOuvVf0YZ2y75hjdAk0UuVRSHyflAXQNSGOkR03r2fll6-Ghx0CuHcQAvD_BwE, **n.d.**
- [29] “United Nations Conference on Sustainable Development, Rio+20 .. Sustainable Development Knowledge Platform,” can be found under <https://sustainabledevelopment.un.org/rio20.html>, **n.d.**
- [30] G. Erbach, *Doha Amendment to the Kyoto Protocol* **2012**, 1.
- [31] T. Jayaraman, *Review of Agrarian Studies* **2015**, Volume 5.
- [32] M. Usman, A. Jahanger, M. S. A. Makhdum, D. Balsalobre-Lorente, A. Bashir, *Energy* **2022**, 241, 122515.
- [33] A. Anwar, A. Sinha, A. Sharif, M. Siddique, S. Irshad, W. Anwar, S. Malik, *Environ Dev Sustain* **2022**, 24, 6556–6576.
- [34] “Advisory Opinion (OC-23/17) - Inter-American Court of Human Rights | ELAW,” can be found under https://www.elaw.org/IACHR_CO2317, **n.d.**
- [35] Presidente della Repubblica, *Decreto del Presidente della Repubblica, n. 203* **1988**, 8.
- [36] D. E. Painter, *Air Pollution Technology*, Reston Pub. Co, Reston, Va, **1974**.
- [37] S. Sonwani, P. Saxena, **2016**, 6, 21.
- [38] N. Hickey, I. Boscarato, J. Kaspar, in *Current Environmental Issues and Challenges* (Eds.: G. Cao, R. Orrù), Springer Netherlands, Dordrecht, **2014**, pp. 15–43.
- [39] O. US EPA, “AP-42: Compilation of Air Emissions Factors,” can be found under <https://www.epa.gov/air-emissions-factors-and-quantification/ap-42-compilation-air-emissions-factors>, **2016**.
- [40] M. A. Khan, A. M. Ghouri, **2011**.

- [41] Y. Sadanaga, J. Matsumoto, Y. Kajii, *Journal of Photochemistry and Photobiology C: Photochemistry Reviews* **2003**, *4*, 85–104.
- [42] “Mapping of Tree Damage Classification in The Western Part of Medan City Green Belts Using Geographic Information System - IOPscience,” can be found under <https://iopscience.iop.org/article/10.1088/1755-1315/166/1/012020>, **n.d.**
- [43] P. C. Jain, *Renewable Energy* **1993**, *3*, 403–420.
- [44] O. US EPA, “Overview of Greenhouse Gases,” can be found under <https://www.epa.gov/ghgemissions/overview-greenhouse-gases>, **2015**.
- [45] R. Tuckett, in *Encyclopedia of Analytical Science* (Eds.: P. Worsfold, A. Townshend, C. Poole, M. Miró), Elsevier, **2019**, pp. 362–372.
- [46] D. Kweku, O. Bismark, A. Maxwell, K. Desmond, K. Danso, E. Oti-Mensah, A. Quachie, B. Adormaa, *JSRR* **2018**, *17*, 1–9.
- [47] “Radiation Budget Diagram for Earth’s Atmosphere | Center for Science Education,” can be found under <https://scied.ucar.edu/image/radiation-budget-diagram-earth-atmosphere>, **n.d.**
- [48] B. Kaur, J. Singh, R. K. Gupta, H. Bhunia, *Journal of Environmental Management* **2019**, *242*, 68–80.
- [49] O. H. P. Gunawardene, C. A. Gunathilake, K. Vikrant, S. M. Amaraweera, *Atmosphere* **2022**, *13*, 397.
- [50] R. Cassia, M. Nocioni, N. Correa-Aragunde, L. Lamattina, *Front. Plant Sci.* **2018**, *9*, 273.
- [51] M. Deng, H. G. Park, *Langmuir* **2019**, *35*, 4453–4459.
- [52] L. D. Danny Harvey, *Energy Policy* **1993**, *21*, 24–34.
- [53] EPA - United State Environmental Protection Agency, **2018**.
- [54] C. Scheutz, P. Kjeldsen, E. Gentil, *Waste Manag Res* **2009**, *27*, 716–723.
- [55] G. A. Schmidt, R. A. Ruedy, R. L. Miller, A. A. Lacis, *J. Geophys. Res.* **2010**, *115*, D20106.

- [56] N. US Department of Commerce, “NOAA/ESRL Global Monitoring Laboratory - THE NOAA ANNUAL GREENHOUSE GAS INDEX (AGGI),” can be found under <https://gml.noaa.gov/aggi/>, **n.d.**
- [57] J. Zhao, Y. Li, R. Dong, *Science of The Total Environment* **2021**, *800*, 149667.
- [58] L. Lombardi, G. Francini, *Renewable Energy* **2020**, *156*, 440–458.
- [59] J. B. Holm-Nielsen, T. Al Seadi, P. Oleskowicz-Popiel, *Bioresource Technology* **2009**, *100*, 5478–5484.
- [60] P. Styring, Ed. , *Carbon Dioxide Utilisation: Closing the Carbon Cycle*, Elsevier, Amsterdam Heidelberg, **2015**.
- [61] E. S. Sanz-Pérez, C. R. Murdock, S. A. Didas, C. W. Jones, *Chem. Rev.* **2016**, *116*, 11840–11876.
- [62] Z. Liu, *Applied Energy* **2016**, *166*, 239–244.
- [63] F. Sher, S. Z. Iqbal, S. Albazzaz, U. Ali, D. A. Mortari, T. Rashid, *Fuel* **2020**, *282*, 118506.
- [64] X. Yuan, J. Wang, S. Deng, M. Suvarna, X. Wang, W. Zhang, S. T. Hamilton, A. Alahmed, A. Jamal, A.-H. A. Park, X. Bi, Y. S. Ok, *Renewable and Sustainable Energy Reviews* **2022**, *162*, 112413.
- [65] International Energy Agency, **2021**, 14.
- [66] N. US Department of Commerce, “Global Monitoring Laboratory - Carbon Cycle Greenhouse Gases,” can be found under <https://gml.noaa.gov/ccgg/trends/>, **n.d.**
- [67] B. Kaur, R. K. Gupta, H. Bhunia, *Chemical Engineering Communications* **2020**, *207*, 1031–1047.
- [68] D. Y. C. Leung, G. Caramanna, M. M. Maroto-Valer, *Renewable and Sustainable Energy Reviews* **2014**, *39*, 426–443.
- [69] B. Sreenivasulu, D. V. Gayatri, I. Sreedhar, K. V. Raghavan, *Renewable and Sustainable Energy Reviews* **2015**, *41*, 1324–1350.

- [70] L. Shao, Y. Sang, J. Huang, Y.-N. Liu, *Chemical Engineering Journal* **2018**, 353, 1–14.
- [71] S. Salehi, M. Anbia, *Applied Organometallic Chemistry* **2018**, 32, e4390.
- [72] D. Tiwari, H. Bhunia, P. K. Bajpai, *Applied Surface Science* **2018**, 439, 760–771.
- [73] R. Ben-Mansour, M. A. Habib, O. E. Bamidele, M. Basha, N. A. A. Qasem, A. Peedikakkal, T. Laoui, M. Ali, *Applied Energy* **2016**, 161, 225–255.
- [74] J. Han, L. Zhang, B. Zhao, L. Qin, Y. Wang, F. Xing, *Industrial Crops and Products* **2019**, 128, 290–297.
- [75] N. S. Sifat, Y. Haseli, *Energies* **2019**, 12, 4143.
- [76] K. S. Lackner, in *Issues in Environmental Science and Technology* (Eds.: R.E. Hester, R.M. Harrison), Royal Society Of Chemistry, Cambridge, **2009**, pp. 1–40.
- [77] Y. Zhang, X. Lu, X. Ji, in *Deep Eutectic Solvents* (Eds.: D.J. Ramón, G. Guillena), Wiley, **2019**, pp. 297–319.
- [78] C. Gunathilake, R. S. Dassanayake, N. Abidi, M. Jaroniec, *J. Mater. Chem. A* **2016**, 4, 4808–4819.
- [79] A. Alabadi, S. Razzaque, Y. Yang, S. Chen, B. Tan, *Chemical Engineering Journal* **2015**, 281, 606–612.
- [80] S.-Y. Lee, S.-J. Park, *Journal of Industrial and Engineering Chemistry* **2015**, 23, 1–11.
- [81] eva, “Carbon Capture (CCUS) | Enrag,” can be found under <https://www.enrag.at/en/ccus/>, **2022**.
- [82] R. Chatterjee, B. Sajjadi, W.-Y. Chen, D. L. Mattern, N. Hammer, V. Raman, A. Dorris, *Frontiers in Energy Research* **2020**, 8.
- [83] S. Topham, A. Bazzanella, S. Schiebahn, S. Luhr, L. Zhao, A. Otto, D. Stolten, in *Ullmann’s Encyclopedia of Industrial Chemistry* (Ed.: Wiley-VCH Verlag GmbH & Co. KGaA), Wiley-VCH Verlag GmbH & Co. KGaA, Weinheim, Germany, **2014**, pp. 1–43.

- [84] J. Singh, H. Bhunia, S. Basu, *Environmental Technology & Innovation* **2020**, *20*, 101104.
- [85] P. Babu, P. Linga, R. Kumar, P. Englezos, *Energy* **2015**, *85*, 261–279.
- [86] F. Carrasco-Maldonado, R. Spörl, K. Fleiger, V. Hoenig, J. Maier, G. Scheffknecht, *International Journal of Greenhouse Gas Control* **2016**, *45*, 189–199.
- [87] R. M. Cuéllar-Franca, A. Azapagic, *Journal of CO₂ Utilization* **2015**, *9*, 82–102.
- [88] Y. Li, R. Xu, B. Wang, J. Wei, L. Wang, M. Shen, J. Yang, *Nanomaterials* **2019**, *9*, 266.
- [89] A. D. Igalavithana, S. W. Choi, J. Shang, A. Hanif, P. D. Dissanayake, D. C. W. Tsang, J.-H. Kwon, K. B. Lee, Y. S. Ok, *Science of The Total Environment* **2020**, *739*, 139845.
- [90] V. Benedetti, E. Cordioli, F. Patuzzi, M. Baratieri, *Journal of CO₂ Utilization* **2019**, *33*, 46–54.
- [91] R. S. Dassanayake, S. Acharya, N. Abidi, in *Advanced Sorption Process Applications* (Ed.: S. Edebali), IntechOpen, **2019**.
- [92] J. Chen, L. Jiang, W. Wang, Z. Shen, S. Liu, X. Li, Y. Wang, *Journal of Colloid and Interface Science* **2022**, *609*, 775–784.
- [93] R. Czarnota, E. Knapik, P. Wojnarowski, D. Janiga, J. Stopa, *Archives of Mining Sciences* **2019**, 487–498.
- [94] H. Yang, Z. Xu, M. Fan, R. Gupta, R. B. Slimane, A. E. Bland, I. Wright, *Journal of Environmental Sciences* **2008**, *20*, 14–27.
- [95] A. Al-Mamoori, A. Krishnamurthy, A. A. Rownaghi, F. Rezaei, *Energy Technol.* **2017**, *5*, 834–849.
- [96] C. K. C. Cabriga, K. V. B. Clarete, J. A. T. Zhang, R. M. P. Pacia, Y. S. Ko, J. C. Castro, *Biomass Conv. Bioref.* **2021**, DOI 10.1007/s13399-021-01719-z.
- [97] M. Nandi, H. Uyama, *The Chemical Record* **2014**, *14*, 1134–1148.

- [98] F. O. Ochedi, Y. Liu, Y. G. Adewuyi, *Process Safety and Environmental Protection* **2020**, *139*, 1–25.
- [99] A. D. Igalavithana, S. W. Choi, P. D. Dissanayake, J. Shang, C.-H. Wang, X. Yang, S. Kim, D. C. W. Tsang, K. B. Lee, Y. S. Ok, *Journal of Hazardous Materials* **2020**, *391*, 121147.
- [100] Y.-S. Bae, R. Q. Snurr, *Angewandte Chemie International Edition* **2011**, *50*, 11586–11596.
- [101] A. A. Abd, S. Z. Naji, A. S. Hashim, M. R. Othman, *Journal of Environmental Chemical Engineering* **2020**, *8*, 104142.
- [102] C. Graham D. A. Imrie R. E. Raab, *Molecular Physics* **1998**, *93*, 49–56.
- [103] C. Gunathilake, A. S. Manchanda, P. Ghimire, M. Kruk, M. Jaroniec, *Environ. Sci.: Nano* **2016**, *3*, 806–817.
- [104] M. Yao, L. Wang, X. Hu, G. Hu, M. Luo, M. Fan, *J Mater Sci* **2015**, *50*, 1221–1227.
- [105] H. A. Patel, J. Byun, C. T. Yavuz, *ChemSusChem* **2017**, *10*, 1303–1317.
- [106] H. Rasoulzadeh, S. Motesaddi Zarandi, M. Massoudinejad, M. M. Amini, *International Journal of Environmental Analytical Chemistry* **2021**, *0*, 1–22.
- [107] G. Gan, X. Li, S. Fan, L. Wang, M. Qin, Z. Yin, G. Chen, *European Journal of Inorganic Chemistry* **2019**, *2019*, 3126–3141.
- [108] G. Gómez-Pozuelo, E. S. Sanz-Pérez, A. Arencibia, P. Pizarro, R. Sanz, D. P. Serrano, *Microporous and Mesoporous Materials* **2019**, *282*, 38–47.
- [109] M. L. Gray, K. J. Champagne, D. Fauth, J. P. Baltrus, H. Pennline, *International Journal of Greenhouse Gas Control* **2008**, *2*, 3–8.
- [110] R. Tu, Y. Sun, Y. Wu, X. Fan, J. Wang, S. Cheng, Z. Jia, E. Jiang, X. Xu, *Renewable Energy* **2021**, *167*, 82–90.
- [111] F. E. C. Othman, N. Yusof, A. F. Ismail, *Chemical Engineering & Technology* **2020**, *43*, 2023–2030.
- [112] U. Kamran, J. R. Choi, S.-J. Park, *Frontiers in Chemistry* **2020**, *8*.

- [113] X. Liu, C. Sun, H. Liu, W. H. Tan, W. Wang, C. Snape, *Chemical Engineering Journal* **2019**, *361*, 199–208.
- [114] H. Zhao, X. Luo, H. Zhang, N. Sun, W. Wei, Y. Sun, *Greenhouse Gas Sci Technol* **2018**, *8*, 11–36.
- [115] P. Samanta, A. V. Desai, S. Let, S. K. Ghosh, *ACS Sustainable Chem. Eng.* **2019**, *7*, 7456–7478.
- [116] S. Choi, J. H. Drese, C. W. Jones, *ChemSusChem* **2009**, *2*, 796–854.
- [117] A. W. Chester, E. G. Derouane, Eds. , *Zeolite Chemistry and Catalysis*, Springer Netherlands, Dordrecht, **2009**.
- [118] J. C. Abanades, B. Arias, A. Lyngfelt, T. Mattisson, D. E. Wiley, H. Li, M. T. Ho, E. Mangano, S. Brandani, *International Journal of Greenhouse Gas Control* **2015**, *40*, 126–166.
- [119] R. V. Siriwardane, M.-S. Shen, E. P. Fisher, *Energy Fuels* **2003**, *17*, 571–576.
- [120] S. Cavenati, C. A. Grande, A. E. Rodrigues, *J. Chem. Eng. Data* **2004**, *49*, 1095–1101.
- [121] P. J. E. Harlick, F. H. Tezel, *Microporous and Mesoporous Materials* **2004**, *76*, 71–79.
- [122] R. H. Huesca, J. P. Arcos, D. V. Hernández, M. A. P. Cruz, *Revista Internacional de Contaminación Ambiental* **2016**, *32*, 237–242.
- [123] H.-C. “Joe” Zhou, S. Kitagawa, *Chem. Soc. Rev.* **2014**, *43*, 5415–5418.
- [124] R.-B. Lin, S. Xiang, W. Zhou, B. Chen, *Chem* **2020**, *6*, 337–363.
- [125] J. L. C. Rowsell, O. M. Yaghi, *Microporous and Mesoporous Materials* **2004**, *73*, 3–14.
- [126] M. Gheytnazadeh, A. Baghban, S. Habibzadeh, A. Esmaili, O. Abida, A. Mohaddespour, M. T. Munir, *Sci Rep* **2021**, *11*, 15710.
- [127] J. H. Choe, H. Kim, C. S. Hong, *Mater. Chem. Front.* **2021**, *5*, 5172–5185.
- [128] Z. Li, P. Liu, C. Ou, X. Dong, *ACS Sustainable Chem. Eng.* **2020**, *8*, 15378–15404.

- [129] F. Xu, Y. Yu, J. Yan, Q. Xia, H. Wang, J. Li, Z. Li, *Chemical Engineering Journal* **2016**, *303*, 231–237.
- [130] C. Chen, B. Li, L. Zhou, Z. Xia, N. Feng, J. Ding, L. Wang, H. Wan, G. Guan, *ACS Appl. Mater. Interfaces* **2017**, *9*, 23060–23071.
- [131] M. He, T. Xu, Z. Jiang, L. Yang, Y. Zou, F. Xia, X. Wang, X. Wang, Y. He, *Inorg. Chem. Front.* **2019**, *6*, 1177–1183.
- [132] C. Chen, N. Feng, Q. Guo, Z. Li, X. Li, J. Ding, L. Wang, H. Wan, G. Guan, *Journal of Colloid and Interface Science* **2018**, *521*, 91–101.
- [133] A. Ö. Yazaydın, R. Q. Snurr, T.-H. Park, K. Koh, J. Liu, M. D. LeVan, A. I. Benin, P. Jakubczak, M. Lanuza, D. B. Galloway, J. J. Low, R. R. Willis, *J. Am. Chem. Soc.* **2009**, *131*, 18198–18199.
- [134] S. E. M. Elhenawy, M. Khraisheh, F. AlMomani, G. Walker, *Catalysts* **2020**, *10*, 1293.
- [135] J.-R. Li, R. J. Kuppler, H.-C. Zhou, *Chem. Soc. Rev.* **2009**, *38*, 1477.
- [136] S. Mukherjee, A. Kumar, M. J. Zaworotko, in *Metal-Organic Frameworks (MOFs) for Environmental Applications*, Elsevier, **2019**, pp. 5–61.
- [137] F. Qin, Z. Guo, J. Wang, S. Qu, P. Zuo, W. Shen, *Applied Surface Science* **2019**, *491*, 607–615.
- [138] L. Li, X.-F. Wang, J.-J. Zhong, X. Qian, S.-L. Song, Y.-G. Zhang, D.-H. Li, *Ind. Eng. Chem. Res.* **2018**, *57*, 11608–11616.
- [139] X. Zhang, I. Elsayed, X. Song, R. Shmulsky, E. B. Hassan, *Science of The Total Environment* **2020**, *748*, 142465.
- [140] S. Liu, L. Rao, P. Yang, X. Wang, L. Wang, R. Ma, L. Yue, X. Hu, *Journal of Environmental Sciences* **2020**, *93*, 109–116.
- [141] S. Liu, Q. Li, L. Wang, R. Ma, J. Zou, L. Huang, X. Hu, *Energy Fuels* **2019**, *33*, 11544–11551.
- [142] M. S. Shafeeyan, W. M. A. W. Daud, A. Shamiri, N. Aghamohammadi, *Chemical Engineering Research and Design* **2015**, *104*, 42–52.

- [143] J. Silvestre-Albero, A. Wahby, A. Sepúlveda-Escribano, M. Martínez-Escandell, K. Kaneko, F. Rodríguez-Reinoso, *Chem. Commun.* **2011**, 47, 6840.
- [144] M. E. Casco, M. Martínez-Escandell, E. Gadea-Ramos, K. Kaneko, J. Silvestre-Albero, F. Rodríguez-Reinoso, *Chem. Mater.* **2015**, 27, 959–964.
- [145] P. N. E. Diagboya, E. D. Dikio, *Microporous and Mesoporous Materials* **2018**, 266, 252–267.
- [146] G. Celoria, V. Miglio, G. Paul, C. Bisio, G. Golemme, E. Boccaleri, *Processes* **2022**, 10, 964.
- [147] V. Miglio, C. Zacccone, C. Vittoni, I. Braschi, E. Buscaroli, G. Golemme, L. Marchese, C. Bisio, *Molecules* **2021**, 26, 1316.
- [148] C. Vittoni, G. Gatti, I. Braschi, E. Buscaroli, G. Golemme, L. Marchese, C. Bisio, *Materials* **2020**, 13, 2690.
- [149] Y. Fan, X. Jia, *Energy Fuels* **2022**, 36, 1252–1270.
- [150] N. A. Brunelli, S. A. Didas, K. Venkatasubbaiah, C. W. Jones, *J. Am. Chem. Soc.* **2012**, 134, 13950–13953.
- [151] E. Vilarrasa-García, J. A. Cecilia, P. A. S. Moura, D. C. S. Azevedo, E. Rodríguez-Castellón, *Front. Chem.* **2020**, 8, 591766.
- [152] R. Kapoor, P. Ghosh, M. Kumar, S. Sengupta, A. Gupta, S. S. Kumar, V. Vijay, V. Kumar, V. Kumar Vijay, D. Pant, *Bioresource Technology* **2020**, 304, 123036.
- [153] Adnan, Ong, Nomanbhay, Chew, Show, *Bioengineering* **2019**, 6, 92.
- [154] C. Moya, R. Santiago, D. Hospital-Benito, J. Lemus, J. Palomar, *Chemical Engineering Journal* **2022**, 428, 132103.
- [155] S. Chaemchuen, K. Zhou, F. Verpoort, *ChemBioEng Reviews* **2016**, 3, 250–265.
- [156] S. Fu, I. Angelidaki, Y. Zhang, *Trends in Biotechnology* **2021**, 39, 336–347.
- [157] A. Mishra, M. Kumar, N. S. Bolan, A. Kapley, R. Kumar, L. Singh, *Bioresource Technology* **2021**, 338, 125514.

- [158] F. Ardolino, G. F. Cardamone, F. Parrillo, U. Arena, *Renewable and Sustainable Energy Reviews* **2021**, *139*, 110588.
- [159] H. Thunman, C. Gustavsson, A. Larsson, I. Gunnarsson, F. Tengberg, *Energy Sci Eng* **2019**, *7*, 217–229.
- [160] K. R. Chew, H. Y. Leong, K. S. Khoo, D.-V. N. Vo, H. Anjum, C.-K. Chang, P. L. Show, *Environ Chem Lett* **2021**, *19*, 2921–2939.
- [161] M. Mofijur, I. M. R. Fattah, P. S. Kumar, Sk. Y. A. Siddiki, S. M. A. Rahman, S. F. Ahmed, H. C. Ong, S. S. Lam, I. A. Badruddin, T. M. Y. Khan, T. M. I. Mahlia, *Journal of Environmental Chemical Engineering* **2021**, *9*, 105657.
- [162] I. S. Thakur, M. Kumar, S. J. Varjani, Y. Wu, E. Gnansounou, S. Ravindran, *Bioresource Technology* **2018**, *256*, 478–490.
- [163] X. Xiong, I. K. M. Yu, D. C. W. Tsang, N. S. Bolan, Y. Sik Ok, A. D. Igalavithana, M. B. Kirkham, K.-H. Kim, K. Vikrant, *Chemical Engineering Journal* **2019**, *375*, 121983.
- [164] D. Díaz-Vázquez, S. C. Alvarado-Cummings, D. Meza-Rodríguez, C. Senés-Guerrero, J. de Anda, M. S. Gradilla-Hernández, *Sustainability* **2020**, *12*, 3527.
- [165] S. Sahota, G. Shah, P. Ghosh, R. Kapoor, S. Sengupta, P. Singh, V. Vijay, A. Sahay, V. K. Vijay, I. S. Thakur, *Bioresource Technology Reports* **2018**, *1*, 79–88.
- [166] P. Merlin Christy, L. R. Gopinath, D. Divya, *Renewable and Sustainable Energy Reviews* **2014**, *34*, 167–173.
- [167] D. Divya, L. R. Gopinath, P. Merlin Christy, *Renewable and Sustainable Energy Reviews* **2015**, *42*, 690–699.
- [168] P. Bohutskyi, E. Bouwer, in *Advanced Biofuels and Bioproducts* (Ed.: J.W. Lee), Springer New York, New York, NY, **2013**, pp. 873–975.
- [169] O. W. Awe, Y. Zhao, A. Nzihou, D. P. Minh, N. Lyczko, *Waste Biomass Valor* **2017**, *8*, 267–283.
- [170] J. Mata-Alvarez, Ed. , *Biomethanization of the Organic Fraction of Municipal Solid Wastes*, IWA-Publ, London, **2003**.

- [171] I. Angelidaki, L. Treu, P. Tsapekos, G. Luo, S. Campanaro, H. Wenzel, P. G. Kougias, *Biotechnology Advances* **2018**, *36*, 452–466.
- [172] M. U. Khan, J. T. E. Lee, M. A. Bashir, P. D. Dissanayake, Y. S. Ok, Y. W. Tong, M. A. Shariati, S. Wu, B. K. Ahring, *Renewable and Sustainable Energy Reviews* **2021**, *149*, 111343.
- [173] R. Muñoz, L. Meier, I. Diaz, D. Jeison, *Rev Environ Sci Biotechnol* **2015**, *14*, 727–759.
- [174] H. M. Mahmudul, M. G. Rasul, D. Akbar, R. Narayanan, M. Mofijur, *Science of The Total Environment* **2021**, *753*, 141920.
- [175] N. Pr eat, S. E. Taelman, S. De Meester, F. Allais, J. Dewulf, *Algal Research* **2020**, *45*, 101737.
- [176] A. Pertl, P. Mostbauer, G. Obersteiner, *Waste Management* **2010**, *30*, 92–99.
- [177] S. Achinas, G. J. Willem Euverink, *Renewable and Sustainable Energy Reviews* **2020**, *119*, 109566.
- [178] F. Ardolino, U. Arena, *Waste Management* **2019**, *87*, 441–453.
- [179] P. Weiland, *Appl Microbiol Biotechnol* **2010**, *85*, 849–860.
- [180] Y. Xu, Y. Huang, B. Wu, X. Zhang, S. Zhang, *Chinese Journal of Chemical Engineering* **2015**, *23*, 247–254.
- [181] I. Ullah Khan, M. Hafiz Dzarfan Othman, H. Hashim, T. Matsuura, A. F. Ismail, M. Rezaei-DashtArzhandi, I. Wan Azelee, *Energy Conversion and Management* **2017**, *150*, 277–294.
- [182] C. Song, Q. Liu, S. Deng, H. Li, Y. Kitamura, *Renewable and Sustainable Energy Reviews* **2019**, *101*, 265–278.
- [183] R. Kadam, N. L. Panwar, *Renewable and Sustainable Energy Reviews* **2017**, *73*, 892–903.
- [184] K. Zhou, S. Chaemchuen, F. Verpoort, *Renewable and Sustainable Energy Reviews* **2017**, *79*, 1414–1441.
- [185] Q. Sun, H. Li, J. Yan, L. Liu, Z. Yu, X. Yu, *Renewable and Sustainable Energy Reviews* **2015**, *51*, 521–532.

- [186] A. Bose, R. Lin, K. Rajendran, R. O'Shea, A. Xia, J. D. Murphy, *Biotechnology Advances* **2019**, *37*, 107444.
- [187] N. Abatzoglou, S. Boivin, *Biofuels, Bioprod. Bioref.* **2009**, *3*, 42–71.
- [188] S. F. Ahmed, M. Mofijur, K. Tarannum, A. T. Chowdhury, N. Rafa, S. Nuzhat, P. S. Kumar, D.-V. N. Vo, E. Lichtfouse, T. M. I. Mahlia, *Environ Chem Lett* **2021**, *19*, 4137–4164.
- [189] J. W. Lim, T. Park, Y. W. Tong, Z. Yu, in *Advances in Bioenergy* (Eds.: Y. Li, S.K. Khanal), Elsevier, **2020**, pp. 1–61.
- [190] M. Kumar, S. Dutta, S. You, G. Luo, S. Zhang, P. L. Show, A. D. Sawarkar, L. Singh, D. C. W. Tsang, *Journal of Cleaner Production* **2021**, *305*, 127143.
- [191] V. Paolini, F. Petracchini, M. Segreto, L. Tomassetti, N. Naja, A. Cecinato, *Journal of Environmental Science and Health, Part A* **2018**, *53*, 899–906.
- [192] F. Bauer, T. Persson, C. Hulteberg, D. Tamm, *Biofuels, Bioprod. Bioref.* **2013**, *7*, 499–511.
- [193] Q. Wang, Y. Yu, Y. Li, X. Min, J. Zhang, T. Sun, *Separation and Purification Technology* **2022**, *283*, 120206.
- [194] F. Bauer, C. Hulteberg, T. Persson, D. Tamm, **n.d.**, 83.
- [195] T. Patterson, S. Esteves, R. Dinsdale, A. Guwy, *Energy Policy* **2011**, *39*, 1806–1816.
- [196] S. Nakao, K. Yogo, K. Goto, T. Kai, H. Yamada, *Advanced CO₂ Capture Technologies: Absorption, Adsorption, and Membrane Separation Methods*, Springer International Publishing, Cham, **2019**.
- [197] E. Hunter-Sellars, J. J. Tee, I. P. Parkin, D. R. Williams, *Microporous and Mesoporous Materials* **2020**, *298*, 110090.
- [198] S. Sircar, *Ind. Eng. Chem. Res.* **2002**, *41*, 1389–1392.
- [199] R. L. S. Canevesi, K. A. Andreassen, E. A. da Silva, C. E. Borba, C. A. Grande, *Ind. Eng. Chem. Res.* **2018**, *57*, 8057–8067.
- [200] S. K. Wahono, J. Stalin, J. Addai-Mensah, W. Skinner, A. Vinu, K. Vasilev, *Microporous and Mesoporous Materials* **2020**, *294*, 109871.

- [201] G. Vilardi, C. Bassano, P. Deiana, N. Verdone, *Energy Conversion and Management* **2020**, 226, 113482.
- [202] R. Kapoor, P. Ghosh, M. Kumar, V. K. Vijay, *Environ Sci Pollut Res* **2019**, 26, 11631–11661.
- [203] J. C. Kuo, K. H. Wang, C. Chen, *Journal of Natural Gas Science and Engineering* **2012**, 7, 52–59.
- [204] T. A. Makal, J.-R. Li, W. Lu, H.-C. Zhou, *Chem. Soc. Rev.* **2012**, 41, 7761.
- [205] A. Yu. Tsivadze, O. E. Aksyutin, A. G. Ishkov, I. E. Men'shchikov, A. A. Fomkin, A. V. Shkolin, E. V. Khozina, V. A. Grachev, *Russ. Chem. Rev.* **2018**, 87, 950–983.
- [206] E. Mahmoud, *Surfaces* **2020**, 3, 433–466.
- [207] N. Byamba-Ochir, W. G. Shim, M. S. Balathanigaimani, H. Moon, *Applied Energy* **2017**, 190, 257–265.
- [208] S. J. Bhadra, S. Farooq, *Ind. Eng. Chem. Res.* **2011**, 50, 14030–14045.
- [209] K. Kalantar-zadeh, *Sensors: An Introductory Course*, Springer, New York, **2013**.
- [210] M. Tonezzer, S. C. Izidoro, J. P. A. Moraes, L. T. T. Dang, *Front. Mater.* **2019**, 6, 277.
- [211] X. Ren, T. Sun, J. Hu, S. Wang, *Microporous and Mesoporous Materials* **2014**, 186, 137–145.
- [212] S. Cavenati, C. Grande, A. Rodrigues, *Separation Science and Technology* **2005**, 40, 2721–2743.
- [213] T. E. Rufford, S. Smart, G. C. Y. Watson, B. F. Graham, J. Boxall, J. C. Diniz da Costa, E. F. May, *Journal of Petroleum Science and Engineering* **2012**, 94–95, 123–154.
- [214] Z. Yang, D. Wang, Z. Meng, Y. Li, *Separation and Purification Technology* **2019**, 218, 130–137.
- [215] J. A. Delgado, M. A. Uguina, J. L. Sotelo, B. Ruíz, *Separation and Purification Technology* **2006**, 50, 192–203.

- [216] “International Decade for Action ‘Water for Life’ 2005-2015. Focus Areas: The human right to water and sanitation,” can be found under https://www.un.org/waterforlifedecade/human_right_to_water.shtml, **n.d.**
- [217] “National Environmental Act 1980 (No. 47 of 1980). | FAOLEX,” can be found under <https://www.fao.org/faolex/results/details/en/c/LEX-FAOC013492/>, **n.d.**
- [218] P. M. Chapman, *Environment International* **2007**, *33*, 492–501.
- [219] R. Kumar, M. Qureshi, D. K. Vishwakarma, N. Al-Ansari, A. Kuriqi, A. Elbeltagi, A. Saraswat, *Case Studies in Chemical and Environmental Engineering* **2022**, *6*, 100219.
- [220] **N.d.**
- [221] **N.d.**
- [222] J. J. Peirce, R. F. Weiner, P. A. Vesilind, in *Environmental Pollution and Control*, Elsevier, **1998**, pp. 31–55.
- [223] I. Ali, *Chem. Rev.* **2012**, *112*, 5073–5091.
- [224] M. Kumar, P. Borah, P. Devi, in *Inorganic Pollutants in Water*, Elsevier, **2020**, pp. 33–49.
- [225] C. Yan, Z. Qu, J. Wang, L. Cao, Q. Han, *Chemosphere* **2022**, *286*, 131870.
- [226] A. E. Burakov, E. V. Galunin, I. V. Burakova, A. E. Kucherova, S. Agarwal, A. G. Tkachev, V. K. Gupta, *Ecotoxicology and Environmental Safety* **2018**, *148*, 702–712.
- [227] D. Han, M. J. Currell, *Science of The Total Environment* **2017**, *580*, 602–625.
- [228] K. C. Jones, P. de Voogt, *Environmental Pollution* **1999**, *100*, 209–221.
- [229] Q. Liu, *IOP Conf. Ser.: Earth Environ. Sci.* **2020**, *514*, 052001.
- [230] M. Rajabi, K. Mahanpoor, O. Moradi, *RSC Adv.* **2017**, *7*, 47083–47090.
- [231] M. Marcucci, G. Nosenzo, G. Capannelli, I. Ciabatti, D. Corrieri, G. Ciardelli, *Desalination* **2001**, *138*, 75–82.
- [232] A. Gürses, M. Açıkyıldız, K. Güneş, M. S. Gürses, in *Dyes and Pigments*, Springer International Publishing, Cham, **2016**, pp. 31–45.

- [233] P. E. Rosenfeld, L. G. H. Feng, in *Risks of Hazardous Wastes*, Elsevier, **2011**, pp. 215–222.
- [234] L. B. Barber, in *Comprehensive Water Quality and Purification*, Elsevier, **2014**, pp. 245–266.
- [235] S. Rasalingam, R. Peng, R. T. Koodali, *Applied Catalysis B: Environmental* **2015**, *174–175*, 49–59.
- [236] R. Jain, M. Mathur, S. Sikarwar, A. Mittal, *Journal of Environmental Management* **2007**, *85*, 956–964.
- [237] J. Chen, X. Zhu, *Food Chemistry* **2016**, *200*, 10–15.
- [238] K. G. Bhattacharyya, S. SenGupta, G. K. Sarma, *Applied Clay Science* **2014**, *99*, 7–17.
- [239] Z.-L. Cheng, Y. Li, Z. Liu, *Ecotoxicology and Environmental Safety* **2018**, *148*, 585–592.
- [240] F. Hayeeye, M. Sattar, W. Chinpa, O. Sirichote, *Colloids and Surfaces A: Physicochemical and Engineering Aspects* **2017**, *513*, 259–266.
- [241] T. Santhi, A. L. Prasad, S. Manonmani, *Arabian Journal of Chemistry* **2014**, *7*, 494–503.
- [242] R. Ianoş, C. Păcurariu, S. G. Muntean, E. Muntean, M. A. Nistor, D. Nižňanský, *Journal of Alloys and Compounds* **2018**, *741*, 1235–1246.
- [243] A. A. Al-Gheethi, Q. M. Azhar, P. Senthil Kumar, A. A. Yusuf, A. K. Al-Buriah, R. M. S. Radin Mohamed, M. M. Al-shaibani, *Chemosphere* **2022**, *287*, 132080.
- [244] P. Sarkar, A. Dey, *Process Safety and Environmental Protection* **2021**, *147*, 214–225.
- [245] G. Muthuraman, T. T. Teng, *Journal of Industrial and Engineering Chemistry* **2009**, *15*, 841–846.
- [246] A. R. Tripp, D. A. Clifford, *Journal - American Water Works Association* **2006**, *98*, 105–114.

- [247] A. Leudjo Taka, K. Pillay, X. Yangkou Mbianda, *Carbohydrate Polymers* **2017**, *159*, 94–107.
- [248] J. A. Lara-Ramos, J. Diaz-Angulo, F. Machuca-Martínez, *Chemical Engineering Journal* **2021**, *405*, 126978.
- [249] M. M. Bello, A. A. Abdul Raman, A. Asghar, *Process Safety and Environmental Protection* **2019**, *126*, 119–140.
- [250] M. R. Gadekar, M. M. Ahammed, *Desalination and Water Treatment* **2016**, *57*, 26392–26400.
- [251] R. Gusain, K. Gupta, P. Joshi, O. P. Khatri, *Advances in Colloid and Interface Science* **2019**, *272*, 102009.
- [252] D. A. Tran, C. T. Nguyen Pham, T. Nguyen Ngoc, H. Nguyen Phi, Q. T. Hoai Ta, D. H. Truong, V. T. Nguyen, H. H. Luc, L. T. Nguyen, N. N. Dao, S. J. Kim, V. Vo, *Journal of Physics and Chemistry of Solids* **2021**, *151*, 109900.
- [253] T. O. Ajiboye, O. A. Oyewo, D. C. Onwudiwe, *FlatChem* **2021**, *29*, 100277.
- [254] W. Rao, P. Piliouras, X. Wang, A. Guido, K. Kugler, B. Sieren, L. Wang, G. Lv, Z. Li, *Applied Clay Science* **2020**, *197*, 105790.
- [255] F. Azeez, E. Al-Hetlani, M. Arafa, Y. Abdelmonem, A. A. Nazeer, M. O. Amin, M. Madkour, *Sci Rep* **2018**, *8*, 7104.
- [256] K. He, C. Zhao, G. Zhao, G. Han, *J Sol-Gel Sci Technol* **2015**, *75*, 557–563.
- [257] S. Rasalingam, R. Peng, R. T. Koodali, *Journal of Environmental Management* **2013**, *128*, 530–539.
- [258] X. Wu, C. Liu, X. Li, X. Zhang, C. Wang, Y. Liu, *Materials Science in Semiconductor Processing* **2015**, *32*, 76–81.
- [259] N. M. Flores, U. Pal, R. Galeazzi, A. Sandoval, *RSC Adv.* **2014**, *4*, 41099–41110.
- [260] Z. M. Saigl, *Indones. J. Chem.* **2021**, *21*, 1039.
- [261] S. Singh, N. Parveen, H. Gupta, *Environmental Technology & Innovation* **2018**, *12*, 189–195.

- [262] M. Berradi, R. Hsissou, M. Khudhair, M. Assouag, O. Cherkaoui, A. El Bachiri, A. El Harfi, *Heliyon* **2019**, *5*, e02711.
- [263] S. S. Imam, H. F. Babamale, *AJOCS* **2020**, 25–37.
- [264] W. Xiao, Z. N. Garba, S. Sun, I. Lawan, L. Wang, M. Lin, Z. Yuan, *Journal of Cleaner Production* **2020**, *253*, 119989.
- [265] T. Senthilkumar, S. K. Chattopadhyay, L. R. Miranda, *Chemical Engineering Communications* **2017**, *204*, 238–248.
- [266] Z. N. Garba, A. A. Rahim, *Process Safety and Environmental Protection* **2016**, *102*, 54–63.
- [267] J. Wu, J. Yang, G. Huang, C. Xu, B. Lin, *Journal of Cleaner Production* **2020**, *251*, 119717.
- [268] Z. Esvandi, R. Foroutan, S. J. Peighambaroust, A. Akbari, B. Ramavandi, *Surfaces and Interfaces* **2020**, *21*, 100754.
- [269] Z.-L. Cheng, Y.-X. Li, Z. Liu, *Journal of Alloys and Compounds* **2017**, *C*, 255–263.
- [270] X. Tao, S. Wang, Z. Li, *Journal of Environmental Management* **2020**, *255*, 109834.
- [271] B. Damiyine, A. Guenbour, R. Boussen, **2017**, *8*, 860–871.
- [272] M. Ali Khan, <void> Momina, M. Siddiqui, M. Otero, S. Alshareef, M. Rafatullah, *Polymers* **2020**, *12*, 500.
- [273] A. V. Alves, M. Tsianou, P. Alexandridis, *Surfaces* **2020**, *3*, 516–566.
- [274] E. Gagliano, M. Sgroi, P. P. Falciglia, F. G. A. Vagliasindi, P. Roccaro, *Water Research* **2020**, *171*, 115381.
- [275] J. Li, F. Guo, Y. Wang, J. Liu, Z. Cai, J. Zhang, Y. Zhao, Y. Wu, *Journal of Chromatography A* **2012**, *1219*, 54–60.
- [276] M. K. So, S. Taniyasu, N. Yamashita, J. P. Giesy, J. Zheng, Z. Fang, S. H. Im, P. K. S. Lam, *Environ. Sci. Technol.* **2004**, *38*, 4056–4063.
- [277] D. M. Wanninayake, *Journal of Environmental Management* **2021**, *283*, 111977.

- [278] R. C. Buck, J. Franklin, U. Berger, J. M. Conder, I. T. Cousins, P. de Voogt, A. A. Jensen, K. Kannan, S. A. Mabury, S. P. van Leeuwen, *Integr Environ Assess Manag* **2011**, *7*, 513–541.
- [279] H. Kadar, B. Veyrand, A. Barbarossa, G. Pagliuca, A. Legrand, C. Boshier, C.-Y. Boquien, S. Durand, F. Monteau, J.-P. Antignac, B. Le Bizec, *Chemosphere* **2011**, *85*, 473–480.
- [280] C. Lau, in *Molecular, Clinical and Environmental Toxicology* (Ed.: A. Luch), Springer Basel, Basel, **2012**, pp. 47–86.
- [281] K. Prevedouros, I. T. Cousins, R. C. Buck, S. H. Korzeniowski, *Environ. Sci. Technol.* **2006**, *40*, 32–44.
- [282] J. M. Conder, R. A. Hoke, W. de Wolf, M. H. Russell, R. C. Buck, *Environ. Sci. Technol.* **2008**, *42*, 995–1003.
- [283] C. Lau, K. Anitole, C. Hodes, D. Lai, A. Pfahles-Hutchens, J. Seed, *Toxicological Sciences* **2007**, *99*, 366–394.
- [284] N. Jacquet, M. A. Maire, Y. Landkocz, P. Vasseur, *Arch Toxicol* **2012**, *86*, 305–314.
- [285] M. E. Andersen, J. L. Butenhoff, S.-C. Chang, D. G. Farrar, G. L. Kennedy, C. Lau, G. W. Olsen, J. Seed, K. B. Wallace, *Toxicological Sciences* **2008**, *102*, 3–14.
- [286] N. Merino, Y. Qu, R. A. Deeb, E. L. Hawley, M. R. Hoffmann, S. Mahendra, *Environmental Engineering Science* **2016**, *33*, 615–649.
- [287] T. Anumol, S. Dagnino, D. R. Vandervort, S. A. Snyder, *Chemosphere* **2016**, *144*, 1780–1787.
- [288] M. Ateia, A. Maroli, N. Tharayil, T. Karanfil, *Chemosphere* **2019**, *220*, 866–882.
- [289] I. Ross, J. McDonough, J. Miles, P. Storch, P. Thelakkat Kochunarayanan, E. Kalve, J. Hurst, S. S. Dasgupta, J. Burdick, *Remediation* **2018**, *28*, 101–126.
- [290] V. A. Arias Espana, M. Mallavarapu, R. Naidu, *Environmental Technology & Innovation* **2015**, *4*, 168–181.

- [291] Z. Du, S. Deng, Y. Bei, Q. Huang, B. Wang, J. Huang, G. Yu, *Journal of Hazardous Materials* **2014**, 274, 443–454.
- [292] D. M. Wanninayake, *Journal of Environmental Management* **2021**, 283, 111977.
- [293] Y. Yao, K. Volchek, C. E. Brown, A. Robinson, T. Obal, *Water Science and Technology* **2014**, 70, 1983–1991.
- [294] D. Q. Zhang, W. L. Zhang, Y. N. Liang, *Science of The Total Environment* **2019**, 694, 133606.
- [295] D. N. Kothawala, S. J. Köhler, A. Östlund, K. Wiberg, L. Ahrens, *Water Research* **2017**, 121, 320–328.
- [296] P. McCleaf, S. Englund, A. Östlund, K. Lindegren, K. Wiberg, L. Ahrens, *Water Research* **2017**, 120, 77–87.
- [297] A. Zaggia, L. Conte, L. Falletti, M. Fant, A. Chiorboli, *Water Research* **2016**, 91, 137–146.
- [298] A. Maimaiti, S. Deng, P. Meng, W. Wang, B. Wang, J. Huang, Y. Wang, G. Yu, *Chemical Engineering Journal* **2018**, 348, 494–502.
- [299] E. K. Stebel, K. A. Pike, H. Nguyen, H. A. Hartmann, M. J. Klonowski, M. G. Lawrence, R. M. Collins, C. E. Hefner, P. L. Edmiston, *Environ. Sci.: Water Res. Technol.* **2019**, 5, 1854–1866.
- [300] Y. Feng, Y. Zhou, P.-H. Lee, K. Shih, *RSC Adv.* **2016**, 6, 113773–113780.
- [301] C. T. Vu, T. Wu, *Critical Reviews in Environmental Science and Technology* **2022**, 52, 90–129.
- [302] L. Zhao, J. Bian, Y. Zhang, L. Zhu, Z. Liu, *Chemosphere* **2014**, 114, 51–58.

Chapter 2

Outline

Cleaning up the environment of pollutants is one of the greatest challenges currently facing humanity. As illustrated in Chapter 1, air pollution is directly related to climate change due to the presence of greenhouse gases such as CO₂ and CH₄ in the atmosphere. In addition, water pollution also causes great damage to the environment and ecosystem. From the literature survey reported in Chapter 1, it can be derived that adsorption processes can be helpful in limiting the amount of pollutants in the environment.

For this reason, different types of porous adsorbents, from both commercial and synthetic origin, were used in this PhD thesis to remove pollutants from both gas and aqueous phases (Figure 2.1).

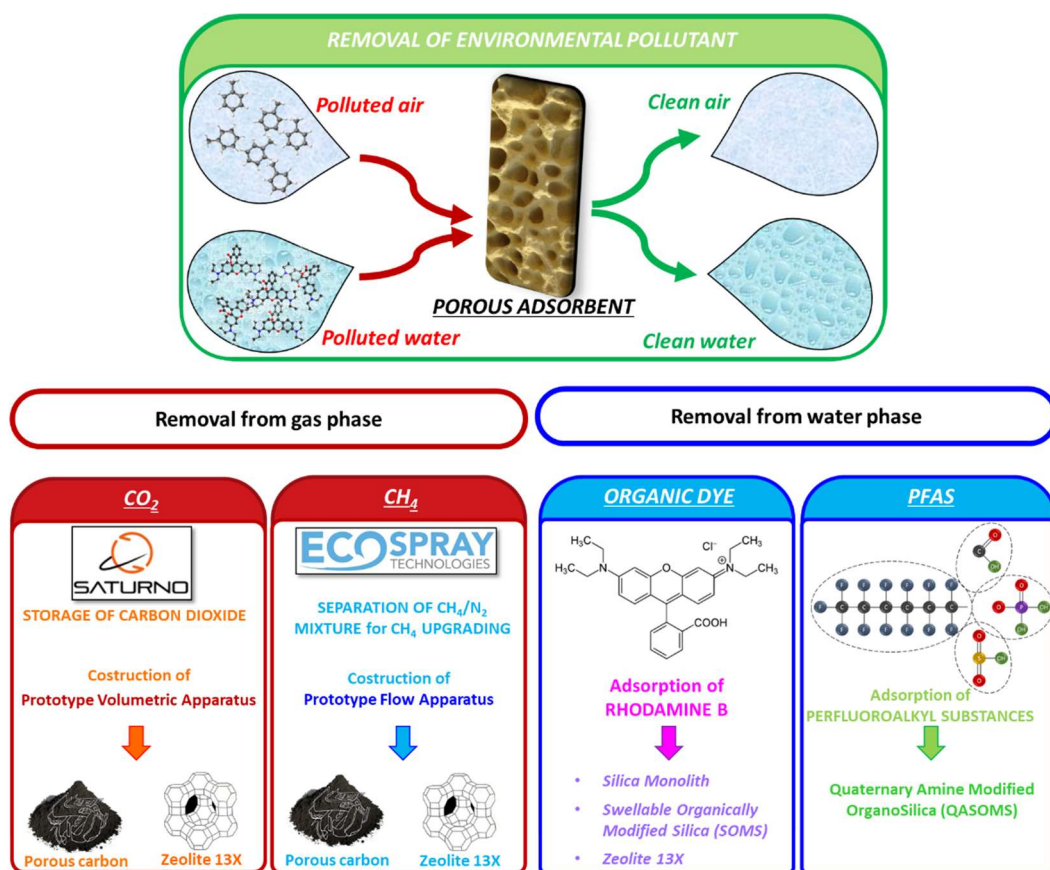


Figure 2.1 – Schematic representation of the aspects investigated in this PhD thesis work.

Specific attention was given to the synthesis of porous silicas (*i.e.* silica-based monoliths and organically modified hybrid silicas) and to the preparation of porous carbons derived from a Hyper Cross-linked Polymers (HCP). HCP a class of microporous organic polymers that possess an extremely flexible structure; through chemical treatments, the material can be activated and transformed into a higher value-added activated carbon.

Moreover, several commercial porous carbons and commercial zeolite 13X (a low-Silica zeolites, with a Na^+ ions in its microporous crystalline structure) are used as a comparison. First of all, the solids are characterised using a multidisciplinary experimental approach to explore their morphological, structural, surface, and textural chemical-physical properties (Chapters 3 and 4). Subsequently, the interaction between adsorbents and different pollutants is investigated to understand phenomena playing an important role in the adsorption process (Chapter 6 and Chapter 7).

Concerning the adsorption of pollutants from the gas phase (Chapter 6), the thesis work was mainly focused on studying the adsorption capacity of different materials to sequester two of the main greenhouse gases related to human activities: CO_2 and CH_4 .

The CO_2 recovery processes were studied in the frame of the SATURNO Project (*Scarti organici e Anidride carbonica Trasformati in carbURanti, fertilizzanti e prodotti chimici; applicazione concreta dell'ecoNOmia circolare*), funded by the Piedmont region through the Bioeconomy Technology Platform^[1]. The project aims to develop a circular bioeconomy supply chain through the creation of new processes and new products, with a focus on carbon dioxide recovery and reuse. The SATURNO biorefinery represents a practical example of a circular economy at the urban level through the creation of new processes and new products.

For this purpose, commercial porous carbons were tested, since they are a material characterized by a high degree of porosity, high specific surface area and a high

reactive degree of the surface. In addition, their performance in CO₂ uptake was compared with that of a synthetic carbon obtain from a Hyper Cross-linked Polymer, and with that of a commercial zeolite 13X.

Moreover, the ability of commercial porous carbons and commercial zeolite 13X to adsorb methane and nitrogen has been tested.

The possibility to use porous sorbents for the separation of methane and nitrogen is also studied. As reported in Chapter 1, in the field of biogas upgrading, the separation of N₂ from CH₄ is especially challenging because of their molecular similarities^[2].

Therefore, in order to obtain biomethane at high concentrations, it is necessary to separate it from the nitrogen in the mixture. The studies concerning methane upgrading was developed in collaboration with the Ecospray Technologies Company, that is mainly dedicated to the research and development, design and implementation of innovative technologies and systems for the treatment and/or cooling of air and gases in various industrial applications^[3].

In order to volumetrically determine the adsorption of carbon dioxide and methane by the different materials tested, as part of the SATURNO project, two different prototypes were constructed (Chapter 5): the first prototype was used to perform static measurements of individual gases, while the second prototype apparatus was coupled with a mass spectrometer, in order to perform dynamic measurement and investigating the ability of the adsorbent material to separate gases from mixture in flow conditions.

Regarding the removal of pollutants in the liquid phase, this work focused on the removal of two types of main pollutants from water: organic dyes and emerging pollutants (Chapter 7).

Organic dyes widely used in the textile, cosmetic, photographic, leather, paper, and plastics industries, and also in the food industry; in chemistry it is used as a

fluorescent tracer, or as a metal chelating reagent, even if this molecule is toxic to animals and humans^[4-9].

Among the different type of organic dyes, Rhodamine B was chosen since it is a model molecule capable of simulating a generic organic pollutant, very similar to those that can be spilled into the waters due to urban and industrial disaster. Being an organic pigment, it has a high capability to alter the environment and interfere with biological cycles related to photosynthetic processes^[10].

Moreover, perfluoroalkyl substances (PFAS) are a class of amphiphilic molecules consisting of a hydrophobic alkyl chain, fully or partially fluorinated, and a hydrophilic functional group at the head of the chain. These molecules have been widely used industrially over the past 40 years and today, they are considered first priority pollutants due to their chemical persistence and widespread occurrence in water, food and living organisms^[11-13].

Two types of mesoporous materials, silica monoliths and Swellable Organically Modified Silica (SOMS), were used to sequester Rhodamine B from water, and they were compared with a commercial zeolite 13X. On one hand, monoliths were chosen because they can be easily synthesized in a single step by sol-gel synthesis; from the other hand, SOMS possess the interesting property of increasing their volume when placed in an organic solvent; this characteristic gives them excellent adsorption performance and the ability to trap organic pollutants.

Regarding the removal of PFAS, SOMS and SOMS functionalized with molecules containing quaternary amine groups (QASOMS), to make them more selective, have been tested.

References

- [1] “SATURNO - L’economia circolare applicata al territorio piemontese,” can be found under <https://saturnobioeconomia.it/>, **n.d.**
- [2] T. E. Rufford, S. Smart, G. C. Y. Watson, B. F. Graham, J. Boxall, J. C. Diniz da Costa, E. F. May, *Journal of Petroleum Science and Engineering* **2012**, 94–95, 123–154.
- [3] “Ecospray – Technologies for the planet,” can be found under <https://ecospray.eu/>, **n.d.**
- [4] F. Hayeeye, M. Sattar, W. Chinpa, O. Sirichote, *Colloids and Surfaces A: Physicochemical and Engineering Aspects* **2017**, 513, 259–266.
- [5] T. Santhi, A. L. Prasad, S. Manonmani, *Arabian Journal of Chemistry* **2014**, 7, 494–503.
- [6] R. Jain, M. Mathur, S. Sikarwar, A. Mittal, *Journal of Environmental Management* **2007**, 85, 956–964.
- [7] J. Chen, X. Zhu, *Food Chemistry* **2016**, 200, 10–15.
- [8] K. G. Bhattacharyya, S. SenGupta, G. K. Sarma, *Applied Clay Science* **2014**, 99, 7–17.
- [9] Z.-L. Cheng, Y. Li, Z. Liu, *Ecotoxicology and Environmental Safety* **2018**, 148, 585–592.
- [10] R. Ianoş, C. Păcurariu, S. G. Muntean, E. Muntean, M. A. Nistor, D. Nižňanský, *Journal of Alloys and Compounds* **2018**, 741, 1235–1246.
- [11] P. Grandjean, R. Clapp, *New Solut* **2015**, 25, 147–163.
- [12] I. Ross, J. McDonough, J. Miles, P. Storch, P. Thelakkat Kochunarayanan, E. Kalve, J. Hurst, S. S. Dasgupta, J. Burdick, *Remediation* **2018**, 28, 101–126.
- [13] M. I. Gomis, R. Vestergren, D. Borg, I. T. Cousins, *Environment International* **2018**, 113, 1–9.

Chapter 3

*Synthesis and characterization of silica-based
materials for environmental purposes*

Introduction

In this chapter, the preparation methods and the physico-chemical properties of inorganic and hybrid materials used for environmental purposes are described.

First, the synthesis and characterization of silica monoliths is presented. These are mesoporous silica materials that have the distinctive feature that they can be synthesized directly in monolithic form in a single step.

Next, the synthesis and characterization of hybrid silicas is discussed. These materials can increase their volume when placed in an organic solvent; this process is completely reversible and repeatable. This property gives them excellent adsorption performances and the ability to trap organic pollutants.

Finally, the characterization of a commercial zeolite (Zeolite 13X) in pelletized form, which serve as a reference material, is presented.

3.1 Silica monoliths

Mesoporous silicas are characterized by high surface area and pore volume, adjustable and controlled particle size and morphology^[1,2].

They are usually synthesized and used in the form of powder; nevertheless, the use of powder, especially at the industrial level, is severely hampered due to handling and recycling limitations^[3].

To overcome these problems, one possible option is to use pre-synthesized silica powder to form pellets, using one or more binders and also pressing the material under heating; however this multistep time-consuming procedure could adversely affect the structure of mesoporous silica, thus causing performance alteration^[4].

For this reason, in recent years research has aimed on the development of single-step synthesis methods for the direct formation of silica-based monoliths^[5-8]: in this case, homogeneous and compact structures can be produced, thus allowing an easier recovering and recycling processes.

Siliceous monoliths possess low bulk density, as they are materials that possess high porosity. They are also mechanically stable materials, and their large surface area can be functionalized^[9]. They are also of great relevance as porous model materials for studying ion or molecule transport phenomena, avoiding any dust formation by compaction^[5].

Their hierarchical pore structure, consisting of interconnected macropores and mesopores, is exploited in applications that require high efficiencies^[10], such as industrial and automotive exhaust gas purification, liquid chromatography, high-speed catalysis, biomedical screening or as components of supercapacitors and sensors^[10-13].

Silica monoliths are synthesized by a classical sol-gel process (Figure 3.1), that is a synthesis methods in which the material is pre-formed in a liquid phase and at a low temperature ($T < 100\text{ }^{\circ}\text{C}$)^[14].

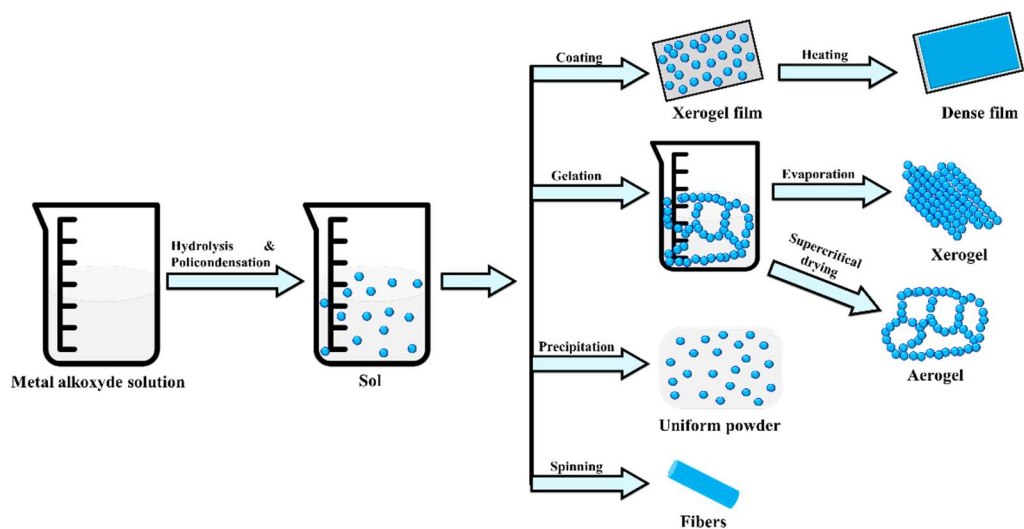


Figure 3.1 – Scheme of sol-gel process, adapted from^[15].

In the work of Galarneau and co-workers, hierarchical mesoporous/macroporous silicate monoliths are prepared by spinodal chemical decomposition in an acidic medium using polyethylene glycol (PEO)^[5]. Spinodal chemical decomposition is used as a mechanism to rapidly mix a homogeneous mixture of hydrated silica, polymer, and water to form two distinct, consistent phases from a single phase^[16]. The two phases grow simultaneously, and the final state is reached when the silica oligomers are condensed, at the sol-gel transition of the silica (Figure 3.2).

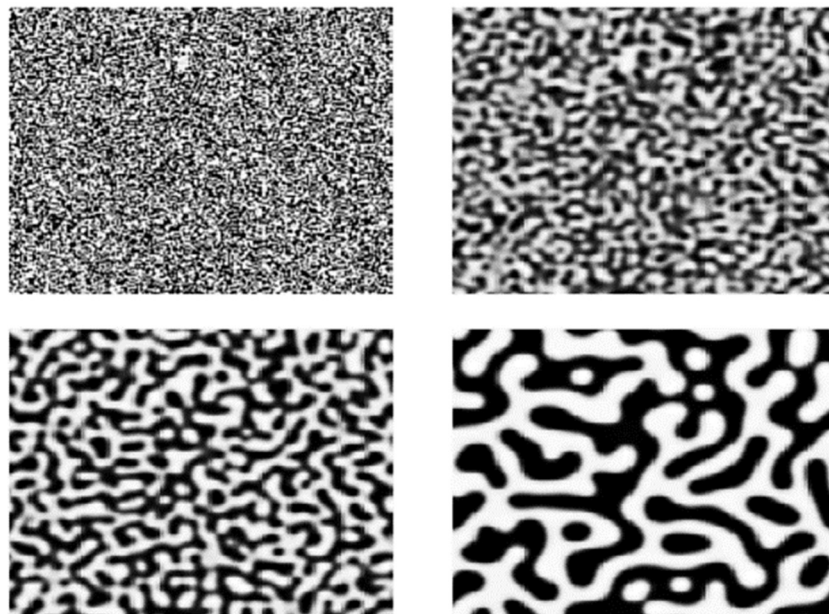


Figure 3.2 – Scheme of Spinodal Decomposition, during time^[5].

The homogeneous initial mixture is kept at low temperature (0-20 °C) in a single thermodynamic phase, where water molecules and polymer molecules surround silica species; the mixture is then heated to temperatures above 45 °C so that the silica species condense and the polymers begin to interact with the newly formed silica surface^[17].

The spinodal decomposition that begins at this point leads to the separation of the parent phase into two distinct phases: a silica- and polymer-rich phase and a water-rich phase^[5].

The amount and topology of the silica-rich phase determine the size and topology of the monolithic framework; the size and topology of the water-rich phase in turn determine the size and topology of the pore network^[18].

In addition, the pore size is also regulated by the degree of silica condensation, which in turn is determined by temperature, the amount of acid, and the amount and type of polymer^[19].

3.1.1 Synthesis of Silica Monoliths

Silica monoliths were obtained by adapting the procedure described by Galarneau *et al.*^[5].

In detail, a mixture of nitric acid, polyethylene oxide (PEO) and deionized water was prepared and refrigerated at $-19\text{ }^{\circ}\text{C}$ for 1 h. Then, tetraethyl orthosilicate (TEOS), previously cooled at $-19\text{ }^{\circ}\text{C}$ for 1 h, was added to the mixture (molar ratios of the optimized final composition: 1 Si/0.60 PEO/0.26 HNO_3 /14.21 H_2O).

Polyvinylchloride tubes (8 mm in diameter and 10 cm length) were then filled with the mixture and closed with a cap, paying particular attention to keep everything cold throughout the whole process by means of an ice bath. The filled tubes were then put in vertically, held in place by an appropriate support, in a 4 L water bath at $40\text{ }^{\circ}\text{C}$ for 3 days.

The formed monoliths were then removed from the tubes and placed in a water bath at room temperature. The washing process consists of changing water, every 30 min, to pH neutrality.

The monoliths were then immersed in 1 L of 0.1 M ammonia aqueous solution (NH_4OH) in a Teflon bottle and placed in oven at $40\text{ }^{\circ}\text{C}$ for 1 day, to catalyse the Ostwald ripening of the weakly condensed silica^[20]. Finally, the monoliths were recovered, further washed in a water bath until pH neutrality, dried at room temperature for 4 days and then calcined in O_2 flow at $550\text{ }^{\circ}\text{C}$, with a rate of $3^{\circ}\text{C}/\text{min}$, for 6 h to remove the PEO still present. The obtained silica monoliths were named Mono-ICE (Figure 3.3)^[21].



Figure 3.3 - Silica monoliths (Mono-ICE) samples.

3.1.2 Characterization of Silica Monoliths

The morphology of the silica monoliths (Mono-ICE) was studied by using scanning electron microscopy (SEM). The micrographs of samples before (A) and after (B) the calcination step (needed to remove the polyethylene oxide (PEO) template), are reported in Figure 3.4.

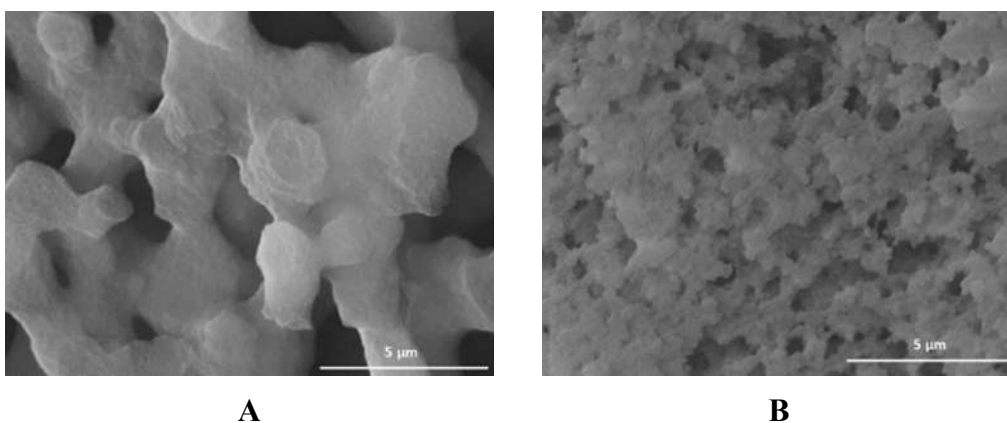


Figure 3.4 - SEM micrographs (20000x) of Mono-ICE before (A) and after calcination (B).

Before calcination (Figure 3.4A), the Mono-ICE sample is characterized by an irregular morphology, where the particle aggregation gives origin to interconnected macropores with a diameter of approximately 4 μm and a skeleton thickness of 3 μm , on average. After the formation of the macroporous monoliths in acidic medium at low temperature, the ammonia treatment at 40 °C brings about the rearrangement of the weakly condensed silica network into denser nanodomains and the formation of larger mesopores.

After the calcination step (Figure 3.4B), the sample morphology appears deeply modified, with a strong reduction of macropore dimensions (0.5–1 μm).

The surface properties of the calcined silica monolith were then monitored by infrared spectroscopy (Figure 3.5).

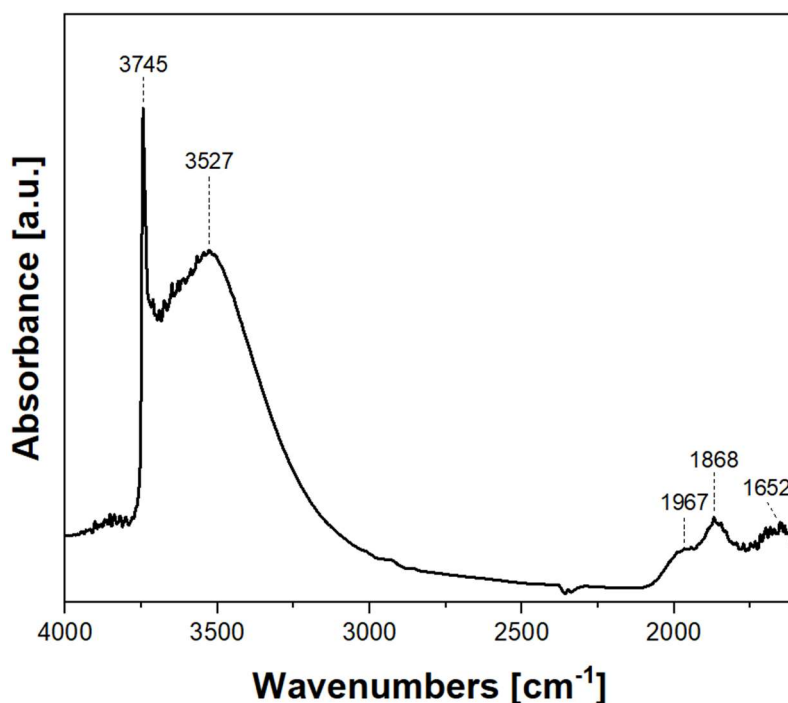


Figure 3.5 - FT-IR spectrum of self-supported pellets of calcined Mono-ICE sample after treatment in vacuum at beam temperature (b.t. 35°C) for 30 min.

The FT-IR spectrum of Mono-ICE sample shows an intense band at 3745 cm^{-1} , due to the O-H stretching mode of isolated silanol groups present on the silica surface, and a broad band between 3700 and 3200 cm^{-1} with a maximum at 3527 cm^{-1} and a shoulder at *ca.* 3654 cm^{-1} , due to different surface silanol groups interacting with each other through hydrogen bonds^[21,22]. The spectrum, in the low frequency region, is characterized by three bands at 1967 , 1868 and 1652 cm^{-1} , due to overtones and combination modes of the silica framework^[21,22].

Textural properties of the monoliths were determined by N_2 adsorption–desorption isotherms at 77 K . To investigate whether the physico-chemical properties were homogeneous throughout the entire length of the cylindrical monoliths, the samples were divided into three parts of 1 cm in length each and of weight of about 50 mg : the obtained samples were named Mono-ICE-Lateral A, Mono-ICE-Lateral B, Mono-ICE-Central C, respectively.

Results are reported in Figure 3.6.

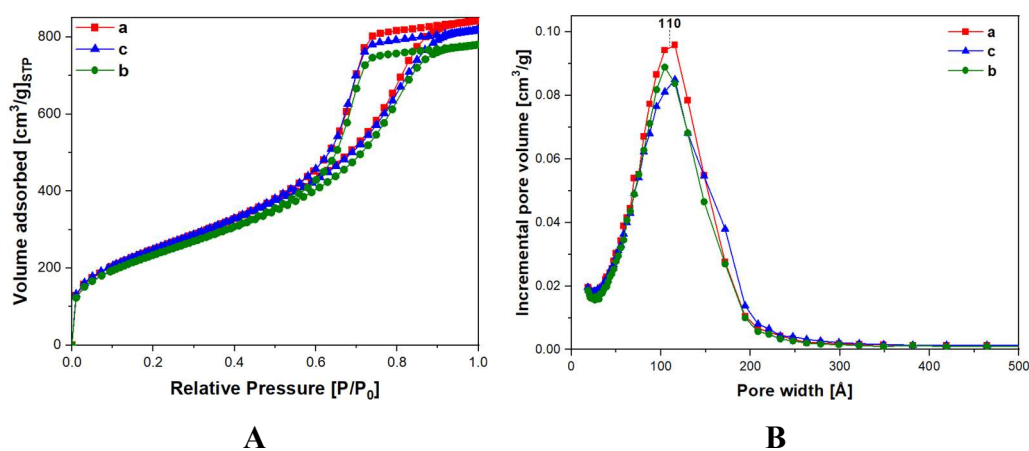


Figure 3.6 – A) N_2 adsorption and desorption isotherms at 77 K and B) pores size distributions of calcined Mono-ICE-Lateral A (a), Mono-ICE-Lateral B (b), and Mono-ICE-Central C (c).

Following the IUPAC classification, all the obtained isotherms (Figure 3.6A) are of type IVa, thus indicating a multilayer adsorption, which is typical of mesoporous

solids^[23]. Hysteresis loops of type H2, due to disordered materials with a distribution of pore size and shape that is not well-defined, are found^[23]. All samples show a monomodal pore size distribution between 50 and 200 Å with maxima at around 110 Å (Figure 3.6B). The pore size distribution was calculated by applying the BJH (Barrett, Joyner, and Halenda) method on the adsorption branch (Thickness Curve: Halsey, Correction: Standard).

The textural properties of the three samples are similar, and this strongly suggests that the cylindrical monolith under investigation is structurally homogeneous along the entire length (Table 3.1)^[21].

Table 3.1 - Specific Surface Area and Total Pore Volume of calcined Mono-ICE Lateral A, Lateral B and Central C samples.

Sample	SSA_{BET}¹ (m² g⁻¹)	V_P² (cm³ g⁻¹)
Mono-ICE Lateral A	909	1.3
Mono-ICE Central C	906	1.3
Mono-ICE Lateral B	853	1.2

¹ Brunauer-Emmet-Teller (BET) specific surface area (SSA);

² Total pore volume by BJH (Barrett, Joyner, and Halenda) method

3.2 Swellable Organically Modified Silica (SOMS)

SOMS (Swellable Organically Modified Silica) are hybrid material consisting of organic units linked to an inorganic matrix by a covalent metal-carbon bond. It is synthesized by polycondensation of a bridged polysiloxane precursor, under basic conditions^[24]. These types of hybrid silicas were synthesized by Paul L. Edmiston, in collaboration with Colleen M. Burkett, in 2005^[25] and patented in 2010^[24].

Typical bridging silane precursors are *bis(trialkoxysilylalkyl)benzenes*, having the following structure: (alkoxy)₃-Si-(CH₂)_n-Ar-(CH₂)_m-Si-(alkoxy)₃ (Figure 3.7).

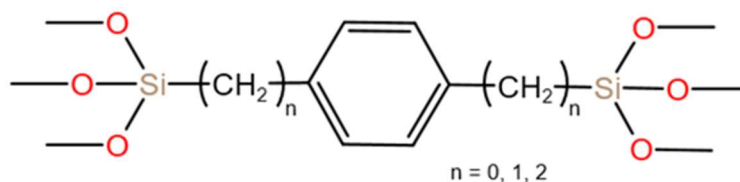


Figure 3.7– Generic structure of bis(trialkoxysilylalkyl)benzenes.

The inorganic precursor matrix can be built around the organic part through hydrolytic polycondensation, to obtain a highly cross-linked solid.

After gelling, the material is aged to induce syneresis, which is the shrinkage of the gel that accompanies solvent evaporation, and catalyst extraction^[24].

After rinsing, residual silanols on the surface of the material are derivatized using silazanes, disilazanes or halosilane agents that include one or more silanol-reactive groups (halogen groups) and at least one nonreactive alkyl groups.

The derivatization process leads to the end-capping of the silanol-terminated polymers present in the materials^[24].

A general scheme of the synthetic steps required for the preparation of SOMS silicas from bridged silane precursors, is shown in Figure 3.8.

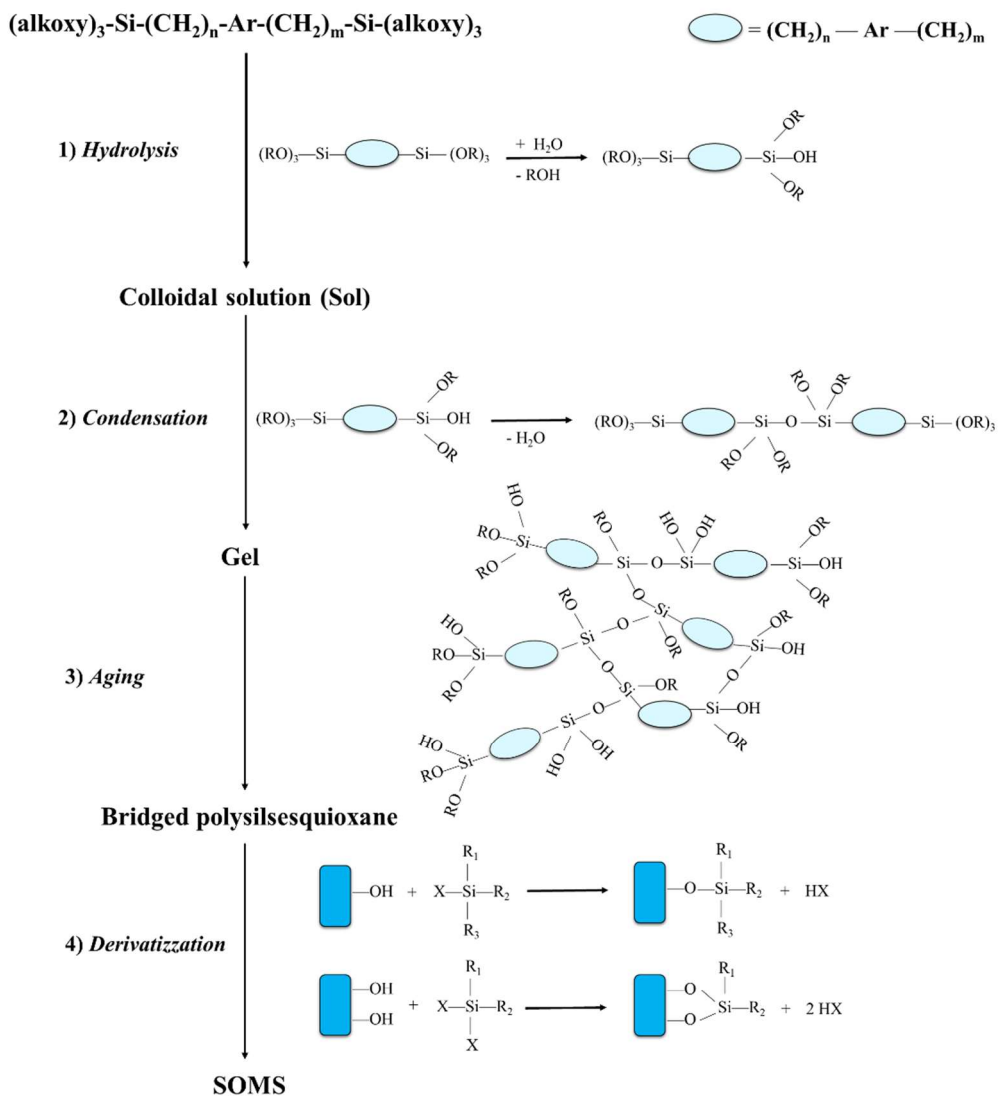


Figure 3.8 – Schematization of sol-gel synthesis steps to obtain SOMS from bridged-silane precursors. Adapted from^[26].

These materials, when placed in a nonpolar organic solvent, are capable of swelling from 2 to 8 times their original volume^[25].

The term "swellable" refers to the ability of the sol-gel material to enlarge its structure to more than 1.5 times its dried volume when placed in contact with a

nonpolar solvent, while "highly swellable" refers to the ability of the sol-gel to swell to more than 7 times its dried volume^[24].

Swelling results from the fact that the material in the gel state has a morphology consisting of interconnected structures of organosilicates, which give the material flexibility and allow volume expansion^[27]. When the material is dried in gel form after the derivatization step, mechanical stresses occur in the polymer due to the non-covalent interactions that keep it compressed; when the material comes into contact with an organic solvent, capillary collapse of the polymer matrix occurs, resulting in release of the internal stresses with consequent swelling of the material^[24,25,27-29].

SOMS are hydrophobic materials that can swell only in contact with organic species, while they do not swell in the presence of water.

To increase the ability to swell, some synthetic parameters have to be properly controlled^[29]:

- the material must be synthesized from monomers with bridged organic groups, with flexible organic functionalities combined with an alkoxy silane unit;
- the synthesis must be carried out in a nonpolar solvent, using a very basic catalyst (such as fluoride);
- gel must be aged to syneresis and then the silanol groups must be derivatized before drying.

Due to their ability to swell, SOMS silicas can capture a wide variety of organic contaminants and can adsorb a wide variety of dissolved polar organic pollutants^[28,30-32]. One of the features of SOMS is that the swelling behaviour is completely reversible: when the solvent evaporates, the material shrinks back to its original state, from which it can swell again^[27].

3.2.1 Quaternary Amine Modified Organosilica (QA-SOMS)

To make SOMS more selective, they can be functionalized directly during the synthesis step. Organosilane precursors can be co-polymerized with bis(trialkoxysilylalkyl)benzenes (BTEB) to change the surface chemistry while maintaining the flexible pore structure^[30].

To make SOMS more selective, studies have been carried out in which it was functionalized with three different precursors: a fluoroalkylsilane ((tridecafluoro-1,1,2,2-tetrahydrooctyl)trimethoxysilane) to obtain the F-SOMS, a quaternary aminesilane (N-(trimethoxysilylpropyl)-N,N,N-trimethylammonium chloride), to obtain the QA-SOMS, and a cationic polymer (poly[(3-methyl-1-vinylimidazolium chloride)-co-(1-vinylpyrrolidone)]) was intercalated into the SOMS by swelling to obtain the poly-SOMS^[30]. These three materials have slightly different chemical and physical properties, but all showed swelling abilities.

Since one of the goals of this work is to remove perfluoroalkyl substances (PFAS) from water (see Chapter 7), which are hydrophobic molecules that have a negative surface charge in water, QA-SOMS have been synthesized and used in this work.

QA-SOMS silicas are organo-modified silicas that are functionalized, during the synthesis step, by molecules containing quaternary amine groups, an example of which is reported/shown in Figure 3.9.

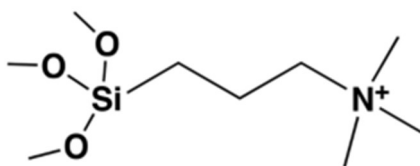


Figure 3.9 – Structure of alkoxy silane precursor (N-(trimethoxy)silylpropyl)-N,N,N-trimethylammonium chloride) used for QA-SOMS synthesis.

Compared with the synthesis of non-functionalized SOMS, simultaneously with the condensation of BTEB molecules, the formation of -Si-O-Si- bonds between aggregates of BTEB and N-(trimethoxy)silylpropyl-N,N,N-trimethylammonium chloride (TMA) also occurs (Figure 3.10).

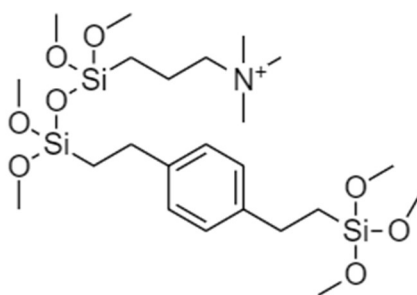


Figure 3.10 – Product of the condensation reaction between one molecule of BTEB and one molecule of (trimethoxy)silylpropyl-N,N,N-trimethylammonium chloride.

To stop the condensation reaction and to make the structure more hydrophobic, the residual surface silanols react with hexamethyldisilazane (Figure 3.11).

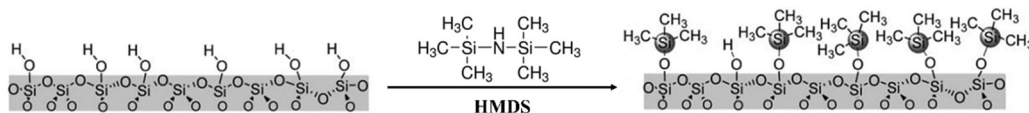


Figure 3.11 – Schematic reaction between the surface of a silica and hexamethyldisilazane (HMDS). Adapted from^[33].

In this step, hexamethyldisilazane (HMDS) replaces the chlorosilanes normally used for the synthesis of SOMS. HMDS allows to stop the polymerization reaction by binding to the silanol groups on the surface and thus making the material more hydrophobic (Figure 3.12).

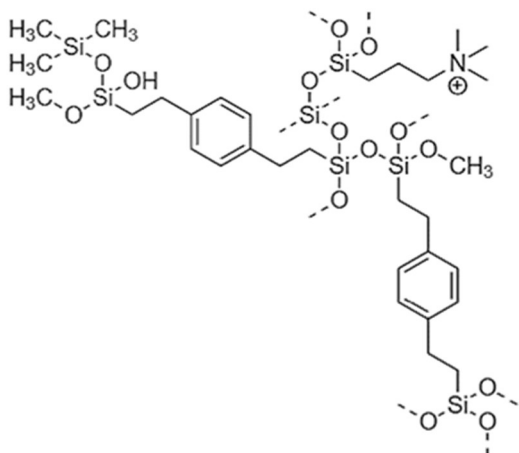


Figure 3.12 – Schematic image of the molecular structure of QA-SOMS silica.

3.2.2 Synthesis of SOMS

The first step of the reaction is the hydrolysis of the precursor (1,4-Bis(triethoxysilyl)benzene - BTEB) in an organic solvent (THF), using tetrabutylammonium fluoride (TBAF) as a catalyst (Figure 3.13)^[24]. A nucleophilic attack by a water molecule on the Si atom of the BTEB molecule occurs, generating a hydroxyl group, then the silanol (Si-OH) is formed with liberation of an alcohol molecule.

A scheme of this reaction is reported in Figure 3.13.

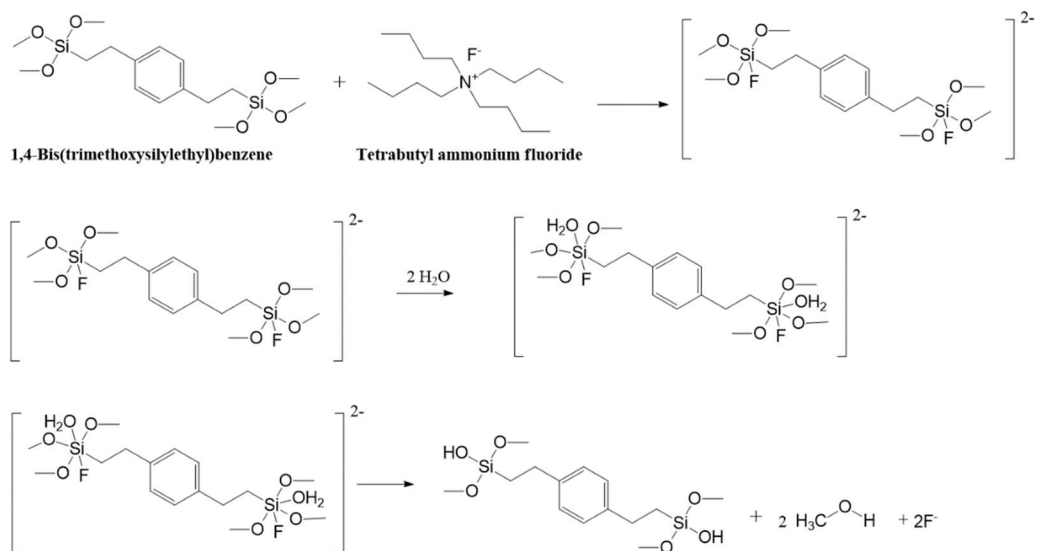
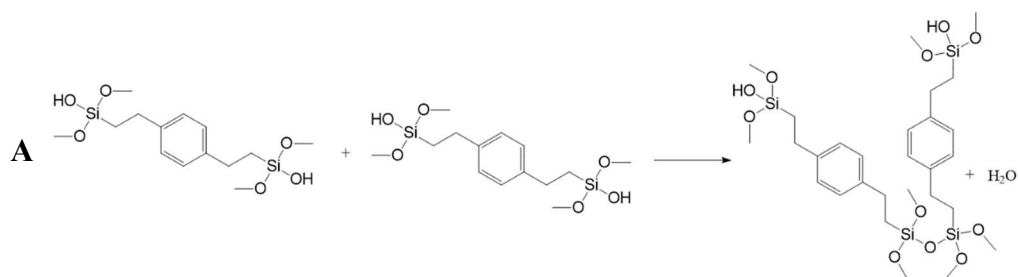


Figure 3.13 – Schematization of hydrolysis process for the preparation of SOMS.

After the hydrolysis process condensation occurs, leading to the formation of Si-O-Si type bonds by two possible routes^[26,34]:

- Homocondensation, in which two hydroxyl groups (-OH) undergo a condensation reaction releasing a water molecule (Figure 3.14A).
- Heterocondensation, in which a hydroxyl group (-OH) and an alkoxy group (-OR) undergo a condensation reaction releasing an alcohol molecule (CH₃OH) (Figure 3.14B).



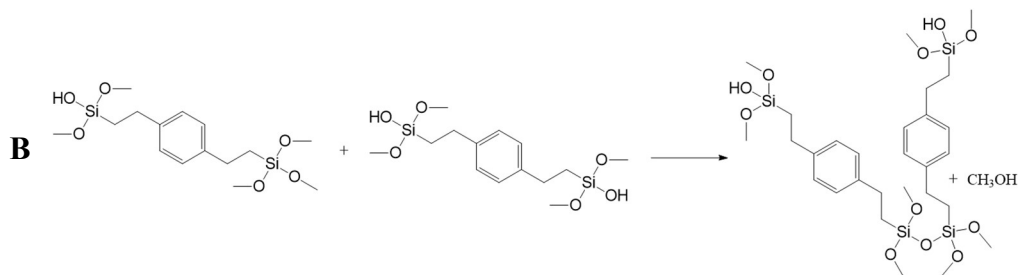


Figure 3.14 – Schematization of homocondensation (A) and heterocondensation (B) process for the SOMS.

Both steps lead to the formation of the gel. During the aging step, the gel shrinks spontaneously, releasing the solvent contained within the three-dimensional network, allowing further condensations to occur (Figure 3.15)^[26,34].

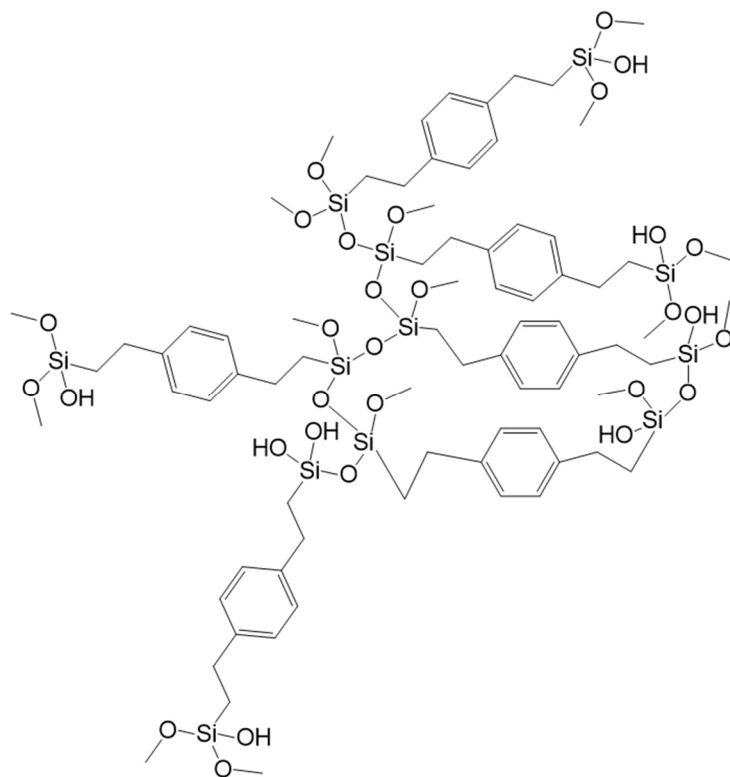


Figure 3.15 – Schematization of the possible structure of SOMS silica after the condensation phase^[34].

Finally, derivatization of the gel is carried out by means of a chlorosilane (chloromethyldimethylchlorosilane), which reacts with the residual silanols to achieve end-capping of the material and prevent further condensation (Figure 3.16).

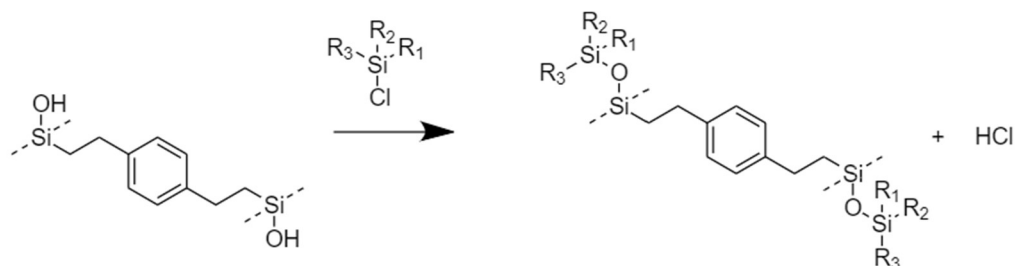


Figure 3.16 – Schematization of derivatization process for the SOMS.

Finally, the gel is dried by evaporation, resulting in a dry gel, named xerogel.

The resulting material is a highly crosslinked solid, obtained by a one-pot process.

In this thesis work, solutions containing 140 μ L of TBAF (1.0 M in THF) as a catalyst, 27.6 mL of tetrahydrofuran (THF), 6.24 mL of BTEB and 972 μ L of H₂O are prepared. After gelation, occurring in about 15 minutes, the material is left to react for 6 days, in a close container, at room temperature. Then, the resulting material, which appears as solid, was reduced into small pieces to allow a more rapid exchange between the solvent and the gel; subsequently, the material were extracted twice with ethanol and twice with acetonitrile over a period of 4 day. Next, the material is derivatized by adding 20 mL of a 5% v/v solution of chloromethyldimethylchlorosilane in acetonitrile. The material is left 48 hours at room temperature. The gel was then rinsed three times with acetonitrile over 3 days and then dried in oven for 2 h at 80 $^{\circ}$ C. The material was then ground to generate a powder. The sample was named Silica-SOMS.

3.2.3 Synthesis of QA-SOMS

The one-sol-gel method was also used for the synthesis of the Quaternary Amine Modified OrganoSilica (QA-SOMS)^[30].

A sol was prepared using a solution of 800 μ l N-trimethoxysilylpropyl-N,N,N-trimethylammonium chloride (50% in methanol), 3.0 g BTEB, and 580 μ l 0.225 M TBAF solution. After gelation, the material was stored in a closed container at 25°C for 6 days, for the aging phase. The material was grounded and rinsed twice with acetone. It was then immersed in a solution of 20 ml 5% v/v of hexamethyldisilazane and acetone for 48 hours at 25°C to carry out the derivatization of the surface silanols.

The gel pieces were then rinsed by Soxhlet extraction with acetone and dried at room temperature.

The sample was named Silica-QA-SOMS.

3.2.4 Characterization of Silica-SOMS

The chemical composition and amount of the organic moieties of the Silica-SOMS was determined by CHN elemental analyses (Table 3.2).

Table 3.2 - CHN elemental analyses of Silica-SOMS sample.

Sample	N wt%	C wt %	H wt %
Average	0.322	44.133	5.457
Std. Deviation	0.091	1.666	0.155

CHN analysis shows that Silica-SOMS sample is composed by *ca.* 44 wt% of carbon probably deriving from both the benzene ring and the -CH₂-CH₂- bridging groups between the silicon atom and the benzene ring, and from the -CH₃ groups of the chlorosilane used in the derivatization. For comparison with the obtained results, the weight percentage of carbon was calculated considering only the repeating units

formed by the hydrolysis of the BTEB precursor, and it was found to be about 42.24%. The weight percentage of C resulting from the CHN analysis is higher than the estimated value. Carbon content derived from the derivatization step is not accounted for in the estimation because of the random nature of the distribution of the chlorosilane species within the framework.

The CHN results are consistent with the data found in the literature indicating a 60% organic content for SOMS synthesized with hexamethyldizilazane as derivatizing agent (and not with chloromethyldimethylchlorosilane, as the Silica-SOMS considered here)^[35].

The elemental analysis shows a low percentage of nitrogen, which is probably due to a residue of the catalyst, used for the synthesis, or to the residual presence of acetonitrile as solvent, which was not completely removed by the drying step.

The morphology of Silica-SOMS was studied via Scanning Electron Microscopy (SEM, Figure 3.17).

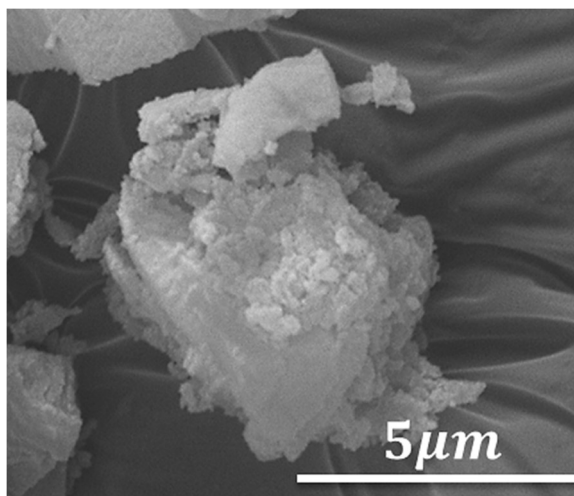


Figure 3.17 - SEM micrograph of Silica-SOMS, 25000x magnification.

From the micrograph in Figure 3.17, it is possible to note the presence of large aggregates (5-10 μm), of irregular morphology. On the surface of the macro-aggregates there are smaller aggregates formed by nanometer-sized particles (300-400 nm). The result is in agreement with what has been reported by Edmiston and coworkers^[27,30]: regardless of the precursor used, Silica-SOMS are composed of aggregates of nanometer-sized particles.

Electrophoretic mobility measurements were performed to test the surface potential as the pH of the solution changes. A range of pH between 3 and 10 was explored to stay within the pH limits of the material stability (Figure 3.18).

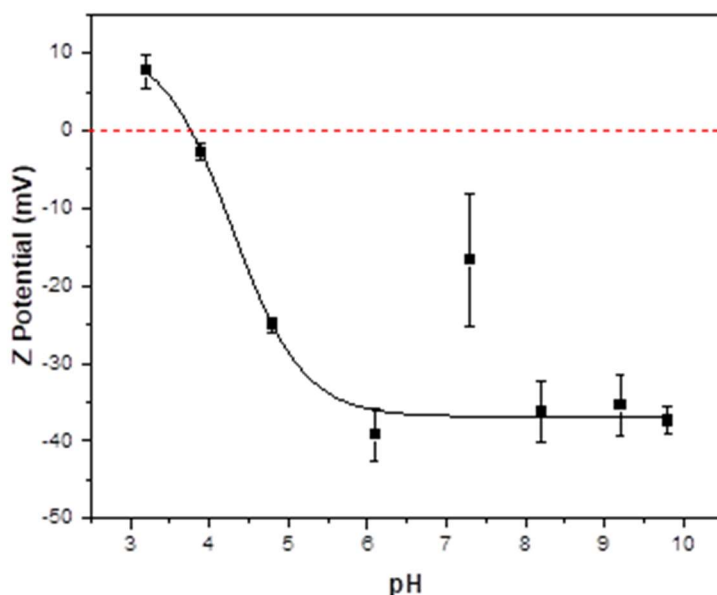
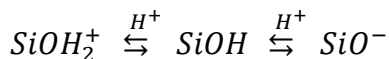


Figure 3.18 – Z potential of Silica-SOMS.

Silica-SOMS shows a negative Z potential in the pH range from 10 to 4, being the point of zero charge at pH 3.7.

The surface potential turned out to be negative probably because not all the surface silanols have been efficiently derivatized. the negative surface charge of the material results from the pH-dependent dissociation of the silanol groups by the process^[36]:



The surface properties were investigated via infrared spectroscopy (FTIR) (Figure 3.19).

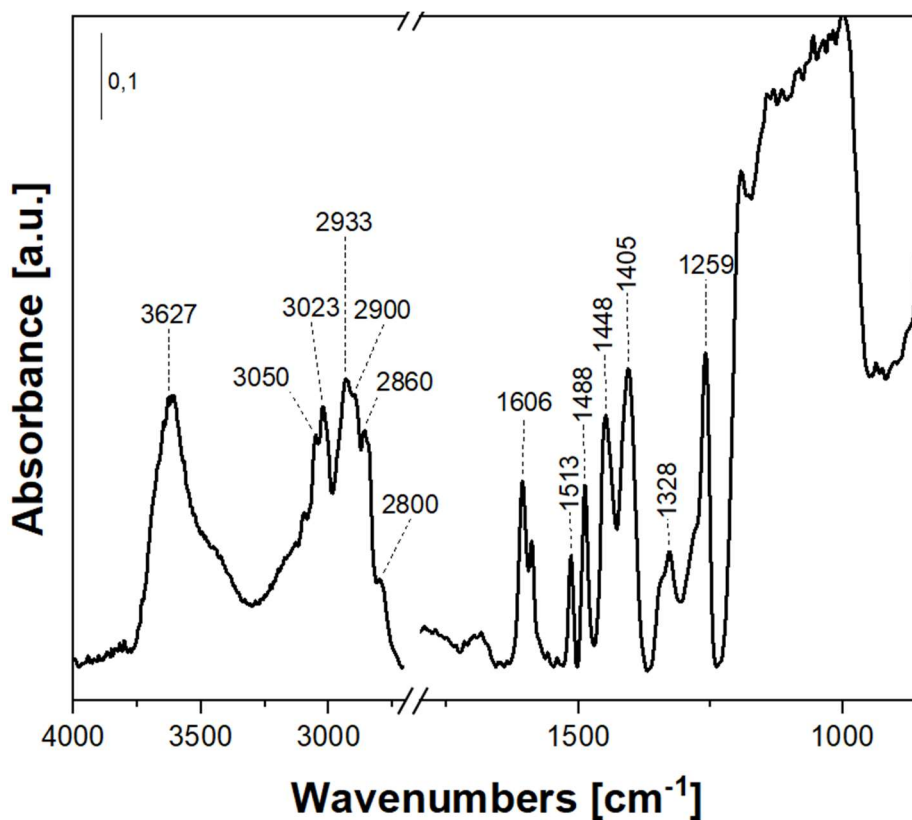


Figure 3.19 – FT-IR spectrum of Silica-SOMS sample after treatment in vacuum at beam temperature (b.t.= 35°C) for 30 min.

The IR spectrum of Silica-SOMS, in the high-frequency region, is characterised by bands in the range between 3800 and 2750 cm^{-1} .

The band at *ca.* 3627 cm^{-1} is related to the stretching mode of the OH groups species interacting with each other^[21,22,29]. As already pointed out in the literature, this is an indication of the fact that not all surface silanols have been derivatized^[25,29]. This is

consistent with the results of the surface potential analysis, which is negative for the presence of non-derivatized surface silanols.

As a result, there are residual silanols that interact with each other as they are bound within a hydrophobic environment, forming a kind of hydrophilic core within the hydrophobic matrix of the material [25,29].

In the range between 3100 and 2800 cm^{-1} the stretching vibrational modes of the aromatic and aliphatic C-H groups are observed^[29,30]. In the region between 1700 and 1500 cm^{-1} the signals associated with the C-C bond stretching vibrational modes of the benzene ring are found. The band centred at 1488 cm^{-1} is due to asymmetric C-H bond bending^[29,37].

Between 1450 and 1400 cm^{-1} two peaks/bands are found related to the bending modes of the aliphatic C-H bonds^[29]. At 1260 cm^{-1} the peak related to the symmetric stretching modes of the Si-CH₃ group is found^[29,37]. A low intense peak is also observed at 1259 cm^{-1} related to the overtone of the out-of-plane bending of the C-H bond of the 1,4-disubstituted aromatic ring^[29]. Below 1200 cm^{-1} the bands due to vibrations of the structural Si-C or Si-O bonds are found.

A more complete assignment of the signals found/shown in the IR spectrum reported in Figure 3.18 is shown in Table 3.3.

Table 3.3 – Assignment of signal in the IR spectrum of Silica-SOMS.

Wavenumbers (cm^{-1})	Vibrational mode^[29,37]
3627	Interaction, through the H bond, of the O-H bond of surface silanols with each other.
3050	ν C-H of Cl-CH ₂ - groups
3023	ν C-H of aromatic ring
2933, 2900	ν_{as} C-H aliphatic of -CH ₂ - groups
2860	ν C-H of -SiOCH ₃
2800	ν_{as} C-H aliphatic of -O-CH ₂ -Si- groups

1606, 1590, 1513	ν C=C aromatic ring
1488	δ_{as} C-H aromatic ring
1448	δ_{as} O-CH ₃ groups
1405	δ_{as} -CH ₃ groups or -CH ₂ groups
1260	ν_{sym} Si-CH ₃
1259	Overtone out of plane δ C-H bond of 1,4-disubstituted aromatic ring
1190	ν Si-C of the Si-CH ₂ -CH ₂ group, or the Si-O-CH ₂ group
1100-1000	ν Si-O of Si-O-Si or Si-O-C groups;
800	ν_{sym} Si-O-CH ₃
570	ν_{sym} Si-O-Si

The correspondence of the signals found in the spectrum with those reported in the literature confirms to us that the material was synthesized correctly^[25,30].

Textural properties of the Silica-SOMS were determined by N₂ adsorption–desorption isotherms at 77 K (Figure 3.20).

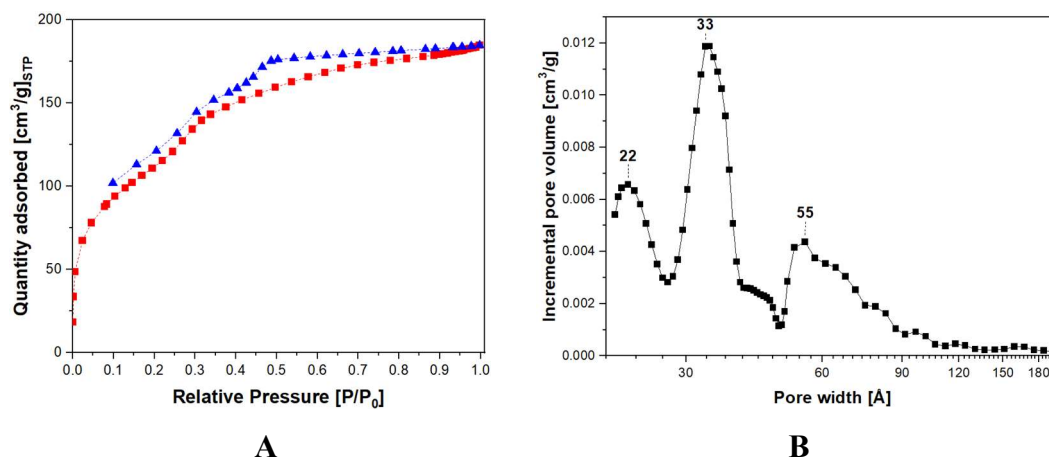


Figure 3.20 – A) N₂ adsorption and desorption isotherms at 77 K and B) pores size distribution of Silica-SOMS.

Following the IUPAC classification, the isotherm obtained (Figure 3.20A) is of type IVa, thus indicating a multilayer adsorption, which is typical of mesoporous solids^[23]. Hysteresis loops of type H2 associated with complex pore structure in which network effects are important^[35]. By inspection of the isotherm, it is seen that the adsorption and desorption branch do not overlap for the entirety of the experiment. The hysteresis extends up to very low relative pressure and loop remains open, up to 0.1 P/P_0 : this suggests the presence of swelling effects associated with the Silica-SOMS framework^[38]. A shoulder between 0.45 and 0.50 relative pressure P/P_0 appears in the desorption branch, due to pore blockage and to cavitation phenomena occurring inside pores with an ink bottle shape, or it may be due to different pore size hierarchies, as seen from the pore distribution, due to swelling^[23]. The Silica-SOMS possesses a specific surface area, calculated according to the BET model, of about 415 m^2/g , and a trimodal pore size distribution, centered at 22, 33 and 55 Å (Figure 3.20B), with a total pore volume of about 0.26 cm^3/g ; the pore size distribution calculated by applying the BJH (Barrett, Joyner and Halenda) method on the adsorption branch, (Thickness Curve: Halsey; correction: standard). These data are in agreement with what has been reported in the literature by Edmiston and coworkers^[31,39], where a surface area of 550 m^2/g and a pore volume of 0.50 cm^3/g were found.

To gain additional information on the Silica-SOMS structure ^{13}C MAS-NMR were carried out (Figure 3.21).

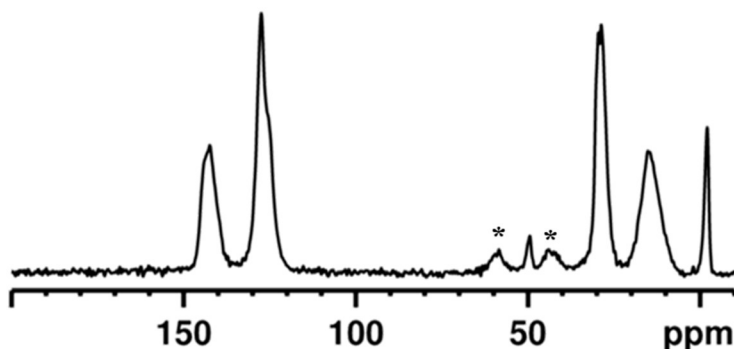


Figure 3.21 – ^{13}C MAS-NMR spectra of silica Silica-SOMS. * is used to indicated spinning side bands.

From the ^{13}C SS-NMR spectrum reported in Fig. 3.21, it can be seen the presence of multiple signals, due to the different aromatic and aliphatic carbon atoms present in the Silica-SOMS structure.

Peaks related with aromatic carbons are found in the range between 150 and 120 ppm; they are due to the resonance of aromatic carbon nuclei originating from the precursor (BTEB)^[40]. The peak centered at 50 ppm is associated to the carbon of the methoxy group bound to a silicon ($-\text{SiOCH}_3$), resulting from the precursor used (BTEB); spinning side bands appear on the sides of this signal. Carbons associated with aryl groups of the precursor used (BTEB) are found at 29 ppm ($\beta\text{-CH}_2$) and 15 ppm ($\alpha\text{-CH}_2$)^[41]. Around -1 ppm the signal is found associated with a methyl group bonded to a silicon ($-\text{SiCH}_3$)^[40,42], arising from the derivatizing agent^[35].

In Figure 3.22 is shown a scheme of a possible structure according to SS-NMR analysis, along with the corresponding peak assignments.

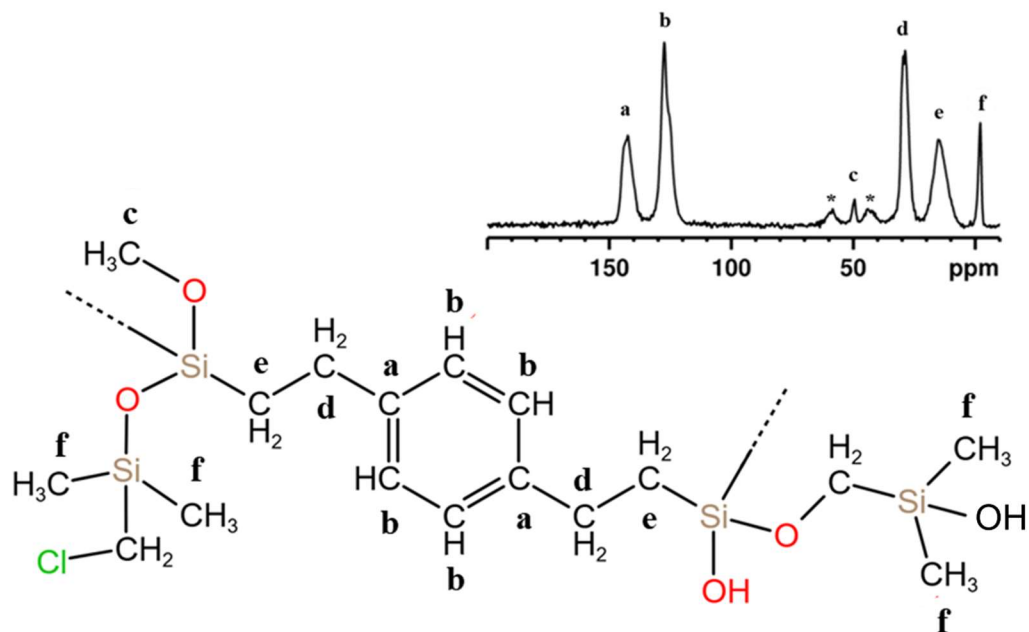


Figure 3.22 – Schematization of a probable structure of the Silica-SOMS and assignment of C cores detected by NMR. * is used to indicated spinning side bands.

^{29}Si MAS-NMR experiment was also recorded (Figure 3.23).

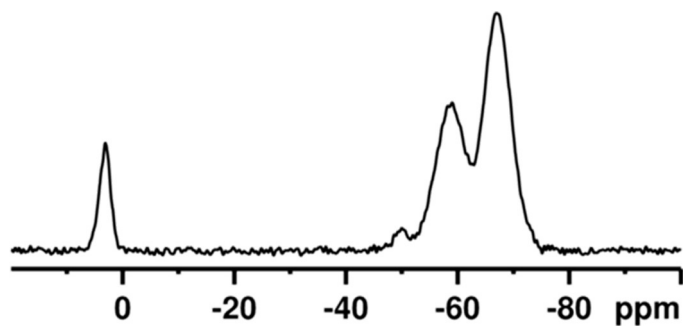


Figure 3.23 – ^{29}Si MAS-NMR spectra of silica Silica-SOMS

The peak centered at 5 ppm is assigned to the M¹ silicon, bonded to (SiO)Si(CH₃)₂(CH₂), or (SiO)Si(CH₃)₃^[43,44]; this species could have originated from derivatization of residual silanol groups^[35]. At -50 ppm the peak associated to T¹ silicon is found, and it is due to (CH₂)Si(OCH₃)₂(OSi) or (CH₂)Si(OH)₂(OSi) bonds^[35,44]. The peak centered at -59 ppm is assigned to the T² silicon, bonded to (SiO)₂Si(OH)(CH₂) or (SiO)₂Si(OCH₃)(CH₂)^[41,44]. The presence of this species indicates that the Silica-SOMS structure is not completely hydrolysed and cross-linked, as some Si atoms are still attached to the -OCH₃ or -OH groups^[35]. At -67 ppm the signal can be assigned to Q³ silicon, related to (SiO)₃Si(CH₂) bond^[44,45]; these species are due to the formation of Si-O-Si bonds between the monomers of BTEB during polycondensation and aging^[35].

Also in this case, in Figure 3.24 a scheme is reported of a possible structure obtained from ²⁹Si NMR data.

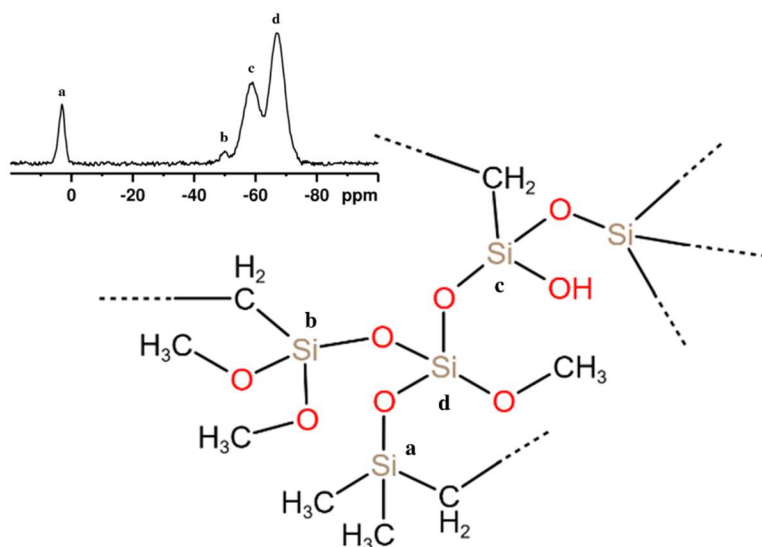


Figure 3.24 – Schematization of the probable structure of the Silica-SOMS and assignment of Si cores detected by NMR.

To evaluate the thermal stability of the Silica-SOMS, a thermogravimetric measurement (TGA) was performed, under nitrogen (Figure 3.25A) and oxygen flow (Figure 3.25B), in the range between 0 and 800 °C.

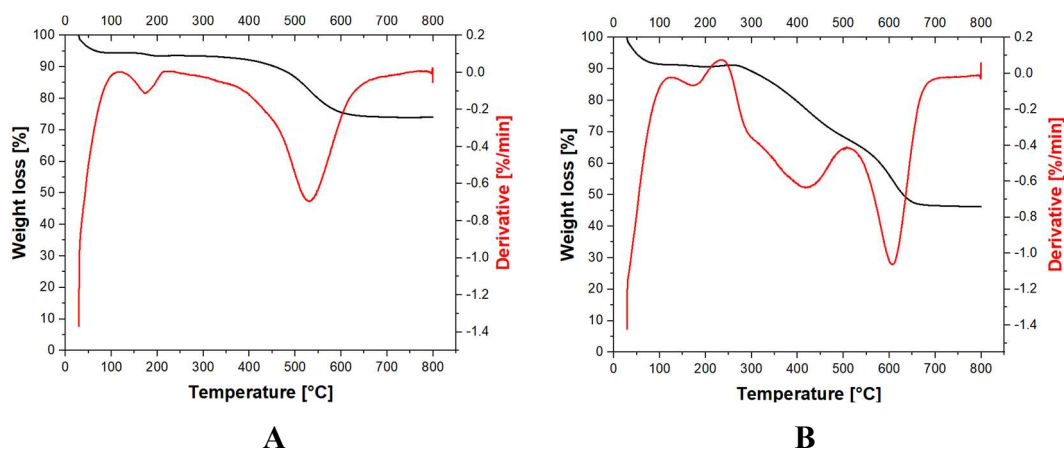


Figure 3.25. TGA/DTG measurement of Silica-SOMS, under 50 mL/min of A) nitrogen flow and B) oxygen flow, from 0°C to 800°C, with a heating of 5°C/min.

From the TGA profile obtained under nitrogen flow (Figure 3.25A) an initial weight loss of 5 wt% below 100°C is observed. This is due to the evaporation of the physisorbed water. The weight loss in the range between 100 and 400°C of *ca.* 10-15 wt% is due to the partial thermal decomposition of organic fractions of the material's framework^[35]. The additional weight loss at higher temperature (> 500°C) can be associated to the collapse of the organic structure.

For the analysis performed under oxygen atmosphere (Figure 3.25B), there is an initial weight loss of 5-10% between 25°C and 100°C, corresponding to the loss of water and physisorbed species. From 250 to 450 °C, a further weight loss is observed of 20 wt%, which is due to the onset of degradation of the organic species /fraction within the Silica-SOMS structure. Finally, from about 550 °C, there is a final weight loss of 20 wt%, which is faster than the previous one due to the increased degradation of the organic component of the material.

The TGA analysis performed in air, in the presence of O₂, leads to combustion phenomena of the organic part of the material and, consequently, to a greater weight loss than the analysis performed in N₂. The presence of oxygen in combination with an increase in temperature leads to faster and greater combustion of the organic portion of the material.

The weight loss observed in air is consistent with the percentage of organic matter determined in the elemental analysis, where it was found that overall carbon, nitrogen and hydrogen content corresponds to 50% of the mass.

3.2.5 Characterization of Silica-QA-SOMS

For the Silica-QA-SOMS sample, it was determined the chemical composition and amount of the organic moieties through the CHN elemental analysis, which is reported in Table 3.4.

Table 3.4 - Results of elemental analysis performed on Silica-QA-SOMS.

Sample	N wt%	C wt%	H wt%
Average	0.781	49.097	5.997
Std. Deviation	0.005	1.710	0.023

Analysis of the results shows that the percentage of carbon is 49wt%, The nitrogen is assessed around 0.8wt% and is probably found in the structure as a quaternary ammonium group. The percentages obtained are in agreement with the amount of reagents used for the synthesis.

The result is in agreement with the data reported in the literature, which indicate a quantity of about 60% for the organic part of SOMS structure^[35].

The morphology of Silica-QA-SOMS was investigated using Scanning Electron Microscope (SEM), and the micrograph is reported in Figure 3.26.

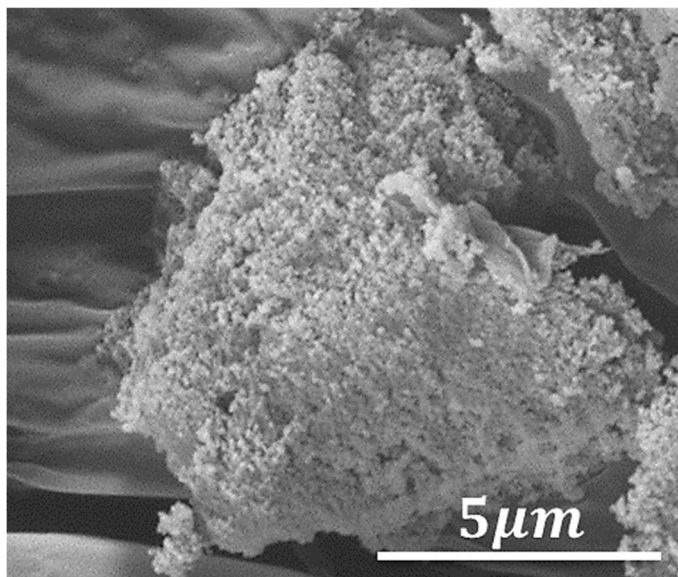


Figure 3.26 - SEM micrograph of Silica-QA-SOMS, registered at 25000x.

Silica-QA-SOMS particles appear of irregular morphology, characterized by the presence of aggregates. Macro-aggregates have a size between 5 and 10 μ m. it can also be seen the presence of smaller particles of nanometer size.

Silica-QA-SOMS, both for the presence of aromatic groups and for derivatization with hexamethyldisilazane, is a material with a strong hydrophobic character, so in the absence of organic molecules, its particles tend to remain compact and form aggregates.

The surface potential trend was evaluated over a pH range of 3 to 10. The results of the analysis are shown in Figure 3.27.

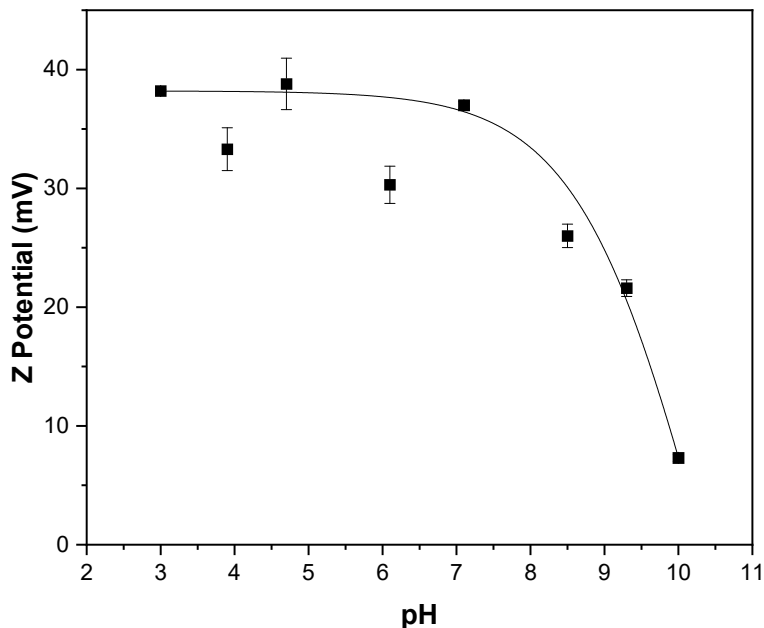


Figure 3.27 – Z potential of Silica-QA-SOMS versus pH.

As shown in Figure 3.27, the Silica-QA-SOMS shows a positive Z potential throughout the considered pH range and the zero point charge seems to be above pH 10. The positive surface charge of the material is attributed to the presence of the pH-independent quaternary ammonium group within the structure.

IR spectroscopy was used to investigate the surface properties of the material; the spectrum obtained is shown in Figure 3.28.

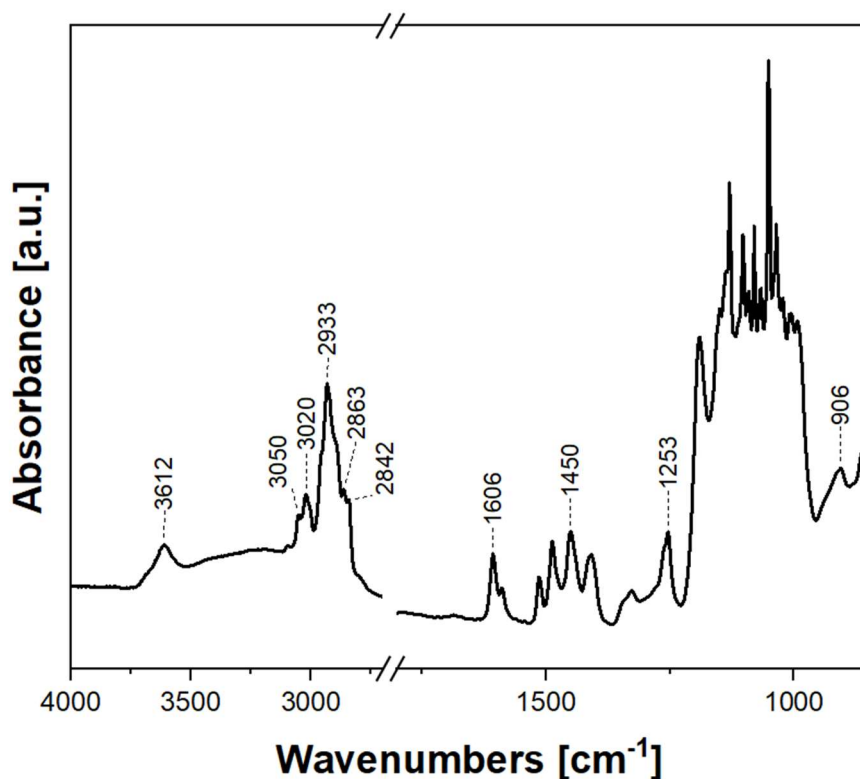


Figure 3.28 – FT-IR spectra of Silica-QA-SOMS sample after treatment in vacuum at beam temperature (b.t., 35°C) for 30 min.

In the high frequency region, the IR spectrum of Silica-QA-SOMS is characterised by bands in the range between 3600 and 2700 cm^{-1} .

The band at *ca.* 3612 cm^{-1} is related to the stretching mode of the O-H groups species interacting with each other^[22]. The bands at 3021 and 2935 cm^{-1} correspond to the stretching of the C-H bond of the aromatic ring and the ethyl groups bound to them^[25]. The signal at 2840 cm^{-1} is attributed to the C-H bond stretching of the residual methoxy groups (-OCH₃) or hexamethyldisilazane groups (-SiCH₃). The absorption band at 3610 cm^{-1} is attributed to O-H bond stretching of residual silanols that are likely in areas not accessible to HMDS. Around 1500 cm^{-1} is the frequency

of the C=C bond stretching of the aromatic rings and at 1450 cm^{-1} is the bending of the C-H bonds. In contrast, the absorption band at 1250 cm^{-1} is due to the stretching of the Si-CH₃ bonds. The occurrence of a band located at 906 cm^{-1} , characteristic of a Si-O bond with a non-bridging oxygen^[46], is correlated with reduced crosslinking of Silica-QA-SOMS, respect to the Silica-SOMS^[30].

Textural properties of Silica-QA-SOMS were determined by nitrogen physisorption analysis at 77 K. The nitrogen adsorption isotherm and the pore size distribution is reported in Figure 3.29.

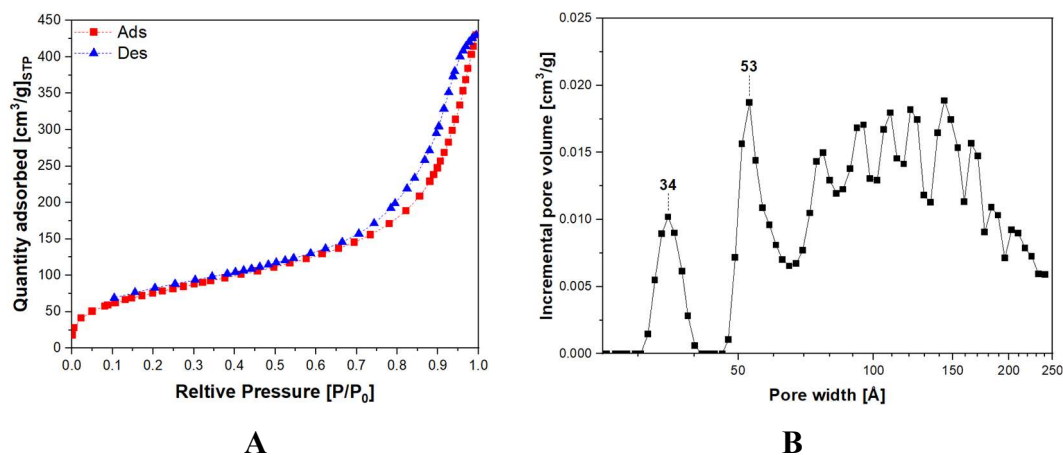


Figure 3.29 – A) Nitrogen adsorption isotherm and B) pore size distribution of Silica-QA-SOMS.

Following the IUPAC classification, the obtained isotherm is comparable to the type IV isotherm, related to multilayer adsorption up to high relative pressures; an H3-type hysteresis loop, typical of non-rigid plate-like particle aggregates, appears in the desorption branch^[23]. The Silica-QA-SOMS possesses a specific surface area, calculated according to the BET model, of about $283\text{ m}^2/\text{g}$ and a very wide pore distribution with a total pore volume of about $0.65\text{ cm}^3/\text{g}$, calculated by applying the BJH method on the adsorption branch (Thickness Curve: Halsey; correction: standard); this result is in agreement with what is reported in the literature: a surface

area of 240 m²/g and a pore volume of 0.81 cm³/g are indicated^[39]. As reported in the literature, the introduction of quaternary amine groups resulted in a reduction in surface area and an increase in pore volume compared to Silica-SOMS^[39].

The Silica-QA-SOMS possess several pore families between 30 and 200 Å (Figure 3.29B). The physisorption measurement of N₂ at 77 K was conducted on the powdered material as it is (without addition of organic solvents, and thus without swelling). However, as reported in literature, in the presence of organic solvent the material possesses the ability to swell, so the textile properties of the Silica-QA-SOMS may change due to the flexibility of the lattice^[39].

The structure of Silica-QA-SOMS was studied by solid-state Nuclear Magnetic Resonance (ssNMR) spectroscopy. ssNMR spectra of the active nuclei in the material, ²⁹Si and ¹³C, were recorded to obtain structural information.

The ssNMR ¹³C CPMAS spectrum, shown in Figure 3.30, allows identification of the different types of carbon atoms found in the Silica-QA-SOMS structure.

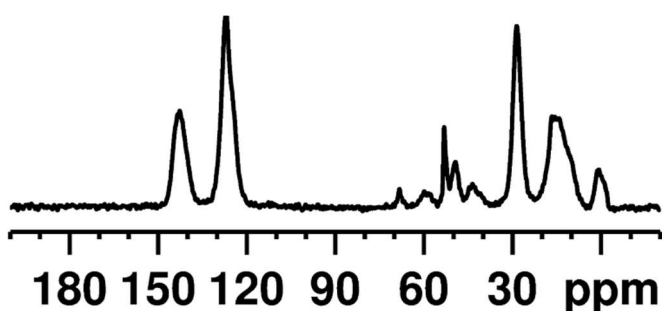


Figure 3.30 –SS-NMR spectra of ¹³C CPMAS

From the ¹³C SS-NMR spectrum, it can be seen the presence of multiple signals, due to the different aromatic and aliphatic carbon atoms present in the Silica-QA-SOMS structure.

Peaks related with aromatic carbons are found in the range between 150 and 120 ppm, due to the resonance of aromatic carbon nuclei originating from the precursor (BTEB)^[40]. The peak centered at 68 ppm is assigned to the carbon near to the N atom (-CH₂N(CH₃)₃⁺).

The peak centered at 50 ppm is assigned to the carbon of the methoxy group bounded to a silicon (-SiOCH₃). Carbons associated with aryl groups are found at 29 ppm (β-CH₂) and 15 ppm (α-CH₂)^[41]. Around 0.6 ppm the signal as associated with a methyl group bonded to a silicon (-SiCH₃)^[40,42], arising from hexamethyldisilazane^[35].

To gain additional information on the Silica-QA-SOMS structure, in Figure 3.31 is shown a scheme of the possible structure according to SS-NMR analysis, along with the corresponding peak assignments.

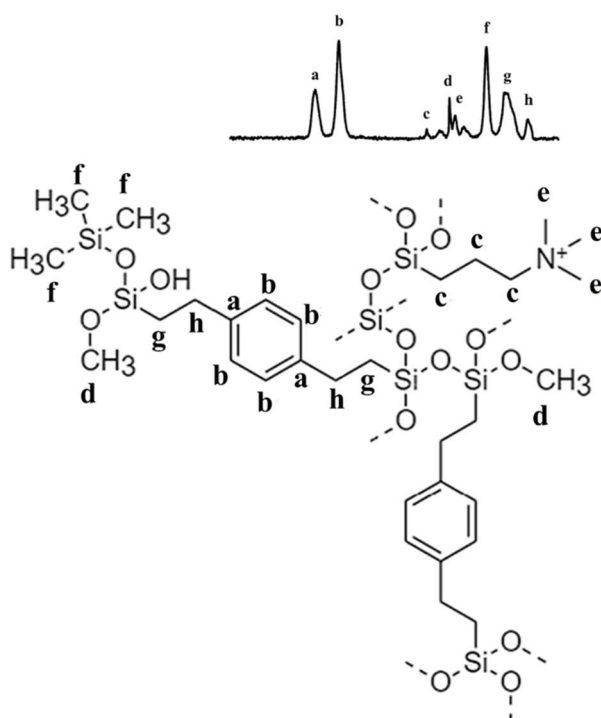


Figure 3.31 – Schematization of the probable structure of the Silica-QA-SOMS and assignment of C cores detected by NMR.

^{29}Si MAS-NMR experiment was also recorded (Figure 3.32).

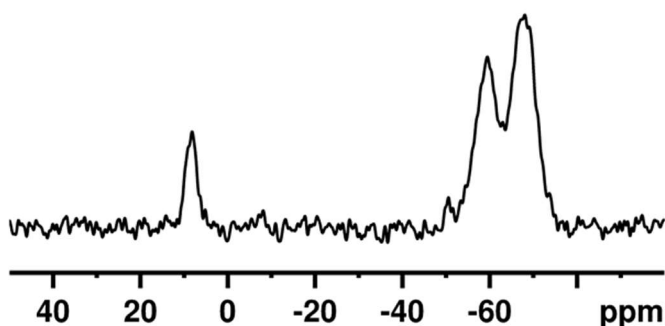


Figure 3.32 –SS-NMR spectra of ^{29}Si CPMAS.

From the ^{29}Si SS-NMR spectrum, it can be seen a peak centered at 8 ppm, assigned to the M^1 silicon, bonded to $(\text{SiO})\text{Si}(\text{CH}_3)_3$, due to the derivatization of silanol groups with hexametyldisilazane^[43]. At -50 ppm a peak associated to T^1 silicon is found, and it's due to $(\text{SiO})\text{Si}(\text{OCH}_3)_2(\text{CH}_2)-$ or $(\text{SiO})\text{Si}(\text{OH})_2(\text{CH}_2)-$ bonds^[35,44].

The peak centered at -59 ppm is assigned to the T^2 silicon, bonded to $(\text{SiO})_2\text{Si}(\text{OH})(\text{CH}_2)-$ or $(\text{SiO})_2\text{Si}(\text{OCH}_3)(\text{CH}_2)-$ ^[41]. At -67 ppm the signal can be assigned to T^3 silicon, related to $(\text{SiO})_3\text{Si}(\text{CH}_2)$ bond^[45].

Also in this case, in Figure 3.33 is reported a scheme of the possible structure according to the SS-NMR spectrum obtained.

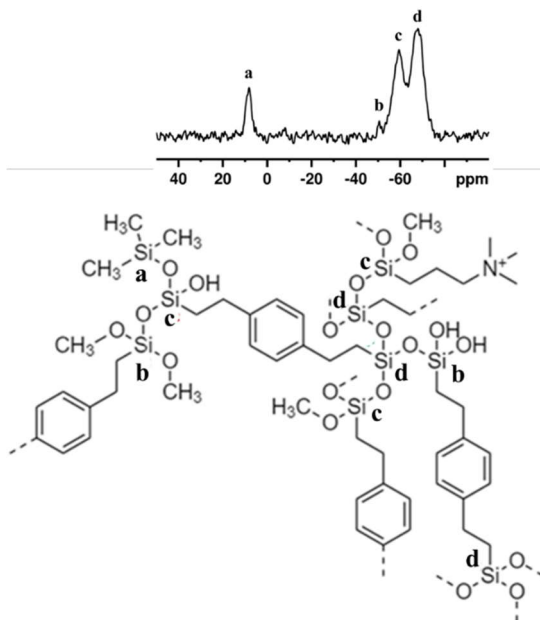


Figure 3.33 – Schematization of the probable structure of the Silica-QA-SOMS and assignment of Si cores detected by NMR.

To evaluate the thermal stability of the Silica-QA-SOMS material, a thermogravimetric measurement was performed.

Figure 3.34 shows the thermogravimetric measurement under nitrogen flow (A) and under oxygen flow (B) in the range between 0 and 800 °C.

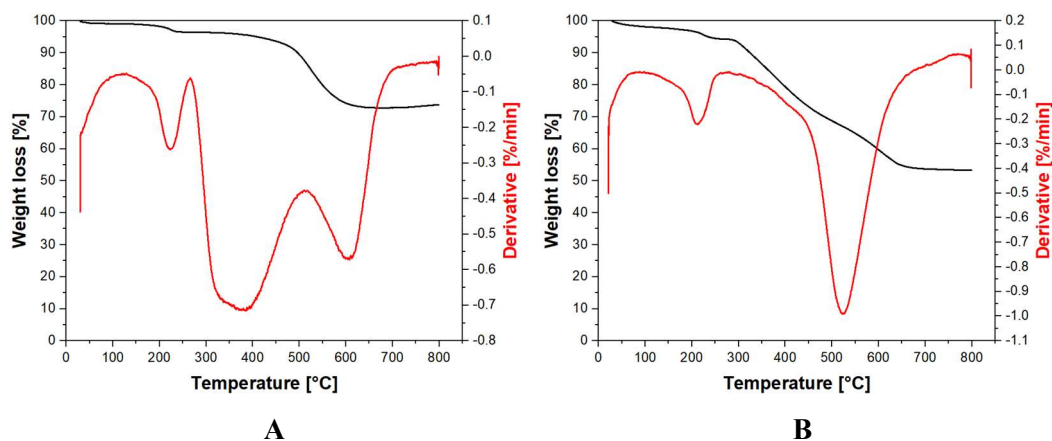


Figure 3.34. TGA/DTG measurement of Silica-QA-SOMS, under 50 mL/min of A) nitrogen flow and B) oxygen flow, from 0°C to 800°C, with a heating of 5°C/min.

From the TGA profile obtained in an inert atmosphere of N_2 (Figure 3.34A), an initial weight loss of 5% below $200^\circ C$ is noted, due to the evaporation of the adsorbed water, and one above $300^\circ C$ of about 20%, which corresponds to the partial thermal decomposition of the organic part of the material. In the analysis conducted in air, on the other hand, there is a 5% loss in weight below $200^\circ C$ and above $300^\circ C$ a gradual loss of up to 40% reduction in mass. Comparison of the two thermograms shows that the weight loss is similar up to $300^\circ C$ but reaches 40% when the material is heated in air and only 20% in N_2 .

The TGA analysis performed in air (Figure 3.34B), with the presence of O_2 , involves the establishment of combustion phenomena of the organic part of the material with the consequent release of CO_2 , CO , NO_x and therefore greater weight loss than that conducted in N_2 , in which there is only the decomposition of the structure. The weight loss observed in air is in agreement with the percentage of organic matter found in the elemental analysis, where it could be observed that the sum of the percentages of carbon, nitrogen and hydrogen corresponds to 50% by mass.

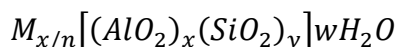
3.3 Commercial Zeolite 13X

Zeolites are well known crystalline aluminosilicates; they possess well-defined porous structures and pore sizes of molecular dimensions in the range 0.3–2 nm. Zeolites are highly ordered microporous solids, according to the IUPAC classification^[47–49].

Zeolites are composed of an elementary structure of TO_4 tetrahedra, where T can be aluminium cations (Al^{3+}) or silicon cations (Si^{4+}), connected with each other by sharing oxygen atoms (O^{2-})^[47]. The electrovalence of the aluminium-containing tetrahedra is balanced by the inclusion of a cation (Me^{n+}), usually an alkaline metal or alkaline earth metal^[50,51].

The basic units that form the secondary structures are organized in space in a very regular way, forming the three-dimensional tertiary structural units^[52].

The structural formula of zeolite is based on the atoms located in the crystallographic unit cell:



where (M) represents an alkaline or alkaline earth cation and (n) is its valence, (w) is the number of water molecules per cell unit, (x) and (y) are the total number of tetrahedra per unit cell^[53].

Due to the presence of aluminium in the structure of zeolites, this class of materials can adsorb certain types of gases (such as CO_2 , CH_4). Aluminium is present as an isomorphic substitute for silicon: it introduces a structural negative charge that is balanced by the cations in the pore space^[51]. Zeolites become capable to adsorb acid gases (such as CO_2) if alkali cations are present in their structure^[54]. This class of materials adsorbs molecules mainly by physical adsorption; in particular, the Lewis acid-base interactions that occurs between surface silanol/silanoate groups and alkali cations create an electric field that affects adsorption^[51].

A commercial zeolite, available in pellet form, was used in this thesis work. Zeolite 13X was provided by Ecospray Technology Company and then characterized and later used for the separation of gas mixtures (See Chapter 7).

3.3.1 Characterization of Zeolite 13X

Zeolite 13X is a low-silica zeolites (or aluminium-rich zeolites) with a molar ratio $\text{Si}/\text{Al} \approx 1-1.5$ and with a Na^+ ions in its structure (sites I/I' in the sodalite cages, sites II/II' at the hexagonal rings inside the cavities, and sites III/III' at the entrance of the supercage, as shown in Figure 3.34A)^[55]. It possessed strong hydrophilic surface selectivity and a high pore volume, with a pore diameter of 0.9-1.0 nm^[56].

The structure of Zeolite 13X is a faujasite type, and it's shown in Figure 3.35.

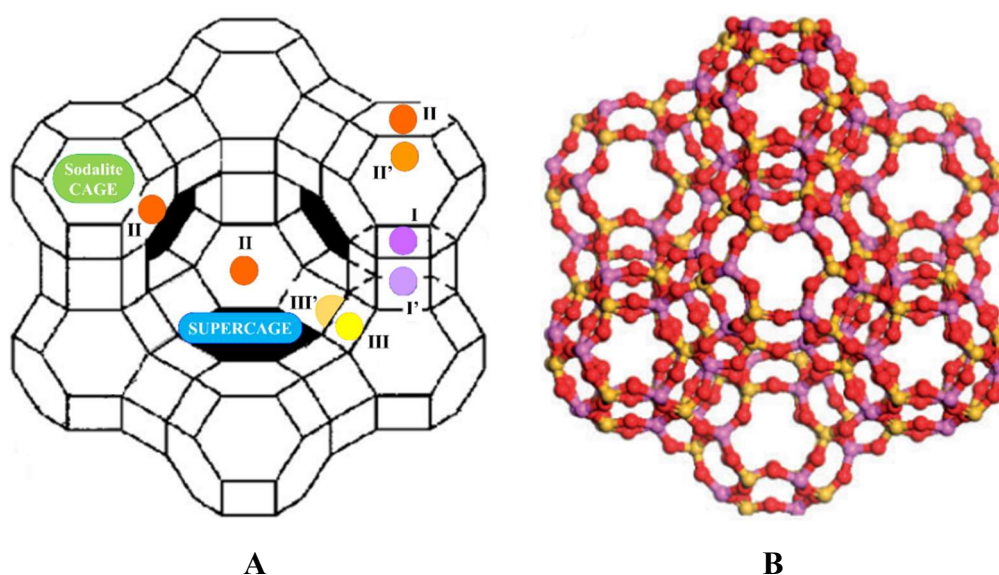


Figure 3.35 – A) Zeolite 13X framework structure and B) molecular structure. Adapted from^[55-57].

Zeolite 13X has a faujasite structure that consists of ten sodalite cages connected by hexagonal prisms^[58]. This structure forms an internal cavity of 7.4 Å, which is called supercage, because of the high aluminium content and the corresponding number of

cations^[59]. Therefore, it has a high ion storage capacity and a high attraction to polar molecules.

The structural properties of Zeolite 13X were investigated by XRD analysis (Figure 3.36).

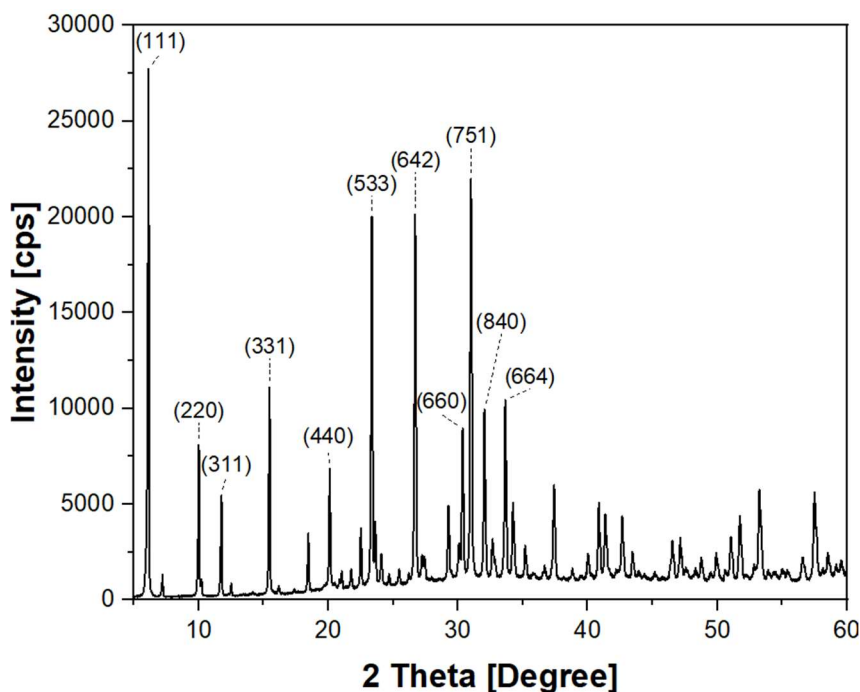


Figure 3.36 - XRD diffraction pattern of Zeolite 13X.

The XRD powder pattern of Zeolite 13X shows different Bragg reflections, typical of a highly crystalline material.

The pattern is characterized by peaks at ca. 9°, 23°, 26°, 31° 2 θ , that are assigned respectively to the (111), (533), (642), (751) planes^[60]; other reflections are located at 10°, 12°, 15°, 21°, 30°, 32°, 34° 2 θ , corresponding to (220), (311), (331), (440), (660), (840) and (664) planes^[60]. The pattern matches that of commercial 13X zeolite reported in the literature^[61].

The investigation of the surface morphology of Zeolite 13 X was carried out on a Scanning Electron Microscope (SEM); the obtained micrographs are reported in Figure 3.37.

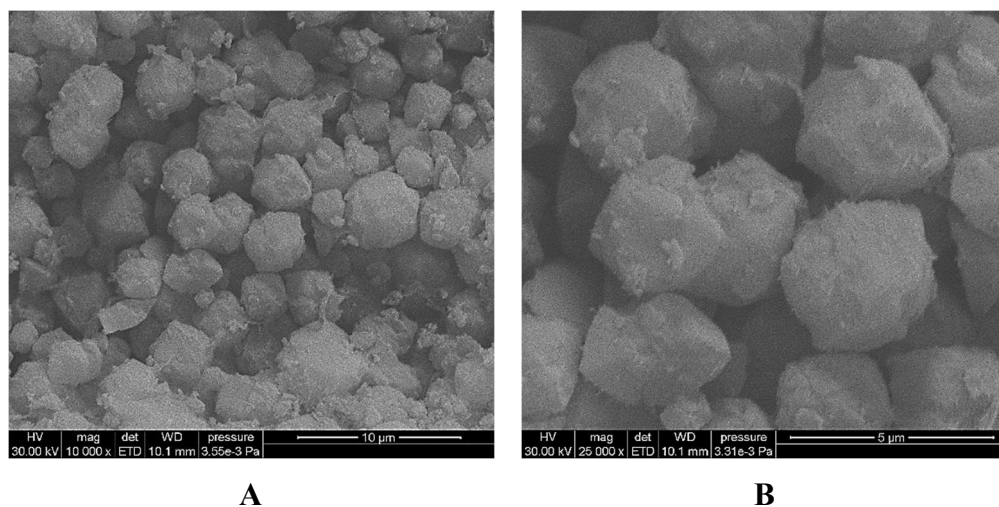


Figure 3.37 – SEM micrographs of Zeolite 13X, registered at A) 10000x and B) 25000x.

The zeolite has a cubic morphology and is composed of particles of *ca.* 2.5 µm in diameter. This is in agreement with the data in the literature: Zeolite 13X in powder form exhibits a well-defined cubic morphology with crystal sizes ranging from 1.3 to 3 µm, while even smaller crystals (approx. 0.8 µm) appear after pelletization that is, after the material has been subjected to high mechanical pressures^[62].

Trend of surface potential was investigated, as a function of pH, over a pH range between 2 to 10 (Figure 3.38).

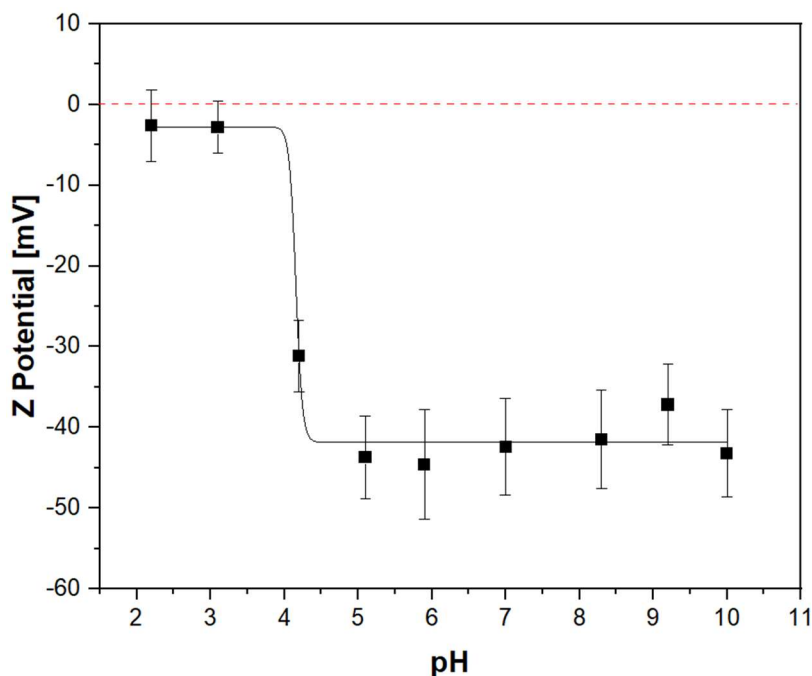
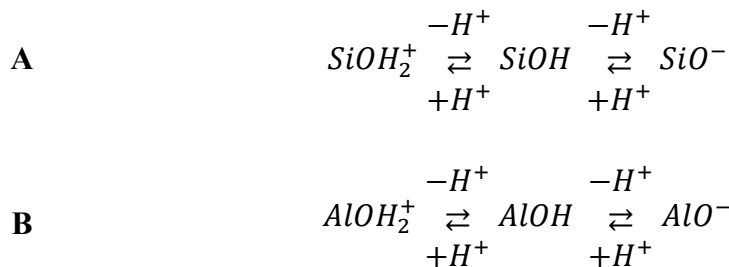


Figure 3.38 – Z potential of Zeolite 13X.

The Z-potential of zeolite is observed to be negative in the entire pH range investigated; in particular, the potential takes on increasingly negative values with increasing pH (> 3) and thus with increasing basicity of the solution, up to pH 5, where it remains almost constant.

The surface charge of zeolite, for different pH values, is due to protonation or deprotonation of hydroxyl groups^[63].

The pH controls the surface charge of the particles, and therefore the zeta potential, through the following mechanisms^[64]:



The zeta potential of zeolites depends on the pH, on the ionic strength of the suspension and the Al content of the structure: the increase in concentrations of Al atoms shifts the isoelectric point to lower pH values, which is attributed to the greater acidic character of the Al atoms [49]. Furthermore, bridged hydroxide groups (Si – OH – Al) on the surface of the Zeolite 13X can be easily deprotonated to form Si – O – Al at a wide pH range, making the surface more negatively charged[65]. As the Si / Al ratio in the zeolite decreases, this effect counterbalances the protonation effect of the silanol groups in acidic solutions thus shifting the isoelectric point to lower pH[63,66].

Textural properties Zeolite 13X were investigated by means of N₂ physisorption at 77 K. The data are shown in Figure 3.39.

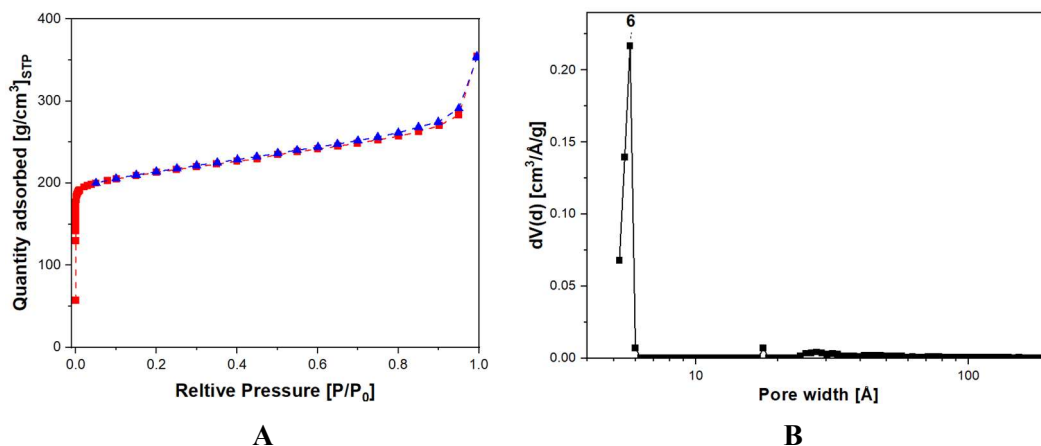


Figure 3.39 - A) N₂ physisorption isotherm recorded at 77 K and B) pore size distribution of the Zeolite 13X sample.

The physisorption isotherm (Figure 3.39A) can be classified as type I, according to the IUPAC definition, which are characteristic of a microporous material; this is consistent with what has been reported in the literature for commercial Zeolite 13X^[67].

Zeolite 13X exhibit a monomodal pore size distribution (Figure 3.39B) centered at 6 Å, confirming the presence of microporosity. The specific surface area (SSA), calculated using the BET method, of the sample was equal to 837 m²/g; the total porous volume, calculated in the adsorption branch with NLDFT method on silica cylindrical pore, was 0.38 cc/g, with a micropore volume of 0.22 cc/g and a mesopore volume (20-100 Å) of 0.09 cc/g. These data are consistent with what Cortès et coworkers described, as they report a surface area value of 729 m²/g with a microporous volume of 0.26 cc/g^[68].

Conclusions

In this chapter, several inorganic materials were synthesized and characterized using a multitechnical approach for later use in contaminant removal.

First, a mesoporous silica was synthesized directly in the form of a monolith during the synthesis stage, and its chemical and physical properties were investigated; in particular, the structural properties were found to be homogeneous along the entire length of the monolith, which has an average surface area of approximately 850 m²/g and a total pore volume of 1.2 cm³/g.

The synthesis method for a hybrid organic-inorganic silica (Silica-SOMS), which has the unique property of being swellable only in the presence of an organic solvent, was then reported. Also reported was a variant of the process that allows the material to be functionalized with quaternary amine groups in one synthesis step (Silica-QA-SOMS), which imparts a positive surface charge to the material, as indicated by surface potential measurements.

Characterization of the structural properties of both materials showed that the introduction of the quaternary amine groups into the material leads to a decrease in surface area, from 415 m²/g to 283 m²/g for Silica-SOMS and Silica-QA-SOMS, respectively, and an increase in pore volume, from 0.26 cm³/g to 0.65 cm³/g for Silica-SOMS and Silica-QA-SOMS, respectively.

Finally, a zeolite of commercial origin was characterized: Zeolite 13X

Zeolite 13X is a low-Silica zeolites, with a Na⁺ ions in its faujasitic structure. It is a microporous crystalline solid, which has a specific surface area of 837 m²/g, with a microporous volume of 0.22 cc/g and a total pore volume of 0.38 cc/g.

References

- [1] M. Kruk, M. Jaroniec, A. Sayari, *Microporous and Mesoporous Materials* **2000**, 35–36, 545–553.
- [2] E. Da'na, *Microporous and Mesoporous Materials* **2017**, 247, 145–157.
- [3] B. Fotoohi, M. Kazemzad, L. Mercier, *Ceramics International* **2018**, 44, 20199–20210.
- [4] N.-L. Michels, S. Mitchell, J. Pérez-Ramírez, *ACS Catal.* **2014**, 4, 2409–2417.
- [5] A. Galarneau, Z. Abid, B. Said, Y. Didi, K. Szymanska, A. Jarzębski, F. Tancret, H. Hamaizi, A. Bengueddach, F. Di Renzo, F. Fajula, *Inorganics* **2016**, 4, 9.
- [6] T. Amatani, K. Nakanishi, K. Hirao, T. Kodaira, *Chem. Mater.* **2005**, 17, 2114–2119.
- [7] R. Kohns, C. P. Haas, A. Höltzel, C. Splith, D. Enke, U. Tallarek, *React. Chem. Eng.* **2018**, 3, 353–364.
- [8] A. Roucher, A. Bentaleb, E. Laurichesse, M.-A. Dourges, M. Emo, V. Schmitt, J.-L. Blin, R. Backov, *Chem. Mater.* **2018**, 30, 864–873.
- [9] K. Kanamori, K. Nakanishi, *Chem. Soc. Rev.* **2011**, 40, 754–770.
- [10] D. Enke, R. Gläser, U. Tallarek, *Chemie Ingenieur Technik* **2016**, 88, 1561–1585.
- [11] C. Aydoğan, A. Gökaltun, A. Denizli, Z. El-Rassi, *J. Sep. Sci.* **2019**, jssc.201801051.
- [12] R. Du, Q. Zhao, N. Zhang, J. Zhang, *Small* **2015**, 11, 3263–3289.
- [13] H.-P. Cong, J.-F. Chen, S.-H. Yu, *Chem. Soc. Rev.* **2014**, 43, 7295–7325.
- [14] C. J. Brinker, G. W. Scherer, *Sol-Gel Science: The Physics and Chemistry of Sol-Gel Processing*, Academic Press, Boston, **1990**.
- [15] N. Aboualigaedari, M. Rahmani, *jcc* **2021**, 2, 25–42.
- [16] S. A. El-Safty, Y. Kiyozumi, T. Hanaoka, F. Mizukami, *J. Phys. Chem. C* **2008**, 112, 5476–5489.

- [17] K. Kanamori, K. Nakanishi, T. Hanada, *Soft Matter* **2009**, *5*, 3106.
- [18] K. Nakanishi, *Journal of Porous Materials* **1997**, *4*, 67–112.
- [19] C. Triantafillidis, M. S. Elsaesser, N. Hüsing, *Chem. Soc. Rev.* **2013**, *42*, 3833.
- [20] D. J. Belton, O. Deschaume, C. C. Perry, *FEBS Journal* **2012**, *279*, 1710–1720.
- [21] V. Miglio, C. Zaccone, C. Vittoni, I. Braschi, E. Buscaroli, G. Golemme, L. Marchese, C. Bisio, *Molecules* **2021**, *26*, 1316.
- [22] C. Vittoni, V. Sacchetto, D. Costenaro, S. Mastroianni, A. Hinsch, L. Marchese, C. Bisio, *Solar Energy* **2016**, *124*, 101–113.
- [23] M. Thommes, K. Kaneko, A. V. Neimark, J. P. Olivier, F. Rodriguez-Reinoso, J. Rouquerol, K. S. W. Sing, *Pure and Applied Chemistry* **2015**, *87*, 1051–1069.
- [24] P. L. Edmiston, *Swellable Sol-Gels, Methods of Making, and Use Thereof*, **2010**, US 7,790,830 B2.
- [25] C. M. Burkett, P. L. Edmiston, *Journal of Non-Crystalline Solids* **2005**, *351*, 3174–3178.
- [26] R. Corriu, *Polyhedron* **1998**, *17*, 925–934.
- [27] P. L. Edmiston, L. A. Underwood, *Separation and Purification Technology* **2009**, *66*, 532–540.
- [28] G. Celik, S. A. Ailawar, H. Sohn, Y. Tang, F. F. Tao, J. T. Miller, P. L. Edmiston, U. S. Ozkan, *ACS Catal.* **2018**, *8*, 6796–6809.
- [29] C. M. Burkett, L. A. Underwood, R. S. Volzer, J. A. Baughman, P. L. Edmiston, *Chem. Mater.* **2008**, *20*, 1312–1321.
- [30] E. K. Stebel, K. A. Pike, H. Nguyen, H. A. Hartmann, M. J. Klonowski, M. G. Lawrence, R. M. Collins, C. E. Hefner, P. L. Edmiston, *Environ. Sci.: Water Res. Technol.* **2019**, *5*, 1854–1866.
- [31] P. L. Edmiston, L. J. West, A. Chin, N. Mellor, D. Barth, *Ind. Eng. Chem. Res.* **2016**, *55*, 12068–12079.
- [32] H. Hartmann, C. Hefner, E. Carter, D. Liles, C. Divine, P. L. Edmiston, *AWWA Water Science* **2021**, *3*, DOI 10.1002/aws2.1237.
- [33] Y. Liang, R. Anwander, *J. Mater. Chem.* **2007**, *17*, 2506.

- [34] G. Cerveau, R. J. P. Corriu, *Coordination Chemistry Reviews* **1998**, 178–180, 1051–1071.
- [35] D. Basu, S. Ailawar, G. Celik, P. Edmiston, U. S. Ozkan, *ChemCatChem* **2020**, 12, 3753–3768.
- [36] G. Xu, J. Zhang, G. Song, *Powder Technology* **2003**, 134, 218–222.
- [37] G. Socrates, G. Socrates, *Infrared and Raman Characteristic Group Frequencies: Tables and Charts*, Wiley, Chichester ; New York, **2001**.
- [38] G. Paul, F. Begni, A. Melicchio, G. Golemme, C. Bisio, D. Marchi, M. Cossi, L. Marchese, G. Gatti, *ACS Appl. Polym. Mater.* **2020**, 2, 647–658.
- [39] P. L. Edmiston, A. R. Gilbert, Z. Harvey, N. Mellor, *Adsorption* **2018**, 24, 53–63.
- [40] D. E. Leyden, D. S. Kendall, T. G. Waddell, *Analytica Chimica Acta* **1981**, 126, 207–212.
- [41] E. J. R. Sudhölter, R. Huis, G. R. Hays, N. C. M. Alma, *Journal of Colloid and Interface Science* **1985**, 103, 554–560.
- [42] G. Gerbaud, S. Hediger, M. Bardet, L. Favennec, A. Zenasni, J. Beynet, O. Gourhant, V. Jousseau, *Phys. Chem. Chem. Phys.* **2009**, 11, 9729.
- [43] P.-Y. Mabboux, K. K. Gleason, *J. Electrochem. Soc.* **2005**, 152, F7.
- [44] G. Paul, C. Bisio, I. Braschi, M. Cossi, G. Gatti, E. Gianotti, L. Marchese, *Chem. Soc. Rev.* **2018**, 47, 5684–5739.
- [45] E.-B. Cho, K. Char, *Chem. Mater.* **2004**, 16, 270–275.
- [46] H. Aguiar, J. Serra, P. González, B. León, *Journal of Non-Crystalline Solids* **2009**, 355, 475–480.
- [47] D. L. Bish, D. W. Ming, Eds. , *Natural Zeolites: Occurrence, Properties, Applications*, Mineralogical Society Of America, Washington, DC, **2001**.
- [48] E. Koohsaryan, M. Anbia, *Chinese Journal of Catalysis* **2016**, 37, 447–467.
- [49] V. Nikolakis, *Current Opinion in Colloid & Interface Science* **2005**, 10, 203–210.

- [50] J. García-Martínez, K. Li, M. E. Davis, Eds. , *Mesoporous Zeolites: Preparation, Characterization and Applications*, Wiley-VCH, Weinheim, **2015**.
- [51] A. Palčić, V. Valtchev, *Applied Catalysis A: General* **2020**, *606*, 117795.
- [52] J. E. Šponer, Z. Sobalík, J. Leszczynski, B. Wichterlová, *J. Phys. Chem. B* **2001**, *105*, 8285–8290.
- [53] I. Petrov, T. Michalev, **2012**, *6*.
- [54] O. Cheung, Z. Bacsik, N. Fil, P. Krokidas, D. Wardecki, N. Hedin, *ACS Omega* **2020**, *5*, 25371–25380.
- [55] K. S. Walton, M. B. Abney, M. Douglas LeVan, *Microporous and Mesoporous Materials* **2006**, *91*, 78–84.
- [56] B. Kozera-Sucharda, B. Gworek, I. Kondzielski, *Minerals* **2020**, *10*, 343.
- [57] Y. Guo, H. Zhang, Y. Liu, *Adsorption Science & Technology* **2018**, *36*, 1389–1404.
- [58] M. Anbia, M. Aghaei, *Scientia Iranica* **2018**, *0*, 0–0.
- [59] A. Håkansson, A. Hakansson, *Sustainability in Energy and Buildings: Proceedings of the 4th International Conference on Sustainability in Energy and Buildings (SEB'12)*, Springer, Berlin New York, **2013**.
- [60] H. Thakkar, S. Eastman, A. Hajari, A. A. Rownaghi, J. C. Knox, F. Rezaei, *ACS Appl. Mater. Interfaces* **2016**, *8*, 27753–27761.
- [61] A. R. Sowunmi, C. O. Folayan, F. O. Anafi, O. A. Ajayi, N. O. Omisanya, D. O. Obada, D. Dodoo-Arhin, *Data in Brief* **2018**, *20*, 90–95.
- [62] E. Kirilova, F. Lamari, C. Chilev, E. Simeonov, I. Penchev, **2013**, pp. 167–172.
- [63] M. Boronat, A. Corma, *ACS Catal.* **2019**, *9*, 1539–1548.
- [64] T. Kuzniatsova, Y. Kim, K. Shqau, P. K. Dutta, H. Verweij, *Microporous and Mesoporous Materials* **2007**, *103*, 102–107.
- [65] W. Yang, X. Wang, Y. Tang, Y. Wang, C. Ke, S. Fu, *Journal of Macromolecular Science, Part A* **2002**, *39*, 509–526.
- [66] M. Trachta, R. Bulánek, O. Bludský, M. Rubeš, *Sci Rep* **2022**, *12*, 7301.

- [67] C. Chen, D.-W. Park, W.-S. Ahn, *Applied Surface Science* **2014**, 292, 63–67.
- [68] F. B. Cortés, F. Chejne, F. Carrasco-Marín, C. Moreno-Castilla, A. F. Pérez-Cadenas, *Adsorption* **2010**, 16, 141–146.

Chapter 4

Porous carbons for environmental purposes

Introduction

In this chapter, the physico-chemical properties of different porous carbons from both commercial and synthetic origin are discussed.

Four different samples of porous carbons from commercial origin (Maxsorb, Norit, Carbotech and Xintao) have been purchased in pellet form. This feature is very useful for gas adsorption and storage applications as the problems of using and handling powders can be avoided.

Furthermore, a synthetic method to obtain a porous carbon from a Hyper Cross-linked Polymer (HCP) is presented. HCPs are nanoporous organic polymers possessing a highly interconnected framework. Through heat and chemical treatments, the material can be activated and transformed into a higher value-added activated carbon.

The synthesis and characterization of a HCP will be initially described, and then the its carbonization procedure will be illustrated. It was chosen to use waste polystyrene as a starting aromatic monomer for both economic and recycling issues.

Finally, the obtained carbon will be characterized using a multi-technique approach. All these materials have been tested for gas storage applications (CO_2 , CH_4 , N_2) and the results will be presented in Chapter 6. Commercial porous carbons have also been tested for separation of gaseous mixtures (CH_4 - N_2).

4.1 Activated Porous Carbons

Activated carbons are a wide range of materials characterized by a high degree of porosity and a high specific surface area^[1]. Activated carbons, or porous carbons, are part of the graphite family, and are composed of graphitic planes folded back on themselves (Figure 4.1)^[2].



Figure 4.1 - Schematic representation of the microstructure of an activated carbon. Adapted from^[2].

The porous structure of activated carbon consists of a set of irregular channels, generating porosity of different sizes (micro, meso and macroporosity)^[3–6].

Within the carbon structure, different types of carbon bond hybridization can occur (Figure 4.2), giving rise to different possible structure both crystalline and amorphous^[7].

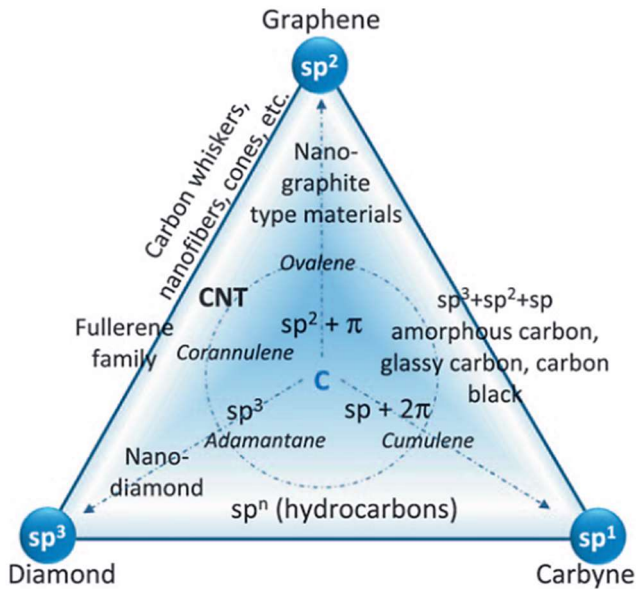


Figure 4.2 - Different types of carbon structures, based on the hybridization of carbon atoms^[7].

In addition to the limiting structures carbines (sp), graphene (sp^2) and diamond (sp^3), other materials with a mixed structure are distinguished such as amorphous carbons, vitreous or carbon black and materials containing carbon with sp^2 and sp^3 hybridization, such as nano diamonds, nanocrystalline structures of graphite and nanotubes^[8].

In general, an amorphous carbon can have any combination of sp^3 , sp^2 and sp carbon atoms with an hydrogen content up to 60% (based on the number/moles of atoms)^[9].

Activated carbons can be produced from organic matter with a high carbon content (wood, carbon, peat, coconuts, shells, etc.), which can be activated to increase the sorbent characteristics of the final carbon^[4,10,11].

The raw material from which the carbon is produced has an important and decisive effect on the distribution of porosities and the surface area value: depending on the starting material, the activation method can vary^[5].

4.1.1 Methods for the preparation of activated carbons

Activated carbons can be prepared by the following processes^[12]:

– *Physical activation method*

In physical activation, the organic matter is first carbonized in an inert environment (pyrolysis), such as in the presence of a nitrogen flow, to eliminate most of the volatile matter and impurities; subsequently, it is activated by subjecting the carbon to activating gases (CO₂, air, steam) at a high temperature^[10,13,14]. As a result, there is a release of carbon oxides from the coal surface^[14,15].

– *Chemical activation method*

In chemical activation, the carbonization process and the activation process are performed at the same time.

The raw material is mixed with an inorganic chemical substance, capable of degrading or dehydrating organic molecules during carbonization, and preventing the deposition of hydrocarbons on the carbon surface (usually alkaline earth compounds, acids and salts are used)^[16].

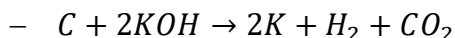
Subsequently, carbonization is carried out at high temperatures (up to 800°C) in the absence of air (vacuum or inert gas); finally, the residual impregnating agent is removed by washing with water^[17].

4.1.2 Chemical activation with KOH

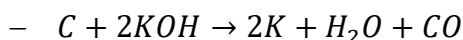
Chemical activation with KOH for carbon-based materials is a redox reaction, which causes partial oxidation of the materials. Once reduced, metallic potassium has the ability to intercalate itself throughout the carbonaceous structure^[11].

The KOH activation process generally requires two steps: the first is the activation of the starting material with a KOH solution and the second is the subsequent carbonization by calcination at elevated temperatures^[18].

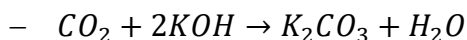
The activation process can be divided into three steps^[18,19]:



The activating agent (KOH) through redox reactions attacks the carbonaceous framework, leading to the formation of a porous net.



The formation of water contributes to the development of porosity through the gasification of carbon giving a physical activation effect.



The metal K formed goes to intercalate in the carbonaceous lattice during activation; consequently, a permanent expansion of the lattice occurs, which remains unchanged even after the final washing with a consequent increase in the surface area and porous volume.

4.2 Physico-chemical properties of commercial porous carbons

Four porous carbons of commercial origin, in pelletized form, were used in this thesis work: Carbon Maxsorb, Carbon Norit, Carbon Carbotech and Carbon Xintao; they were purchased, respectively, from: Kansai Coke & Chemicals Co., Cabot, CarboTech, Xintao Technology.

In this paragraph, results obtained from the physico-chemical characterization of these reference porous carbons are reported.

The morphology of the carbon samples was studied via Scanning Electron Microscopy (Figure 4.3).

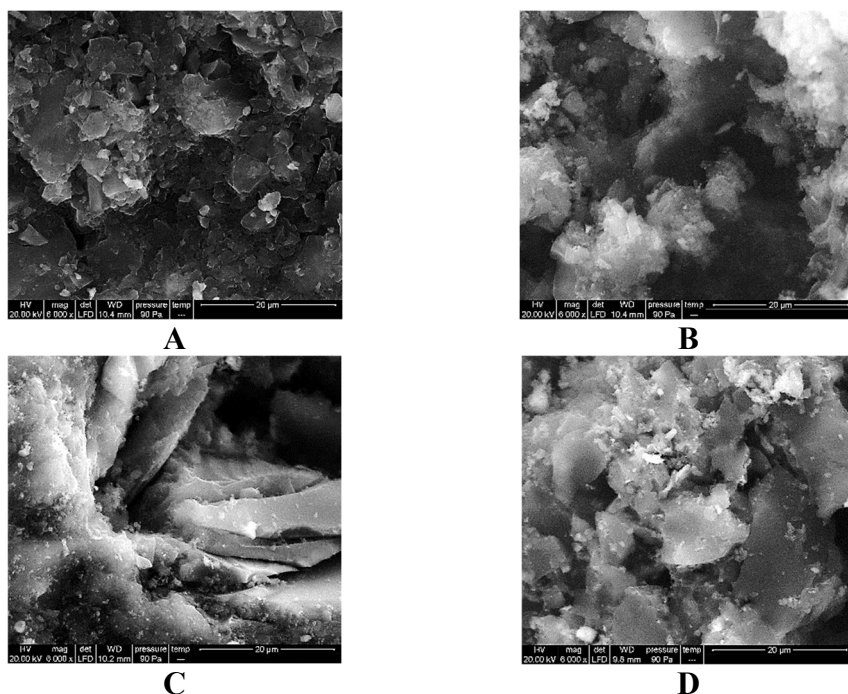


Figure 4.3 - SEM micrographs of reference carbons, registered at 6000x: A) Carbon Maxsorb, B) Carbon Norit, C) Carbon Carbotech, D) Carbon Xintao.

The micrographs of all samples show the presence of carbon particles with inhomogeneous morphology and dimensions.

In the micrograph of Maxsorb carbon, the presence of flat aggregates of different sizes between 1 and 10 microns can be seen. Norit carbon is characterized by the presence of large aggregates (20 microns) on the surface of which are particles of significantly smaller size (about 1 micron). Carbotech carbon, on the other hand, is characterized by large, elongated particles larger than 20 nanometers in size. Xintao carbon is also characterized by larger particles (10-15 microns) on whose surface are smaller particles (about 1 micron).

The inhomogeneous morphology of the carbons can be attributed to the presence of binders, which have been added to the carbons in order to render them in pelletized form^[20].

Raman spectroscopy was also used to assess the structural features of the sample (Figure 4.4). Particularly, from the ratio between the intensity of D (1330 cm^{-1}) and G (1590 cm^{-1}) bands (I_D/I_G), referred to as the degree of graphitization, which are typical of this kind of system, it is possible to define the structural disorder of the framework^[21].

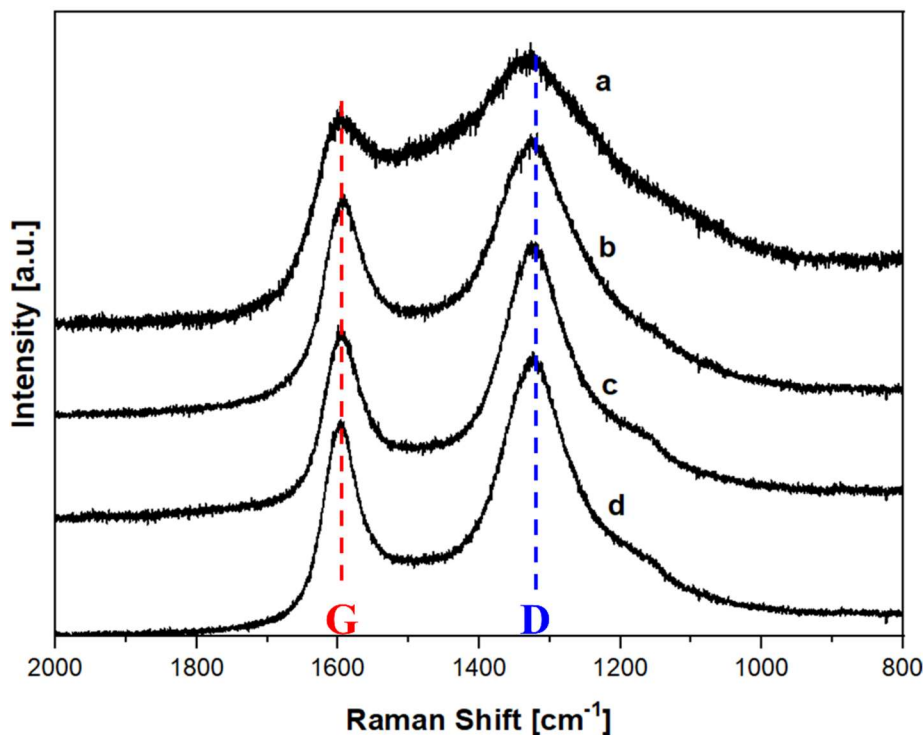


Figure 4.4 - Raman spectra recorded under standard conditions of temperature and pressure of the carbons: a) Carbon Maxsorb, b) Carbon Carbotech, c) Carbon Xintao, d) Carbon Norit.

As a general feature, in the Raman spectra of the carbons two main bands are present, located at 1330 and 1590 cm^{-1} .

The 1590 cm^{-1} mode (G peak) it is commonly assigned to stretching vibrational modes between pairs of sp^2 carbon atoms in aromatic rings or chains, belonging to disordered microcrystalline domains^[9]; for crystalline graphite, the G peak is related to the Raman-allowed E_{2g} mode (Figure 4.5) ^[22].

The 1330 cm^{-1} mode (D peak) corresponds to the disorder-induced band, which is related to the large density of phonon states^[6]. In fact, a intense D-band peak reveals that the porous carbon possesses a low degree of graphitization, with a significant amount of disordered sections and defects^[9].

The D band is assigned to an A_{1g} symmetry lattice breathing mode (Figure 4.5) which is forbidden in ideal graphite crystals, but which becomes Raman active in the

presence of structural disorder^[23]. In particular, it has been suggested that it derives from carbon atoms near the edge of a graphene layer^[24].

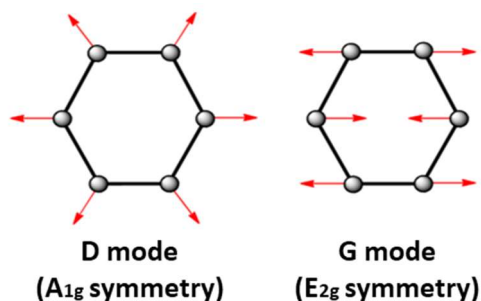


Figure 4.5 – Vibration motions of Carbon in D and G modes. Adapted from^[25].

In the spectra, the relative intensity between the D (1330 cm^{-1}) and G (1590 cm^{-1}) band provides information on the structural order of the carbonaceous framework, in addition to the presence of defects^[26].

Table 4.1 shows the intensity of the D and G bands of studied carbons and their ratio; band intensities were obtained after deconvolution of the obtained Raman spectra, using Fityk software, considering five different components: D (1330 cm^{-1}), D₂ ($1610\text{-}1620\text{ cm}^{-1}$), D₃ ($1450\text{-}1500\text{ cm}^{-1}$), D₄ (1200 cm^{-1}), G ($1580\text{-}1600\text{ cm}^{-1}$)^[27,28]. As described in the literature, the G and D₂ bands arise in graphitic lattices, while the D₁ band arises from the double-resonant disorder-induced mode^[28-31]. The D₃ band is usually due to the amorphous carbon content in the carbon, and the D₄ band is due to the presence of sp²-sp³ carbons or the stretching vibrations of C-C and C=C bonds^[28-31].

Table 1.1 - Intensity of the D and G bands of commercial carbons and their ratio.

CARBON	I_D	I_G	I_D/I_G
Maxsorb	0.94	0.74	1.27
Carbotech	0.96	0.75	0.97
Xintao	0.97	0.67	1.45
Norit	0.98	0.76	1.15

Carbon Xintao, having a higher ratio I_D/I_G , has a higher number of defects and is the most disordered carbon; while Carbon Carbotech has a lower ratio I_D/I_G among all, consequently it is the less disordered carbon among those analysed.

Defects in carbon materials can be intrinsic or extrinsic (Figure 4.6)^[32,33].

Intrinsic defects include *topological defects* (the presence of rings composed of a different number of carbons from 6, forming pentagons or heptagons), *edge defects* (the graphene layer structure may end in a zigzag or armchair geometry), *vacancies* (absence of C atoms)^[32,33]; extrinsic defects are caused by *complex defects* (in the end zones of the graphene layer there may be H atoms bonded to C atoms via σ -bonds, or functional groups that can change the surface properties of carbon materials), or by the presence of heteroatoms or active metal sites in the structure of the material^[32,33].

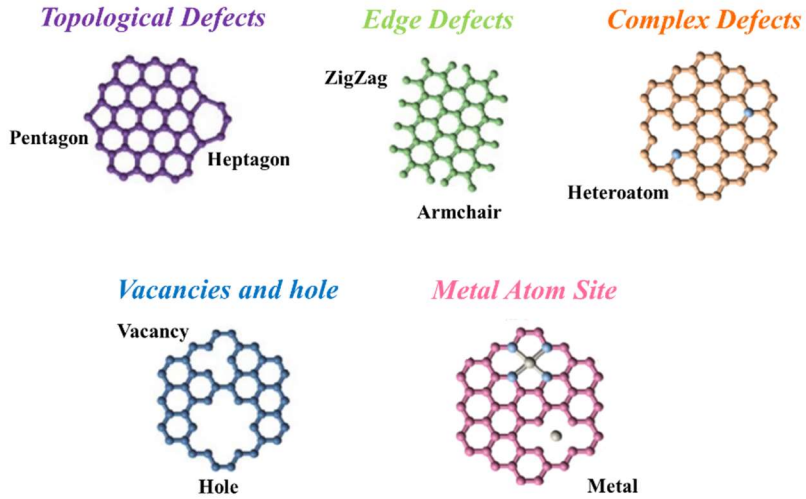
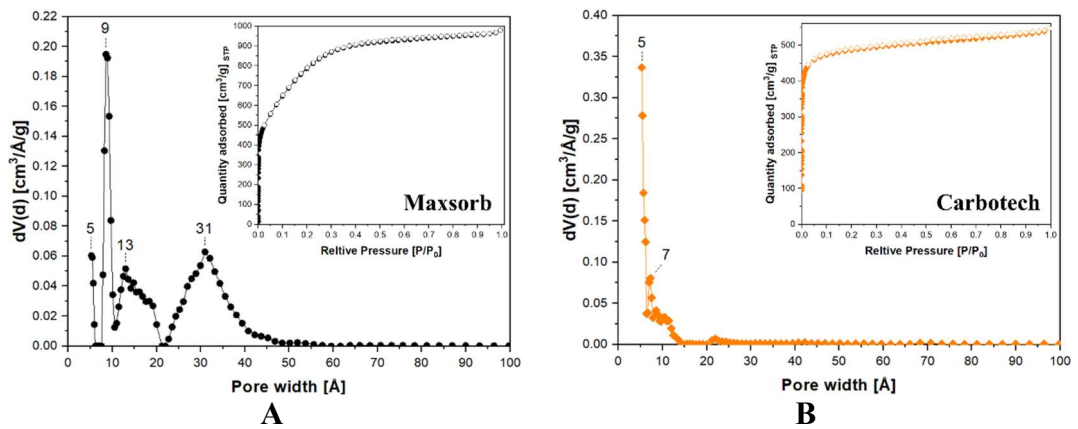


Figure 4.6 – Schematic illustration of the possible defects presents in the carbonous structure.
Adapted from^[33].

Textural properties of the porous carbons were determined by N₂ adsorption–desorption isotherms at 77 K. Results are reported in Figure 4.7.



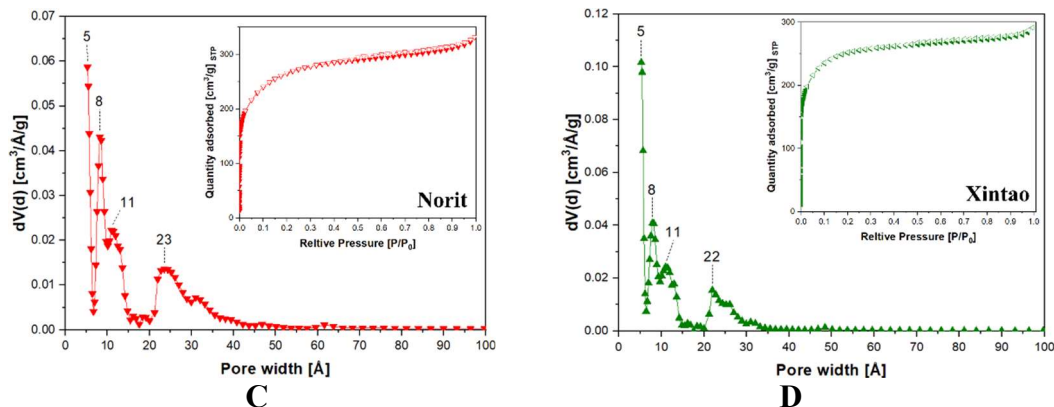


Figure 4.7- N_2 adsorption and desorption isotherms at 77K and pores size distribution of four commercial carbons: A) Maxsorb (\bullet), B) Carbotech (\blacklozenge), C) Norit (\blacktriangledown) and D) Xintao (\blacktriangleleft).

According to IUPAC classification, the physisorption isotherms of Maxsorb, Norit, and Xintao exhibit a mixed form between the type I isotherm (typical of microporous materials) and the type IV isotherm^[34]. Indeed, a hysteresis loop occurs suggesting that gas condensation has occurred within the mesoporosity. The Carbotech isotherm is associated with Type I.

This is consistent with the pore size distribution results calculated for all carbons using the Quenched Solid Density Functional Theory (QSDFT) model applied to slit/cylindrical pores, in the adsorption branch.

In fact, the pore distributions show that the Carbotech carbon has only two pore families in the micropore region, centered at 5 and 7 Å, while the other carbons have a four-modal distribution of pore sizes, mainly in the micropore region but also in the smaller mesopores. The distributions of pore dimensions of Maxsorb are centered at 5, 9, 13 and 31 Å, while those of Xintao and Norit are centered at 5, 8, 11 and 23 Å.

The detail of textural properties of all the porous carbons samples are reported in Table 4.2.

Table 4.2 - Textural properties of commercial porous carbons, assessed via N₂ physisorption analysis performed at 77 K.

Sample	SS_{ABET} (m²/g)	Total P_V (cc/g)	V_{microP} (20 Å) (cc/g)	V_{mesoP} (20-100 Å) (cc/g)
Maxsorb	2881	1.39	0.68	0.69
Carbotech	1928	0.76	0.66	0.08
Norit	962	0.46	0.26	0.17
Xintao	935	0.40	0.28	0.10

Maxsorb carbon has the largest surface area and pore volume of all the carbons tested. Its microporous volume is similar to that of Carbotech, while it has a mesoporous volume that is significantly larger than other carbons.

Carbotech turned out to be a totally microporous carbon.

Norit and Xintao carbons possess similar textural properties to each other. They are mainly microporous carbons with a small mesoporous volume.

4.3 Porous carbon derived from Hyper Cross-linked Polymers (HCPs)

One of the strategies to obtain activated carbons is to use a Hyper Cross-linked Polymer (HCP) as the starting porous precursor.

Several studies in the literature have revealed that porous carbon derived from HCPs shows great potential in gas adsorption^[35-38].

In this PhD work, it was chosen to use waste polystyrene as a starting aromatic monomer for both economic and recycling issues.

4.3.1 Hyper Cross-linked Polymers (HCPs)

Hyper Cross-linked polymers (HCPs) are a class of microporous hyper-crosslinked, nanoporous organic polymers that can be prepared from cheap organic monomers under reaction conditions that are easy to manage and control^[39].

First, second and third generation HCPs can be distinguished^[39].

Those of the *first-generation* were prepared for the first time in 1930s by Staudinger and Heuer, from a homogeneous gel copolymerized from styrene^[40]. A small percentage (5-8%) of divinylbenzene (DVB) was added as crosslinking agent^[41]; toluene or dichloroethane was used as nonpolar organic solvent^[39]. The obtained gel-like polystyrene was then functionalized with amine or sulfone groups to obtain an ion-exchange resin capable of swelling in water or very polar alcohols^[42]. However, the material obtained exhibited low permeability and low porosity.

The *second-generation* materials were first prepared by copolymerizing styrene with DVB (6-12%) in the presence of a miscible porogenic monomer^[43]; in this way, phase separation occurs, resulting in permanent porosity, although the resulting materials have a low surface area (20-300 m²/g) with macroporosity.

The *third-generation* allows for materials with a high degree of crosslinking, which are also called "Davankov resins" because they were first introduced in 1970 by Davankov and Tsyurupa^[44].

The synthesis of these HCPs is mainly based on the Friedel-Crafts alkylation chemistry which provides fast kinetics for forming strong bonds resulting in a highly cross-linked network with predominant porosity^[45].

Initially, the starting aromatic monomer/polymer (polystyrene is one of the most used) is dissolved in a solvent to allow the opening of the polymeric chains. Then, the cross-linker is added to the reaction mixture. The addition of the crosslinker to the polymer in its swollen state allows for a better crosslinked polymeric framework. Finally, by eliminating the solvent, a material is obtained which keeps its cross-linked bonds, resulting in a permanent porosity^[46] (Figure 4.8).

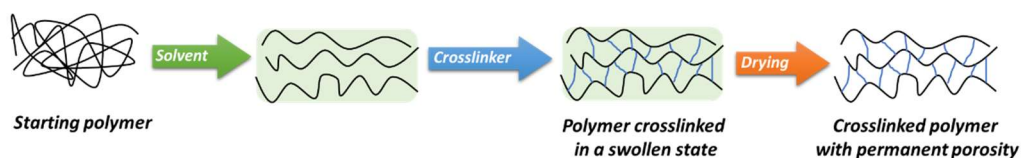


Figure 4.8 - Schematic representation of the hyper crosslinking process. Adapted from^[39].

The resulting materials are highly expansive and swellable, and possess extremely high surface areas (600-2000 m²/g) and a permanent porosity^[47].

The Friedel-Crafts alkylation reaction (Figure 4.9) is an electrophilic substitution reaction in which, on an aromatic ring, a hydrogen ion is replaced by a carbocation: benzene, or a derivative thereof, reacts with an alkyl halide (R-X), in the presence of a Lewis acid as catalyst, to form an alkylbenzene^[48,49].

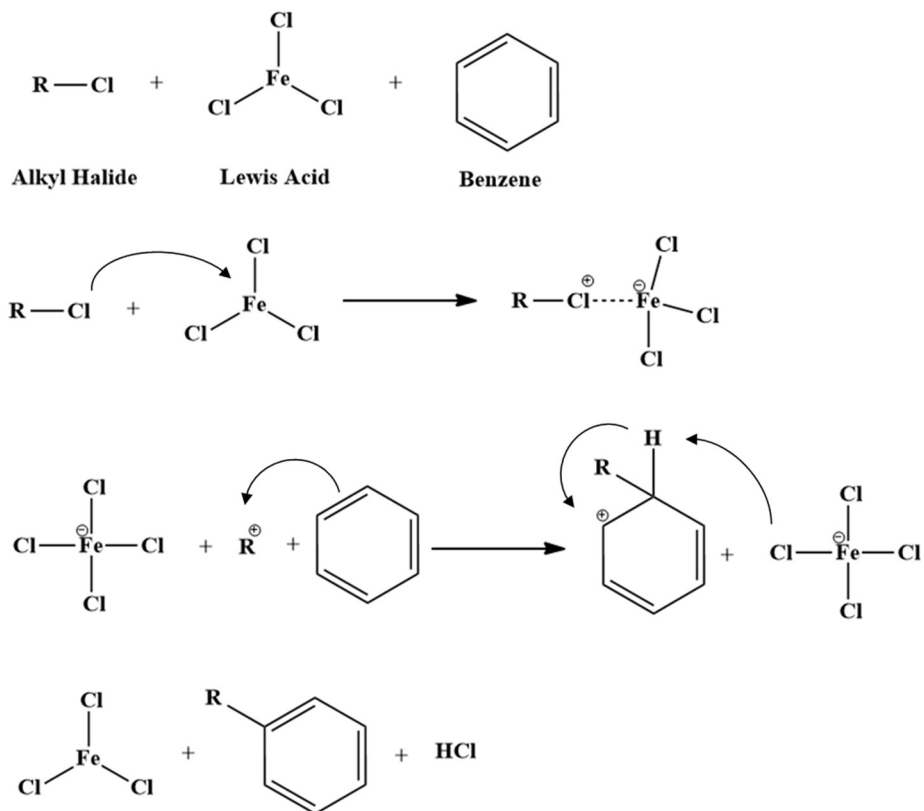


Figure 4.9 - Reaction mechanism of Friedel-Craft alkylation reaction. Adapted from^[48].

When the Lewis acid attacked the halogen atom of the alkyl halide, heterolysis between the C and the halogen takes place with the formation of the Lewis acid-base complex; this attack turns the halogen into a better leaving group.

The formed carbenium ion, being strongly electrophilic, reacts with the π electron cloud of the aromatic ring.

After that, a deprotonation of the formed intermediate takes place, which restores the catalyst, returning the final product and releasing a hydride (HCl or HBr).

Over the years, several modifications have been made to the Friedel Craft reaction in order to synthesize HCPs. For example, some of them use a different type of crosslinker (such as organochloride or dechlorinated alkanes)^[50–52].

4.3.1.1 Preparation methodology of HCP from polystyrene waste (HCP-PS)

The process for the preparation of a microporous carbon from a hyper-crosslinked polymer has been studied and patented by our research group^[53].

The following will firstly illustrate the preparation of the polymer, and then its transformation into the porous carbon.

Hyper cross-linked polymers (HCPs) were obtained through the Friedel-Crafts; expanded polystyrene (PS) is used as starting polymer, ferric chloride is used as a catalyst and formaldehyde dimethyl acetal (FDA) is used as a bridging agent (Figure 4.10)^[54]. The resulting materials were named HCP-PS.

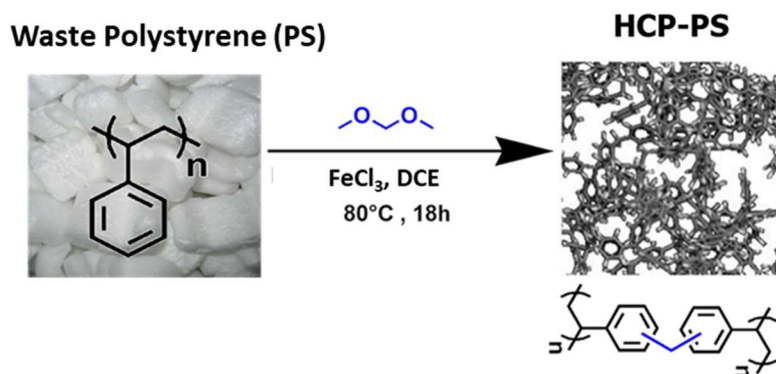


Figure 4.10 - Scheme of the synthesis of HCP, with Fidel-Craft reaction. Polystyrene is mixed with the catalyst (FeCl₃) with 1,2-dichloroethane; then, FDA is added dropwise.

In this case, a modified Friedel-Crafts alkylation reaction was used, which involves the use of formaldehyde dimethylacetal (FDA) as a cross-linking agent^[55,56,54].

The reaction mechanism differs from the classical Friedel-Crafts alkylation in that Lewis acid causes the FDA carbon-oxygen bond to split with subsequent formation of a carbocation (Figure 4.11).

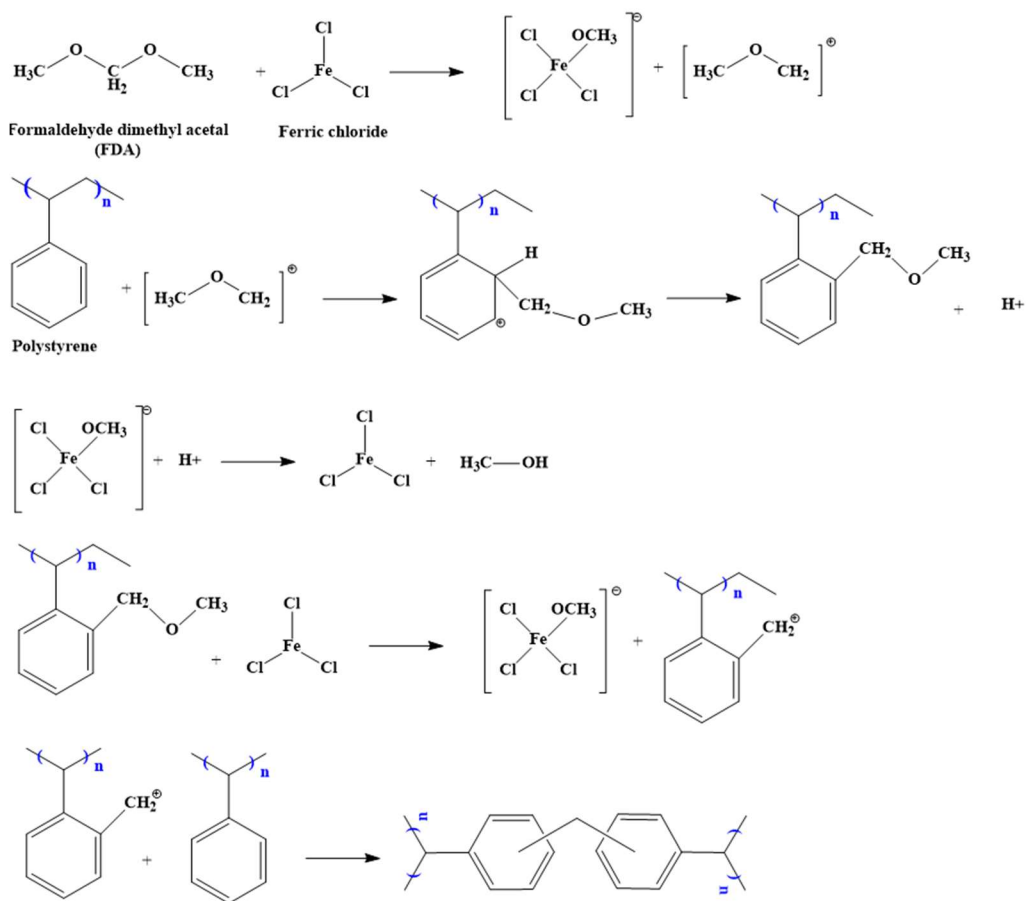


Figure 4.11 – Reaction scheme for the synthesis of hyper-crosslinked polymers (HCPs), starting from polystyrene. Adapted from^[57].

After having performed several synthetic tests, it was noticed that it is possible to use waste polystyrene as a starting aromatic monomer; consequently, it was chosen for both economic and recycling issues.

The ratio between polymer (PS) and the crosslinker/catalyst is 1:4, as it has been found in the literature that this is the best ratio to obtain an HCP with properties that provide excellent performance for CO₂ sequestration^[55].

4.3.2 Synthesis of HCP-PS

In a 250 mL three necked round bottom flask, 1.1 g of polystyrene flakes from recovery material (PS) were suspended in 100 mL of dichloroethane (DCE) at room temperature. After the complete dissolution of the polystyrene, 6.8 g of FeCl₃ were added to the flask. To obtain a homogeneous solution, the mixture was mechanically stirred for 20 minutes at room temperature. Then, 3.2 mL of Formaldehyde Dimethyl Acetal (FDA) were added dropwise to the reaction mixture, which is left under stirring at room temperature, for 30 minutes. The mixture is then heated at 80°C overnight, under nitrogen flux. The thick gel was allowed to cool to room temperature, after which it was washed several times with ethanol and water until a neutral pH was reached. Finally, a dark-colored powder is obtained, which is dried in an oven at 110 °C overnight. The obtained material obtained is named HCP-PS.

4.3.3 Characterization of HCP-PS

The synthesized materials were characterized by IR spectroscopy and N₂ physisorption analysis at 77 K to study their surface and textural properties.

Figure 4.12 shows the IR spectrum of the hyper-cross-linked polymer HCP-PS.

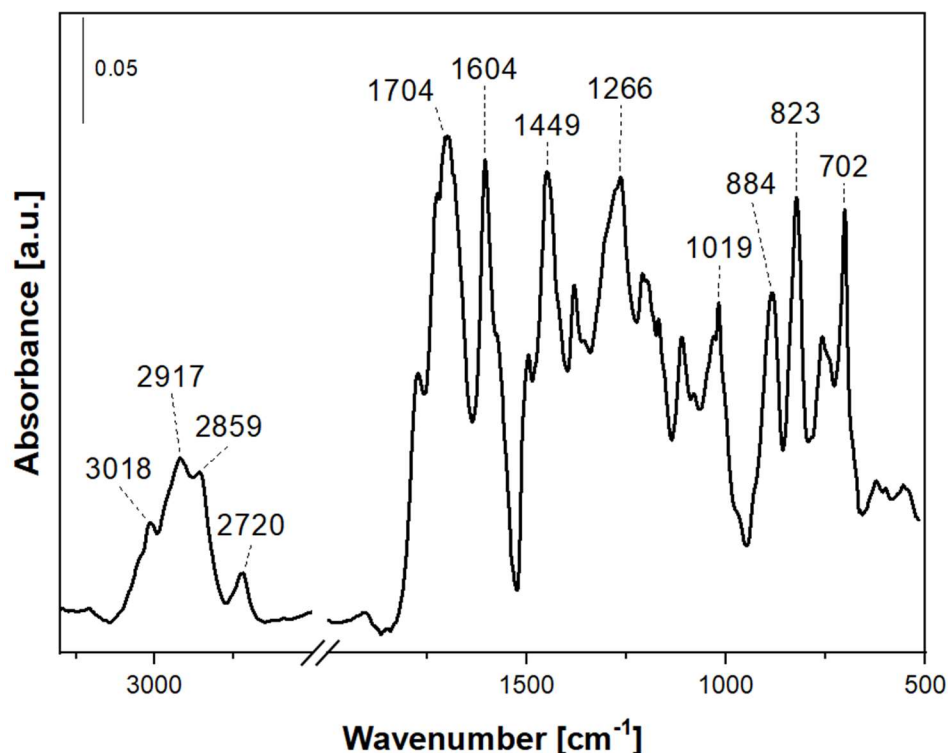


Figure 4.12 - FTIR spectrum of HCP-PS sample recorded at beam temperature an in vacuum ($1 \cdot 10^{-4}$ mbar).

The IR spectrum of HCP-PS present signals, at high frequencies, in the range between 3100 and 2700 cm^{-1} and, at low frequencies, in the range between 1800 and 500 cm^{-1} .

The high frequencies spectrum is dominated by signals at ca. 3018 cm^{-1} and between 2917-2720 cm^{-1} attributable, respectively, to the symmetric and asymmetric stretching modes of the aromatic and aliphatic -C-H groups, the latter linked to -CH₂- and -CH- groups^[55,58,59].

In the low frequency region multiple bands are found. The bands located between 1700-1266 cm^{-1} are due to the presence of vibrational stretching modes related to the presence of -C=C- groups (vibrations of the aromatic rings)^[55,58,59]. The bending

vibrations associated with the aromatic C-H groups are located in the region between 1290-1019 cm^{-1} , while the signals 884 and 823 cm^{-1} are attributable to breathing modes of the ortho and para-substituted aromatic ring, therefore associated with the formation of the polymeric network following the crosslinking reaction^[55,58,59].

Textural properties of HCP-PS were determined by N_2 physisorption analysis at 77 K (Figure 4.13).

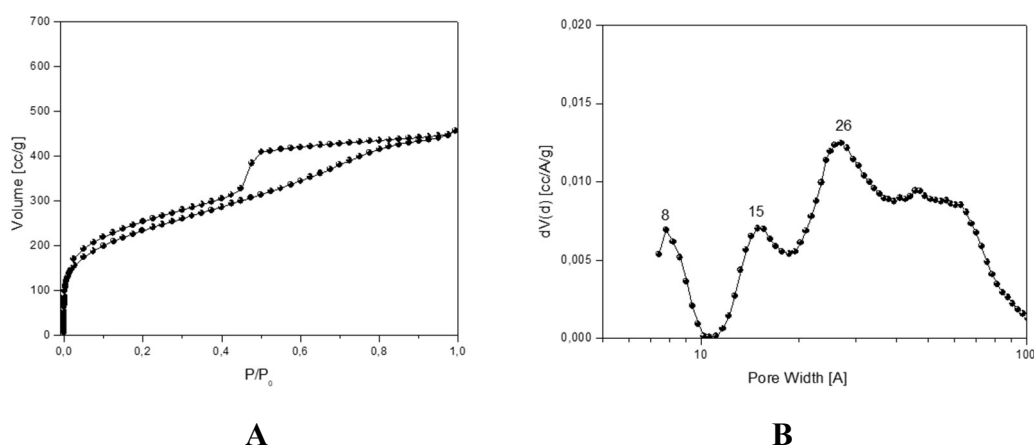


Figure 4.13 - A) N_2 adsorption and desorption isotherms at 77 K and B) pore size distribution of the HCP-PS sample.

The physisorption isotherm of HCP-PS sample (Figure 4.13A) can be classified as type IV, according to the IUPAC definition, presenting an H2-type hysteresis loop that indicates the presence of micro- and meso-porosity, and an interconnected pore network^[34]. During the desorption phase, it can be seen that the hysteresis loop presents a step at the pressure of 0.5 P/P_0 ; this indicates that there is almost complete desorption, over the time frame of the experiment, due to good channel interconnection^[60].

The presence of a hysteresis loop that remains open up to low pressures indicates that the structure of the material changes during the analysis, due to its flexibility.

The presence of a hysteresis loop that remains open up to low relative pressures indicates successful expansion of the polymer network^[34,61].

In Figure 4.13B families of pores ranging in size from 8-100 Å are visible, confirming the presence of micro- and meso-porosity. The specific surface area (SSA), calculated using the BET method, of the HCP-PS sample was equal to 845 m²/g, with a total pore volume of 0.67 cc/g.

4.3.4 Synthesis of Porous Carbon (C-PS) form HCP-PS

After the synthesis, the HCP-PS were activated via thermal and chemical treatments. We choose to use a pre-activation method, with KOH at high temperatures: 1.0 g of HCP-PS polymers was added to a solution 1M of KOH in EtOH (95% v/v in water), and stirred for 20 h at room temperature; The weight ratio between KOH and polymer was 1:4.

Subsequently, after drying the mixture at 50°C, it was placed in a crucible of alumina and thermally treated under N₂ flow up to 800 °C, with a ramp of 2°C/min, and then held under isothermal conditions for 1 h.

The resulting carbon (C-PS), after the chemical activation (Figure 4.14), was washed with deionized water (250 mL), to remove potassium salts, and neutralized with 2 M HCl (200 mL). Finally the carbon was dried at 110 °C for 18 h^[62].



Figure 4.14 - Scheme of the preparation treatment HCP-PS with KOH, to obtain porous carbon (C-PS).

4.3.5 Characterization of C-PS

Figure 4.15 shows the data related to the physisorption of N₂ conducted on the carbon sample C-PS.

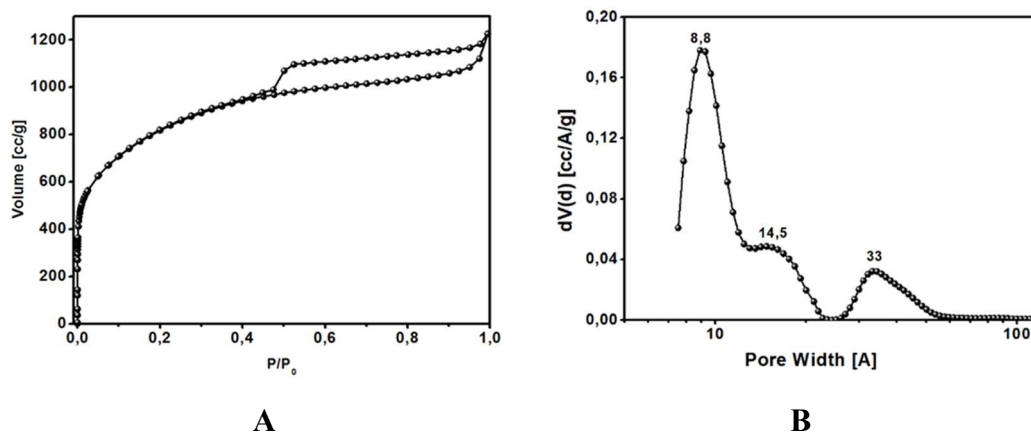


Figure 4.15 - A) N₂ adsorption and desorption isotherms at 77 K and B) pore size distribution of the C-PS sample.

The physisorption isotherm (Figure 4.15A) can be classified as a combination between type I (indicating the presence of micropores) and type IV (indicating the presence of mesopores), according to the IUPAC definition, as evidenced by the pore size distribution (Figure 4.15B)^[34].

The isotherm presents a hysteresis loop of type H4 that closes by cavitation at $P/P_0 \approx 0.49$, and it is typical of hierarchical carbons^[60]. During the desorption phase the hysteresis loop reduces dramatically at the pressure between 0.4-0.6 P/P_0 ; this indicates that there is good interconnection between the pore network within the material's framework on the time scale of the experiment^[60].

Pore families in the C-PS sample showed sizes ranging from 9-30 Å (Figure 4.15B). The SSA value, calculated by the BET method, is 2944 m²/g, with a total porous volume of 1.60 cc/g.

It is therefore evident that there is an excellent improvement in textural properties, in fact the carbons obtained (C-PS) have a much greater specific surface area and a

significantly larger pore volume than the starting HCP polymers (respectively, 845 m²/g and 0.67 cc/g); consequently, they could be more effective in gas capture applications.

Conclusions

In this chapter, four different commercially available porous carbons (Maxsorb, Carbotech, Norit and Xintao) were characterized using SEM techniques, Raman spectroscopy, and N₂ adsorption analysis, to investigate their physico-chemical properties.

Raman Spectroscopy showed that Carbon Xintao, having a higher ratio I_D/I_G, has a higher number of defects and is the most disordered carbon; while Carbon Carbotech, having a lower ratio I_D/I_G, it is the less disordered carbon among those analysed.

Maxsorb carbon has the largest surface area (2881 m²/g) and pore volume (1.39 cc/g) of all the carbons tested. Carbotech turned out to be a totally microporous carbon, with a large presence of micropores in its structure (0.66 cc/g).

Norit and Xintao carbons possess similar textural properties to each other, shown a specific surface area of 962 and 935 m²/g and a total pore volume of 40 cc/g and 46 cc/g, respectively.

In addition, a synthetic method to obtain a high-performance porous carbon from a Hyper Cross-linked Polymer (HCP) was presented, since one of the strategies to obtain activated carbons with excellent textural properties is to use a Hyper Cross-linked Polymer (HCP) as the starting porous precursor.

HCPs are a class of microporous hyper-crosslinked organic polymers, obtained using the Friedel-Crafts reaction from polystyrene.

Also in this case, both the starting material (HCP-PS) and the final carbon (C-PS) were characterized to study their surface and textural properties.

Infrared analysis of the HCP sample showed the presence of bands due to stretching vibrations of aliphatic and aromatic carbons, as well as bands related to the formation of the polymer network as a consequence of the crosslinking reactions.

Physisorption analysis of HCP reveals the presence of micro- and mesoporosity. The material exhibits a flexible structure, as evidenced by the shape of the hysteresis loop, which remains open even at low relative pressures.

The porous carbon resulting from the carbonization of the HCP loses the flexibility of the starting material, but significantly increases both the porous volume and the specific surface area.

In fact, from a starting polymer with a surface area of 845 m²/g and a total pore volume of 0.67 cc/g, a porous carbon with greatly improved textural properties was obtained, having a surface area of 2944 m²/g and a total pore volume of 1.60 cc/g.

References

- [1] K. Dujearic-Stephane, M. Gupta, A. Kumar, V. Sharma, S. Pandit, P. Bocchetta, Y. Kumar, *J. Compos. Sci.* **2021**, *5*, 66.
- [2] *IJASRE* **2018**, DOI 10.7324/IJASRE.2018.32615.
- [3] J. Lee, J. Kim, T. Hyeon, *Adv. Mater.* **2006**, *18*, 2073–2094.
- [4] Y. X. Gan, *C* **2021**, *7*, 39.
- [5] O. Boujibar, F. Ghamouss, A. Ghosh, O. Achak, T. Chafik, *Journal of Power Sources* **2019**, *436*, 226882.
- [6] D. B. Schuepfer, F. Badaczewski, J. M. Guerra-Castro, D. M. Hofmann, C. Heiliger, B. Smarsly, P. J. Klar, *Carbon* **2020**, *161*, 359–372.
- [7] G. Centi, S. Perathoner, *ChemSusChem* **2011**, *4*, 913–925.
- [8] E. F. Sheka, Ye. A. Golubev, N. A. Popova, *Fullerenes, Nanotubes and Carbon Nanostructures* **2021**, *29*, 107–113.
- [9] A. C. Ferrari, J. Robertson, *Phys. Rev. B* **2000**, *61*, 14095–14107.
- [10] J. Laine, A. Calafat, M. Labady, *Carbon* **1989**, *27*, 191–195.
- [11] L. Borchardt, Q.-L. Zhu, M. E. Casco, R. Berger, X. Zhuang, S. Kaskel, X. Feng, Q. Xu, *Materials Today* **2017**, *20*, 592–610.
- [12] A. Mohammad-Khah, R. Ansari, **n.d.**, 6.
- [13] Y. Sudaryanto, S. B. Hartono, W. Irawaty, H. Hindarso, S. Ismadji, *Bioresource Technology* **2006**, *97*, 734–739.
- [14] J. Zhou, A. Luo, Y. Zhao, *Journal of the Air & Waste Management Association* **2018**, *68*, 1269–1277.
- [15] S. J. Allen, L. Whitten, G. McKay, *Dev. Chem. Eng. Mineral Process.* **2008**, *6*, 231–261.
- [16] I. Yang, M. Jung, M.-S. Kim, D. Choi, J. C. Jung, *J. Mater. Chem. A* **2021**, *9*, 9815–9825.
- [17] N. A. Rashidi, S. Yusup, *Journal of CO2 Utilization* **2016**, *13*, 1–16.

- [18] O. Oginni, K. Singh, G. Oporto, B. Dawson-Andoh, L. McDonald, E. Sabolsky, *Bioresource Technology Reports* **2019**, 7, 100266.
- [19] T. S. Hui, M. A. A. Zaini, *Carbon letters* **2015**, 16, 275–280.
- [20] T. K. Bose, R. Chahine, J.-M. St-Arnaud, *High-Density Adsorbent and Method of Producing Same*, **1991**, US4999330A.
- [21] Puech, Kandara, Paredes, Moulin, Weiss-Hortala, Kundu, Ratel-Ramond, Plewa, Pellenq, Monthieux, *C* **2019**, 5, 69.
- [22] D. Sfyris, G. I. Sfyris, C. Galiotis, **2017**.
- [23] T. Livneh, T. L. Haslett, M. Moskovits, *Phys. Rev. B* **2002**, 66, 195110.
- [24] A. Lazzarini, A. Piovano, R. Pellegrini, G. Leofanti, G. Agostini, S. Rudi, M. R. Chierotti, R. Gobetto, A. Battiato, G. Spoto, A. Zecchina, C. Lamberti, E. Groppo, *Catalysis Science & Technology* **2016**, 6, 13.
- [25] F. Rosenburg, E. Ionescu, N. Nicoloso, R. Riedel, *Materials* **2018**, 11, 93.
- [26] N. Shimodaira, A. Masui, *Journal of Applied Physics* **2002**, 92, 902–909.
- [27] A. Croce, G. Re, C. Bisio, G. Gatti, S. Coluccia, L. Marchese, *Res Chem Intermed* **2021**, 47, 419–431.
- [28] B. Manoj, *Russ. J. Phys. Chem.* **2015**, 89, 2438–2442.
- [29] A. Kaniyoor, S. Ramaprabhu, *AIP Advances* **2012**, 2, 032183.
- [30] B. Manoj, A. G. Kunjomana, *Russ J Appl Chem* **2014**, 87, 1726–1733.
- [31] I. K. Moon, J. Lee, R. S. Ruoff, H. Lee, *Nat Commun* **2010**, 1, 73.
- [32] Q. Wu, X. Yan, Y. Jia, X. Yao, *EnergyChem* **2021**, 3, 100059.
- [33] D. Xue, H. Xia, W. Yan, J. Zhang, S. Mu, *Nano-Micro Lett.* **2021**, 13, 5.
- [34] M. Thommes, K. Kaneko, A. V. Neimark, J. P. Olivier, F. Rodriguez-Reinoso, J. Rouquerol, K. S. W. Sing, *Pure and Applied Chemistry* **2015**, 87, 1051–1069.
- [35] C. Zhang, R. Kong, X. Wang, Y. Xu, F. Wang, W. Ren, Y. Wang, F. Su, J.-X. Jiang, *Carbon* **2017**, 114, 608–618.
- [36] A. Modak, A. Bhaumik, *Journal of Solid State Chemistry* **2015**, 232, 157–162.
- [37] X. Yang, M. Yu, Y. Zhao, C. Zhang, X. Wang, J.-X. Jiang, *J. Mater. Chem. A* **2014**, 2, 15139–15145.

- [38] R. Vinodh, A. Abidov, M. M. Peng, C. M. Babu, M. Palanichamy, W. S. Cha, H.-T. Jang, *Journal of Industrial and Engineering Chemistry* **2015**, *32*, 273–281.
- [39] J. Huang, S. R. Turner, *Polymer Reviews* **2018**, *58*, 1–41.
- [40] H. Staudinger, W. Heuer, *Ber. dtsh. Chem. Ges. A/B* **1934**, *67*, 1159–1164.
- [41] A. G. F. D, *Production of Synthetic Polymeric Compositions Comprising Sulphonated Polymerizates of Poly-Vinyl Aryl Compounds and Treatment of Liquid Media Therewith*, **1944**, US2366007A.
- [42] I. M. Abrams, J. R. Millar, *Reactive and Functional Polymers* **1997**, *35*, 7–22.
- [43] C. H. Mcburney, *Resinous Insoluble Reaction Products of Tertiary Amines with Haloalkylated Vinyl Aromatic Hydrocarbon Copolymers*, **1952**, US2591573A.
- [44] V. Davankov, V. Rogozhin, M. Tsjurupa, *Macronet Polystyrene Structures for Ionites and Method of Producing Same*, **1973**, US3729457A.
- [45] Z.-Y. Duan, Y.-Y. Wang, Q.-W. Pan, Y.-F. Xie, Z.-Y. Chen, *Chin J Polym Sci* **2022**, *40*, 310–320.
- [46] J. Germain, J. M. J. Fréchet, F. Svec, *J. Mater. Chem.* **2007**, *17*, 4989.
- [47] J. Germain, J. M. J. Fréchet, F. Svec, *Small* **2009**, *5*, 1098–1111.
- [48] M. M. Heravi, V. Zadsirjan, in *Recent Applications of Selected Name Reactions in the Total Synthesis of Alkaloids*, Elsevier, **2021**, pp. 59–105.
- [49] M. Rueping, B. J. Nachtsheim, *Beilstein J. Org. Chem.* **2010**, *6*, DOI 10.3762/bjoc.6.6.
- [50] R. Dawson, E. Stöckel, J. R. Holst, D. J. Adams, A. I. Cooper, *Energy Environ. Sci.* **2011**, *4*, 4239.
- [51] A. Krusenbaum, J. Geisler, F. J. L. Kraus, S. Grätz, M. V. Höfler, T. Gutmann, L. Borchardt, *Journal of Polymer Science* **2022**, *60*, 62–71.
- [52] D. G. Barar, K. P. Staller, N. A. Peppas, *Ind. Eng. Chem. Prod. Res. Dev.* **1983**, *22*, 161–166.

- [53] L. Marchese, M. Errahali, G. Gatti, L. Tei, M. Cossi, D. Valtolina, *A Method of Preparing a Microporous Carbon and the Microporous Carbon Thereby Obtained*, **2017**, EP3421126.
- [54] G. Gatti, M. Errahali, L. Tei, E. Mangano, S. Brandani, M. Cossi, L. Marchese, *Nanomaterials* **2019**, *9*, 726.
- [55] M. Errahali, G. Gatti, L. Tei, G. Paul, G. A. Rolla, L. Canti, A. Fraccarollo, M. Cossi, A. Comotti, P. Sozzani, L. Marchese, *J. Phys. Chem. C* **2014**, *118*, 28699–28710.
- [56] Z. Jia, J. Pan, D. Yuan, *ChemistryOpen* **2017**, *6*, 554–561.
- [57] H. Masoumi, A. Ghaemi, H. Gannadzadeh Gilani, *Journal of Hazardous Materials* **2021**, *416*, 125923.
- [58] G. Socrates, G. Socrates, *Infrared and Raman Characteristic Group Frequencies: Tables and Charts*, Wiley, Chichester ; New York, **2001**.
- [59] J. Coates, in *Encyclopedia of Analytical Chemistry* (Ed.: R.A. Meyers), John Wiley & Sons, Ltd, Chichester, UK, **2006**, p. a5606.
- [60] K. A. Cychoz, R. Guillet-Nicolas, J. García-Martínez, M. Thommes, *Chem. Soc. Rev.* **2017**, *46*, 389–414.
- [61] G. Gatti, D. F. Olivás Olivera, G. Paul, R. Bagatin, A. Carati, M. Tagliabue, C. Bisio, L. Marchese, *Dalton Trans.* **2019**, *48*, 11781–11790.
- [62] G. Gatti, M. Errahali, L. Tei, M. Cossi, L. Marchese, *Polymers* **2019**, *11*, 588.

Chapter 5

Prototypes for gas adsorption measurements

Introduction

As part of the two projects pursued during the work of this PhD thesis, the SATURNO project and the collaboration with Ecospray Technologies, it was necessary to measure the gas adsorption capacities the selected materials described in previous chapters.

To this end, two prototypes were built to track the adsorption measurements.

Specifically, one prototype was designed to perform static measurement in order to obtain adsorption isotherms of single gas (mainly CO₂, CH₄ and N₂) for the evaluation of the excess adsorption capacities of the selected materials. This step was particularly interesting to have a screening of the different adsorption capacities of solids of interest of the PhD work.

A second apparatus was built in order to perform dynamic measurements by exposing the adsorbents to a gas flow, composed by a mixture of CH₄ and N₂.

The SATURNO project concerns to test the adsorption performances towards CO₂ of porous carbons (C-PS) made from hyper cross-linked polymers (HCPs) and selected commercial carbons at an equilibrium pressure of 1 bar.

The aim of the collaboration with Ecospray Technologies was to test the performances of commercial carbons and a commercial zeolite to separate methane from a binary gas mixture of methane and nitrogen (in defined proportions) under flow conditions.

First, the volumetric prototype was used to evaluate the storage capacity of the materials with respect to individual gases (CH₄ and N₂) to assess their affinity.

Then, a second prototype was built and coupled with a mass spectrometer to investigate the separation capacity of the two gases in the mixture under flow conditions.

5.1 Volumetric apparatus for gas adsorption in static conditions

A schematic view and a picture of the volumetric prototype built in the frame of the PhD thesis is reported in Figure 5.1.

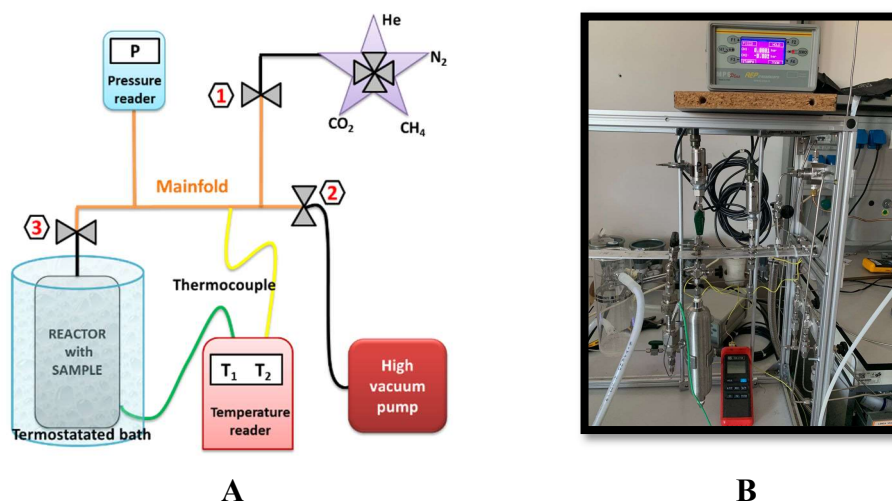


Figure 5.1 – A) Scheme and B) photo of the prototype built for gas storage measurements.

This system is composed of a stainless-steel vacuum line, allowing to operate in a wide pressure range (from 0-100 bar). The system consists of a *five-way valve* that allows the selected gas to be sent in a reserve (*manifold*), a *pressure head* (Pressure Transducer TP14 - AEP Transducer)^[1] and a digital indicator for reading pressure up to 100 bar (MP6 Plus – AEP Transducer)^[1], and a *reactor* hosting the material to be studied. All metal components were purchased from Nordival Srl -Swagelok^[2]. The whole system is connected to a vacuum pump (HiCube 80 Eco – Pfeiffer Vacuum)^[3].

Finally, two thermocouples are connected to the gas reserve and the cell.

To allow the experiment to be performed at isothermal conditions, the cell is placed a thermostatic bath (Circulator bath SBF15 – Falc Instruments)^[4].

Before the measurements, the material can be activated by thermal treatments in vacuum conditions, using a heating band placed around the reactor, to remove physisorbed species. Details on the activation treatments are given in Chapters 6.

5.1.1 Calibration of the components of the system

After the prototype was assembled, it was necessary to calibrate the volumes of all the components. The assessment of the void volumes of the apparatus was performed via the dosing and expansion of gas/helium in the desired volumes.

Initially, the empty reactor is connected to the reserve opening Valve 3, and the whole system is put under vacuum (10^{-4} bar), by open Valve 2.

Then a first measurement is made with helium:

- About 1 bar of He is sent into the reactor-reserve system, opening Valve 1, and a pressure P_0 is recorded:

$$P_0 = P_{Reactor+Manifold} ;$$

- Through the closing of Valve 3 the reactor is isolated from the reserve area, and a second equilibrium pressure P_1 is recorded:

$$P_1 = P_{Reactor} = P_{Manifold};$$

- keeping the reactor closed, the helium contained in the reserve is emptied completely by means of the vacuum pump (opening Valve 2);
- then, by opening the connection valve (Valve 3), the helium contained in the reactor in the reserve is expanded, and a new pressure P_2 is recorded:

$$P_2 = P_{(Reactor+Manifold)}.$$

This procedure is repeated 5 times, to obtain average values of P_0 , P_1 and P_2 .

Table 5.1 shows an example of the pressure values obtained for the first stage of the calibration of the apparatus.

Table 5.1 – Pressure values obtained during the system calibration.

	P_0 (R+M)	P_1 (R=M)	P_2 (R+M) _{eq}
	(bar)	(bar)	(bar)
1	1.0000	0.9996	0.5100
2	1.0002	1.0000	0.5103
3	1.0001	0.9999	0.5102
4	0.9999	0.9998	0.5102
5	1.0001	1.0000	0.5105
Average	1.0001 ± 0.0001	0.9999 ± 0.0002	0.5102 ± 0.0002

After this first measurement, the reactor is filled with metal spheres (*calibration spheres*) of different diameters (from 1.966 to 3.513 ± 0.0001 mm). The reactor is then connected to the reserve and the whole system is put again under vacuum. The same previous procedure is repeated, using helium, obtaining pressure values defined as P'_0 , P'_1 and P'_2 .

Table 5.2 shows an example of the pressure values obtained for the second stage of system calibration.

Table 5.2 – Pressure values obtained during the system calibration, filled with the calibration spheres.

	P'_0 (R+M)	P'_1 (R=M)	P'_2 (R+M) _{eq}
	(bar)	(bar)	(bar)
1	0.9996	0.9992	0.4814
2	1.0002	1.0001	0.4821
3	1.0005	1.0003	0.4823
4	1.0003	1.0001	0.4825

5	1.0003	1.0001	0.4825
Average	1.0002 ± 0.0003	1.0000 ± 0.0004	0.4822 ± 0.0005

After the second measurement, the diameters of all the spheres are calculated with a calibre.

Finally, the total volume occupied by the metal spheres (V_{cal}) is calculated with the formula:

$$V_{cal} = \sum_n \pi \left(\frac{d^3}{6} \right)$$

where d is the diameter of the sphere, and n is the number of spheres used for the calibration.

Knowing the values of P_1, P_2, P'_1, P'_2 and V_{cal} , it is possible to calculate the reactor and reserve volumes using the following formulas^[5]:

$$A) \quad V_{Manifold} = \frac{V_{cal}}{\left[\left(\frac{P_1}{P_2} \right) - 1 \right] - \left[\left(\frac{P'_1}{P'_2} \right) - 1 \right]}$$

$$B) \quad V_{Reactor} = \frac{V_{cal}}{1 - \left[\frac{1 - \left(\frac{P_1}{P_2} \right)}{1 - \left(\frac{P'_1}{P'_2} \right)} \right]}$$

Table 5.3 shows an example of the value of the volume of manifold and reactor obtained from the calibration.

Table 5.3 – Determined values used to calculate the manifold and reactor volume of the prototype system.

P_1 (bar)	P_2 (bar)	P'_1 (bar)	P'_2 (bar)	V_{cal} (cm ³)	V_M (cm ³)	V_R (cm ³)
0.9999	0.5102	1.0000	0.4822	0.8206	7.397	7.708

5.1.2 Operating method for adsorption measurements

After the calibration of the volumes of the apparatus, adsorption measurements can be performed to obtain adsorption isotherms.

The reactor is filled with the material which is outgassed under vacuum conditions at target temperature which depends on the thermal stability of the adsorbent; during the actual adsorption measurements it is maintained at a constant temperature by means of a thermostatic bath.

To obtain the adsorption isotherm, dosing steps with increasing gas pressure are required. First, a certain known gas pressure is passed over the sample; after waiting for a certain adsorption equilibrium time, the pressure change after adsorption is recorded. In this way, the so-called *excess adsorption* can be determined, i.e. the difference between the amount of gas in the system and the amount that would be present at the same temperature and pressure without adsorption^[6].

The adsorption measurement can be divided into various operational steps, which will be explained in detail below:

1. *Thermal activation of the sample*

The reactor, filled with a approximately 0.5 g of material (g_{sample}) is connected to the reserve, and a vacuum is created throughout the system (opening Valve 2 and Valve 3).

The material is heated to a high temperature (which depends on the type of material to be treated), in the range between 80-200 °C, by placing a heating band around the reactor, and kept under vacuum for at least 8 hours; this allows to activate the material by eliminating the molecules physisorbed on his surface.

2. Calibration of the cell volume containing the sample

To know the available empty volume of the reactor after introduction of the sample, a helium calibration measurement is performed.

After closing Valve 2, helium is sent into the reactor-reserve portion of the apparatus, and a pressure P_0 is recorded: $P_0 = P_{Reactor+Manifold}$. Then, through Valve 3, the reactor is isolated from the reserve area, and a second equilibrium pressure P_1 is recorded: $P_1 = P_{Reactor} = P_{Manifold}$.

Keeping the reactor isolated, the helium contained in the reserve is emptied completely by means of the vacuum pump (opening Valve 2). Finally, by closing Valve 2 and opening the connection valve (Valve 3), the helium contained in the reactor in the reserve is expanded, and a new pressure P_2 is recorded: $P_2 = P_{(Reactor+Manifold)}$.

Assuming the constant temperature, it is now possible to calculate the new cell volume, using the following equation:

$$P_{1(Reactor)} \cdot V_{(Reactor+Sampl)} = P_{2(Reactor+Manifold)} \cdot (V_{(Reactor)} + V_{(Manifold)})$$

By rearranging the equation, it obtains:

$$V_{(Reactor+Sampl)} = \left[\frac{P_{2(Reactor+Manifold)} \cdot V_{(Reactor)}}{P_{1(Reactor)} - P_{2(Reactor+Manifold)}} \right]$$

3. Gas adsorption

Once the desired vacuum conditions are achieved, it is possible to start the adsorption experiment.

A certain pressure of gas (a few mbar) is sent to the manifold. The exact gas pressure (P_M) and temperature (T_M) in the manifold area are recorded.

Thanks to the NIST database of thermophysical properties of gasses and fluids (National Institute of Standards and Technology)^[7], it is possible to obtain the density of the gas (ρ_M) at the desired conditions of temperature and pressure.

Then, the Valve 3 is opened, thus allowing the expansion of the gas into the cell

An equilibrium time is waited (about 15 min), and the equilibrium pressure between the cell and the reserve area ($P_{(R=M)eq}$), the reactor temperature (T_{Req}) and the manifold temperature (T_{Meq}) are recorded.

Again, through the site of the NIST, by inserting the values of temperature and pressure, it is possible to obtain the density of the gas in those conditions, both in reactor area (ρ_{Req}) and in the manifold area (ρ_{Meq}).

4. Calculation of the gas adsorbed quantity

It is now possible to calculate the quantity of gas adsorbed (excess adsorption) after the first gas adsorption step; it is calculated as moles adsorbed ($mol_{(ads)}$) on a gram of material (g_{sample}) using the following formula:

$$\frac{mo_{(ads)}}{g_{sample}} = \frac{\left[V_M \cdot \frac{(\rho_M - \rho_{Meq})}{10^6} \right] - \left[V_{(Reactor+Sample)} \cdot \frac{(\rho_{Req})}{10^6} \right]}{g_{(Sample)}}$$

After closing Valve 2, one proceeds to carry out successive gas deliveries, increasing the pressure of the gas sent at each step.

It is possible to calculate the total amount (Q_{ads}) in moles, adsorbed per gram of material.

$$\frac{mol(ads)}{g_{sample}} = \frac{mol(ads)}{g_{sample} \text{ (previous pt)}} + \frac{\left[V_M \cdot \frac{(\rho_M - \rho_{M_{eq}})}{10^6} \right] - \left[V_{(R+S)} \cdot \frac{(\rho_{Req} - \rho_{Req(prev pt)})}{10^6} \right]}{g(Sample)}$$

The amount of gas adsorbed can then also be expressed as grams of gas adsorbed per kg of adsorbent material, knowing the molecular weight of the gas under consideration.

Table 5.4 shows, as an example, the data obtained for a methane adsorption measurement on a commercial carbon.

Table 5.4 - Values of pressure, temperature, density and adsorbed amount recorded during a methane adsorption measurement on a commercial carbon.

P_M (bar)	T_M (°C)	ρ_M (mol/m ³)	$P_{(R=M)_{eq}}$ (bar)	$T_{M_{eq}}$ (°C)	$T_{R_{eq}}$ (°C)	$\rho_{M_{eq}}$ (mol/m ³)	$\rho_{R_{eq}}$ (mol/m ³)	Q_{ads} (mol/kg)	Q_{ads} (g/kg)
0.0303	24.8	1.2232	0.0137	24.8	25.0	0.55303	0.55266	0.002	0.025
0.0502	24.7	2.0273	0.0298	24.6	25.0	1.20380	1.20220	0.00	0.066
0.0802	24.5	3.2411	0.0516	24.5	25.0	2.08520	2.08170	0.01	0.134
0.1002	24.4	4.0509	0.0723	24.4	25.0	2.92280	2.91690	0.01	0.207
0.1501	24.4	6.0687	0.1051	24.3	25.0	4.25040	4.24040	0.02	0.333
0.2501	24.3	10.117	0.1662	24.2	25.0	6.7244	6.7063	0.04	0.568
0.3502	24.2	14.1740	0.2445	24.2	24.9	9.8937	9.8671	0.05	0.849
0.5000	24.2	20.242	0.3544	24.2	25.0	14.344	14.305	0.08	1.21
0.7502	24.2	30.384	0.5249	24.1	24.9	21.258	21.200	0.11	1.76
1.0000	24.1	40.532	0.7251	23.9	24.9	29.396	29.297	0.16	2.53

2.4998	23.9	101.660	1.3382	24.9	24.7	54.126	54.162	0.56	8.96
5.104	24.9	207.79	2.360	25.2	24.8	90.49	90.61	1.50	24.1
10.034	25.4	411.28	4.630	25.4	24.8	188.02	188.41	2.72	43.7
15.403	25.5	637.00	8.093	25.1	24.9	330.96	331.20	4.22	67.7
20.048	25.2	836.72	12.156	24.9	24.9	501.18	501.00	5.60	89.8
30.301	25.4	1286.20	18.690	24.8	24.9	779.38	779.09	7.25	116.2
50.593	25.0	2226.60	31.020	24.5	24.9	1323.20	1321.00	9.25	148.3
100.03	24.9	4741.20	59.500	24.5	25.0	2663.70	2657.30	12.04	193.1
100.00	24.7	4745.20	76.000	24.4	25.0	3494.30	3483.20	13.29	213.2

Using this prototype, adsorption isotherms can be obtained, up to high pressures. Figure 5.2 shows, as an example, the isotherm obtained by sending CH₄ onto a commercial carbon. The amount adsorbed is expressed as gram of adsorbed gas per kg of material.

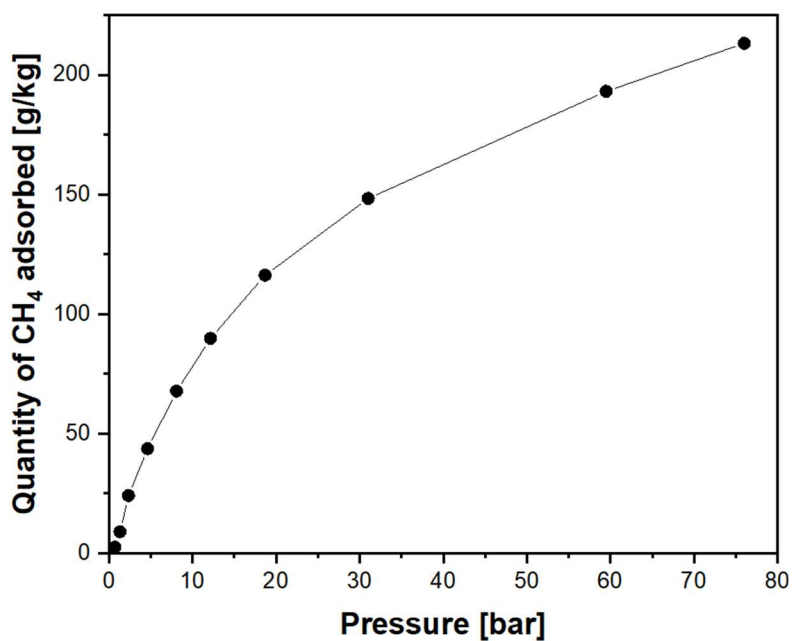


Figure 5.2 – Example of an adsorption isotherm, obtained by sending CH₄ on a commercial carbon, using the prototype volumetric apparatus for static measurements.

5.1.3 Validation of measurements

In order to validate the measurements made with the constructed prototype, two isotherms of the same commercial carbon were recorded under the identical measurement conditions (Figure 5.3): the first one was carried out with the prototype system (performed by UniUPO), the second one in the laboratories of the University of Turin (UniTO) with an automated system (Micromeritics).

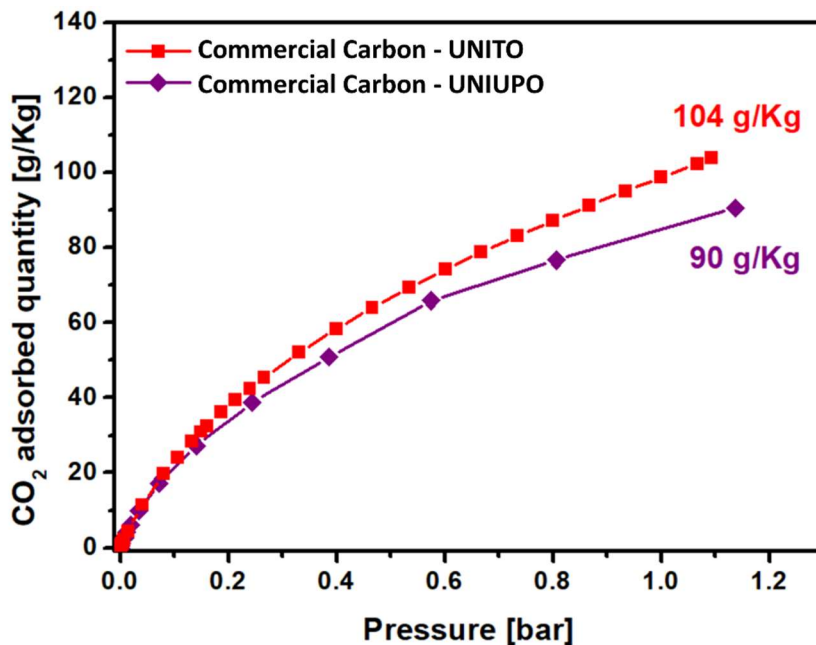


Figure 5.3 – CO₂ adsorption isotherms, recorded at 25°C, of a commercial carbon, performed on both the manual system of UniUPO (♦) and the automatic system of UniTO (■).

As observed in Figure 5.3, the isotherm recorded by automatic system exhibits adsorption that is about 15% greater than the measurement recorded by the prototype system.

This evidence suggests that the measurements made with the prototype underestimate the actual adsorptive capacity of the materials tested, especially at high pressure.

This can be explained by the fact that it is difficult to achieve thermodynamic equilibrium with the manual system, as, by necessity, adsorption measurements were made over the course of a day.

However, because the system similarly underestimates the adsorption capacities of the tested materials, it is still useful to conduct an initial screening of their gas storage performances.

5.2 Volumetric apparatus for adsorption measurements in flow conditions

To evaluate the adsorption performance of the materials under flow conditions, a second prototype was designed and built. This system (Figure 5.4).was also coupled to a mass spectrometer (GC/MSD 5975 C - Agilent Technologies)^[8].

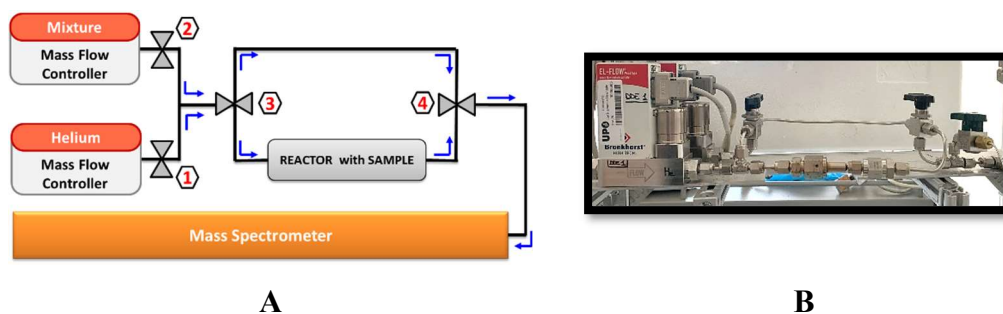


Figure 5.4 – Scheme (A) and photo (B) of prototype built for adsorption measurements in gas flow, coupled with a mass spectrometer.

By using this prototype, it is possible to introduce a constant stream of a binary gas mixture (methane and nitrogen), of known composition, into a reactor containing the material to be tested. This allows to obtain a chromatogram showing the variation of the flow concentration; the chromatogram allows to evaluate the capacity of the material to selectively adsorb one of the two components of the mixture, hence it is possible to determine the selectivity towards one of the two gas components.

The prototype consists of two mass flow controllers (EL-FLOW prestige - Bronkhorst)^[9], one for the controlled delivery of He, and the other for the controlled delivery of the mixture of gases; they are connected to a main line via valves (Valve 1 for He, and Valve 2 for gas mixture); Valve 3 can be used to determine the direction of the flow: it can be directed either into a main line that carries the flow into the reactor (where the sample under tested is placed) or into a secondary line that

bypasses the reactor. Through both lines, the flow reaches the mass spectrometer via Valve 4. All valves and metal components were purchased from Nordival Srl - Swagelok^[2].

Since no vacuum is possible within this system, unlike the previous prototype, before carrying out the measurement, the sample was treated at 200° C, under a flow of 20 cc/min of He, for 7 hours, to activate the material by eliminating the molecules physisorbed on his surface. In fact, helium can be used as a stripping gas because it is not absorbed by the material.

Initially the mixture under examination is sent to the mass spectrometer, bypassing the reactor containing the sample; subsequently the mixture is put in contact with the material and then sent to the mass spectrometer. From the chromatogram (Figure 5.5) it is possible to observe the trend of the abundance of the total flow before, during and after the contact with the material, and how the concentration of gases in the mixture changes after the contact phase with the sample.

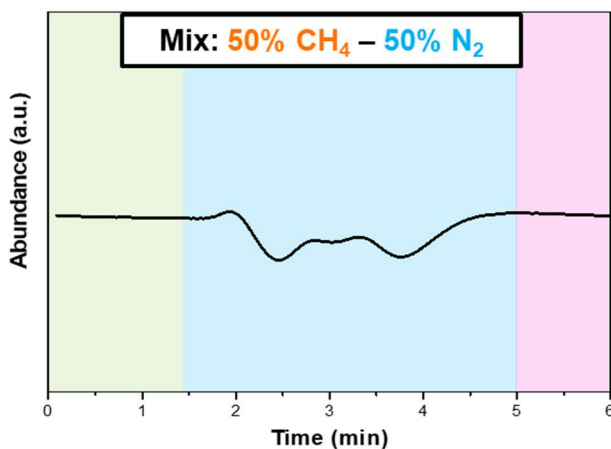


Figure 5.5 – Example of a chromatogram obtained by sending a mixture 50% methane and 50% nitrogen to the mass spectrometer. The raw data correspond to three distinct steps: the gas mixture is sent over the sample (frame green); the gas mixture it is passed over the material (frame blue); helium is sent into the system to stripe the mixture (frame pink).

During the contact step between the gas mixture and the sample (Figure 5.5, frame blue), a change is observed in the composition of the initial mixture.

From the elaboration of raw data, obtain from the mass spectrometer, it is possible to break down the total flow chromatogram into the contributions due to the two single gases present in the mixture, and to express it as the percentage abundance of gases present in the mixture. Then, it is possible to calculate the percentage variation of the single gases after contact with the sample under examination.

Figure 5.6 shows, as an example, the chromatogram obtained by sending a 50-50 mixture of methane and nitrogen on a commercial carbon.

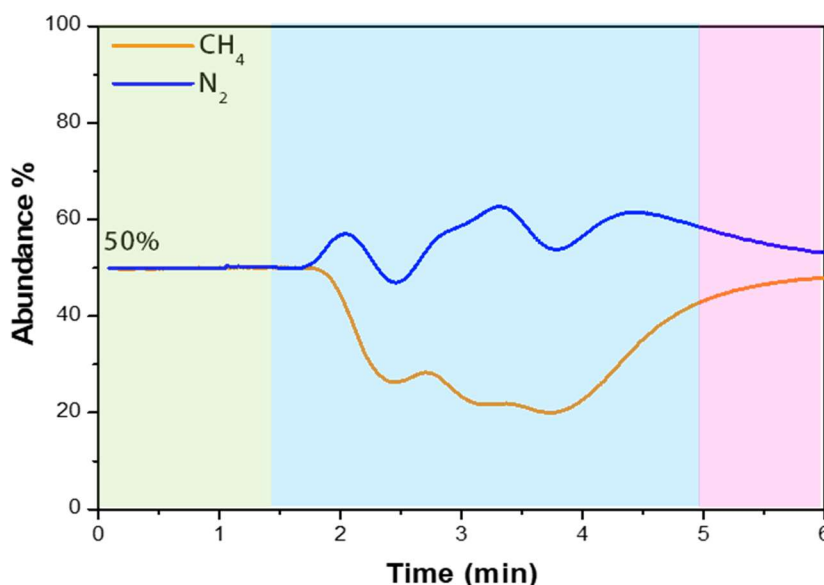


Figure 5.6 – Example of the raw data processing, obtained from the chromatogram: the total flux, composed of 50% CH₄ and 50% N₂, is divided into the contributions due to the two individual gases in the mixture. The methane flux decreases after contact with the sample, meaning that a fraction of the gas has been adsorbed by the material, while the nitrogen flux increases, synonymous with the fact that the final mixture is enriched in nitrogen and depleted in methane.

Initially, before the contact phase, the flux of both gases in the mixture is fixed/remains at 50 percent. As soon as the mixture comes in contact with the

material, it is observed a drop in the methane concentration, next to an increase in the nitrogen concentration. This indicates that more methane is being adsorbed by the material with respect to nitrogen, resulting in a change in the single gas concentrations in the mixture. As it can be seen in Figure 5.6, parallel to a decrease in the methane concentration it is observed an increase in the nitrogen concentration. After saturation of the material, the mixture of the two gases again becomes composed of 50 percent of both.

Conclusions

Two different prototypes for tracking gas adsorption measurements were developed as part of the PhD thesis projects.

The first prototype allows a single gas to be sent onto an adsorbing solid and its volumetric adsorption to be followed under thermodynamic conditions; adsorption isotherms can be derived from these measurements.

After filling the reactor with the material to be tested, it is degassed under vacuum conditions to a temperature that allows removal of the physisorbed species on its surface. The gas is then added in several steps with increasing pressure. By knowing the pressure added and recording the pressure after a certain equilibrium time, the amount of gas adsorbed by the material, expressed as adsorption excess, can be determined and the adsorption isotherm obtained.

The second prototype, coupled with a mass spectrometer, on the other hand, allows the evaluation of the ability of adsorbents to separate a gas from a binary mixture; these measurements are performed under kinetic flow conditions.

By introducing a mixture of known composition into a reactor containing the adsorbent, the chromatogram obtained from the mass spectrometer can be used to determine the change in flux concentration and to evaluate the ability of the material to selectively adsorb either component of the mixture.

References

- [1] *AEP transducers* **n.d.**
- [2] “Nordival Srl - Swagelok Italia,” can be found under <https://www.swagelok.com/it/distributors/l-n/nordival>, **n.d.**
- [3] “HiCube Eco | Pfeiffer Vacuum,” can be found under <https://www.pfeiffer-vacuum.com/en/products/vacuum-generation/pumping-stations/turbo-pumping-stations/hicube-eco/20020/hicube-80-eco-dn-63-iso-k-mvp-015-4>, **n.d.**
- [4] “FALC Instruments. Produzione e distribuzione articoli da laboratorio chimico e farmaceutico - FALC Instruments,” can be found under <https://www.falcinstruments.it/it/>, **n.d.**
- [5] S. Lowell, J. E. Shields, M. A. Thomas, M. Thommes, *Characterization of Porous Solids and Powders: Surface Area, Pore Size and Density*, Springer Netherlands, Dordrecht, **2004**.
- [6] S. Brandani, E. Mangano, L. Sarkisov, *Adsorption* **2016**, 22, 261–276.
- [7] “National Institute of Standards and Technology,” can be found under <https://www.nist.gov/>, **n.d.**
- [8] “Chemical Analysis, Life Sciences, and Diagnostics | Agilent,” can be found under https://www.agilent.com/?gclid=Cj0KCQjwkt6aBhDKARIsAAyeLJ0jInoI0GR4-NLVWSMrFLx_mXh4g6QUJetogwtQDG6j_imhcfHKty8aAkSDEALw_wcB&gclsrc=aw.ds, **n.d.**
- [9] “EL-FLOW Prestige,” can be found under <https://www.bronkhorst.com/int/products/gas-flow/el-flow-prestige/>, **n.d.**

Chapter 6

*Study of carbon dioxide storage capacity
by porous carbons and valorisation of biomethane*

Introduction

Carbon dioxide (CO₂) and methane (CH₄) are the main greenhouse gas released by human activities.

In addition to reducing the use of fossil fuels, which are the main source of CO₂ emissions, it is critical to capture and store the carbon dioxide already in the atmosphere. As mentioned in Chapter 2, this PhD work is in the frame of SATURNO Project; for this reason, the CO₂ adsorption capacities of different porous carbons, both of commercial origin and synthesized in the laboratory (derived from HCPs), and of a commercial zeolite were studied. The storage capacities of the materials were tested using a volumetric device for measurements under thermodynamic equilibrium conditions.

In addition, various porous adsorbents will be tested for CH₄ and N₂ adsorption and for gas separation from a binary mixture, consisting of methane and nitrogen (in defined proportions).

This application is in collaboration with Ecospray Technologies Company.

To this purpose, several commercial materials (porous activated carbon and zeolite 13X) were tested to determine which material was best suited for purifying biogas into biomethane.

Specifically, these materials were tested to determine which material could most efficiently remove methane from a binary mixture of methane and nitrogen, as their unique structural characteristics of high porosity, large surface area, and modifiable functionality make them very promising for gas separation.

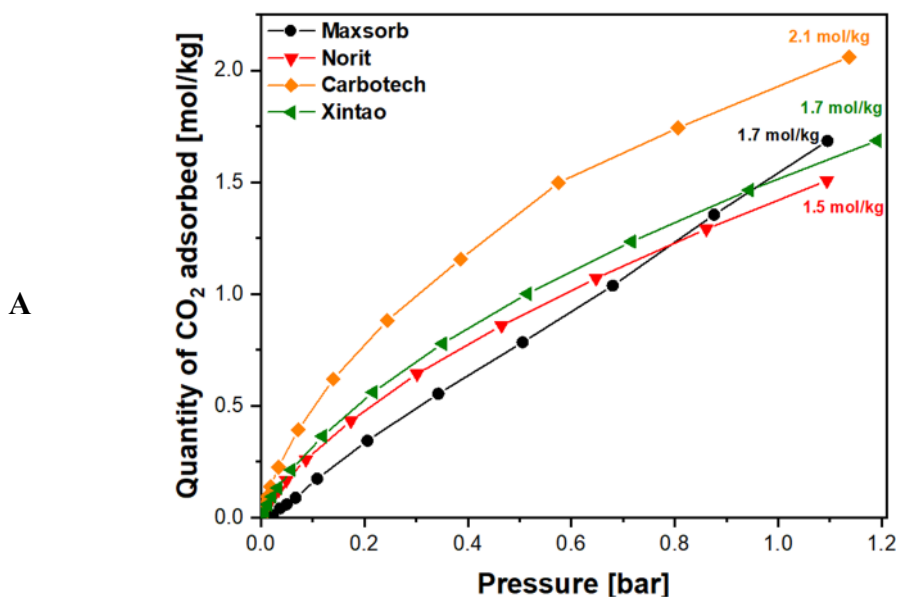
First, the materials were tested for the storage capacity of the two individual gases (methane and nitrogen) under static conditions. Then, the separation capability of two binary mixtures was investigated: the first consisted of 85% methane and 15% nitrogen, and the second was composed of 50% methane and 50% nitrogen.

6.1 CO₂ adsorption isotherms

CO₂ adsorption measurements were performed, until the pressure of 1 bar of equilibrium, using the volumetric prototype apparatus, both on porous carbons (commercial and synthetic) and on commercial zeolite.

Initially, the material to be tested (about 0.5 g) was activated by heating at 200°C for 8 hours under vacuum conditions to remove physically absorbed water. The measurement was kept under isothermal conditions (at 25°C) using a thermostatic bath.

The CO₂ adsorption isotherms of the four commercial porous carbon are reported in Figure 6.1.



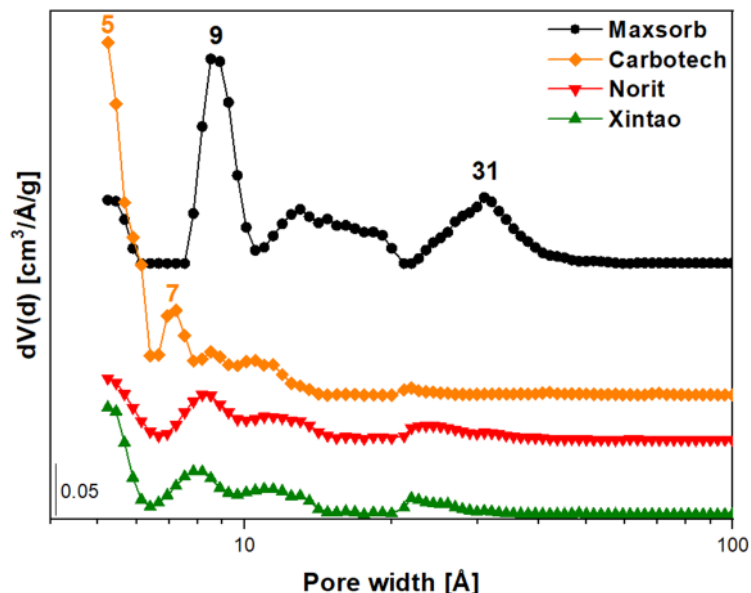
B

Figure 6.1 – A) Adsorption isotherms of CO₂ on commercial carbons, collected at 25°C;

B) Pore size distribution of commercial carbons

Carbotech (♦), Maxsorb (●), Norit (▼) and Xintao (◄)

All isotherms obtained belong to type I of the IUPAC classification^[1]. The uptake capacity is mainly due to the physical properties of the adsorbent; the adsorbent with a higher microporous structure tends to adsorb more gas, i.e., it has a higher equilibrium uptake^[2]. The influence of pressure on CO₂ capacity can also be observed: adsorption is greater at higher pressure. This phenomenon occurs because the high pressure forces the CO₂ molecules onto the adsorption site in the pore^[3]. As can be seen from Figure 6.1A, Carbotech adsorbs more CO₂ at low pressure than the other carbons; this is consistent with the porosity distribution of the materials. In fact, as describe in Chapter 4, Carbotech carbon has only two pore families in the micropore region, centered at 5 and 7 Å, while the other carbons have a four-modal distribution of pore sizes, mainly in the micropore region but also in the smaller mesopores (Figure 6.1B).

For a better understanding, in Table 6.1 detail of textural properties of all the porous carbons samples are reported.

Table 6.1 - Textural properties of commercial porous carbons, assessed via N₂ physisorption analysis performed at 77 K.

Sample	SSA_{BET} (m²/g)	Total P_v (cc/g)	V_{microP} (20 Å) (cc/g)	V_{mesoP} (20-100 Å) (cc/g)
Maxsorb	2881	1.39	0.68	0.69
Carbotech	1928	0.76	0.66	0.08
Norit	962	0.46	0.26	0.17
Xintao	935	0.40	0.28	0.10

It has been shown in the literature that micropores with a width lower than 7 Å are particularly suitable for CO₂ capture at atmospheric pressure, since pores with a size from two to three times larger than the kinetic diameter of CO₂ (0.33 nm) are the most appropriate candidates for CO₂ adsorption^[4-6].

Moreover, it has been demonstrated that the presence of a narrow pore size distribution leads to excellent performance in the storage of CO₂^[7,8].

At a pressure of about 1 bar, the materials have comparable storage capacity, ranging from 1.5 to 1.7 mol/kg (66-74 g/kg), except Carbotech carbon, which has the best performance with a storage of 2.1 mol/kg (91 g/kg); this value is in agreement with that reported in the work of Martin et al^[2].

At high pressures, the adsorption capacities are related to the specific surface area, to the amount of mesopores and the total pore volume^[9,10].

As can be seen from the textural analysis of the materials (Table 6.1), the Maxsorb and Carbotech carbons have the largest surface area of 2881 m²/g and 1928 m²/g, respectively, and the largest total pore volume of 1.39 and 0.76 cc/g, respectively, compared to the other carbons tested.

It has to be pointed out that Maxsorb carbon has both families of micropores and mesopores (Figure 6.1B), and for this reason its CO₂ adsorption capacity is low at low pressure, while it increases rapidly with increasing pressure.

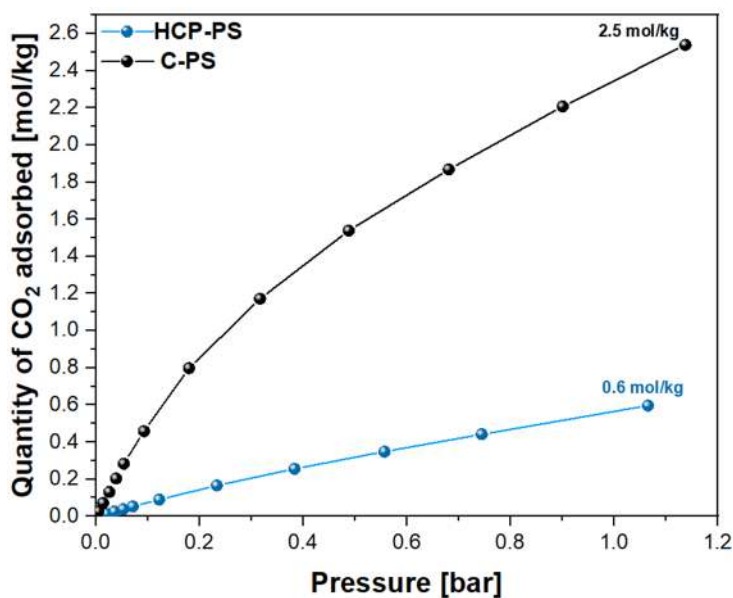
The Carbotech carbon, on the other hand, is completely microporous and has an optimal pore size for CO₂ adsorption at both low and high pressure.

Moreover, Raman characterization of Carbotech revealed that it has a low degree of graphitization, which can be attributed to an ordered structure of the graphene sheets. A more disordered structure seems to have a higher trapping capacity than a more ordered structure^[11].

The adsorption capacities of the synthetic porous carbon (C-PS) were tested and compared with those of hyper cross-linked starting polymer (HCP-PS).

The obtained adsorption isotherms are shown in Figure 6.2A.

A



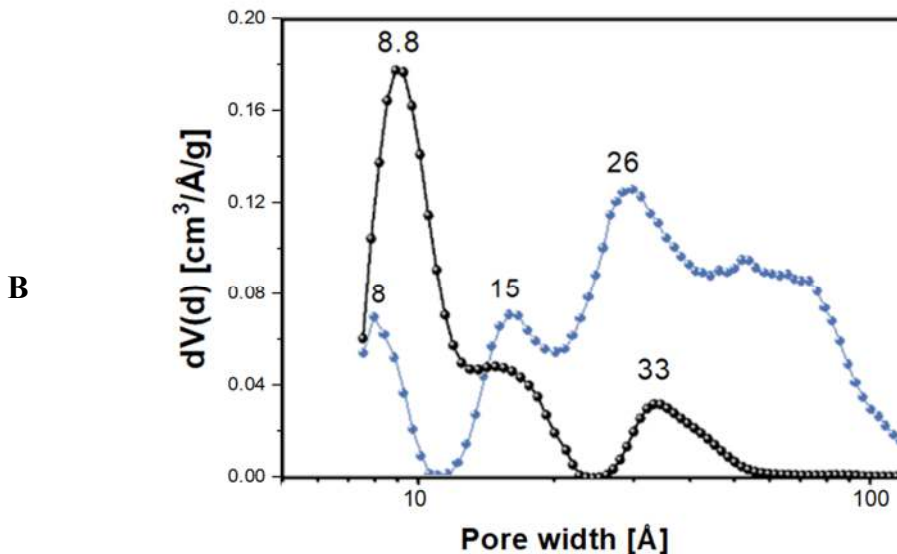


Figure 6.2 – A) CO₂ adsorption isotherms collected at 25°C;

B) Pore size distribution of C-PS (●) and HCP-PS (●) stem from N₂ sorption isotherms at 77 K.

In Figure 6.2A, two different ranges of adsorption can be distinguished for both samples. At low pressure, a steep increase in CO₂ adsorption is observed for porous carbon, which is due to the adsorption of carbon dioxide within the microporosities. In contrast, at higher pressures, a less steep increase in adsorption capacity is observed.

In fact, narrow micropores are important for gas adsorption at low pressures, since adsorption under these conditions is dominated by host-host interactions between gas molecules and pore walls^[12]. At high pressures, the contribution due to high surface area and porous volume, given by the presence of small-diameter micropores and mesopores, predominates^[12].

However, at a pressure of 1 bar, the adsorption capacity of C-PS is 2.5 mol/kg (111 g/kg). In contrast, HCP-PS exhibits a lower adsorption capacity at both low and higher pressures. This is due to an increased amount of micropores in the C-PS sample, as evidenced by the pore size distribution (Figure 6.2B); for better understanding, in Table 6.2 textural properties of HCP-PS and C-PS are reported.

Table 6.2 - Textural properties of HCP-PS and C-PS samples, assessed via N₂ physisorption analysis performed at 77 K.

Sample	SSA_{BET} (m²/g)	Total P_v (cc/g)
HCP-PS	845	0.67
C-PS	2944	1.60

Since the molecular size of CO₂ is 0.33 nm, only pores less than 1.0 nm are effective towards CO₂ capture at atmospheric pressure^[13].

The hyper crosslinked polymer has a CO₂ adsorption capacity of 0.6 mol/kg (26 g/kg) at a pressure of 1 bar. This value is consistent with the data reported by Martin and coworkers^[14]: they performed several CO₂ storage tests at room temperature and pressure and obtained values of about 0.6 mol/kg (27 g/kg). They also show that CO₂ adsorption, at room pressure and temperature, correlates with the presence of narrow micropores in the material^[14].

It is therefore clear that HCPs have lower adsorption capacities than porous carbons because they have a smaller volume of micropores.

In addition, Sevilla et al. performed CO₂ adsorption measurements on porous carbons obtained from a biomass by chemical activation with KOH^[15].

They found that a porous carbon with a surface area of 2850 m²/g and a total pore volume of 1.35 cc/g adsorbed about 132 g/kg of CO₂ at a pressure of 1 bar and a temperature of 25°C. This result is also in agreement with those obtained for C-PS. C-PS carbon is characterised by higher CO₂ adsorption performances with respect to the tested commercial samples. This can be partially related to the powder form of this specific sample. Indeed, it has to be taken into account that the pelletization process usually leads to a change in their chemical and physical properties, especially in their structural and textural properties^[16]. In addition, gas diffusion in the pelletized material is much slower than in the powdered material^[17].

The CO₂ adsorption isotherm of the commercial zeolite 13X is reported in Figure 6.3.

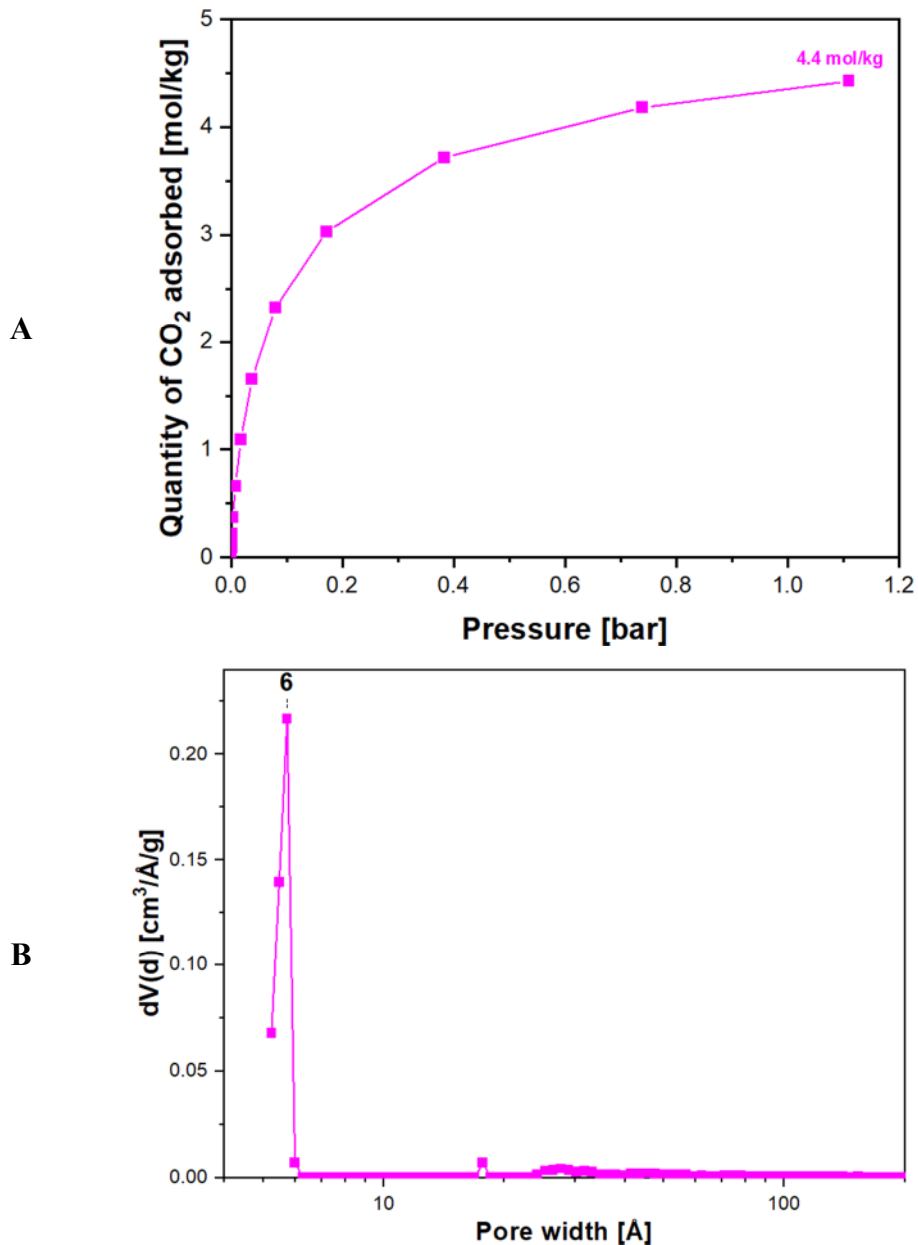


Figure 6.3 – A) CO₂ adsorption isotherm of commercial zeolite 13X, collected at 25°C; B) Pore size distribution of zeolite 13X.

The CO₂ adsorption isotherm reported in Figure 6.3 is a Type 1 according to IUPAC classification^[1].

At a pressure of 1 bar, the CO₂ uptake capacity of zeolite is 4.4 mol/kg (195 g/kg). This data is in agreement with what has been reported in the work of Wilkins and coworkers^[18]: in fact, they performed CO₂ adsorption measurements at different temperatures on zeolite 13X, up to a pressure of 5 bar; they found, at a temperature of 25°C and a pressure of 1 bar, a CO₂ uptake capacity of *ca.* 220 g/kg. Also in the work of Chen *et al.*, the CO₂ adsorption isotherms carried out on a zeolite 13X, obtained from a bentonite, are reported; it exhibits an adsorption capacity of 211 g/kg at a pressure of 1 bar and a temperature of 25°C^[19].

The high CO₂ adsorption capacity of zeolite 13X can be attributed to its high surface area (837 m²/g), its microporous structure (Figure 6.3B) and micropore volume of 0.22 cc/g, since the kinetic diameter of CO₂ is 0.33 nm, and the presence of Na cations within its cavities; in fact, the permanent quadrupole of CO₂ can interact with both cations and basic sites in the zeolite^[20].

6.2 CH₄ adsorption isotherms

For methane adsorption, since it is related to an industrial application, only commercial samples (carbons and zeolite) were chosen to be tested in pellet form. For commercial carbon, adsorption isotherms were recorded up to an elevated pressure of 40 bar; for commercial zeolite, adsorption isotherms were recorded only up to the ambient pressure of 1 bar. This choice was made because literature reports that adsorption at low pressure is due to the presence of micropores, while adsorption at high pressure is also due to the presence of mesoporosity.

CH₄ storage experiments were carried out on the four commercial carbons, and the adsorption isotherms obtained are shown in Figure 6.4.

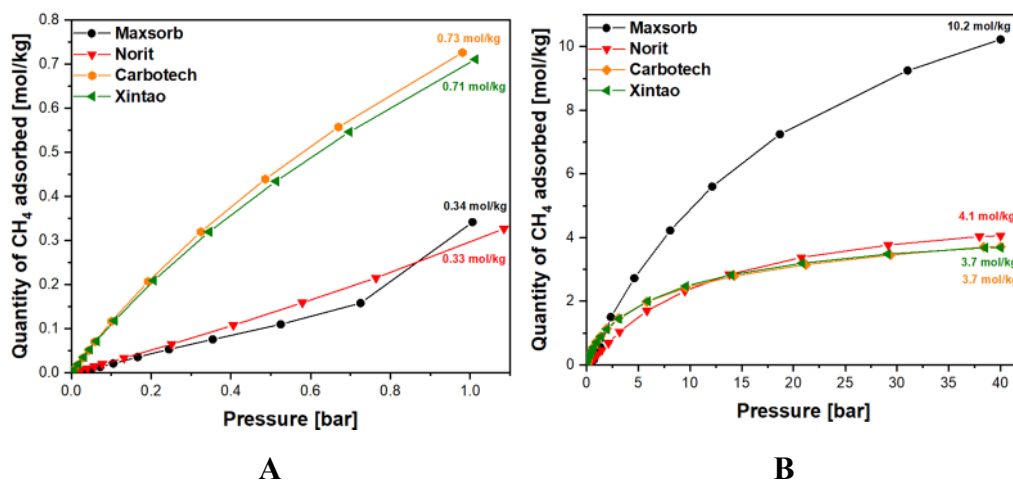


Figure 6.4 - Adsorption isotherms, collected at 25°C, of CH₄, recorded up to 1 bar (A) and 40 bar (B) of pressure on commercial carbon.

Carbotech (◆), Maxsorb (●), Norit (▼) and Xintao (◄)

For all sample, the adsorbed amount increases rapidly with increasing pressure because of the small pore sizes and then reaches a plateau as the pores get filled.

As can be seen from Figure 6.4A, at low pressure Carbotech and Xintao carbons have the best performance, adsorbing a similar amount of methane (0.7 mol/kg), while the other carbons have significantly lower adsorption.

At high pressure (Figure 6.4B) Carbon Maxsorb is much more efficient than other commercial carbons in capturing methane. Carbon Carbotech, Carbon Xintao and Carbon Norit show a very similar behaviour.

Again, as with CO₂, good adsorption of CH₄ at low pressures is attributed to the high presence of microporosity, while at high pressures the contribution of the presence of micropores coupled with a large fraction of small mesopores (20-40 Å wide) becomes important^[21]. The adsorption process is based on the principles of affinity between the porous architecture of the material and the molecular dimensions of CH₄ molecules (0.38 nm)^[22,23].

In Table 6.3 the quantities in g/kg and mol/kg of CH₄ adsorbed at a low and high pressure are reported.

Table 6.3 - Amount of methane adsorbed by commercial carbons at low and high pressure.

	CH ₄ ads [mol/kg]		CH ₄ ads [g/kg]	
	1 bar	40 bar	1 bar	40 bar
Maxsorb	0.3	10.2	5.9	164
Norit	0.3	4.1	5.2	65.1
Carbotech	0.7	3.7	12.1	59.5
Xintao	0.7	3.7	11.5	59.1

These data are in agreement with work published in the literature by Casco and co-workers in which eight porous carbon with different structural characteristics were tested for methane storage^[24]. In their work, they report that the two carbons with the largest surface area (3290 m²/g and 3425 m²/g) and larger pore volume (2.25 and

2.44 cc/g), especially mesoporous volume (1.15 cc/g and 1.31 cc/g), showed the best performance in methane adsorption; in particular, at 35 bar pressure, the adsorption excess of the best carbons was 191 g/kg and 184 g/kg.

These results are consistent with those reported in this work: Maxsorb that exhibited the best ability to adsorb methane has a surface area of 2881 m²/g, a total pore volume of 1.39 cm³/g, and a mesoporous volume of 0.69 cm³/g.

CH₄ storage experiments were also conducted on commercial Zeolite 13X; the measurements were performed until the equilibrium pressure of 1 bar was reached, since the material has only one family of micropores (at 6 Å) and does not possess mesoporosity. The adsorption isotherms obtained are shown in Figure 6.5.

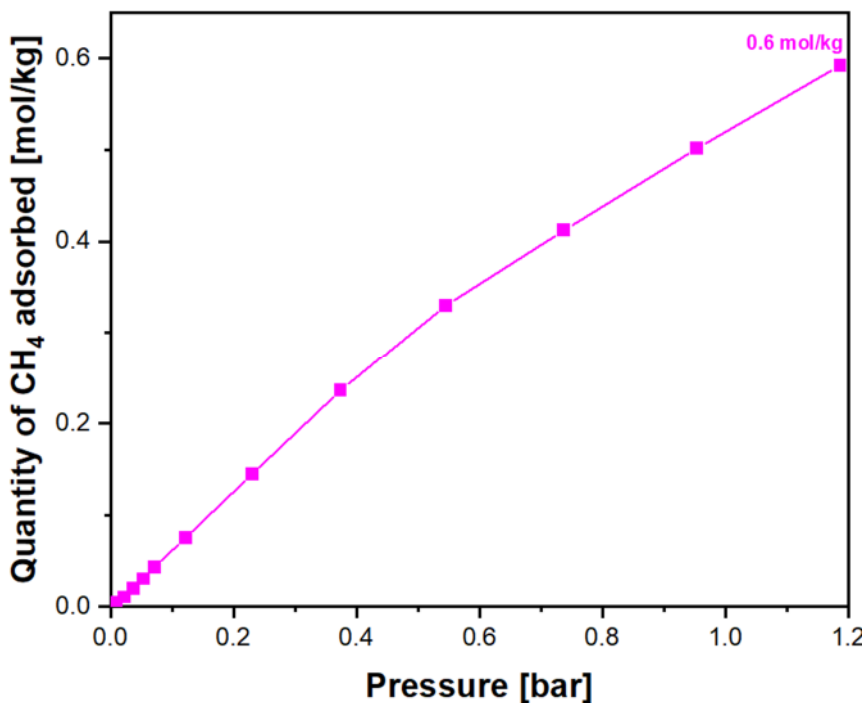


Figure 6.5 - Adsorption isotherms of CH₄ on commercial Zeolite 13X collected at 25°C.

In agreement with the literature reports, the isotherm obtained indicate that the adsorption capacity of methane is relatively low in the zeolite^[25].

As can be seen from the Figure 6.5, Zeolite 13X adsorb about 0.6 mol/kg (9 g/kg) of CH₄ at a pressure of 1 bar. This data is in agreement with what has been reported in the literature by Mofarahi and Bakhtyari^[25], and with the work done by Park and collaborators^[26].

CH₄ molecules can interact with the zeolite surface through the oxygen atoms of the lattice, the accessible cations outside the frame, and the Si and Al atoms^[27]. The Si and Al atoms in the center of the tetrahedra are not directly exposed to the gas molecules; consequently, their interactions with the CH₄ molecules are negligible^[28]. The main interactions of the gas molecules with the zeolite surface occur via the oxygen atoms of the lattice and the cations in the extraframeworks^[28].

6.3 N₂ adsorption isotherms

The ability of the materials to capture nitrogen was also tested. Also in this case, N₂ storage experiments were carried out only on commercial samples (carbons and zeolite), until the pressure of 40 bar for the carbons, and until the pressure of 1 bar for commercial zeolite.

Initially, N₂ storage experiments were carried out on the four commercial carbons, and the adsorption isotherms obtained are shown in Figure 6.5.

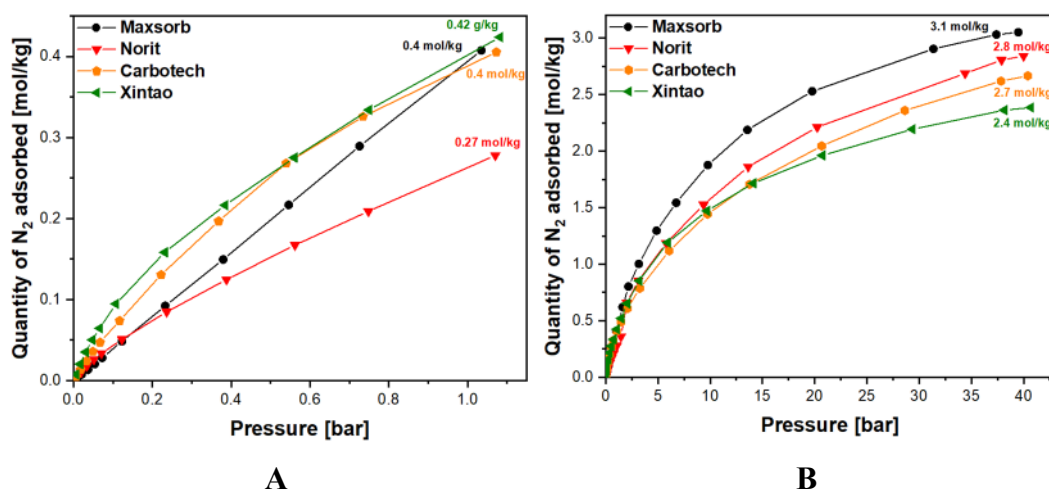


Figure 6.5- Adsorption isotherms, collected at 25°C, of N₂, recorded up to 1 bar (A) and 40 bar (B), on commercial carbon.

Carbotech (◊), Maxsorb (●), Norit (▼) and Xintao (◄)

At the pressure of 1 bar (Figure 6.3A) Maxsorb, Xintao and Carbotech carbons show the greatest capacity of storage, respect to Norit carbon.

Instead, at high pressure Maxsorb carbon possess the best storage capabilities, compared with the other carbons tested (Figure 6.3B).

Park et al. performed N₂ adsorption measurements on porous carbons derived from waste agricultural products^[29]. The best performance, among the carbons they tested,

they obtained from a carbon had a surface area of 790 m²/g with a total porous volume of 0.325 cc/g, a microporous volume of 0.256 cc/g and a mesoporous volume of 0.069 cc/g; this carbon at a pressure of 1 bar, adsorbed 12.6 g/kg of nitrogen.

In addition, Rufford and coworkers performed nitrogen storage measurements on carbon similar to Norit and found that it is capable of adsorbing 73 g/kg nitrogen at a pressure of 40 bar^[30].

In Table 6.4 the quantities in g/kg and mol/kg of N₂ adsorbed at a low and high pressure are reported

Table 6.4 – Amount of nitrogen adsorbed by commercial carbons at low and high pressure.

	N ₂ ads [mol/kg]		N ₂ ads [g/kg]	
	1 bar	40 bar	1 bar	40 bar
Maxsorb	0.4	3.1	11.4	85.4
Norit	0.3	2.8	7.8	79.5
Carbotech	0.4	2.7	11.3	74.7
Xintao	0.4	2.4	11.9	66.8

N_2 storage experiments were conducted on commercial Zeolite 13X, and the adsorption isotherms obtained are shown in Figure 6.6.

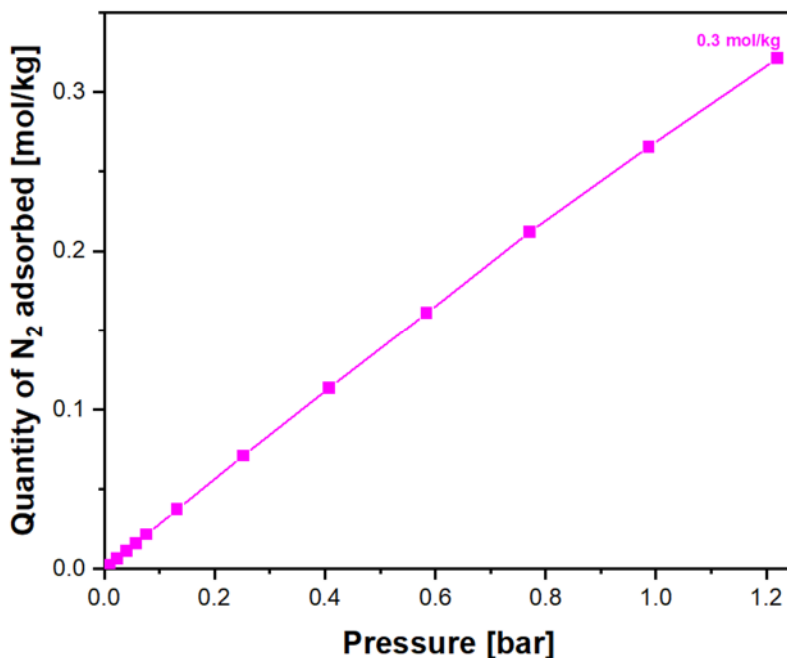


Figure 6.6 - Adsorption isotherms of N_2 on commercial Zeolite 13X collected at 25°C.

The isotherm obtained indicate that also the adsorption capacity of nitrogen is relatively low in the zeolite^[25].

As can be seen from the Figure 6.6, Zeolite 13X adsorb about 0.3 mol/kg (7.5 g/kg) of N_2 at a pressure of 1 bar. This data is in agreement with the work of Mofarahi and Bakhtyari^[25], and with the work of Park and collaborators^[26].

The structure and physicochemical properties of zeolites influence the adsorption; Zeolite 13X with a faujasite structure has an open pore size that allows nitrogen diffusion.

Also for the case of CH_4 , the main interactions of the N_2 molecules with the zeolite surface occur via the oxygen atoms of the lattice and the cations in the extraframeworks^[28]. The adsorption of N_2 is low because it has only a weak quadrupole moment and lower polarizability^[31].

6.4 Adsorption measurements in flow conditions

Subsequently, in collaboration with the company Ecospray Technologies, the ability of commercial adsorbents to separate methane from a binary CH₄/N₂ mixture was investigated, in order to upgrade it.

Since the composition of the two gases in the mixture is not always in fixed proportions under real industrial conditions, but can vary greatly, it was decided to test two mixtures with different proportions (85%CH₄-15%N₂ and 50%CH₄-50%N₂) to determine whether the behaviour of the adsorbents remains the same or whether it is subject to variations.

The selective adsorption capacity was evaluated by flow measurements using the specially designed prototype (Chapter 5). First, a CH₄/N₂ mixture is sent directly into the mass spectrometer, at a volumetric flow rate of 2 cc/min, bypassing the adsorbent: in this way the spectrometer can record a chromatogram containing the initial composition of the mixture; then, the mixture is sent over the adsorbed material (*ca.* 0.3 g, in pellet form), and then the outgoing mixture is sent into the mass spectrometer. In this way, the change in percent composition can be evaluated.

6.4.1 Adsorption measurements of the 85% CH₄ – 15% N₂ gas mixture

Figure 6.7 shows the chromatograms of methane (Figure 6.7A) and nitrogen (Figure 6.7B) streams during the contact phase between the 85%CH₄-15%N₂ mixture and the commercial zeolite 13X.

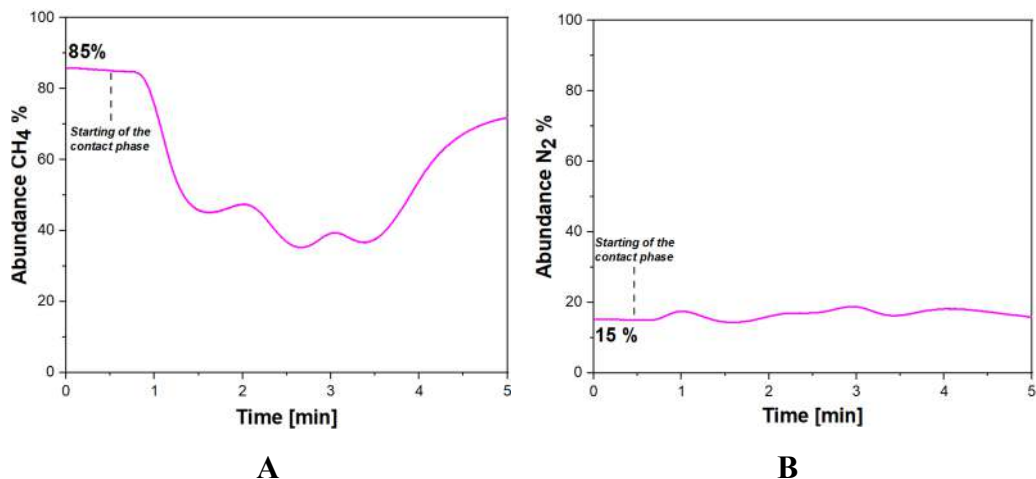


Figure 6.7– Chromatogram of methane (A) and nitrogen (B) stream after sending the mixture (consisting of 85% CH₄ – 15% N₂) into contact with the commercial zeolite.

From the chromatogram in Figure 6.7A, it can be seen that as the mixture comes into contact with the zeolite (min 0.5 in the graph), the percentage abundance of methane (initially 85%) in the outgoing mixture begins to decrease, an indication that CH₄ is being adsorbed by the material.

During the contact time between the material and the mixture, fluctuations related to a change in the percentage composition of the mixture can be seen. However, when the material is fully saturated, the composition of the effluent returns to its initial state (usually after *ca.* 3-5 minutes of contact time).

The percentage fluctuations in the mixture could be due to host-guest interactions between the gas molecules and the surface of the material and guest-guest interactions between the gas molecules themselves, and also to interaction between the incoming gas molecules and those already adsorbed by the material.

Similarly, from the chromatogram in Figure 6.7B, the variation in percentage abundance of nitrogen can be evaluated. It can be seen that after contact between the mixture and zeolite, the percentage abundance of nitrogen (initially 15%) of the output mixture increases. Again, once the saturation of the zeolite is reached, the % of nitrogen in the output mixture returns to its initial values.

This result means that the zeolite, because it adsorbs methane and not nitrogen, enriches the outgoing mixture with nitrogen and depletes it of methane.

All samples tested behave in a similar way, absorbing methane and, consequently, enriching the outgoing mixture with nitrogen and depleting it in methane.

The instantaneous dipole induced by the polarizability of the adsorbates can produce stronger van der Waals interactions with the pore walls of the adsorbents^[32]. Due to the greater polarizability of CH₄ than of N₂, CH₄ molecules exhibit stronger van der Waals interactions with the adsorbent, resulting in preferential adsorption of CH₄.

The percentage changes in gas composition, after the first minute of contact with commercial carbons and zeolite are reported in Table 6.5.

Table 6.5 - Percentage change in gas composition of mixture 85%CH₄-15%N₂, after the first minute of contact with commercial carbons and commercial zeolite.

	Δ Variation CH ₄ %	Δ Variation N ₂ %
Carbon Maxsorb	- 37.1	+ 5.9
Carbon Norit	- 36.3	+ 4.3
Carbon Carbotech	- 36.9	+ 4.3
Carbon Xintao	- 35.9	+ 4.3
Commercial Zeolite 13X	- 40.0	+ 3.1

The gas percentage changes, calculated in the first minute of contact between the material and the mixture, are comparable for all materials tested.

This results are consistent with the literature: in fact, studies have shown that ultramicroporous adsorbents are more able to separate gas mixtures with similar polarizability and size (such as methane and nitrogen) ^[34].

6.4.2 Adsorption measurements of the 50% CH₄ – 50% N₂ gas mixture

Figure 6.8 shows the chromatograms of methane (Figure 6.8A) and nitrogen (Figure 6.8) streams during the contact phase between the 50%CH₄-50%N₂ mixture and the commercial zeolite 13X.

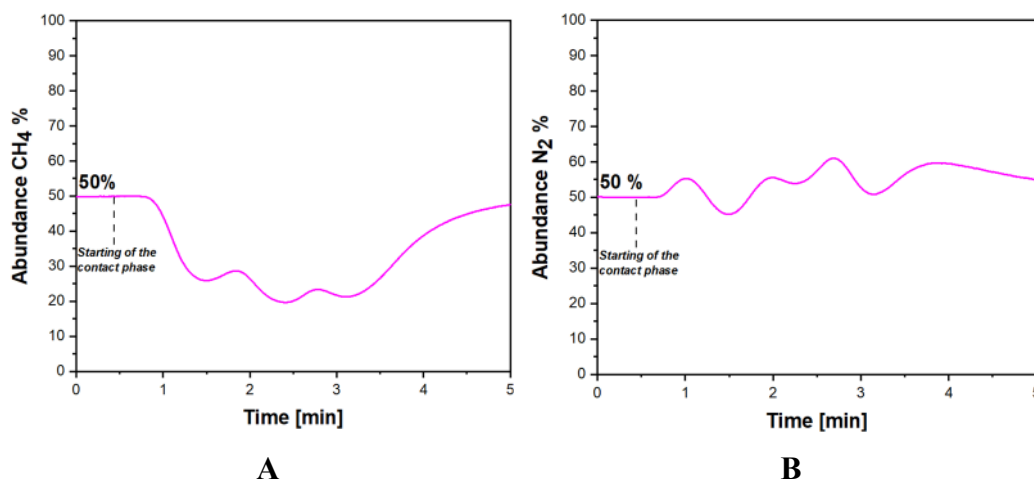


Figure 6.81 – A) Chromatogram of methane stream and B) chromatogram of nitrogen stream after sending the mixture (consisting of 50% CH₄ – 50% N₂) into contact with the commercial zeolite.

Also with this composition of the mixture, since the methane has been adsorbed by the material, the percentage abundance of its flow (initially 50%) decreases after contact with the zeolite, and then returns to the initial level after its saturation; while, as the mixture is enriched with nitrogen and depleted of methane, the percentage abundance of the outgoing nitrogen flow increases and then returns to 50% after the saturation of zeolite.

In this case, the fluxes in the chromatogram are similar for all samples.

In Table 6.6 are reported the percentage changes in gas composition, after the first minute of contact with commercial carbons and commercial zeolite.

Table 6.6 - Percentage change in gas composition, after the first minute of contact between the mixture 50% CH₄ – 50% N₂ and the commercial carbons and commercial zeolite.

	Δ Variation CH ₄ %	Δ Variation N ₂ %
Carbon Maxsorb	- 23.7	+ 7.0
Carbon Norit	- 26.2	+ 5.4
Carbon Carbotech	- 25.1	+ 5.6
Carbon Xintao	- 24.4	+ 5.9
Zeolite 13X	- 23.5	+ 5.7

All of the materials tested behave similarly, depleting the initial mixture of comparable percentages of methane and enriching it with nitrogen.

Moreover, as expected, the percentage change of adsorbed methane due to the variation of the gas composition of the mixture is smaller than in the experiments performed with the mixture 85% CH₄ - 15% N₂, while the percentage change of nitrogen is larger in all tested carbons.

Conclusions

In this chapter, various porous adsorbents (commercial carbons and commercial zeolite) were tested for gas adsorption (CO_2 , CH_4 and N_2) and for gas separation from a binary mixture, consisting of methane and nitrogen.

Regarding CO_2 adsorption, commercial carbons show similar CO_2 storage capacities, with the exception of the Carbotech carbon, which stood out with an adsorption capacity of 2.1 mol/kg (91 g/kg) of CO_2 , since it is completely microporous and has an optimal pore size for CO_2 adsorption at both low and high pressure. Instead, the synthetic C-PS porous carbon, derived from HCP, has a higher carbon dioxide adsorption capacity than all other tested carbons, storing about 2.5 mol/kg (111 g/kg) of CO_2 at a pressure of 1 bar. This is due to its large surface area and high pore volume, especially microporosity. In addition, sample C-PS was tested in powder form compared to commercial carbons, which are in pellet form; this contributed to greater gas diffusion within the material.

However, the best CO_2 adsorption performance was achieved by Zeolite 13 X, storing *ca.* 4.4 mol/kg (195 g/kg) at a pressure of 1 bar. This result can be attributed both to the presence of Na cations within the zeolite cavities, since the permanent quadrupole of CO_2 can interact with both cations and basic sites in the zeolite, and to its microporous structure^[20]. In fact, it has been shown in the literature that micropores with a width of less than 7 Å are particularly suitable for CO_2 capture at atmospheric pressure, as pores with a size two to three times the kinetic diameter of CO_2 (0.33 nm) are the most suitable candidates for its adsorption^[4-6].

Successively, the storage capacities of the commercial materials with respect to CH_4 and N_2 were tested.

At low pressures, CH_4 adsorption is due to the presence of micropores, as it possesses a kinetic diameter of 0.38 nm. For this reason, the best results were obtained from

carbons with a higher fraction of micropores. However, at high pressures, the contribution of the mesoporous fraction of the materials also becomes important; consequently, the best performance was obtained from Maxsorb carbon, which at the pressure of 40 bar adsorbed *ca.* 10.2 mol/kg (164 g/kg).

All commercial carbons and commercial zeolite, under the same conditions, exhibit higher methane adsorption capacity than nitrogen; this fact is a consequence of the larger polarizability of CH₄ with respect to N₂, which is compensated, in part, by the larger quadrupolar electric moment of the latter ^[33].

Finally, the commercial samples were tested for the separation of two binary methane-nitrogen mixtures.

In this flow conditions, for both the mixture tested, in accordance with what has been reported in the literature, all samples tested behave in a similar way, absorbing methane and, consequently, enriching the outgoing mixture with nitrogen and depleting it in methane. Under these conditions, the greater polarizability of CH₄ compared with N₂ plays a key role as CH₄ molecules exhibit stronger van der Waals interactions with the adsorbent, resulting in preferential adsorption of CH₄^[33].

References

- [1] M. Thommes, K. Kaneko, A. V. Neimark, J. P. Olivier, F. Rodriguez-Reinoso, J. Rouquerol, K. S. W. Sing, *Pure and Applied Chemistry* **2015**, *87*, 1051–1069.
- [2] A. Martin, M. Idrus Alhamid, Nasruddin, B. Suryawan, W. Soong Loh, A. Bin Ismail, W. Chun, K. Choon Ng, *Heat Transfer Engineering* **2017**, *38*, 396–402.
- [3] A. Borhan, S. Yusup, J. W. Lim, P. L. Show, *Processes* **2019**, *7*, 855.
- [4] C. F. Martín, M. G. Plaza, J. J. Pis, F. Rubiera, C. Pevida, T. A. Centeno, *Separation and Purification Technology* **2010**, *74*, 225–229.
- [5] L. Li, X.-F. Wang, J.-J. Zhong, X. Qian, S.-L. Song, Y.-G. Zhang, D.-H. Li, *Ind. Eng. Chem. Res.* **2018**, *57*, 11608–11616.
- [6] X. Zhang, I. Elsayed, X. Song, R. Shmulsky, E. B. Hassan, *Science of The Total Environment* **2020**, *748*, 142465.
- [7] S. Liu, L. Rao, P. Yang, X. Wang, L. Wang, R. Ma, L. Yue, X. Hu, *Journal of Environmental Sciences* **2020**, *93*, 109–116.
- [8] S. Liu, Q. Li, L. Wang, R. Ma, J. Zou, L. Huang, X. Hu, *Energy Fuels* **2019**, *33*, 11544–11551.
- [9] U. Kamran, J. R. Choi, S.-J. Park, *Frontiers in Chemistry* **2020**, *8*.
- [10] M. S. Shafeeyan, W. M. A. W. Daud, A. Shamiri, N. Aghamohammadi, *Chemical Engineering Research and Design* **2015**, *104*, 42–52.
- [11] J. Gong, J. Liu, X. Chen, Z. Jiang, X. Wen, E. Mijowska, T. Tang, *J. Mater. Chem. A* **2015**, *3*, 341–351.
- [12] G. Gatti, M. Errahali, L. Tei, M. Cossi, L. Marchese, *Polymers* **2019**, *11*, 588.
- [13] J. Garrido, A. Linares-Solano, J. M. Martin-Martinez, M. Molina-Sabio, F. Rodriguez-Reinoso, R. Torregrosa, *Langmuir* **1987**, *3*, 76–81.
- [14] C. F. Martín, E. Stöckel, R. Clowes, D. J. Adams, A. I. Cooper, J. J. Pis, F. Rubiera, C. Pevida, *J. Mater. Chem.* **2011**, *21*, 5475.
- [15] M. Sevilla, A. B. Fuertes, *Energy Environ. Sci.* **2011**, *4*, 1765.

- [16] E. Tsalaporta, J. M. D. MacElroy, *Heliyon* **2020**, *6*, e04883.
- [17] N. Wakao, J. M. Smith, *Chemical Engineering Science* **1962**, *17*, 825–834.
- [18] N. S. Wilkins, A. Rajendran, *Adsorption* **2019**, *25*, 115–133.
- [19] C. Chen, D.-W. Park, W.-S. Ahn, *Applied Surface Science* **2014**, *292*, 63–67.
- [20] S.-T. Yang, J. Kim, W.-S. Ahn, *Microporous and Mesoporous Materials* **2010**, *135*, 90–94.
- [21] G. Gatti, M. Errahali, L. Tei, E. Mangano, S. Brandani, M. Cossi, L. Marchese, *Nanomaterials* **2019**, *9*, 726.
- [22] T. Patterson, S. Esteves, R. Dinsdale, A. Guwy, *Energy Policy* **2011**, *39*, 1806–1816.
- [23] S. Nakao, K. Yogo, K. Goto, T. Kai, H. Yamada, *Advanced CO₂ Capture Technologies: Absorption, Adsorption, and Membrane Separation Methods*, Springer International Publishing, Cham, **2019**.
- [24] M. E. Casco, M. Martínez-Escandell, E. Gadea-Ramos, K. Kaneko, J. Silvestre-Albero, F. Rodríguez-Reinoso, *Chem. Mater.* **2015**, *27*, 959–964.
- [25] M. Mofarahi, A. Bakhtyari, *J. Chem. Eng. Data* **2015**, *60*, 683–696.
- [26] Y. Park, Y. Ju, D. Park, C.-H. Lee, *Chemical Engineering Journal* **2016**, *292*, 348–365.
- [27] H. Mikosch, E. L. Uzunova, G. St. Nikolov, *J. Phys. Chem. B* **2005**, *109*, 11119–11125.
- [28] G. Sethia, R. S. Somani, H. C. Bajaj, *Ind. Eng. Chem. Res.* **2014**, *53*, 6807–6814.
- [29] J. Park, N. F. Attia, M. Jung, M. E. Lee, K. Lee, J. Chung, H. Oh, *Energy* **2018**, *158*, 9–16.
- [30] T. E. Rufford, G. C. Y. Watson, T. L. Saleman, P. S. Hofman, N. K. Jensen, E. F. May, *Ind. Eng. Chem. Res.* **2013**, *52*, 14270–14281.
- [31] D. A. Kennedy, M. Mujcin, E. Trudeau, F. H. Tezel, *J. Chem. Eng. Data* **2016**, *61*, 3163–3176.

- [32] Y.-S. Bae, O. K. Farha, J. T. Hupp, R. Q. Snurr, *J. Mater. Chem.* **2009**, *19*, 2131.
- [33] Z. Dong, B. Li, H. Shang, P. Zhang, S. Chen, J. Yang, Z. Zeng, J. Wang, S. Deng, *AIChE J* **2021**, *67*, DOI 10.1002/aic.17281.
- [34] M. Tagliabue, D. Farrusseng, S. Valencia, S. Aguado, U. Ravon, C. Rizzo, A. Corma, C. Mirodatos, *Chemical Engineering Journal* **2009**, *155*, 553–566.

Chapter 7

*Evaluation of the adsorption properties of
inorganic and hybrid organic-inorganic
materials from liquid phase*

Introduction

In this chapter, results related to the use of inorganic and hybrid organic-inorganic materials for the removal of toxic molecules from the aqueous phase are reported. Particular attention will be given to two types of pollutants can be found in water media: organic dyes and emerging pollutants such as perfluoroalkyl substances (PFAS)

Silica monoliths and Swellable Organically Modified Silica (Silica-SOMS), prepared in the frame of the thesis work (together with commercial zeolites used as a reference), have been tested for the adsorption of a soluble organic dye, the Rhodamine B, largely used in the literature as a model molecule of organic pollutants^[1].

Moreover, Quaternary Amine Modified OrganoSilica (Silica-QA-SOMS) have been also tested for the removal of different type of PFAS.

7.1 Removal of Rhodamine B by using inorganic and hybrid organic-inorganic materials

Rhodamine B (*N*-[9-(*ortho*-carboxyphenyl)-6-(diethylamino)-3*H*-xanthen-3-ylidene] diethyl ammonium chloride) is a water-soluble dye of xanthene class. Its organic part is a cation in which the positive charge is shared by the two N atoms (Figure 7.1 A).

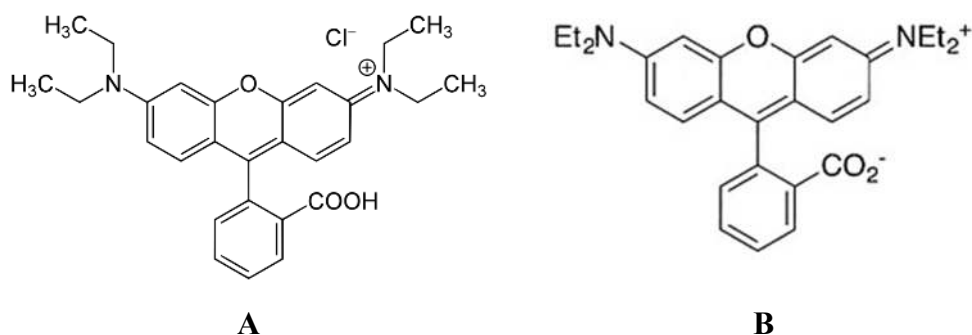


Figure 7.1 – A) Chemical structure of Rhodamine B, and B) zwitterionic form of Rhodamine B prevailing in water at pH ≥ 4.2 .

Rhodamine B is a weak acid (pK_a 4.2) with good solubility (34 g L⁻¹) in water. At low pH values the organic part is a cation in which the positive charge is shared by the two N atoms. At pH values higher than 4.2, the carboxylic group is predominantly deprotonated and the prevalent form of Rhodamine B is a Zwitterion^[1] (Figure 7.1 B). The molecular dimension are 1.44 nm x 1.09 nm x 0.64 nm^[2].

Rhodamine B was chosen since it is a model molecule capable of simulating a generic organic pollutant, very similar to those that can be spilled into the waters due to urban and industrial discharges, or due to accidental injections of oil and/or fuels. It has to be taken into account that this molecule has absorption properties that can be easily studied by UV-visible spectroscopy.

In Figure 7.2 the visible spectrum of Rhodamine B is reported.

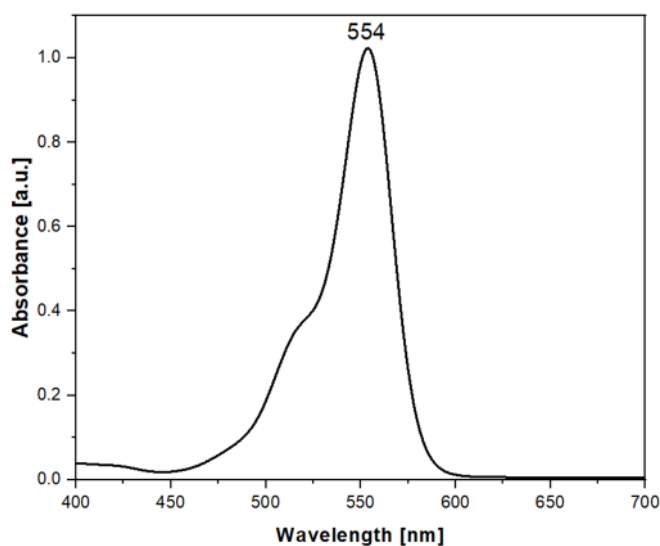


Figure 7.2 - UV-Vis spectrum of Rhodamine B solution (1×10^{-2} mM) in water media.

Rhodamine B possesses an absorption maximum at 554 nm (λ max), due to the $\pi \rightarrow \pi^*$ transition of the chromophore unit (aromatic heterocyclic ring)^[3].

7.1.1 Experimental conditions

The adsorption capacity of Rhodamine B of the different solids studied in the frame of this PhD thesis was evaluated by means of UV-Vis spectroscopy.

Contact tests have been carried out in the following way: *ca.* 250 mg of material was placed in contact with 50 mL of 1×10^{-2} mM Rhodamine B solution (0.24 mg) for 24 hours under constant stirring.

The solution was analyzed by UV-Vis spectrophotometry to follow the variation of the intensity of the signal of the Rhodamine B over the time.

Silica monoliths, Zeolite 13X and Silica-SOMS were tested as adsorbents.

Before performing the contact tests, a calibration procedure was necessary to derive the relationship between absorbance and concentration of the Rhodamine B solution (calibration line).

A 1×10^{-2} mM Rhodamine B stock solution was prepared and diluted to less concentrated standard solutions (5×10^{-3} mM, 2.5×10^{-3} mM, 1.25×10^{-3} mM, 6×10^{-4} mM) by successive dilutions. All solutions were analysed by UV-Vis spectrophotometry, and the resultant spectra are reported in Figure 7.3 A.

By plotting the maximum absorbance of solutions as a function of their concentration on a graph, it is possible to obtain a calibration line (Figure 7.3 B) having equation:

$$A = 86.967 \cdot C$$

where A is the absorbance of the solution and C is the concentration (mM).

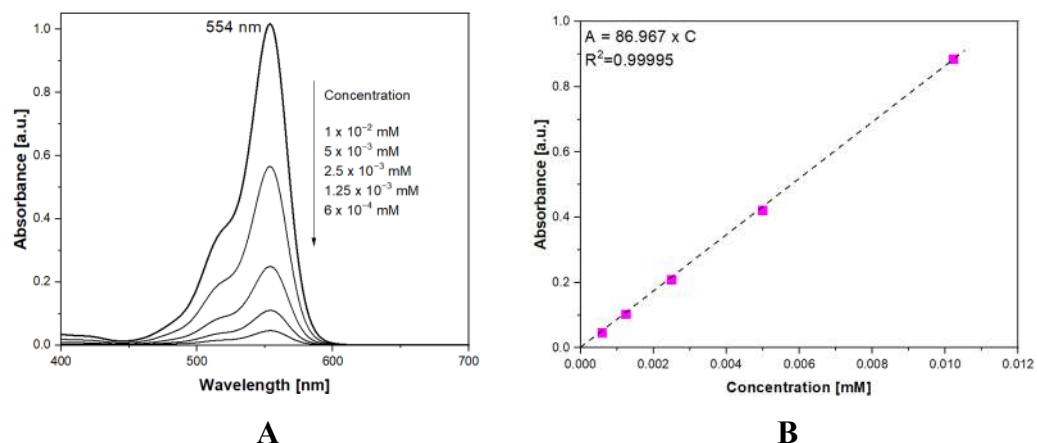


Figure 7.3 – A) UV-Vis absorption spectrum of Rhodamine B, at different concentration (1.5×10^{-2} mM, 5×10^{-3} mM, 2.5×10^{-3} mM, 1.25×10^{-3} mM, 6×10^{-4} mM), recorded between 400 and 700 nm;
B) calibration line

For the contact tests, 250 mg of sample was placed in a sealable glass vial with 50 mL of Rhodamine B solution 1×10^{-2} mM (the pH of solution was 5.5). The bottles have been subsequently closed with teflon-lined caps and placed on a mechanical stirrer (300 rpm) at r.t.

At different time intervals (i.e., 1, 2, 3, 4, 5, 6, 24 h), an aliquot of each solution (ca. 1 mL) was withdrawn and analysed using a UV-Visible spectrometer. Each experiment was repeated 3 times.

As a general feature, with the increase of the contact time with selected materials, the intensity of the absorption band at 554 nm, gradually decreases. As a matter of example, Figure 7.4 shows Visible-range spectra collected upon adsorption of Rhodamine B on silica monolith sample.

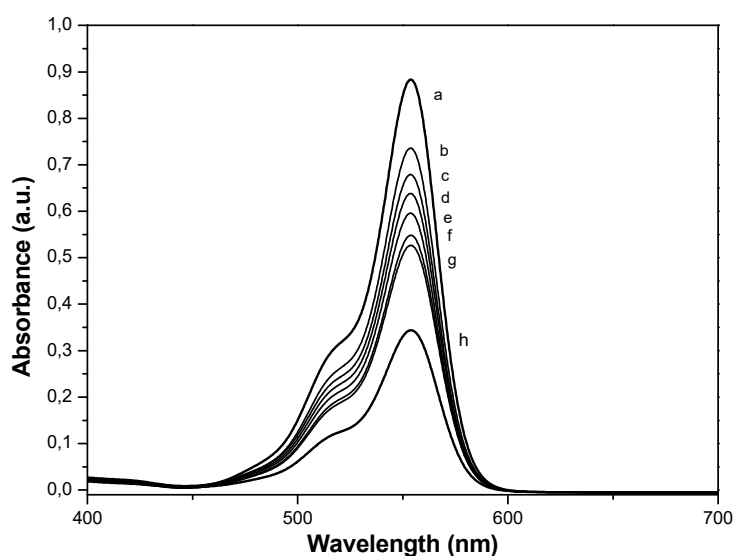


Figure 7.4 - UV-Vis spectra of 1×10^{-2} mM Rhodamine B solution in water media (a) and after 1 (b), 2 (c), 3 (d), 4 (e), 5 (f), 6 (g) and 24 (h) hours of contact with the silica monolith sample.

Contact experiments have been performed at rt.

By means of Lambert-Beer's law ($A = \varepsilon \cdot b \cdot C$), it was possible to correlate the absorbance (A) maximum of the Rhodamine with the concentration (C) of the solutions, using the calibration line previously obtained; consequently, the variation in the concentration of residual Rhodamine B in solution, and thus the amount adsorbed by different materials, was derived.

The adsorption capacity of Rhodamine B by silica monoliths, Zeolite 13X and Silica-SOMS was tested.

As reported in the literature, the SOMS, before being placed in contact with the pollutant solution, must be converted into their "open" form^[4,5]. In this respect, a pre-swelling of the material with a minimum amount of organic solvent must be performed, to open the pores of the material and to create additional empty space that can be useful for the adsorption of pollutant molecules.

To verify this behaviour, therefore, Rhodamine B adsorption tests were performed on both the unswelled and swelled material with three different organic solvents: acetone, ethanol and acetonitrile.

Figure 7.5 shows the relative concentration of the Rhodamine B in aqueous solution after contact with all the tested materials at room temperature over time. The percentage of removal was assessed using the following equation:

$$\frac{C_i - C_f}{C_i} \times 100$$

where C_i is the initial dye concentration and C_f the one after adsorption.

The measurements have been replicated three times and the average values and relative standard deviations are reported in Figure 7.5A.

It is possible to report the same results as a function of the amount of Rhodamine B adsorbed per gram of material (Q_{ads}), expressed in mg/g. It was calculated using the following equation:

$$Q_{ads} = \frac{C_i - C_f}{m} \cdot V$$

Where C_i is the initial concentration of Rhodamine B solution (mg/L), C_f is the final dye concentration, m is the mass of the sample used for adsorption (g), V is the volume of Rhodamine B solution (L).

A graph showing the change in the amount of RhB adsorbed by materials as a function of contact time is shown in Figure 7.5 B.

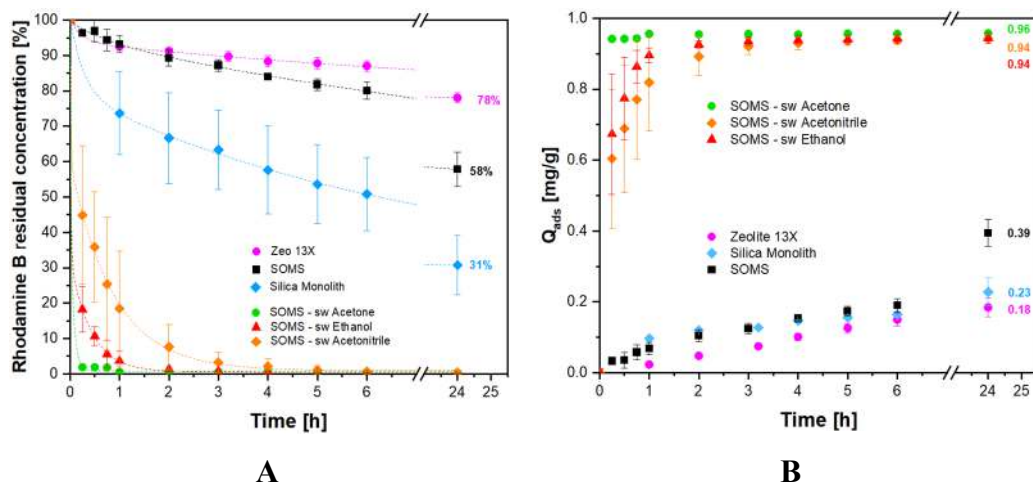


Figure 7.5 - A) Concentration (%) decrease over time of 1×10^{-2} mM Rhodamine B water solution in the presence of the samples; B) Amount of Rhodamine B adsorbed vs. time in water suspensions of the samples.

Zeolite 13X (●), Silica monolith (◆), Silica-SOMS (■), Silica-SOMS swelled with acetone (●), Silica-SOMS swelled with Ethanol (▲) and Silica-SOMS swelled with Acetonitrile (◆).

Error bars represent standard deviations calculated on averaging results collected from three set of experiments.

As can be seen from the Figure, Zeolite 13X is not very effective in sequestering Rhodamine B from the aqueous phase, in fact after 24h of contact it is able to remove only 22% of dye. This behaviour can be explained considering that the molecular size of Rhodamine B (diameter of ca. 1.44 nm) is larger than the pore size of zeolite (1 nm). It is thus probable that RhB is mainly adsorbed on the surface of zeolite, since it cannot access the cages due to steric hinder^[6].

Conversely, the silica monolith is able, after 24 hours of contact, to remove 69% of the dye from the aqueous solution. The adsorption kinetics are rather slow because,

due to the macrostructure of the monoliths, the diffusion processes of Rhodamine B within the material are hindered; in addition, Rhodamine B has to diffuse in the macropore system before it may reach the mesopores^[7].

As reported in the literature, Rhodamine B molecules adsorb on the mesoporous silica materials through electrostatic, hydrogen, nonpolar and π - π bonding interaction. The effective adsorption sites on the silica surface are composed mainly of OH and/or oxygen bridges. At a pH between 5 and 6, Zeta potential of silica was negative, and the surfaces of the adsorbent was negatively charged. The positive moieties in the Rhodamine B zwitterion are attracted by the surface silanolate groups present in silica materials through electrostatic forces. In addition, the residual surface hydroxyls of the mesoporous materials may also form H-bonds with the COO^- group present in the Rhodamine B zwitterion^[1].

The Silica-SOMS proved to be extremely promising, although they have never been used for this application in the literature. They showed excellent adsorption capacity, exceeding that of all tested materials, with fast kinetics.

As pointed out by the results, effective removal of Rhodamine B requires that the Silica-SOMS are allowed to swell prior to contact with the molecule: unswollen Silica-SOMS only adsorb 42% RhB in 24 hours because the material porosity is not open yet under these conditions.

In contrast, if the Silica-SOMS are brought into contact with an organic solvent prior to adsorption, their porous structure can be opened, creating a new porosity and thus increasing the surface area with which Rhodamine B can interact and be rapidly adsorbed^[8]. The improvement in adsorption capacity, both in terms of kinetics and adsorbed amount, is due to the predominance of apolar and π - π -stack interactions, which are established between Rhodamine B and the surface of the Silica-SOMS, despite an electrostatically attractive component^[5,9].

In fact, pre-swollen Silica-SOMS adsorbed nearly 100% Rhodamine B within 24 hours; in addition, Silica-SOMS swollen with acetone and ethanol were able to remove more than 98% of Rhodamine B within the first hour of contact.

7.1.2 Study of the regeneration capacity of Silica-SOMS after Rhodamine B adsorption

Since Silica-SOMS were found to be the best adsorbent material toward Rhodamine B, among all the materials tested, their ability to be regenerated and reused was further investigated.

Silica-SOMS were regenerated by placing them in a beaker in contact with 80 mL of ethanol and sonicating them for 10 min at room temperature. After that, the powders were collected by centrifugation and then dried in an oven at 90 °C for 20 minutes. Five subsequent cycles of adsorption and desorption test were performed on the regenerated material.

Since it was found, in previous experiments, that the Silica-SOMS give the best adsorption performance when they are exposed to an organic solvent before the contact phase, they were swollen with ethanol before each adsorption cycle.

Given the fast adsorption kinetics, the material was placed in contact with Rhodamine B solution for 1 h, taking an aliquot of the solution every 20, 40, 60 min, and analysing it by UV-Vis spectrophotometry.

Figure 7.6 shows the results obtained after 20 minutes of contact, for all the 6 adsorption cycles. Prior to every cycle, the material was regenerated as described above.

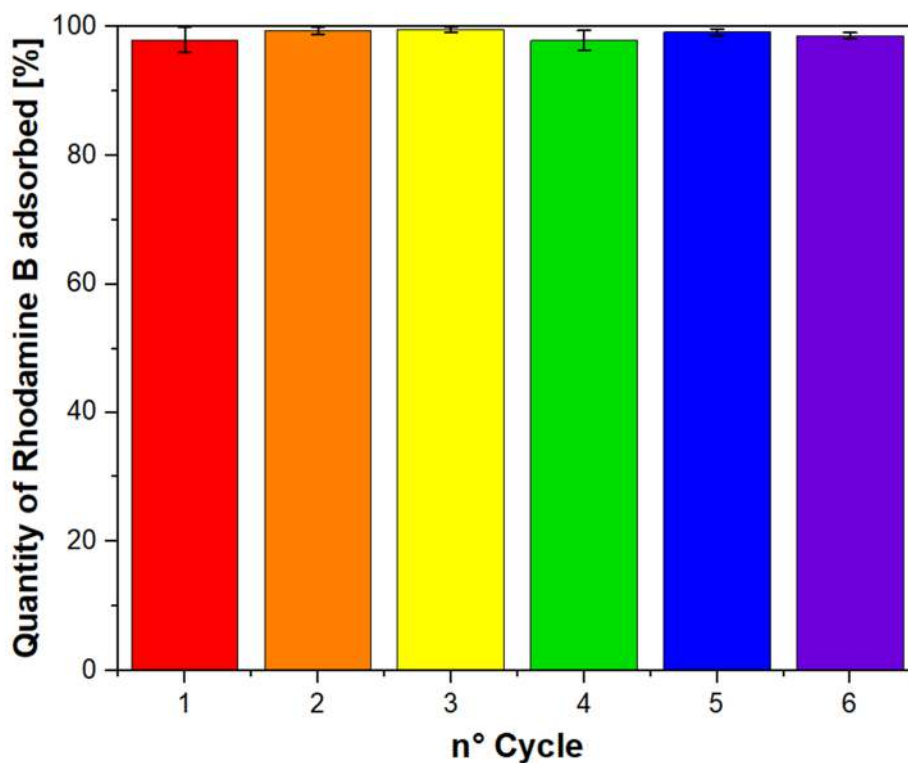


Figure 7.6- Quantity adsorbed (%) of 1×10^{-2} mM aqueous solution of Rhodamine B, after 20 minutes of contact with ethanol-swelled Silica-SOMS, for six successive adsorption cycles. Error bars represent standard deviations calculated on averaging results collected from three replicated experiments.

In Table 7.1 the % adsorption of Rhodamine B after 20 min of contact, and the amount adsorbed, expressed as mg Rhodamine B per gram of ethanol swelled Silica-SOMS, for the six cycled of adsorption are summarized.

Table 7.1 - Adsorption % of Rhodamine B after 20 min of contact, and the amount adsorbed expressed as mg Rhodamine B per gram of Silica-SOMS swolled with ethanol, for the six cycled of adsorption.

	% ads RhB (20 min)	Adsorbed amount [mg/g]
Silica-SOMS - Cycle 1	97.9 ± 1.9	0.816 ± 0.001
Silica-SOMS - Cycle 2	99.4 ± 0.5	0.852 ± 0.001
Silica-SOMS - Cycle 3	99.5 ± 0.4	0.856 ± 0.004
Silica-SOMS - Cycle 4	97.8 ± 1.5	0.826 ± 0.002
Silica-SOMS - Cycle 5	99.2 ± 0.5	0.899 ± 0.011
Silica-SOMS - Cycle 6	98.6 ± 0.5	0.916 ± 0.001

From the obtained results, it appears that the Silica-SOMS is fully regenerable and reusable: in fact, it is able to adsorb almost 100% RhB after only 20 minutes of contact; this is repeated during each adsorption cycle, indicating that the regeneration process of the material does not affect the adsorption performances.

7.2 Removal of Perfluorinated Alkyl Substances (PFAS)

In the PhD, the possibility to remove three PFAS molecules from water media was investigated. Particular attention was given to the study of Perfluorooctanoic Acid (PFOA), Perfluorooctanesulfonic Acid (PFOS) and Perfluorobutanesulfonic Acid (PFBS).

PFOA (Figure 7.7) is an eight-carbon-atom carboxylic acid consisting of a fully fluorinated seven-carbon-atom alkyl chain and a carboxylic end group (-COOH).



Figure 7.7- Molecular structure of Perfluorooctanoic Acid (PFOA).

The pK_a values of PFOA vary from -0.5 to 2.8 depending on the method used for their determination^[10]. Nevertheless, in aqueous solution, at $pH > 3$, the molecules are almost completely in the dissociated form.

PFOS (Figure 7.8) is also part of the long-chain PFAS family; in fact, it consists of a fully fluorinated eight-carbon-atom alkyl chain and a sulfonic (-SO₃⁻) end group.



Figure 7.8- Molecular structure of Perfluorooctanesulfonic Acid (PFOS).

PFOS has a $pK_a < 2$ ^[11] and thus is predominantly found in dissociated anionic form in aqueous solutions at pH above 2.

PFBS (Figure 7.9), on the other hand, was chosen as the reference molecule for the short-chain PFAS class, and has a $pK_a < 0.14$ ^[12]. Again, the polar part of the molecule consists of a sulfonic group while the four-carbon-atom chain represents the apolar part.



Figure 7.9 - Molecular structure of Perfluorobutanesulfonic Acid (PFBS).

Given the chemical and physical properties of these compounds and the low concentrations in which they are present in environmental matrices, special precautions must be taken throughout the analytical process. High performance liquid chromatography (UPLC-ESI(-)-MS/MS) using a triple quadrupole mass detector in "single reaction monitoring" (SRM) mode is the most widely used technique for the analysis of perfluoroalkyl compounds in environmental samples, since it allows the determination of these substances at the concentrations (ppb or ppt) specified in the various regulations^[13].

Current PFAS regulations limit their production and the maximum concentration allowed in tap, surface and waste water; most of them focus on Perfluorooctanoic acid (PFOA) and Perfluorooctanesulfonic acid (PFOS), two of the most spilled PFAS^[14,15].

There are several certified analytical methods developed using these techniques for different matrices and with different types of sample pre-treatment.

For examples, to analyse and determine the concentration of PFAS in environmental media, the Environmental Protection Agency (EPA) has developed and validated several official analytical methods for drinking water, groundwater, surface water,

wastewater, solids (soils, sediments, biota), and biosolids^[16]. These include Method 537.1 (2020) for the determination of selected PFAS in drinking water^[17], and Method 8327.1 (2021) that is related to the determination of PFAS in non-potable water and other environmental media^[18].

They generally involve an initial pre-concentration of PFASs performed by solid-phase extraction (SPE)^[16]. Solid phase extraction is a pre-treatment procedure in which the sample is passed through a prepacked cartridge containing a styrene- and divinylbenzene-based polymer capable of retaining the compounds to be analysed; they are then eluted from the solid phase with 10 ml of a solvent with which they have a high affinity (methanol is usually used), resulting in an increase in the concentration of the sample. The eluate is then injected into the chromatograph, which is equipped with a C18 column and connected to a tandem mass spectrometer^[17]. Preconcentration is followed by analysis by liquid chromatography (LC), which allows separation of the analytes based on their different affinities for the mobile and stationary phases, and mass spectrometric (MS) detection, which uses an external calibration standard to measure the mass-to-charge ratio of the ions and allows their quantification^[16].

The concentration of each analyte is determined using the internal standard technique, and surrogate analytes are added to all samples to monitor the extraction efficiency of the analytes in the method.

Critical issues with these methods include their complexity, the high cost of analysis and the need for dedicated equipment; moreover, certified methods of analysis allow the identification of only a selected and restricted number of molecules over more than 4,700 PFAS compounds discovered^[19].

Therefore, there is a need for faster, cheaper, and simpler methods to detect and quantify PFAS contamination in water^[19,20].

For all these reasons, in addition to HPLC-MS/MS methods, which remain the only ones available for quantifying PFAS at the concentrations required by the regulations, other analytical methods are also used when the PFAS to be determined are present at higher concentrations.

For example, when dealing with process wastewater from facilities that use the perfluoroalkyl molecules, much higher concentrations (of the order of ppm) may be found. In this case, the NMR technique can be used to quantify PFAS concentrations as a viable alternative to classical analytical methods. Since the distinguishing feature of perfluoroalkyl molecules is precisely the presence of one or more fluorine atoms in their structure, and since the concentration of molecules containing natural fluorine atoms is very low in environmental waters, nuclear magnetic resonance spectroscopy of the 19-isotope of fluorine (^{19}F NMR) is becoming a promising alternative to liquid chromatography.

7.2.1 Liquid phase NMR spectroscopy for the determination of PFAS concentration in solution

In the frame of the thesis, liquid phase ^{19}F nuclear magnetic resonance spectroscopy was used to determine the PFAS concentration in water. The ^{19}F isotope, in fact, is an NMR-active nucleus with a nuclear magnetic spin moment of $\frac{1}{2}$, a natural abundance of 100% and a sensitivity of 83.2% of that of hydrogen (^1H)^[21]. In addition, NMR spectroscopy is itself a quantitative technique in that the area under the signal is proportional to the number of atoms giving rise to it and thus to the concentration of the sample.

NMR can then be used for PFAS identification and quantification using an internal standard of known concentration. In the case of the three chosen PFAS molecules, the ^{19}F -NMR signals fall in a wide chemical shift interval ranging from 80 ppm to 120 ppm; in detail, at about 80 ppm the NMR signal of the $-\text{CF}_3$ group at the end of the chain is present, while at around 120 ppm, peaks corresponding to the $-\text{CF}_2-$

groups appear (the number of peaks that appear in the $-CF_2-$ region correspond to number of $-CF_2-$ groups in the molecule based on chain length).

As an example, Figure 7.10 shows the ^{19}F -NMR spectrum of PFOA in solution.

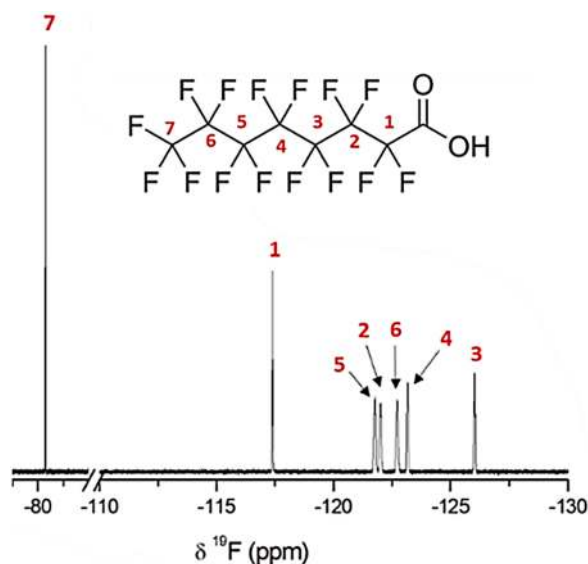


Figure 7.10 - ^{19}F -NMR spectrum of Perfluorooctanoic Acid (PFOA) in solution.

Before performing the adsorption tests, it was necessary to optimize the method in order to quantify the concentration of PFAS remaining in solution after being in contact with the adsorbent material.

A disadvantage of the NMR technique, when compared to other analytical techniques, is the low sensitivity due to the small population difference between the ground state and the excited states. The limit of detection is an important parameter in determining the sensitivity of the method and indicates the lower concentration limit below which an analyte cannot be detected with sufficient statistical probability.

To determine the limit of detection (LOD) and the limit of quantitation (LOQ) of an NMR measurement, the signal-to-noise ratio (S/N) is usually calculated in a series

of experiments performed with samples of increasing concentration, with all other instrumental parameters left unchanged. The value of LOD usually indicates the concentration at which the signal-to-noise ratio is equal to or greater than 3, while the value of LOQ corresponds to the lowest concentration at which the analyte can be quantified, i.e., at which a S/N ratio of 10 or greater is achieved.

In this PhD thesis, we wanted to investigate what instrumental parameters should be used to reach a LOQ of 10 ppm or lower with the ^{19}F -NMR measurements.

For this purpose, a 10 ppm PFOA solution was analysed by performing several experiments increasing the number of scans and thus the analysis time. The measurements were performed with a relaxation delay of 10 seconds, calculated based on T1 data from the literature, which indicate a longitudinal relaxation time of about 2 seconds for the PFAS considered^[22]. At the end of the analyses, the relative signal-to-noise (S/N) ratios were calculated (see Table 7.2).

Table 7.2 - S/N ratios derived from related experiments conducted on PFOA sample at 10 ppm concentration by increasing the number of scans.

n° of scans	Time (min)	Signal-to-noise (S/N)
32	7	2.9
78	16	4.2
160	31	5.8
320	62	8.4
500	96	8.3
625	120	10.1
1000	192	13.2
1250	240	14.7
1600	305	16.8

For the calculation of the "signal area", the range of chemical shift between -80.6 and -81.0 ppm was considered, where there is the signal of -CF₃, while for the "noise area" the spectral range between -79.0 and -80.0 ppm was chosen, where there are no signals.

The signal from the -CF₃ group was chosen because it has a larger area than that from the -CF₂ groups at the same concentration, originating from three equivalent fluorine atoms instead of two.

Assuming a linear relationship between the signal-to-noise ratio and the sample concentration, from the obtained data, it is possible to calculate how the threshold value LOD changes with increasing measurement time; LOQ values were obtained by multiplying the LOD values by 10/3 (Table 7.3).

Table 7.3 - LOD and LOQ related to experiments conducted on PFOA sample at 10 ppm concentration, increasing the measurement time.

Time (min)	LOD	LOQ
30	5.2	17
60	3.6	12
120	2.9	9.9
180	2.3	7.6
240	2.0	6.8
300	1.8	6.0

The results show that for a measurement with a LOQ of 10 ppm (and a LOD of 3 ppm) an analysis of the samples with 625 scans (2 h measurement) is required.

NMR spectroscopy is in itself a quantitative technique, since the area under the recorded signal is proportional to the number of atoms that generate it, and thus to the concentration of the sample. When NMR is used as a quantitative method, it is a

good practice, to improve data reliability, to add to the sample an internal standard whose NMR signal can be used for scaling sample's ones. This reference substance must have NMR signals that do not overlap with the analyte ones; the internal standard must also not react with the analytes in the sample by changing their chemical structure.

An additional advantage of ^{19}F -NMR spectroscopy is that it is possible to quantify any PFAS, which has a resolved NMR signal, without the need to construct a dedicated calibration line for that molecule. In this technique, in fact, the calibration line obtained for one PFAS works for all the fluorine containing molecule in the same sample thus without the need to have a reference standard for all PFASs that one wishes to quantify.

For the quantification of PFAS studied in the unknown samples, a calibration line was made starting from PFOA solutions of known concentration. Solutions of PFOA at known concentration were prepared in the range from 10 to 800 ppm. The solutions were fortified with the internal standard, ammonium trifluoroacetate (TFAA) 0.05% in D_2O (500 μL PFOA solution + 100 μL internal standard). ^{19}F NMR analysis was performed at 300 K by collecting 625 scans with a relaxation delay of 10 seconds that resulted in about 2 h of experimental time. Three genuine replicates were performed for each calibration point. The signal area under the $-\text{CF}_3$ group, normalized by that of the internal standard signal, was plotted as a function of PFOA concentration (Figure 7.11), and this yielded to the calibration line having equation:

$$y = 134.5 \cdot x$$

where y is the intensity of the ^{19}F -NMR signal and x is the PFAS concentration (mM).

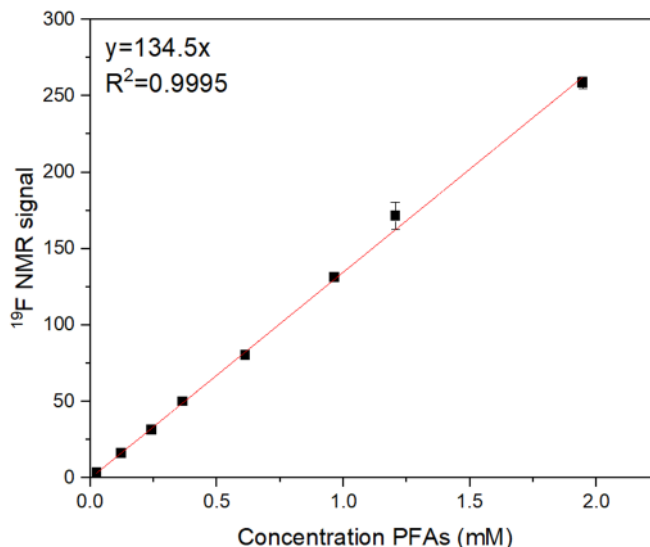


Figure 7.11 - Calibration line obtained from ^{19}F NMR analysis of PFOA solutions at known concentration.

Calibration line shows a good linearity over the entire range of concentrations explored and a good reproducibility of the measurements.

As explained earlier, a calibration line obtained for PFOA can be used to also quantify any other PFAS that has a resolved NMR signal.

7.2.2 Silica-QA-SOMS silicas for PFAS removal

After various preliminary studies conducted on several adsorbent materials, with different characteristics, such as zeolites, silica monolith, Silica-SOMS and porous carbons, the one that was found to be the most promising, and whose results will be reported, is the Silica-QA-SOMS.

To evaluate the adsorption capacity of Silica-QA-SOMS, batch tests were conducted in which 50 mg of material, previously swollen with an organic solvent, was placed in contact with 40 mL of a PFAS solution of known concentration. The samples were kept for 24 h at room temperature under stirring, after which they were centrifuged,

prior to ^{19}F -NMR analysis, and the TFAA internal standard (500 μL PFAS solution + 100 μL TFAA 0.05% D_2O) was added.

The adsorption capacity of the materials was studied in the concentration range from 50 ppm to 800 ppm. The adsorption isotherms obtained, shown in Figure 7.12, describe the relationship that exists between the concentration of the molecule on the surface of the material (q_e , expressed as quantity of PFAS adsorbed per gram of material) and the initial concentration of the molecule in solution (C_i , expressed in mM).

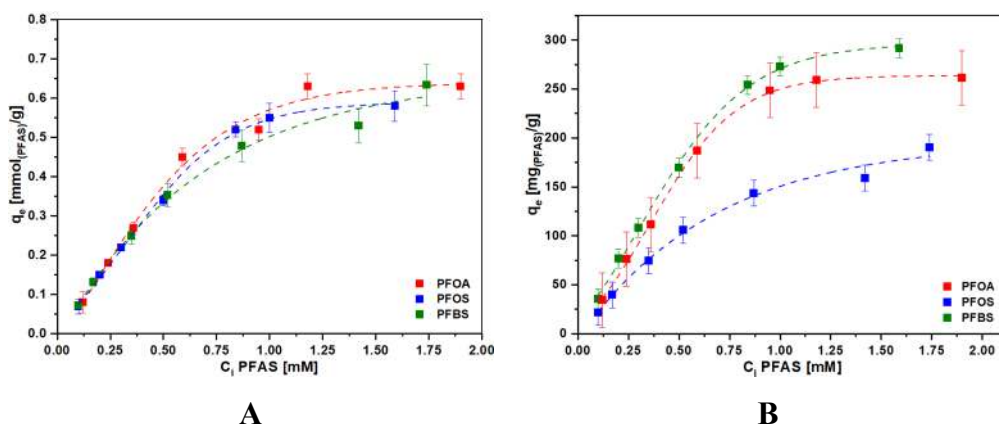


Figure 7.12 - Quantity of PFOA (■), PFOS (■) and PFBS (■), expressed on mmol/g (panel A) or mg/g (panel B) adsorbed on Silica-QA-SOMS, as a function of the initial concentration of the molecules in solution. Error bars represent standard deviations calculated on averaging results collected from three set of experiments.

Silica-QA-SOMS showed high affinity for all the three perfluoroalkyl compounds throughout the whole concentration range tested. The adsorption isotherms reached saturation under the conditions tested, for all the three PFAS molecules. These molecules, when dissolved in water, can have a lower or a higher affinity for the solvent according to their structure: contaminants with higher partition coefficients are hydrophobic. When these molecules come in contact with the surface of Silica-QA-SOMS, they prefer to enter within its porosity rather than staying in solution.

Since Silica-QA-SOMS are highly hydrophobic matrices, which swell during adsorption, when they adsorb these molecules their hydrophobic matrix expands further, generating additional porous volume.

Electrostatic interaction and hydrophobic interaction are the two predominant mechanisms occur during adsorption. Most of the PFAS compounds have both a hydrophobic tail and a hydrophilic anionic group, while the Silica-QA-SOMS, besides having a hydrophobic structure, possesses a quaternary ammonium group that impart a positive surface charge over a wide pH range. As a result, this material allows two adsorption mechanisms, thanks to the combination of cationic groups and hydrophobic pores that makes it possible to capture both long-chain PFASs and the harder-to-process short-chain compounds^[20,23].

There is an effect due to the electrostatic attraction between the positively charged material and the PFAS molecules, which have a negative charge in water; and there is also a confinement effect due to the fact that, being hydrophobic, PFAS tend to remain in the porosity of the material rather than in solution.

Subsequently, the adsorption behaviour of Silica-QA-SOMS in PFAS solutions at low concentrations was investigated. Since, as mentioned above, the method chosen for NMR analysis allows a LOQ of 10 ppm, the samples were analysed by an external laboratory to perform HPLC-MS/MS analyses. The contact method was left unchanged. To verify the correlation between the two methods, the Silica-QA-SOMS samples were put in contact with both solutions at low concentrations of PFOA (10, 1 and 0.1 ppm), and solutions at higher concentrations (50, 100 and 200 ppm) already tested by NMR analysis. The obtained isotherm is shown in Figure 7.13.

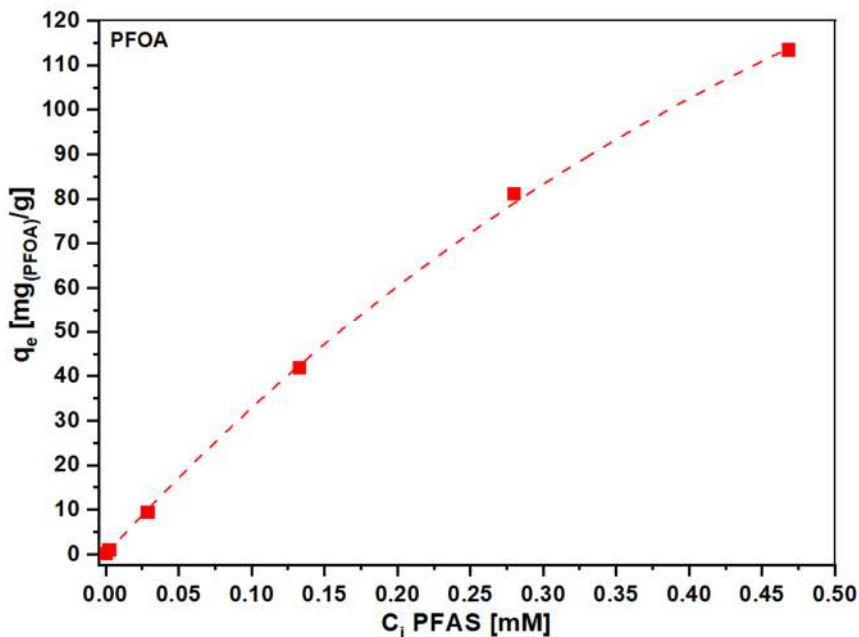


Figure 7.13 - Quantity of PFOA adsorbed on Silica-QA-SOMS (mg/g), as a function of the initial concentration of the molecules in solution. Error bars represent standard deviations calculated on averaging results collected from three set of experiments.

Comparing the data from HPLC analysis with those of NMR analysis (isotherm in Figure 7.12 B), it can be seen that there is a linear correlation between the two methods: the results obtained by the two techniques, after Silica-QA-SOMS was put in contact to PFOA solutions at initial concentrations of 50, 100, and 200 ppm, are in agreement.

A graph was prepared (Figure 7.14), for the values obtained from the solutions at low concentrations, plotting the amount of PFOA adsorbed (mg/g) as a function of the equilibrium PFOA concentration in the solution (ppm) after adsorption, to allow comparison with the data reported in the literature.

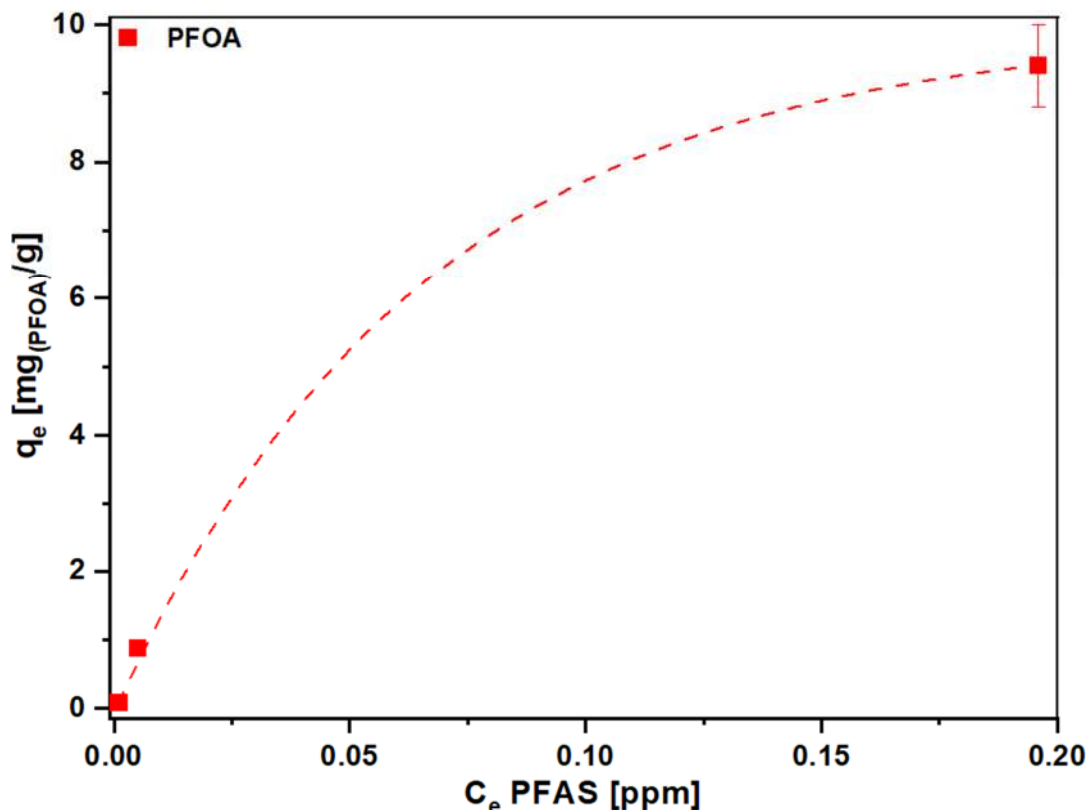


Figure 7.14 - Quantity of PFOA adsorbed on Silica-QA-SOMS (mg/g), as a function of the equilibrium concentration of the PFOA in solution. Error bars represent standard deviations calculated on averaging results collected from three set of experiments.

At the equilibrium concentration of 0.2 ppm, Silica-QA-SOMS adsorbed 9.4 mg/g of PFOA, a value consistent with that reported in the work of Stebel and co-workers, where, at the same equilibrium concentration, Poly-SOMS (a SOMS functionalized with a polymer, Luviquat™ FC 370, containing imidazole and thus characterized by a positively charged repetitive unit), showed a loading of about 10 mg/L^[23]. In the same work, F-SOMS (fluoroalkyl modified SOMS) and SOMS achieved much lower loading of less than 5 mg/g. This result could confirm the key role of the electrostatic interaction between the positively charged material, due to the presence of the ammonium group, and the PFOA molecules in anionic form.

7.2.3 Study of PFAS adsorption kinetic

To study the adsorption kinetics, batch experiments were conducted in which 50 mg of Silica-QA-SOMS, previously swollen with an organic solvent, was placed in contact with 40 mL of a PFAS solution with a concentration of 250 mg/L, under stirring. Aliquots of 500 μL were taken after 15, 30, 45 min and 1, 2, 3, 4, 5, 6, 24 h from the start of the contact. The withdrawn solutions were centrifuged for 3 min at 10000 rpm and analysed by ^{19}F NMR spectroscopy.

Figure 7.15 shows the adsorption kinetics of PFOA, PFOS and PFBS on Silica-QA-SOMS. The adsorption affinity of PFASs was measured as adsorption capacity at equilibrium (q_e).

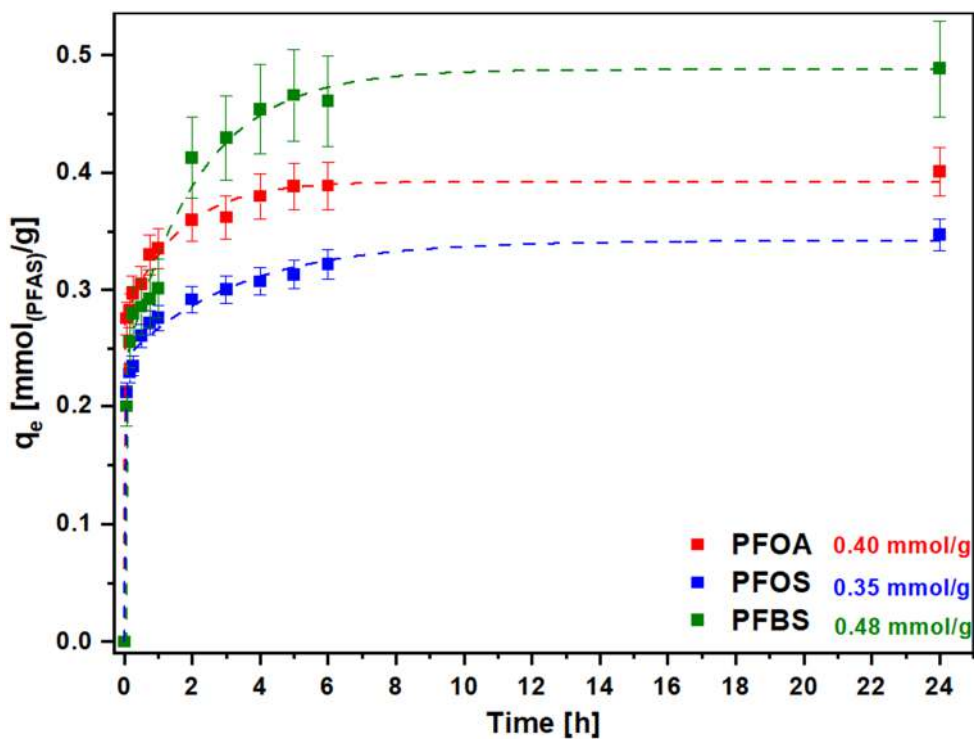


Figure 7.15 - Adsorption kinetic of PFOA (■), PFOS (■) and PFBS (■) on Silica-QA-SOMS, over the time. Error bars represent standard deviations calculated on averaging results collected from three replicated experiments

The adsorption capacity obtained after 24 hours is in agreement with the data shown in the adsorption isotherms.

From the isotherms reported in Figure 7.15, it can be seen that kinetics is fast, especially for PFOS and PFOA adsorption. This is attributed to the open and swollen pore structure, which quickly manages to incorporate PFAS molecules^[23]. Adsorption appears to be facilitated by the open pore system through hydrophobic interactions, however the same number of moles of each PFAS are adsorbed on Silica-QASOMS, independent on the perfluorinated chain length. This fact is a hint that electrostatic interactions govern the amount of PFAS adsorbed.

The pseudo-second-order model is suited to describe the kinetic profiles of Silica-QA-SOMS. This result confirms that electrostatic interaction is crucial in adsorption. The electrostatic interaction is stronger than the hydrophobic interaction, which makes the data better described by a second-order kinetic model that better fits this type of interaction^[24].

Comparing the results obtained with those reported in the literature by Stebel and co-workers^[23], who exposed several materials to a solution containing a concentration of 2 ppm PFOA for 16 hours, it appears that Silica-QA-SOMS exhibits a very fast adsorption kinetics, especially compared to that of activated carbon, and reaches saturation within 2 hours of contact. This is consistent with the data obtained in this work, where Silica-QA-SOMS reached saturation within 6 hours for all three molecules tested, but starting from an initial concentration more than 100 times higher.

Unfortunately, it is difficult to make a more direct comparison with the literature because the reported works usually make adsorption measurements of PFAS in the ppb concentrations range.

7.2.4 Study of the interactions between the Silica-QA-SOMS and PFAS molecules by solid state NMR spectroscopy

The adsorption characteristics of PFAS on Silica-QA-SOMS were studied by solid-state Nuclear Magnetic Resonance Spectroscopy (ss-NMR). NMR spectra of materials before adsorption were compared with those of materials after adsorption of perfluoroalkyl molecules. The presence or absence of signals and their chemical shift can provide important information regarding the adsorption mechanisms.

The materials were characterized by ss-NMR measurements on the two abundant nuclei, ^1H and ^{19}F , and two rare nuclei ^{13}C and ^{29}Si ; the latter nuclei were studied by applying the Cross Polarization (CP) technique on hydrogen or fluorine, since it allowed the polarization from abundant spins (^1H and ^{19}F) to be transferred to dilute spins (^{13}C and ^{29}Si)^[25]. The overall effect is to improve the S/N ratio.

Cross-polarization can be intramolecular, when the polarization is transferred from the ^1H to the ^{29}Si of Silica-QA-SOMS or from the ^{19}F to the ^{13}C of PFAS, or it can be intermolecular: from the ^1H of Silica-QA-SOMS to the ^{13}C of PFAS or from the ^{19}F of PFAS to the ^{13}C of Silica-QA-SOMS. Since a transfer of polarization is only possible when the nuclei involved are close spatial proximity, this gives information about how the PFAS molecules are arranged in the material after adsorption and how they interact with the Silica-QA-SOMS ^[15].

After PFAS adsorption (concentration of 800 ppm), Silica-QA-SOMS samples were dried at room temperature and analysed by ss-NMR. With the aim of obtaining spectra with the best possible S/N ratio, the samples that showed the highest PFAS loadings were analysed.

^1H MAS experiments (Figure 7.16 A) show very broad signals. In order to improve spectral resolution, measurements were repeated using T_2 filter (^1H -ECHO), to reduce signals' width (Figure 7.16 B). Broad signals, in fact, usually arise from short T_2 species, like water, and can be reduced using rotor synchronized spin echo. The measurements were performed with a sample rotation rate of 34 kHz.

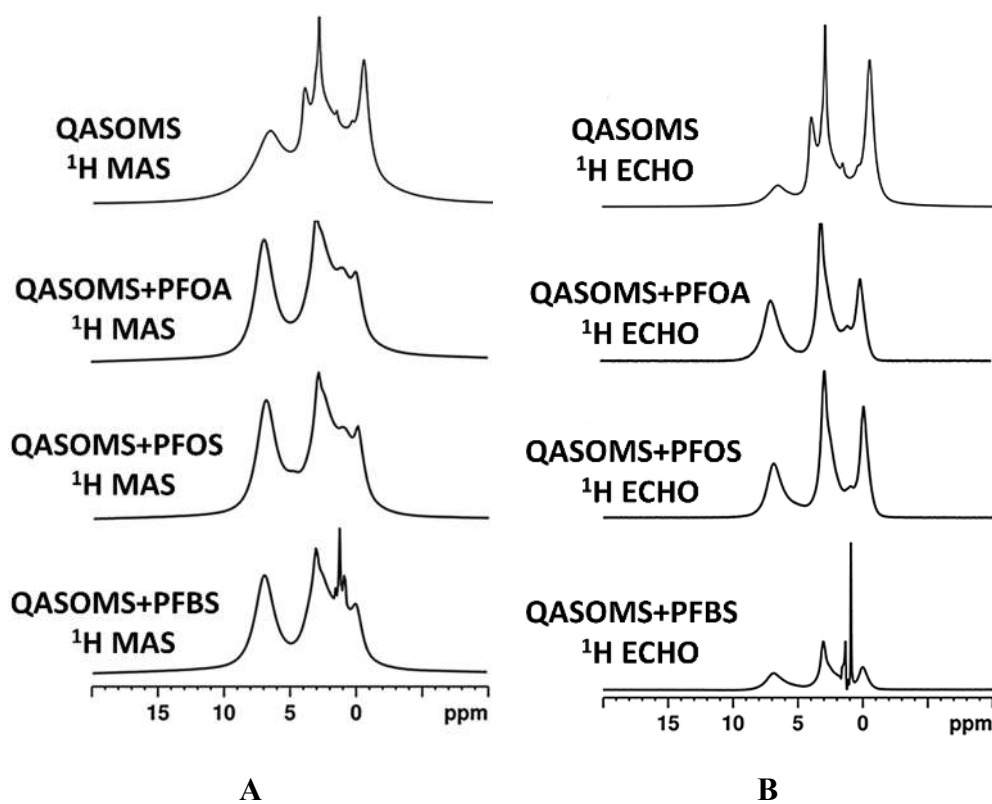


Figure 7.16 - A) ssNMR ^1H MAS spectra of Silica-QA-SOMS before (top) and after adsorption of different PFAS molecules; B) ssNMR ^1H MAS spectra with spin-echo filter of Silica-QA-SOMS before (top) and after adsorption of PFAS molecules

The ^1H NMR spectrum of Silica-QA-SOMS (Figure 7.16A) shows the signal of aromatic hydrogen atoms at 7 ppm, the signals of aliphatic protons at 3 and 1 ppm and the signal of methyl groups directly bonded to silicon at 0 ppm^[26,27].

The comparison of the ^1H MAS spectra of the Silica-QA-SOMS before and after PFAS adsorption shows that the signals remain almost unchanged confirming that the adsorption process has not altered the structure of the material. An increase in the signal at 4.8 ppm, due to the adsorption of water during contact with the aqueous PFAS solutions, can also be observed.

For a better understanding, in Figure 7.17 the molecular structure of Silica-QA-SOMS, PFOA, PFOS and PFBS are reported.

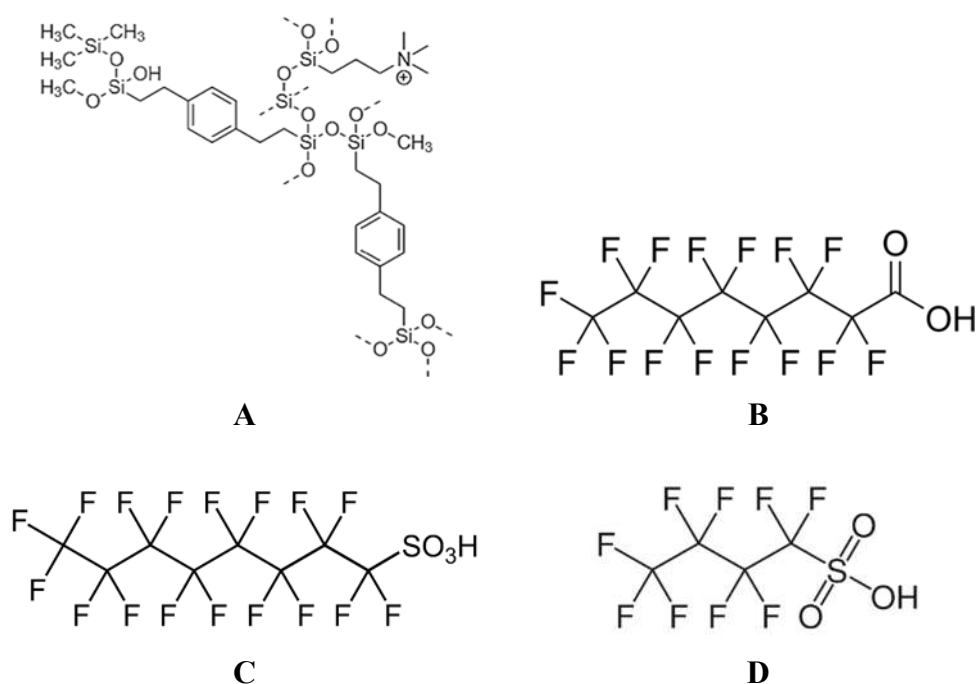


Figure 7.17 - Molecular structure of A) Silica-QA-SOMS, B) PFOA, C) PFOS and D) PFBS.

The ^{13}C NMR analysis was performed by Cross Polarization technique (^{13}C - ^1H CPMAS): the protons of the Silica-QA-SOMS can transfer polarization to its own carbons and to those of the adsorbed PFAS, if sufficiently close (Figure 7.18). Measurements were made by spinning the sample at 10 kHz and with a contact time of 10 ms.

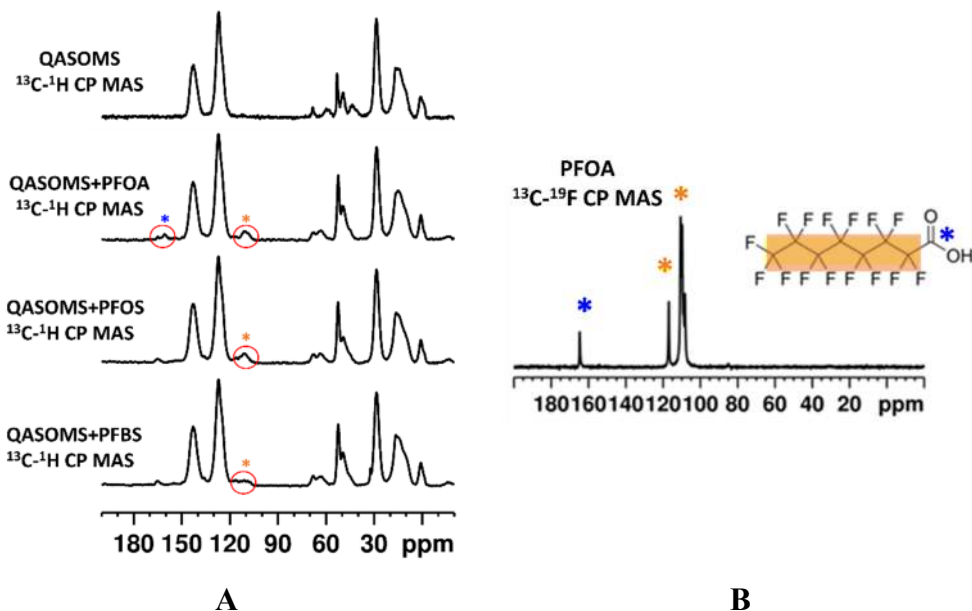


Figure 7.18 - A) ssNMR ^{13}C - ^1H CPMAS spectra of Silica-QA-SOMS before and after PFAS adsorption; B) ssNMR ^{13}C - ^{19}F CPMAS spectrum of the pristine PFOA

In the SS-NMR spectra (Figure 7.18 A), in addition to the signals from the Silica-QA-SOMS carbons, also the ones coming from the perfluoroalkyl molecules can be observed. These signals have a lower intensity because the carbon atoms of PFAS are present in a lower amount compared to those of Silica-QA-SOMS backbone and are more distant (spatially) from the hydrogen atoms of the material. In the NMR spectrum describing PFOA adsorption, in addition to what observed for PFOS and PFBS, a signal coming from the carbon of the carboxyl group also appears.

Figure 7.18 B shows the spectrum of pristine PFOA for comparison.

The presence of the PFAS signals in these spectra is very important because it confirms the presence of the pollutant within the material framework.

Additional ^{13}C - ^{19}F CPMAS measurements were performed with a sample spinning speed of 10 kHz and a contact time of 4, 8 and 14 ms for PFOA, PFOS and PFBS, respectively (Figure 7.19).

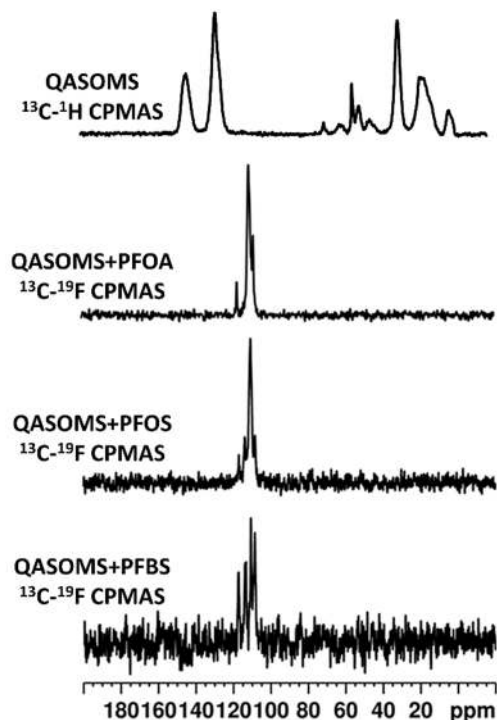


Figure 7.19 - ^{13}C - ^1H CPMAS ss-NMR spectra of Silica-QA-SOMS (top spectra) and ^{13}C - ^{19}F CPMAS ss-NMR spectra of Silica-QA-SOMS after PFAS adsorption.

Only the signals from the carbon atoms of the perfluoroalkyl molecule are visible in the spectrum shown in Figure 7.19, and this may indicate that the carbon atoms of Silica-QA-SOMS are too far from the fluorine atoms to allow polarization transfer. NMR signal for the carboxyl group of PFOA is not observed, since this moiety is probably too far away from the fluorine atoms in the molecule.

It was necessary to use an increasing contact time to optimize the polarization transfer from PFOA to PFOS and PFBS. Normally, a longer contact time is necessary in order to detect molecules with greater mobility or larger distance between the atoms involved in the magnetization transfer^[28].

$^{29}\text{Si}-^1\text{H}$ and $^{29}\text{Si}-^{19}\text{F}$ CP MAS spectra were also recorded (Figure 7.20). The measurements were performed by spinning the sample at 10 kHz and with a contact time of 5 and 12 ms, respectively.

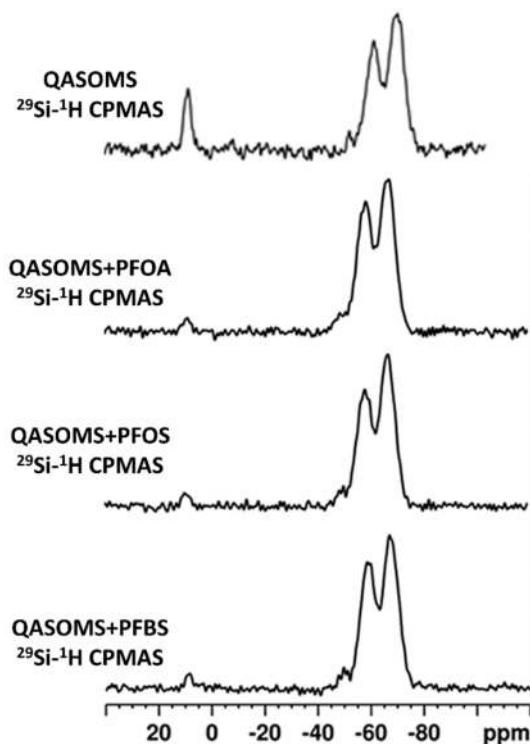


Figure 7.20 - ss-NMR $^{29}\text{Si}-^1\text{H}$ CP MAS spectrum of Silica-QA-SOMS before (high) and after PFAS adsorption;

Figure 7.20 shows the $^{29}\text{Si}-^1\text{H}$ spectra of the Silica-QA-SOMS before and after the adsorption of PFAS molecules. In this case, the polarization transfer can occur inside the adsorbent only. All the obtained spectra show the signals related to the silicon atoms in the Silica-QA-SOMS structure. By comparing the NMR spectra of the Silica-QA-SOMS before and after PFAS adsorption, however, it can be seen that, in the latter, the silicon signal coming from the derivatizing agent (HMDS) has a lower relative intensity. This observation can be explained by considering that during the swelling and adsorption processes the material incorporates some water

molecules. This is confirmed by the ^1H MAS spectra where there is an increase, compared to the material before adsorption, in the signal due to water at 4.8 ppm (Figure 7.16 B). From these observations, it can be hypothesized that the water molecules trapped in the material are mainly near to the silicon atoms that make up the Silica-QA-SOMS structure. This phenomenon causes a greater polarization transfer toward these silicon atoms, rather than the Si-CH₃ groups, affecting the ratios between the areas of the signals in the ^{29}Si NMR spectra.

The ^{29}Si - ^{19}F CP MAS experiments showed no signal; thus, in this case, the transfer of magnetization from the fluorine atoms of the PFAS to the silicon atoms of the material was not achieved. Most likely, the arrangement of the PFAS within the material causes the fluorine atoms to be far from the silicon atoms that make up the structure of the material.

The presence of the perfluoroalkyl molecules within the material was confirmed by the ^{19}F MAS experiment (Figure 7.21).

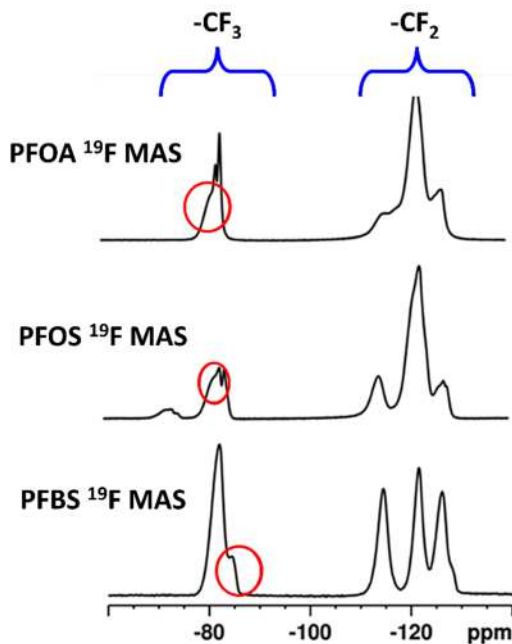


Figure 7.21 - ss-NMR ^{19}F MAS spectra of perfluoroalkyl molecules after adsorption onto the Silica-QA-SOMS.

The spectra, obtained by spinning the sample at 34 kHz, show the same resonances observed in the solution spectra of PFAS. The presence of shoulders and the splitting of signals, particularly visible in the $-\text{CF}_3$ signal, indicate that there are PFAS molecules that have different chemical environments and therefore could be located in different areas of the material.

The analysis of the collected ss-NMR spectra allows us to hypothesize what types of interactions occur between PFAS molecules and Silica-QA-SOMS, and how they are arranged within the adsorbent material.

The electrostatic interaction between the polar groups of the PFAS (negatively charged) and the quaternary amines (positively charged) of the Silica-QA-SOMS is very strong and is the one driving the adsorption process; as a result, the PFAS molecules involved could have reduced mobility. The hydrocarbon PFAS chain could be in hydrophobic interaction with the Silica-QA-SOMS aromatic rings. This

interaction, mainly involving the hydrocarbon chain, is strongly dependent on the swelling degree of the material, and the PFAS mobility is related to the degree of rigidity of the material structure. PFAS molecules interact also with aliphatic groups on the surface of the material (e.g., $-\text{CH}_3$ arising from hexamethyldisilazane). This type of interaction is expected to occur mainly on the outer surface of the material leaving PFAS more mobile.

Conclusions

The adsorption capacities of different inorganic materials (i.e. silica monoliths and zeolite) and hybrid organic-inorganic materials (swellable Organically Modified Silica) toward an organic dye, chosen as a model of a generic pollutant, Rhodamine B, were studied by UV-Vis spectroscopy. Contact tests were conducted in aqueous solution on the different materials, and the decrease in the concentration of Rhodamine B in solution was monitored as a function of the duration of the contact time with the adsorbent material.

Silica-SOMS proved to be an excellent adsorbent material for the removal of Rhodamine B from water. This sample is characterized by excellent performances in both the kinetics of the process and in the amount of pollutant removed. In particular, it was seen that the material must to be firstly "activated" by adding a small amount of organic solvent thus allowing the material to be swollen.

The adsorption mechanism involves both electrostatic phenomena, due to the negative nature of the surface charge of the material and the zwitterionic nature of the molecule, and confinement phenomena, governed by the porosity of the material, which is increased by the pre-swelling operation, but also by the establishment of hydrophobic forces and π - π stacking interactions between the aromatic rings of the material and the molecule. Regeneration of the material was also studied by repeating successive adsorption and desorption cycles of the dye molecule. After six adsorption cycles, it was seen that there is no loss in adsorption performance, which remains quantitatively high and extremely rapid.

Afterwards, the adsorption of three PFAS molecules (PFOA, PFOS and PFBS) on Silica-QA-SOMS was studied through batch experiments by maintaining contact between the adsorbent and PFAS solutions for 24 hours. In this case, the adsorption process was followed using ^{19}F -NMR spectroscopy, as these molecules possess a

fully fluorinated linear chain and ^{19}F is an NMR active nucleus. NMR can, therefore, be used for PFAS identification and quantification using an internal standard at known concentration. Silica-QA-SOMS was previously swelled with an organic solvent before the contact step. It showed excellent adsorption abilities towards all three molecules analysed, both at low and high concentrations.

Electrostatic interactions and hydrophobic interactions were the two predominant mechanisms detected in adsorption processes. There is an effect due to electrostatic attraction between the Silica-QA-SOMS, which are functionalized with a quaternary amine and have a positive charge, and the PFAS molecules, which have a negative charge in water. There is also a confinement effect because the PFAS molecules, which are hydrophobic, tend to be trapped in the hydrophobic porosity of the material rather than in solution.

Finally, the solid-state NMR technique was used to further investigate the interactions between the adsorbed PFAS molecules and the adsorbing solids. The experiments performed confirmed the presence of the adsorbed perfluoroalkyl molecules on the material, and the spectral features showed that the compounds are present in different compartments of the material.

References

- [1] S. Rasalingam, R. Peng, R. T. Koodali, *Applied Catalysis B: Environmental* **2015**, *174–175*, 49–59.
- [2] G. Magnabosco, D. Giuri, A. P. Di Bisceglie, F. Scarpino, S. Fermani, C. Tomasini, G. Falini, *ACS Sustainable Chem. Eng.* **2021**, *9*, 6203–6208.
- [3] A. A. Al-Gheethi, Q. M. Azhar, P. Senthil Kumar, A. A. Yusuf, A. K. Al-Buriahi, R. M. S. Radin Mohamed, M. M. Al-shaibani, *Chemosphere* **2022**, *287*, 132080.
- [4] D. Basu, S. Ailawar, G. Celik, P. Edmiston, U. S. Ozkan, *ChemCatChem* **2020**, *12*, 3753–3768.
- [5] G. Celik, S. A. Ailawar, H. Sohn, Y. Tang, F. F. Tao, J. T. Miller, P. L. Edmiston, U. S. Ozkan, *ACS Catal.* **2018**, *8*, 6796–6809.
- [6] W. Y. Cheng, N. Li, Y. Z. Pan, L. H. Jin, *MAS* **2016**, *10*, 67.
- [7] V. Miglio, C. Zaccone, C. Vittoni, I. Braschi, E. Buscaroli, G. Golemme, L. Marchese, C. Bisio, *Molecules* **2021**, *26*, 1316.
- [8] C. M. Burkett, L. A. Underwood, R. S. Volzer, J. A. Baughman, P. L. Edmiston, *Chem. Mater.* **2008**, *20*, 1312–1321.
- [9] P. L. Edmiston, L. A. Underwood, *Separation and Purification Technology* **2009**, *66*, 532–540.
- [10] K.-U. Goss, *Environ. Sci. Technol.* **2008**, *42*, 456–458.
- [11] J. Cheng, E. Psillakis, M. R. Hoffmann, A. J. Colussi, *J. Phys. Chem. A* **2009**, *113*, 8152–8156.
- [12] D. N. Kothawala, S. J. Köhler, A. Östlund, K. Wiberg, L. Ahrens, *Water Research* **2017**, *121*, 320–328.
- [13] M. Petrovic, M. Farré, M. L. de Alda, S. Perez, C. Postigo, M. Köck, J. Radjenovic, M. Gros, D. Barcelo, *Journal of Chromatography A* **2010**, *1217*, 4004–4017.

- [14] “Directive 2006/122/EC of the European Parliament and of the Council of 12 December 2006 amending for the 30th time Council Directive 76/769/EEC on the approximation of the laws, regulations and administrative provisions of the Member States relating to restrictions on the marketing and use of certain dangerous substances and preparations (perfluorooctane sulfonates),” can be found under <https://eur-lex.europa.eu/eli/dir/2006/122/oj>, **2006**.
- [15] M. Van den Bergh, A. Krajnc, S. Voorspoels, S. R. Tavares, S. Mullens, I. Beurroies, G. Maurin, G. Mali, D. E. De Vos, *Angew. Chem.* **2020**, *132*, 14190–14194.
- [16] O. US EPA, “PFAS Analytical Methods Development and Sampling Research,” can be found under <https://www.epa.gov/water-research/pfas-analytical-methods-development-and-sampling-research>, **2020**.
- [17] US EPA, **2020**.
- [18] US EPA, **2021**.
- [19] D. Camdzic, R. A. Dickman, D. S. Aga, *Journal of Hazardous Materials Letters* **2021**, *2*, 100023.
- [20] I. Ross, J. McDonough, J. Miles, P. Storch, P. Thelakkat Kochunarayanan, E. Kalve, J. Hurst, S. S. Dasgupta, J. Burdick, *Remediation* **2018**, *28*, 101–126.
- [21] D. A. Ellis, J. W. Martin, D. C. G. Muir, S. A. Mabury, *Anal. Chem.* **2000**, *72*, 726–731.
- [22] D. A. Ellis, K. A. Denkenberger, T. E. Burrow, S. A. Mabury, *J. Phys. Chem. A* **2004**, *108*, 10099–10106.
- [23] E. K. Stebel, K. A. Pike, H. Nguyen, H. A. Hartmann, M. J. Klonowski, M. G. Lawrence, R. M. Collins, C. E. Hefner, P. L. Edmiston, *Environ. Sci.: Water Res. Technol.* **2019**, *5*, 1854–1866.
- [24] J.-M. Jian, C. Zhang, F. Wang, X. Lu, F. Wang, E. Y. Zeng, *Environmental Pollution* **2019**, *251*, 425–433.
- [25] W. Kolodziejcki, J. Klinowski, *Chem. Rev.* **2002**, *102*, 613–628.

- [26] I. S. Protsak, Y. M. Morozov, W. Dong, Z. Le, D. Zhang, I. M. Henderson, *Nanoscale Res Lett* **2019**, *14*, 160.
- [27] G. Paul, C. Bisio, I. Braschi, M. Cossi, G. Gatti, E. Gianotti, L. Marchese, *Chem. Soc. Rev.* **2018**, *47*, 5684–5739.
- [28] V. Sacchetto, D. F. Olivas Olivera, G. Paul, G. Gatti, I. Braschi, L. Marchese, C. Bisio, *J. Phys. Chem. C* **2017**, *121*, 6081–6089.

Chapter 8

General Conclusion

This PhD thesis was devoted to the synthesis and characterization of inorganic, organic, and hybrid organic-inorganic materials and to the characterization of commercial materials, both organic and inorganic, for use as solid sorbents for the removal of pollutants from gas and aqueous phases.

In detail, silica-based monoliths, organically modified hybrid silicas and porous carbons, derived from hyper-crosslinked polymers (HCPs), were prepared and, subsequently, characterized through a multidisciplinary approach in order to clarify their physico-chemical properties.

First, a mesoporous silica was synthesized directly in the form of a monolith during the synthesis stage, and its chemical and physical properties were investigated; in particular, the structural properties were found to be homogeneous along the entire length of the monolith, which has an average surface area of approximately 850 m²/g and a total pore volume of 1.2 cm³/g.

The synthesis method for a hybrid organic-inorganic silica (Silica-SOMS), which has the unique property of being swellable only in the presence of an organic solvent, was then reported. Also reported was a variant of the process that allows the material to be functionalized with quaternary amine groups in one synthesis step (Silica-QA-SOMS), which imparts a positive surface charge to the material, as indicated by surface potential measurements. Characterization of the structural properties of both materials showed that the introduction of the quaternary amine groups into the material leads to a decrease in surface area, from 415 m²/g to 283 m²/g for Silica-SOMS and Silica-QA-SOMS, respectively, and an increase in pore volume, from 0.26 cm³/g to 0.65 cm³/g for Silica-SOMS and Silica-QA-SOMS, respectively.

Then, a synthetic method to obtain a high-performance porous carbon from a Hyper Cross-linked Polymer (HCP) was presented, since one of the strategies to obtain activated carbons with excellent textural properties is to use a Hyper Cross-linked Polymer (HCP) as the starting porous precursor. HCP was obtained using the Friedel-Crafts reaction from polystyrene. Infrared analysis of the HCP sample

showed the presence of bands due to stretching vibrations of aliphatic and aromatic carbons, as well as bands related to the formation of the polymer network as a consequence of the crosslinking reactions. Physisorption analysis of HCP reveals the presence of micro- and mesoporosity. The material exhibits a flexible structure, as evidenced by the shape of the hysteresis loop, which remains open even at low relative pressures.

The porous carbon resulting from the carbonization of the HCP loses the flexibility of the starting material, but significantly increases both the porous volume and the specific surface area. In fact, from a starting polymer with a surface area of 845 m²/g and a total pore volume of 0.67 cc/g, a porous carbon with greatly improved textural properties was obtained, having a surface area of 2944 m²/g and a total pore volume of 1.60 cc/g.

In addition, several commercial solids, porous carbons and a zeolite, were characterized using a physico-chemical experimental approach to explore their morphological, structural, surface and textural properties.

Commercial zeolite 13X is a low-Silica zeolites, with a Na⁺ ions in its faujasitic structure. It's a microporous crystalline solid, which has a specific surface area of 837 m²/g, with a microporous volume of 0.22 cc/g and a total pore volume of 0.38 cc/g.

Finally, four different commercially available porous carbons (Maxsorb, Carbotech, Norit and Xintao) were characterized using several techniques.

Raman Spectroscopy showed that Carbon Xintao, having a higher ratio I_D/I_G, has a higher number of defects and is the most disordered carbon; while Carbon Carbotech, having a lower ratio I_D/I_G, it is the less disordered carbon among those analysed. Maxsorb carbon has the largest surface area (2881 m²/g) and pore volume (1.39 cc/g) of all the carbons tested. Carbotech turned out to be a totally microporous carbon, with a large presence of micropores in its structure (0.66 cc/g). Norit and

Xintao carbons possess similar textural properties to each other, shown a specific surface area of 962 and 935 m²/g and a total pore volume of 40 cc/g and 46 cc/g, respectively.

In the second part of this work, the interaction between adsorbents and different pollutants was investigated to understand phenomena playing an important role in the adsorption process.

Concerning the adsorption of pollutants from the gas phase, the adsorption capacity of various materials to sequester two of the main greenhouse gases related to human activities (CO₂ and CH₄) was studied. Then, commercial samples were tested for gas separation from a binary mixture, consisting of methane and nitrogen (in defined proportions).

In order to volumetrically determine the adsorption of gases by the different materials tested two different prototypes were constructed: the first prototype was used to perform static measurements of individual gases, while the second prototype apparatus was coupled with a mass spectrometer, in order to perform dynamic measurement and investigating the ability of the adsorbent material to separate gases from mixture in flow conditions.

Regarding CO₂ adsorption, it was seen that the best adsorption capacities are achieved by materials possessing microporosities, with micropores about two to three times the size of the kinetic diameter of CO₂ (0.33 nm). In fact, the best adsorption performance, at the pressure of 1 bar, was achieved by Zeolite 13 X, storing *ca.* 195 g/kg at a pressure of 1 bar. This result can be attributed both to the presence of Na cations within the zeolite cavities, that interact with the permanent quadrupole of CO₂, since it possesses a micropore family centered at 6 Å. Among

commercial carbons, Carbotech was the most promising, adsorbing 91 g/kg, since it is completely microporous and has an optimal pore size for CO₂ adsorption.

Successively, the storage capacities of the commercial materials with respect to CH₄ and N₂ were tested.

At low pressures (1 bar), CH₄ adsorption is due to the presence of micropores, as it possesses a kinetic diameter of 0.38 nm. For this reason, the best results were obtained from carbon Carbotech that possess a higher fraction of micropores. However, at high pressures (40 bar), the contribution of the mesoporous fraction of the materials also becomes important; consequently, the best performance was obtained from Maxsorb carbon, which at the pressure of 40 bar adsorbed *ca.* 164 g/kg.

In general, although the molecular sizes of CH₄ and N₂ are similar, 0.38 nm and 0.364 nm, respectively, methane should be adsorbed slightly more than nitrogen since it possesses greater polarizability than N₂. However, with the exception of Maxsorb carbon, which adsorbs about 84 g/kg N₂ at a pressure of 40 bar, all other tested carbons showed a slightly higher nitrogen storage capacity than methane. However, the uptake capacity of CH₄ and N₂ in zeolite is comparable, suggesting that it has the same affinity for the two gases.

Therefore, further studies are needed to investigate this aspect.

The ability of commercial adsorbents to separate methane from a binary CH₄/N₂ mixture was also investigated, in order to upgrade it. It was decided to test two mixtures with different proportions (85%CH₄-15%N₂ and 50%CH₄-50%N₂), in flow conditions, to determine whether the behaviour of the adsorbents remains the same or whether it is subject to variations.

In this flow conditions, for both the mixture tested, in accordance with what has been reported in the literature, all samples tested behave in a similar way, absorbing methane and, consequently, enriching the outgoing mixture with nitrogen and depleting it in methane. Under these conditions, the greater polarizability of CH₄

compared with N₂ plays a key role as CH₄ molecules exhibit stronger van der Waals interactions with the adsorbent, resulting in preferential adsorption of CH₄.

Regarding the removal of pollutants in the liquid phase, this work focused on the removal of two types of main pollutants from water: organic dye (Rhodamine B) and emerging pollutants (Perfluoro alkyl substances – PFAS).

Among the different type of organic dyes, Rhodamine B was chosen since it is a model molecule capable of simulating a generic organic pollutant, and it has a high capability to alter the environment and interfere with biological cycles related to photosynthetic processes.

PFAS are a class of amphiphilic molecules consisting of a hydrophobic alkyl chain, fully or partially fluorinated, and a hydrophilic functional group at the head of the chain. These molecules are considered first priority pollutants due to their chemical persistence and widespread occurrence in water, food and living organisms.

The adsorption capacities of silica monoliths, Swellable Organically Modified Silica and commercial zeolite toward an organic dye, Rhodamine B, were studied by UV-Vis spectroscopy.

Silica-SOMS proved to be an excellent adsorbent material for the removal of Rhodamine B from water, adsorbing nearly 100% Rhodamine B within 24 hours, and more than 90% already during the first hour of contact; it was seen that the material must to be firstly "activated" by adding a small amount of organic solvent thus allowing the material to be swollen. The adsorption mechanism involves both electrostatic phenomena, due to the negative nature of the surface charge of the material and the zwitterionic nature of the molecule, and confinement phenomena, governed by the porosity of the material, which is increased by the pre-swelling operation, but also by the establishment of hydrophobic forces and π - π stacking interactions between the aromatic rings of the material and the molecule.

Regeneration of the material was also studied by repeating successive adsorption and desorption cycles of the dye molecule. Silica-SOMS were regenerated by placing them in contact with an organic solvent.

After six adsorption cycles, it was seen that there is no loss in adsorption performance, which remains quantitatively high and extremely rapid. In fact, for all cycles, Silica-SOMS is able to adsorb almost 100% RhB after only 20 minutes of contact.

Afterwards, the adsorption of three PFAS molecules (PFOA, PFOS and PFBS) on Silica-QA-SOMS, previously swelled with an organic solvent, was studied; the adsorption process was followed using ^{19}F -NMR spectroscopy.

Silica-QA-SOMS showed excellent adsorption abilities towards all three molecules analysed, both at low and high concentrations.

Electrostatic and hydrophobic interactions were the two predominant mechanisms detected in adsorption processes. There is an effect due to electrostatic attraction between the Silica-QA-SOMS, which are functionalized with a quaternary amine and have a positive charge, and the PFAS molecules, which have a negative charge in water. There is also a confinement effect because the PFAS molecules, which are hydrophobic, tend to stay in the hydrophobic porosity of the material rather than in solution.

Finally, the solid-state NMR technique was used to further investigate the interactions between the adsorbed PFAS molecules and the adsorbing solids. The experiments performed confirmed the presence of the adsorbed perfluoroalkyl molecules on the material, and the spectral features showed that the compounds are present in different compartments of the material.

List of publications

- 1) Vanessa Miglio, Chiara Zaccone, Chiara Vittoni, Ilaria Braschi, Enrico Buscaroli, Giovanni Golemme, Leonardo Marchese and Chiara Bisio, “*Silica Monolith for the removal of Pollutants from gas and Aqueous Phase*”, *Molecules* 2021, 26, 1316.
<https://doi.org/10.3390/molecules26051316>

- 2) Giorgio Celoria, Vanessa Miglio, Geo Paul, Chiara Bisio, Giovanni Golemme, and Enrico Boccaleri, “*Silica Particles Derived from Natural Kaolinite for the Removal of Rhodamine B from Polluted Water*”, *Processes* 2022, 10, 964.
<https://doi.org/10.3390/pr10050964>

Acknowledgements

I miei più grandi, profondi e sinceri ringraziamenti vanno alla *Prof.ssa Chiara Bisio*, supervisor di questa tesi, che in tutti questi anni mi ha seguita in ogni step, insegnandomi tantissimo, motivandomi, supportandomi e incoraggiandomi sempre. I suoi consigli, preziosissimi e fondamentali, il suo entusiasmo contagioso, la sua bontà e la sua simpatia mi hanno accompagnato durante tutto questo periodo di lavoro, alleviando anche i momenti più difficili. Grazie di cuore per avermi trasmesso la tua passione e per essere sempre stata di esempio e di supporto!

Chiara, lavorare con te è stato (è sarà) sempre un immenso piacere.

Un ringraziamento speciale va al *Prof. Leonardo Marchese*, direttore del nostro Dipartimento, per avermi dato l'opportunità di poter lavorare su questo stupendo progetto.

Un sentito ringraziamento a tutti i membri dell'azienda *Ecospray Technologies* e, in particolare, al presidente *Maurizio Archetti*, con i quali ho avuto il piacere di collaborare durante questo lavoro di tesi.

Un enorme ringraziamento al *Dr. Claudio Cassino* e al *Dr. Geo Paul* per l'interessantissima collaborazione. Lavorare con loro mi ha permesso di imparare molto.

Claudio, Geo, grazie per tutto quello che mi avete insegnato, per tutto l'aiuto, il supporto e i preziosissimi consigli.

Un ringraziamento anche al *Prof. Giorgio Gatti* per l'aiuto datomi durante questo progetto.

Un sentito ringraziamento va anche al *Prof. Giovanni Golemme*, che mi ha accolta con estrema ospitalità all'Università della Calabria, e mi ha permesso di poter lavorare per un periodo nei suoi laboratori, insegnandomi moltissimo.

Acknowledgements

Un enorme ringraziamento va anche ai miei colleghi, nonché amici, del gruppo di Chimica Fisica: *Dr. Stefano Marchesi, Dr. Federico Begni, Dott. Giorgio Celoria e Dott. Lorenzo Maccarino.*

Grazie per il sostegno che mi avete dato durante questi anni, e grazie per tutte le risate e i bei momenti passati con voi.

Ci tengo ad esprimere la mia più profonda gratitudine alla *Dr.ssa Chiara Vittoni* che, nonostante non lavori più con noi, non ha mai smesso di sostenermi dandomi tutto l'appoggio e l'affetto possibile. Oltre ad avermi insegnato moltissimo durante tutto il mio percorso di studi, è diventata una mia carissima amica.

Chiara, sei e sei sempre stata fondamentale! Grazie con tutto il cuore.

Grazie al mio carissimo amico, e collega, *Dott. Alessandro Nucera*, con il quale condivido il raggiungimento di questo importante traguardo, per l'immenso supporto, il sostegno, e per le mille risate che mi fai fare.

Ale, sono davvero felice di aver intrapreso e finito questo percorso insieme a te.

Un grazie alla mia amica e collega *Dott.ssa Chiara Zaccone*, il cui aiuto e supporto (non solo lavorativi) sono stati indispensabili.

Un dovuto e sentito ringraziamento ai miei genitori, *Massimo e Nicoletta*, per avermi sostenuto, spronato e aiutato in ogni modo possibile. Se sono arrivata fino a qui lo devo anche a loro.

Infine, ma assolutamente non meno importante, un infinito ringraziamento a *Edoardo*.

Poche righe non sono sufficienti per esprimere quanto sia grata di averti avuto al mio fianco durante questo lungo percorso. Il tuo amore e il tuo sostegno mi hanno aiutata a superare anche i momenti più difficili.

Appendix

Instrumental Parameters

Scanning Electron Microscopy (SEM)

SEM images were acquired on a Quanta 200 scanning electron microscope (FEI, Eindhoven) equipped with tungsten filament as electron source. Before the analysis, a conductive coating of platinum (20 nm) was deposited on the samples by low-pressure plasma to avoid that insulating particles are electronically charged under the electron beam.

Elemental Analysis

C–H–N elemental contents were determined using an EA 3000 elemental analyser (EuroVector). Helium and oxygen at 120 and 35 kPa pressures were used, respectively. For each material, three measurements were done.

XRPD Analysis

The powder XRD patterns (XRPD) were collected with a Bruker D8 Advance diffractometer (Karlsruhe, Germany) with Bragg–Brentano geometry, with Cu anode ($\lambda = 1.5418 \text{ \AA}$) equipped with a Ni filter and operating at 40 kV and 40 mA. The 2θ interval explored was $5\text{--}50^\circ$, with 2θ steps of 0.01° , 0.5 s/step, and automatic synchronization of the anti-scatter knife; the illumination area of the sample was fixed at 17 mm^2 .

Z Potential

Z potential experiments were carried out at $25 \text{ }^\circ\text{C}$ by using a Malvern Zetasizer NanoZS (Malvern Panalytical, Malvern, UK). 10 mg of powder were dispersed in 10 mL of deionized water and a $0.01 \text{ mol}\cdot\text{L}^{-1}$ HCl (37% w/w (Sigma Aldrich[®])) solution was used until the pH reached a constant value of 5.5 measured with a pH meter. A capillary cell (supplied with the Malvern Zetasizer NanoZS) was used to

carry out the Z potential measurements, and a disposable Pasteur pipette was employed to fill up the cell.

Infrared Spectroscopy (FT-IR)

Infrared spectra were collected by using a Thermo Electron Corporation FT Nicolet 5700 spectrometer with 4 cm^{-1} resolution. Self-supporting pellets of samples were obtained by grinding and compressing the obtained powder with a mechanical press at ca. 7 tons cm^{-2} . To perform the analysis, the obtained pellets were placed into an IR cell equipped with KBr windows permanently attached to a vacuum line (residual pressure $\leq 1 \times 10^{-3}$ mbar), allowing all treatments to be carried out in situ. All the spectra were collected at beam temperature (ca. 35 °C) on samples previously dehydrated at RT for 30 min to completely remove the physisorbed water.

Raman Spectroscopy

Raman analyses were conducted using a LabRAM HR Evolution (Horiba). The spectra were collected at room temperature by taking 6 scans with time acquisition time of 60 seconds. The spectral range considered is in the in the range 100-4100 cm^{-1} . A green laser source at 532 nm was used.

NMR spectroscopy

All spectra were acquired with a Bruker Avance Neo 500 MHz spectrometer and an 11.7 T magnet with operating frequencies for ^{19}F , ^1H and ^{13}C of 470.78, 500.38 and 125.82 MHz, respectively. Glass tubes with a diameter of 5 mm were used.

The experiments were conducted at a temperature of 300 K. The ^{19}F NMR measurements were performed by accumulating 625 scans with a waiting time between accumulations of 10 seconds and a pulse duration i at 90° of 10 μs .

The spectral window used had an amplitude of 100 ppm centered at -100 pm. The zero for the chemical shift scale for the measurements ^{19}F NMR is represented by

the signal of CFCl_3 . The signal of the internal standard trifluoroammonium acetate at -75.5 ppm (vs. CFCl_3).

Solid state NMR spectroscopy

All spectra were acquired with a Bruker Avance III 500 MHz spectrometer and an 11.7 T magnet with operating frequencies for ^{19}F , ^{29}Si , ^1H and ^{13}C of 470.59, 99.36, 500.13 and 125.76 MHz, respectively.

4 mm and 2.5 mm zirconia rotors with kel-F and vespel plugs, respectively, were used. Approximately 50-80 mg of material was placed in the 4 mm rotors, and 10-15 mg in the smaller rotors. The characterization of the materials before adsorption was conducted using 4 mm rotors with MAS rates of 15 kHz and 10 kHz for Cross Polarization mode experiments. The materials after adsorption, on the other hand, were analyzed at a rate of 34 kHz and 10 kHz for the experiments ^{13}C and ^{29}Si in CP mode, using 2.5 mm rotors.

Nitrogen Physisorption Analysis

Nitrogen adsorption measurements were performed at 77 K in the pressure range between 0.01 and 1 p/p₀ of relative pressure using a Autosorb-iQ (Quantachrome Instruments). Prior to adsorption, the samples were outgassed and thermally treated at 150 °C for 5 h. The specific surface area of the samples was determined by the Brunauer–Emmett–Teller (BET) multipoint method in the range between 0.01 and 0.25 p/p₀. The pore size distribution of Silica samples was calculated by applying the BJH (Barrett, Joyner, and Halenda) method on the adsorption branch (Thickness Curve: Halsey, Correction: Standard), and the pore size distribution of porous carbon was calculated by applying Quenched Solid Density Functional Theory (QSDFT) model on slit/cylindrical pores, in the adsorption branch.

Thermogravimetric analysis (TGA)

Thermogravimetric analysis were performed using a Setaram Setys instrument.

A sample of about 10-15 mg was packed in an alumina crucible, which was counterbalanced by an identical empty crucible.

The measurements were done under Argon flow (50 ml min) and under Oxygen (50 ml min) from 20 to 800 °C (5 °C/min heating rate).

